Dust production by evolved stars in the Local Group

A thesis submitted to The University of Manchester for the degree of

Doctor of Philosophy

in the Faculty of Engineering and Physical Sciences

2013

Olivia Jones

Jodrell Bank Centre for Astrophysics

School of Physics and Astronomy

Contents

List of Figures

List of Tables

The University of Manchester

ABSTRACT OF THESIS submitted by Olivia Jones

for the Degree of Doctor of Philosophy and entitled

Dust production by evolved stars in the Local Group. September 2013

Stars on the asymptotic giant branch (AGB) lose a significant fraction of their mass to their surroundings through stellar winds. As a result, they are surrounded by circumstellar shells of gas and dust. This stellar mass loss replenishes and enriches the interstellar medium (ISM) with the products of stellar nucleosynthesis, progressively increasing its metallicity and thereby driving galactic chemical evolution.

In this thesis I present a comprehensive study of oxygen-rich (O-rich) AGB stars and red supergiants (RSG) observed with the *Spitzer* Infrared Spectrograph and *Infrared Space Observatory* Short Wavelength Spectrometer in the Milky Way, the Large and Small Magellanic Clouds, and Galactic globular clusters; focusing on the composition of the dust in the circumstellar envelopes surrounding these stars.

Combining spectroscopic and photometric observations with the   grid of radiative transfer models to derive (dust) mass-loss rates, I detect crystalline silicates in stars with dust mass-loss rates which span over a factor of 1000, down to rates of $\sim 10^{-9}$ $M_\odot$ yr^{-1}. Detections of crystalline silicates are more prevalent in higher mass-loss rate objects, and our results indicate that the dust mass-loss rate has a greater influence on the crystalline fraction than the gas mass-loss rate, suggesting that thermal annealing of amorphous silicate grains is the primary formation mechanism of crystalline silicates in such environments rather than the direct condensation of crystalline silicates from the gas phase. I find that metallicity influences the composition of crystalline silicates, with enstatite seen increasingly at low metallicity, while forsterite becomes depleted at these metallicities due to the different chemical composition of the gas.

To trace the evolution of alumina and silicate dust along the AGB, I present an

alternative grid of   radiative transfer-models for a range of dust compositions, mass-loss rates, dust shell inner radii and stellar parameters. Our analysis shows that the *AKARI* [11]−[15] versus [3.2]−[7] colour is a robust indicator of the fractional abundance of alumina in O-rich AGB stars. From the modelling, I show that a grain mixture consisting primarily of amorphous silicates, with contributions from amorphous alumina and metallic iron provides a good fit to the observed spectra of O-rich AGB stars in the LMC. In agreement with previous studies, we find a correlation between the dust composition and mass-loss rate; the lower the mass-loss rate the higher the percentage of alumina in the shell.

Finally, I present mid-infrared observations of the Local Group dwarf elliptical galaxy M32; where I find a large population of dust-enshrouded stars. These observations will act as a pathfinder for future observations with the *JWST* and *SPICA*.

Declaration

I declare that no portion of the work referred to in the thesis has been submitted in support of an application for another degree or qualification of this or any other university or other institute of learning.

Copyright Statement

To see a World in a Grain of Sand
And a Heaven in a Wild Flower,
Hold Infinity in the palm of your hand
And Eternity in an hour.

William Blake, 1863

Dedication

To Mum, Lillian, Grandpa

with love and thanks,

and for Daddy,

who told me stories but could not stay for mine.

Acknowledgements

First and foremost, I would like to thank my supervisor Ciska Kemper who provided valuable help and guidance over the last few years. I would also like to thank Albert Zijlstra for acting as a second supervisor.

A special mention is due to Iain McDonald, who went out of his way to help me and who always responded with a smile to my pestering/questions. Thank you.

I would like to say thank-you to my all friends at JBCA and in the SAGE collaboration who provided, endless entertainment, discussions, fun and those minute but totally life easing hints and tips. Thanks to everyone in the world of Jod, I am grateful for the opportunity to meet, interview and get to know such a wide range of people across the astrophysics/astronomy community and have a fantastic time while doing it. Also a big shout-out to all the wonderful people I have met on my travels and at conferences particularly those willing to brave karaoke. I am grateful to ASIAA for hosting me in Taiwan and all the friendly people who I encountered who made me feel welcomed and who provided me with many adventures and stories.

Super-massive thanks to all my fab office mates in the office of awesome; especially Jen and Mark for many interesting adventures and shenanigans, Christina for all the random chats, 'just the ones', and her excellent taste in colours with matching ability. To Mike for proof reading, lifts home and for a multi-universe supply of beach balls, Dave for being a top friend from the first welcome, Adam for his colourful plot appreciation skills, George for his non-sequiturs but not for 'pie, sunsets and Spock', Paul for being a fellow SAGE-Spec-er, and Mareike for her super-strength coffee. I am also indebted to Liz, Sundar and Martha for their Cactus care skills.

Outside the world of astronomy, I would like to thank Jamie for impromptu craziness and always being there. Similarly, thanks to my best-friend and life-guru Jemma who has saved me from countless disasters and who has generally made life awesome. You are great.

Mum, Lillian and Grandpa thank you for being wonderful. Without your ever-lasting love and support all my achievements would have not been possible and, more importantly, would have no meaning to me. Finally, a massive thank you to Alan who I love and adore, and who was there share and experience all the joys and stresses along the way.

Supporting Publications

- **Modelling the alumina abundance of oxygen-rich evolved stars in the Large Magellanic Cloud**
  Jones, O. C., Kemper, F., Srinivasan, S., McDonald, I., Sloan, G. C. & Zijlstra, A. A., 2013, MNRAS, Submitted

- **Carbon enrichment of the evolved stars in the Sagittarius dwarf spheroidal**
  McDonald, I., White, J. R., Zijlstra, A. A., Guzman Ramirez, L., Szyszka, C., van Loon, J. Th., Lagadec, E. & **Jones, O. C.** , 2012, MNRAS, 427, 2647

- **On the metallicity dependence of crystalline silicates in oxygen-rich asymptotic giant branch stars and red supergiants**
  Jones, O. C., Kemper, F., Sargent, B., McDonald, I., Gielen, C., Woods, Paul M., Sloan, G. C., Boyer, M. L., Zijlstra, A. A., Clayton, G. C., Kraemer, K. E., Srinivasan, S. & Ruffle, P., 2012, MNRAS, 427, 3209

- **The SAGE-Spec Spitzer Legacy program: The life-cycle of dust and gas in the Large Magellanic Cloud. Point source classification I.**
  Woods, Paul M., Oliveira, J. M., Kemper, F., van Loon, J. Th., Sargent, B. A., Matsuura, M., Szczerba, R., Volk, K., Zijlstra, A. A., Sloan, G. C., Lagadec, E., McDonald, I., **Jones, O. C.**, et al., 2011, MNRAS, 411, 1597

- **The SAGE-Spec Spitzer Legacy Program: The Life Cycle of Dust and Gas in the Large Magellanic Cloud**
  Kemper, F., Woods, Paul M., Antoniou, V., Bernard, J.-P., Blum, R. D., Boyer, M. L., Chan, J., Chen, C.-H. R., Cohen, M., Dijkstra, C., Engelbracht, C., Galametz, M., Galliano, F., Gielen, C., Gordon, K. D., Gorjian, V., Harris, J., Hony, S., Hora, J. L., Indebetouw, R., **Jones, O. C.**, et al., 2010, PASP, 122, 683

1

Introduction

As stars evolve and die, they renew and enrich the interstellar medium (ISM) with the nucleosynthetic products of stellar interiors progressively increasing the ISM's metallicity. This replenishment of matter occurs primarily through dense dusty winds from low–mass asymptotic giant branch (AGB) stars, high–mass red supergiants (RSGs), and supernova. The ISM acts as a repository for this ejecta where, after $\sim 10^8$ years, it is gradually incorporated into the next generation of stars.

Understanding the life-cycle of dust requires detailed analysis of its formation and destruction at each stage in the cycle. Infrared (IR) surveys of Local Group galaxies provide an ideal opportunity to investigate how dust grain properties change with environment on stellar, interstellar and galactic scales. By disentangling the stellar content of nearby galaxies, and by constraining how the mineralogy and chemistry of dust produced by individual evolved stars depends on metallicity, a global picture on the enrichment of the ISM by evolved stars can be obtained.

In the circumstellar environment of evolved stars the dust production depends on the metal abundances with which the star formed. However, the effects of metallicity on the production and properties of circumstellar dust (particularly around oxygen-rich stars) is largely unknown. This work aims to investigate the mineralogical and physical properties of this dust by comparing large numbers of evolved stars in nearby metal-poor galaxies observed with the *Spitzer* Space Telescope.

1.1 Post Main-Sequence Stellar Evolution

1.1.1 Low-intermediate mass stars

The post main-sequence life of a solar-type star of low to intermediate mass (0.8 – 8M$_\odot$) begins once its hydrogen core is exhausted and nuclear fusion processes stop. The hydrogen shell surrounding an inert helium core contracts due to gravity and ignites. As shell burning continues, helium is deposited on the core, which continues to contract until the core density becomes so high that electron degeneracy pressure prevents it from collapsing further. Simultaneously, the higher temperatures cause the star's envelope to expand and become convective. Due to the expansion of the star's outer layers the luminosity rises (while the effective temperature decreases), initiating the star's first ascent on the *red giant branch* (RGB) of the Hertzsprung-Russell (H–R) diagram (Figure 1.1). Further contraction and heating of the red giant core results in temperatures ($\sim 10^8$ K) sufficient for the fusion of helium into carbon by the 3α process (and some burning of carbon into oxygen). The presence of a degenerate core results in localised heating which causes a rapid hydrodynamic explosion known as a *helium flash* (Iben 1968). This flash eliminates the core degeneracy (Härm & Schwarzschild 1961) and a period of core helium burning and hydrogen shell burning ensues. The position the star now occupies on the H–R diagram is governed by metallicity and envelope mass. Population II stars, i.e. those of low metallicity, move to the *Horizontal Branch* (the precise position determined by mass) while the remainder occupy a region known as the red giant clump (see Herwig 2005 and references therein for a more detailed discussion).

Intermediate-mass stars (with masses in the 1.8 – 8M$_\odot$ range) do not develop an electron-degenerate helium core or experience a helium flash (Lattanzio & Wood 2004). Instead, the higher temperatures in the core enables the ignition of helium under non-degenerate conditions. These more massive stars have a similar overall evolution but appear slightly bluer in the H–R diagram.
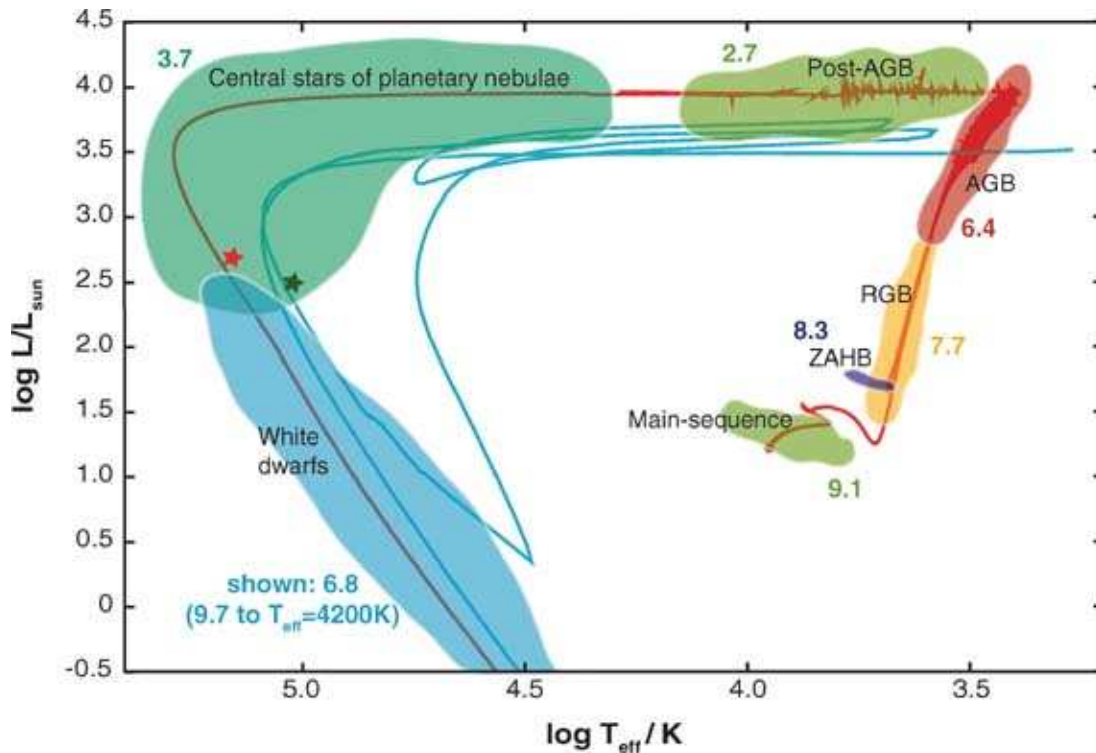
Figure 1.1: Schematic depicting the evolutionary track of a 2 $M_\odot$ star of solar metallicity on a Hertzsprung-Russell diagram, from Herwig (2005). The numbers indicate the log of the approximate timescale spent at each evolutionary phase.

AGB Evolution

In the latter stages of evolution, solar-type stars pass through a region on the HR-diagram known as the *Asymptotic Giant Branch* (AGB), where the star undergoes the last phases of nuclear burning. At the early-AGB stage the stars' degenerate carbon-oxygen core is surrounded by helium and hydrogen burning shells, separated by a He-rich inter-shell region (Figure 1.2). Both shells are enclosed by a convective hydrogen-helium envelope (Sackmann 1980). Initially the H burning shell is inert and He burning provides most of the luminosity (Iben & Renzini 1983). If the star is massive enough ($4 - 8$ $M_\odot$ for solar metallicities) the convective envelope penetrates the hydrogen shell mixing the products of complete H-burning to the surface, significantly altering its
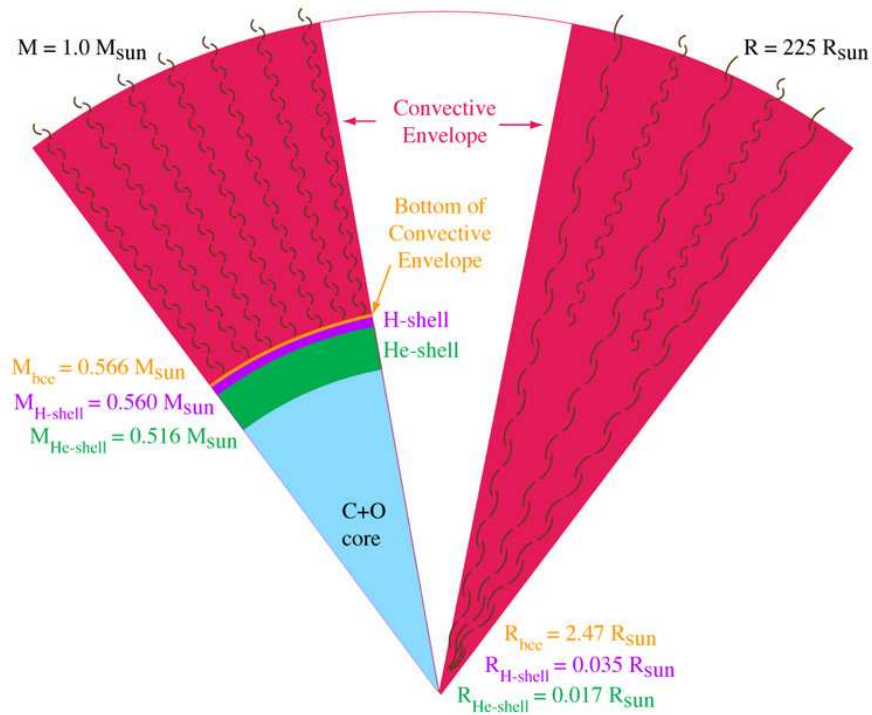
Figure 1.2: Schematic of the inner region of a 1M$_\odot$ AGB star, from Lattanzio & Wood (2004).

composition. This second dredge-up phase only occurs in intermediate mass stars.

Following the second dredge-up (the first dredge-up occurs during the ascent of the RGB) the He burning shell becomes thinner and the hydrogen burning shell reignites. After a short period of time the He shell becomes unstable and the star begins to *thermally pulse*. During this phase the star oscillates between helium and hydrogen shell burning, while periodically (at favourable densities and temperatures) perturbations in the He shell occur (Schwarzschild & Härm 1965). This causes a shell instability and the runaway production of ^{12}C from ^{4}He via the 3α process (similar to that seen in the He-core flash), generating energies of up to 10^8 L$_\odot$ (Habing & Olofsson 2003). As a consequence the local pressure increases, resulting in the expansion and cooling of the star's outer layers, extinguishing hydrogen and (sometime-later) helium shell burning. Between each flash, the luminosity drops and the star again contracts (Habing 1996,
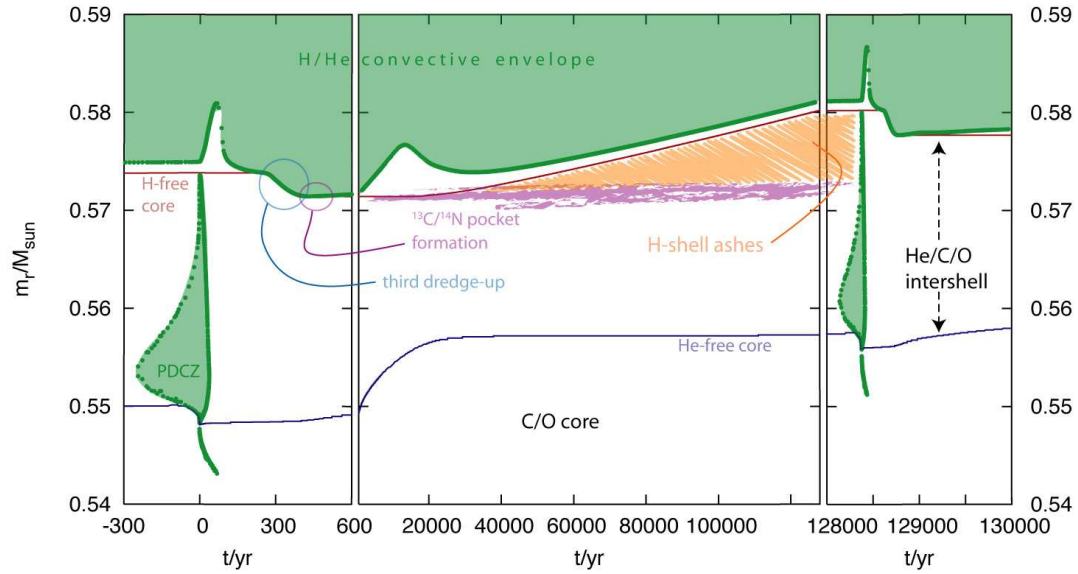
Figure 1.3: Interior evolution during consecutive thermal pulses. The Convective regions are shaded. Image reproduced from Hron et al. (2006).

and references therein). The compression of the hydrogen layer reignites the hydrogen shell. The He shell remains dormant in the inter-pulse phase until a critical mass of helium accumulates on the inner shell initiating another pulse, repeating the cycle. A schematic of the AGB interior during a thermal pulse cycle is shown in Figure 1.3.

Time scales between consecutive pulses range from $\sim 10^4$ to 10^5 years (Lattanzio & Wood 2004), while the number of thermal pulses a star experiences is a function of the initial mass (Marigo & Girardi 2007). After each thermal pulse the convective envelope can penetrate the deeper layers, efficiently bringing the products of nuclear burning to the stellar surface which becomes enriched with ^{4}He, ^{12}C and some s-process elements (Groenewegen 1993). These mixing events or *third dredge-up* episodes increase the C/O abundance ratio of the envelope, where (after a certain number of pulses) it may exceed unity, resulting in a carbon star (Iben 1975; Sugimoto & Nomoto 1975). Thermal pulses continue until the star's convective envelope is dissipated by mass loss (see Section 1.3).
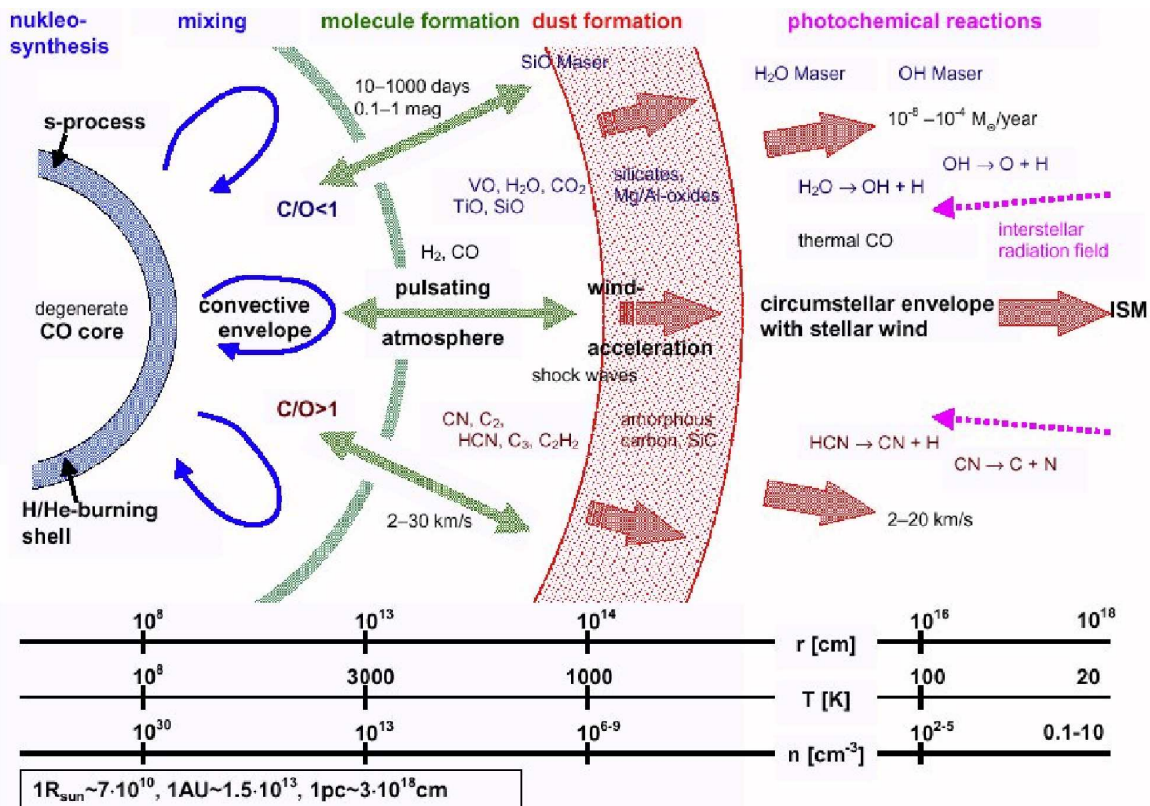
Figure 1.4: Overview of a mass-losing AGB star, indicating the important physical/chemical processes. Image adapted by J. Hron from Le Bertre 1997.

AGB stars are classified into two major spectral types: carbon-rich stars and oxygen-rich stars. The classification depends on the C/O ratio, which is decisive in its future chemical evolution. Once the envelope is cool enough, the stable CO molecule forms until either C or O is exhausted, effectively removing these atoms from further chemical reactions. The types of molecules and solid state particles that can form are thus limited. When more oxygen is available than carbon (i.e. in K or M giants where C/O < 1), oxygen bearing molecules and dust species will form, for instance silicates and oxides such as amorphous aluminium oxide (Al_2O_3). Conversely the chemistry of the envelope surrounding carbon stars (where all the oxygen is trapped in CO) is characterised by the presence of CH, HCN and dust species such as silicon carbide

and amorphous carbon (Grossman 1972; Wallerstein & Knapp 1998; Gail & Sedlmayr 1999; Speck et al. 2000). At lower metallicities there is less initial oxygen and the numerical ratio of carbon to oxygen atom abundances increases. Consequently, the timescales before dredge-up causes the star to become carbon rich are shorter.

Initially all early AGB stars exhibit an oxygen-rich chemistry (C/O ≈ 0.4 at solar metallicity) reflecting the composition of their interstellar birth cloud. As the star evolves, dredge-up gradually increases the C/O ratio from a main-sequence value of C/O ≈ 0.4 to C/O > 1. In this scenario one would expect an intermediate class of objects with C/O ratios close to unity, the *S-stars*. In these objects carbon monoxide depletes both oxygen and carbon, and unusual interstellar dust species like iron silicide (FeSi) are predicted (Gail & Sedlmayr 1999; Ferrarotti & Gail 2002). This has been observationally confirmed by Hony et al. (2009) who identify several unique features (for example SiS) in the spectra of S-stars. These features differ significantly to those in O-rich stars, lacking the characteristic substructure of O-rich species and their peak positions are located at longer wavelengths.

The simplistic picture painted above does not account for AGB stars that have sufficient mass (roughly $M_{ZAMS} > 4M_\odot$) to experience *Hot Bottom Burning*, where a hot thin layer at the base of the convective envelope can sustain proton-capture nucleosynthesis. ^{12}C is converted into ^{14}N, preventing C/O ratios increasing past unity (Boothroyd et al. 1993) and maintaining the oxygen-rich chemistry as the star evolves on the AGB.

Mass loss plays an key evolutionary role along the AGB; this process combines stellar pulsations and radiation pressure acting on dust particles. As the star ascends the AGB, instabilities between gravitational and radiation pressure (cf. Lattanzio & Wood 2004) cause radial pulsations in the outer photospheric region with periods of 100–1000 days. It is generally accepted that these pulsations have a twofold effect: first material is levitated above the photosphere to regions where densities and temperatures are favourable to dust grain formation, and secondly the energy pumped into the atmosphere combined with the radiation pressure on the grains drives the dust and the

coupled gas outward in a stellar wind (Wickramasinghe et al. 1966; Bowen & Willson 1991; Srinivasan et al. 2009). Mass loss increases very rapidly with increasing luminosity (Bloecker 1995). On the lower part of the AGB the stars are non-variable and mass-loss is low but not completely negligible (Reimers 1975; Dupree & Reimers 1987), at this stage the stars do not produce dust or do so only in tiny quantities. Once AGB stars reach a stage in their evolution where they experience pulsations and can be classified as Mira Variables, Semi-regular Variables or Long Period Variables, mass loss is in the region of $10^{-7} - 10^{-6}$ M$_\odot$ yr^{-1} (Willson 2000). At the tip of the AGB a *super-wind* develops, these dense low speed winds (5–30 km s^{-1}) result in mass loss rates of up to 10^{-4} M$_\odot$ yr^{-1} (van Loon et al. 2005). In this super-wind phase the dust formation becomes very efficient, enshrouding the star in an optically thick dust shell. These stars are now referred to as OH/IR stars (unless they are C-rich) due to their strong hydroxyl (OH) masers and IR emission.

Post-AGB Evolution

Once the mass loss from the super-wind and hydrogen shell burning depletes the hydrogen envelope mass to below a critical value of ≈ 0.01 M$_\odot$, the star leaves the AGB. The mass-loss rate then suddenly decreases by several orders of magnitude and the star shrinks with constant luminosity (Kwok 2005). During this transitional period wind velocities increase causing the matter surrounding the core to disperse, the column density drops and a transitional *post*-AGB star becomes optically identifiable (van Winckel 2003; Gielen et al. 2008, 2011). When the effective temperature of the star reaches about 30000 K, temperatures are sufficient for the degenerate C-O core to emit ultraviolet photons, which can illuminate and ionise the ejected circumstellar shell, forming a *planetary nebula*. Eventually the remaining fuel in the H-burning shell will be consumed and all nucleosynthesis processes cease. All that remains is the degenerate core which cools as a *white dwarf* (Paczyński 1971), and the planetary nebula gradually disperses into the general ISM.

1.1.2   Stellar evolution of moderately massive stars

The post main-sequence evolution of moderately massive stars (8-25 $M_\odot$) is complex, and they follow a rather divergent evolutionary track through the HR-diagram compared to AGB stars. In these massive stars the temperature and pressure in the core is sufficient for the fusion of helium into carbon and oxygen preventing a degenerate core developing. Instead, the successive fusion of ever heavier elements occurs until an iron core is produced and the core collapses in a Supernova explosion.

Red supergiants (RSG) are a short-lived stage in the evolution of moderately massive stars. These stars have exhausted their supply of hydrogen and are undergoing core helium burning. During this phase of evolution their cool effective temperatures and high luminosity resembles that of the lower-mass AGB stars. Furthermore, these stars experience similar phenomena, including dust condensation, radial pulsations (albeit with smaller amplitudes) and mass loss through a slow, dense dusty wind.

1.2   Dust Life Cycle

The perpetual cycling of matter between stars and interstellar space gradually alters the chemical composition of a galaxy. Dust provides an excellent tracer of this cyclical interaction, and by studying its formation, evolution, and destruction we can resolve the crucial physics in each stage in the cycle. Outlined below are the many steps involved in the life-cycle of dust, from its formation in the atmospheres of evolved stars, to where dust grains ultimately become consumed by star formation.

1.2.1   Dust formation on the AGB at solar metallicities

The evolution of dust in galaxies is intrinsically linked with that of the stars, with the formation of new grain material coinciding with stellar deaths. In our galaxy AGB stars dominate the injection of new dust into the ISM (Whittet 1992, 2004; Sloan et al. 2008) while high-mass stars in the RSG phase of evolution also contribute significantly (Gail

2003). Other sources that may produce dust are Wolf-Rayet stars, novae (although only in small quantities) and supernovae (Gehrz 1989). The relative contribution of dust from supernovae remains controversial as they also destroy dust (Dunne et al. 2003; Dwek 2004; Krause et al. 2004; Sugerman et al. 2006; Matsuura et al. 2011; Gomez et al. 2012), but at the current epoch it is assumed that supernova produce only moderate amounts of dust. For the purpose of this work the discussion will be limited to the production of dust around AGB stars, although a similar description can be applied to the RSGs.

Dust Condensation Zone

In order for grain formation in evolved stars to occur, several rather specific conditions need to be fulfilled. In AGB stars it is believed that radial pulsations levitate gaseous material above the surface of the star (Habing & Olofsson 2003), resulting in a cooling outflow from which new molecular species form and (at temperatures below ∼1400 K) dust grains condense (Höfner et al. 1998).

Evolved stars on the AGB are cool, with photosphere temperatures between $T \approx$ 2000 – 4000K (this can be higher at low metallicities; Lattanzio & Wood 2004), surrounded by a dense circumstellar envelope of molecular gas and dust that can extend to 10^3 to $10^4 R_*$, where R_* is the stellar radius (Olofsson 2004; Sargent et al. 2010). Close to the photosphere temperatures are too warm for solids to condense, but at greater radial distances ($R > 2.5\ R_*$) the gas temperature is sufficiently low (i.e. below the condensation temperature; $T_C \leq 1500K$) and densities are sufficiently high for dust formation to occur (Gail 2003).

Around two stellar radii, a quasi-static, dense, *warm molecular layer* forms (Tsuji et al. 1997; Woitke et al. 1999; Yamamura et al. 1999; Cami et al. 2000; Matsuura et al. 2002; Ohnaka et al. 2005), the physical conditions of which make it an ideal site for dust formation. Various kinds of molecules inhabit this extended atmosphere. Close to the photosphere where densities and temperatures are high the molecular abundances are determined by local thermodynamic equilibrium, CO, H_2O and SiO are formed

in abundance (Ohnaka et al. 2005; Decin et al. 2010). Within the warm molecular layer dynamical effects due to pulsations and radiation pressure on molecules and dust produce a stratified atmosphere (Helling & Winters 2001) in which molecules group according to the physical conditions they experience.

The mineralogy of the dust shell depends strongly on the composition of the warm molecular layer and the dust condensation radius (Grossman 1972; Tielens 1998; Gail & Sedlmayr 1999; Dijkstra et al. 2005; Karakas & Lattanzio 2007), while the efficiency of dust formation depends on the physical conditions within the envelope. Solid state particles can condense out of the gas if the partial pressure of the condensable species is (much) larger than the species' vapour pressure (Gail & Sedlmayr 1999) within a temperature range of $\approx$ 1800 K for corundum (Al_2O_3) to $\approx$ 500 K for magnetite (Fe_3O_4) (Tielens 1990). Variations in gas pressure, C/O ratios and overall metallicity have been shown to alter the condensation temperature of the dust by several hundred degrees, and therefore need to be taken into consideration (Lodders & Fegley 1999) when drawing comparisons between different populations. The density distribution of the envelope (which is a function of mass-loss rate) also influences the dust mineralogy. In low mass-loss rate objects the premature termination of the condensation sequence can occur if there is a steep decline in dust density with distance from the star (i.e., the wind density deviates from a $1/r^2$ distribution), thus the density drops below the density required for the next step in the condensation sequence.

Nucleation

Dust formation is a complex process in which the details of how simple molecules grow into large assemblies are poorly understood. Models of grain formation require nucleation sites that form the grain core from which the dust species grows (Gail & Sedlmayr 1988). The intricacies involved make the first step in grain formation, the nucleation of small clusters, difficult to model from first principles. To simplify matters, many studies on the condensation sequences in evolved stars do not consider the problem of nucleation of grains but simply assume seed nuclei are formed at tempera-

tures above the stability limit of the main dust components.

Nucleation models, particularly in O-rich atmospheres, are poorly developed as the understanding of the grain nucleation process is still limited. In carbon chemistries nucleation is less problematic as pulsations aid the formation of large polycyclic aromatic hydrocarbon (PAH) molecules (Cau 2002). These can then form larger particles through direct chemical reactions with acetylene. In oxygen-rich chemistries large molecules do not form in sufficient quantities, and an alternative nucleus is required.

Condensation Sequence

In general, dust condensation occurs in several stages. The order in which the different dust species occur depends on the physical conditions and the raw material available for condensation of solids. In order to predict which types of condensates will be dominant, studies generally adopt thermodynamic equilibrium. The thermodynamic condensation sequence for O-AGBs with a solar composition is shown in Figure 1.5.

Equilibrium condensation for a cooling gas of solar composition was first addressed by Grossman (1972) and adapted for circumstellar outflows by Tielens (1990, 1998), who compared the results to spectra obtained by the *Infrared Space Observatory* (ISO). These calculations show that, for conditions in circumstellar shells with an oxygen-rich element mixture, the main dust components expected to be formed in chemical equilibrium are forsterite (Mg_2SiO_4) followed by enstatite ($MgSiO_3$) and metallic iron. Additionally several very refractory compounds such as TiO and ZrO condense out at temperatures above the stability limits of the main components. These are not abundant enough to form quantifiable dust species but may be important seed nuclei for the growth of dust grains formed by more abundant elements. For example, simple oxides of aluminium or the less abundant titanium are often proposed as the basis of seeds in O-rich environments (Jeong et al. 2003). The stability limits for some important condensates are shown in Figure 1.6.

In circumstellar regions the condensation of dust occurs in a rapidly cooling and diluted environment; in these conditions it is unlikely that the molecular gas will obtain

[1760-1300K]
Al_2O_3, Alumina

⬇

[1625-1400K]
$Ca_2Al_2SiO_7$, Gehlinite

⬇

[1440-1050K]
Mg_2SiO_4, Forsterite

[1450-1100K]
$CaMgSi_2O_6$, Diopside

⬇

⬇

[1360-1000K]
$CaAl_2Si_2O_8$, Anorthite

[1350-1040K]
$MgSiO_3$, Enstatite

⬇

[1100-950K]
$[Mg,Fe]_2SiO_4$, Olivine
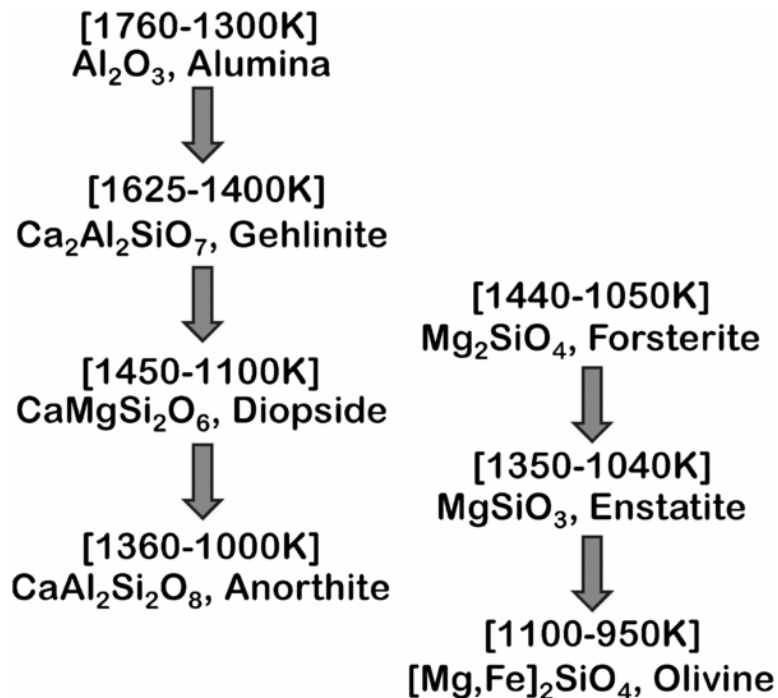
Figure 1.5: The thermodynamic condensation sequence for a gas of solar composition. The temperature refers to the first appearance of the mineral at the pressure relevant for stellar outflows (P $\sim 10^{-6} - 10^{-3}$ bar). Image reproduced from Tielens (1998); after Grossman (1972).

a state of equilibrium. Dust formation and growth under non-equilibrium conditions requires mantle growth of each condensate to be solved simultaneously with the consumption of stellar material and the equations which govern the complex dynamics of the stellar wind. Solutions for these equations for a spherically symmetric stationary outflow with a chemical composition typical of an oxygen-rich AGB star have been obtained by Gail & Sedlmayr (1999). They found that the chemical composition of the condensates mainly consist of compounds formed from the refractory compounds Mg, Si and Fe together with oxygen, although some dust may be formed from the less abundant elements Al and Ca. Olivine ($Mg_{2x}Fe_{2(1-x)}SiO_4$) and iron grains were found to dominate the multicomponent dust composition, with some periclase (MgO) forming in the outflow. Correspondingly, Ferrarotti & Gail (2001) explored the con-
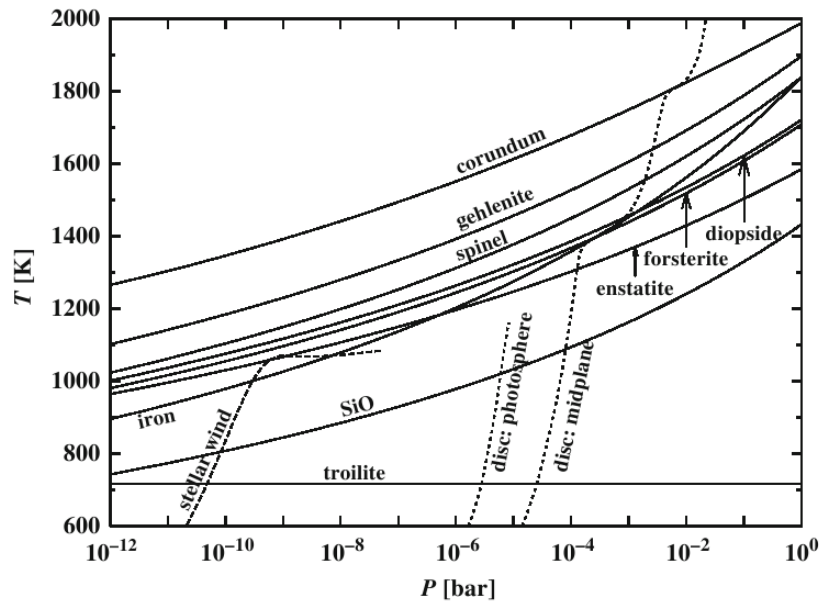
Figure 1.6: Stability limits in the P–T plane for some important dust species formed by the most abundant refractory elements in a oxygen-rich element mixture, from Gail (2010).

sequences of variations in Mg and Si abundance ratios on the composition of silicate grains, like Gail & Sedlmayr they found that olivine-type materials are favoured over pyroxene-type ($Mg_xFe_{1-x}SiO_3$) condensates for the abundant dust component.

Experimental studies on condensation sequences provide an alternative approach for determining the dust mineralogy in stellar outflows. The advantage of such an approach is the freedom from equilibrium situations or highly idealised environments. However, achieving the densities, temperatures and timescales analogous to stellar out-flows is challenging. The first such study was conducted by Day & Donn (1978). In their experiment Mg and SiO solids were evaporated into an atmosphere of argon or hydrogen. They found that the condensates from the silicate material were mostly amorphous with widely varying stoichiometries. These grains were vary stable upon heating in a vacuum, requiring temperatures of 1100 K for conversion into crystalline forsterite (Mg_2SiO_4). Subsequent condensation experiments on a wide range of vapour

compositions (Nelson et al. 1989; Rietmeijer et al. 1999; Nuth et al. 2002; Rietmeijer et al. 2009) produced amorphous grains that had a limited number of mixed compositions. For example, Rietmeijer et al. (1999) found that condensates from a mixed Fe-Mg-SiO vapour does not produce solids with mixed Mg-Fe-O composition but pure Fe-rich or pure Mg-rich silicates. Other techniques that are used in laboratory experiments to produce grains with a controlled composition or structure include laser ablation, sol-gel reactions and arc discharge (for more details on these methods see Brucato et al. 2002 and references therein).

1.2.2 Interstellar Medium

Ultimately the stellar wind from AGB stars expels the newly formed dust grains into the diffuse ISM where they are subjected to a number of collisional and destructive mechanisms. The standard residence time for dust injected into the ISM of the Milky Way is $\sim 2.5 \times 10^9$ years (Jones et al. 1996; Jones & Nuth 2011) before incorporation into new proto-stellar systems, yet due to the various destruction mechanisms the average dust lifetime is approximately $(2.2 - 6) \times 10^8$ years (Tielens 1998), thus interstellar dust grains must rapidly re-form under conditions appropriate to the ISM. While dust formation processes in the ISM are not clear, it probably takes place in dense molecular clouds (Sofia et al. 1994).

In molecular clouds grain growth most likely occurs through the accretion of metal elements onto grains and coagulation. (Boulanger et al. 2000; Zhukovska et al. 2008; Hirashita 2012). Injected circumstellar dust probably serves as condensation centres for heavy elements not incorporated into grains, and these may be further processed into more complex species. Thus, due to the processing of dust and the vastly different conditions in molecular clouds to those in circumstellar outflows, the majority of dust in the ISM will reflect interstellar compositions and conditions. At a later point this newly-formed dust will be recycled back into the diffuse ISM where it is again destroyed; this cycle occurs many times before the dust is locked up in star forming

regions.

High-velocity shocks (> 200 km s^{-1}) from supernova explosions dominate grain destruction in the ISM through thermal sputtering (Draine & Salpeter 1979; Seab & Shull 1983; Jones et al. 1994, 1996), while in lower velocity shocks grain-grain collisions cause shattering as well as vaporisation. The cumulative effects of many strong shocks essentially lead to the complete disruption of all large (≈ 1000 Å) grains, significantly altering the grain size distribution. In addition, cosmic ray impacts may also process the grain, transforming its physical structure through the deposition of energy in the mineral lattice, this has been seen in some pre-solar grains (extracted from meteorites) that have survived with relatively little damage from their residence in the ISM. In these grains tracks are clearly visible from cosmic ray collisions (Bradley 1994).

1.2.3   Star-Forming Regions

Eventually, if a grain is not destroyed by interstellar shocks it will probably end up in a dense cloud core of a collapsing protostellar region (Suttner et al. 1999; Dullemond & Dominik 2005). In order for the cloud to collapse fully, the excess gravitational energy needs to be radiated away, otherwise thermal pressure will prevent further contraction. Dust dominates the cloud's opacity, effectively absorbing the optical photons and re-radiating the excess energy in the infrared where the cloud is optically thin. Thus dust plays a pivotal role in the development of a hydrostatic core. The formation of a new star and the subsequent accretion and coagulation of the grains into various bodies essentially ends the life cycle of dust in a galaxy.

1.3   Dusty Winds

The outflow dynamics, and in particular the density and velocity of the wind, play an important role in the formation and evolution of dust. Winds of cool luminous AGB stars are accelerated in their outer atmospheric region, driven by radiation pressure on

the newly formed dust grains. These grains have a high opacity in the ultraviolet, optical and near-IR, thus are efficient absorbers of stellar photons. The strong radiation fields from the stellar photosphere impinges on the grains transferring momentum resulting in a net acceleration outwards (Gehrz & Woolf 1971; Bowen 1988; Lafon & Berruyer 1991; Fleischer et al. 1992; Sedlmayr & Dominik 1995; Höfner 2008). In densities typical of AGB stars the gas and dust are collisionally coupled, mostly via grain-H_2 collisions (Gilman 1972), and so the surrounding gas is also expelled from the star at velocities between 5 and 30 km s^{-1} (Marshall et al. 2004) resulting in mass-loss rates of up to 10^{-4} M$_\odot$ yr^{-1}.

Observations of the winds in AGB stars show that velocities exceeding the local escape velocity occur at several stellar radii above the photosphere (Richards et al. 1999), supporting the idea that dust is the driving mechanism of the winds in these cool luminous objects. Stars with similar mass, luminosity and effective temperature can have quite different winds and mass-loss rates (Höfner & Andersen 2007). Metallicity can also influence the wind properties: this is discussed in detail in Section 1.5.

The momentum coupling between the grains and the gas sets a lower limit to the mass-loss rates that can be driven by dust, on the order of 10^{-7} M$_\odot$ yr^{-1}. The momentum exchange per collision and the rate of collisions depend on the velocity of grains with respect to the gas. At low mass-loss rates early in the AGB phase, the drift velocity (the relative velocity of the dust grains with respect to the gas) is high. This means that the grains rapidly pass through the region where grain growth is efficient, consequently the average grain size will be small (Simis et al. 2001). Due to their large surface to mass ratio, grain acceleration becomes more efficient and the drift velocity increases. If the drift velocity becomes too high the resulting collisions with the gas particles will be energetic enough to destroy the grains. This limits the terminal speed of the dust particle as it travels through the gas.

High mass-loss rates occur when the drift velocity is low and the density is high. The gradual increase of the average grain radius with time leads to lower drift velocities. Consequently the mean free path is shorter and more outward momentum is

transferred to the gas. As the dust is accelerated outwards and gas densities quickly decrease, grain growth effectively halts.

In recent years the driving mechanism for the super-wind of the oxygen-rich case has been queried, whereas in carbon stars the mass-loss mechanism appears to be relatively well understood, as demonstrated by comparisons between observations and dynamical models (Gautschy-Loidl et al. 2004; Nowotny et al. 2005). Detailed dynamical models for M-type stars require the silicate grains condensing in AGB atmospheres to have an extremely low iron content (cf. Woitke 2006; Höfner & Andersen 2007). Increasing the Fe content would cause too much radiative heating of the silicate grains, and consequently the re-evaporation of the grain. Analysis of astronomical spectra support this conclusion. Observations show that circumstellar crystalline silicates (e.g., olivine [$(Mg, Fe)_2SiO_4$] and pyroxene [$(Mg, Fe)SiO_3$]) are magnesium-rich (Tielens 1998; Bowey & Adamson 2002), however it is conceivable that amorphous silicates have an Fe component (Molster et al. 1999a; Kemper et al. 2004; van Boekel et al. 2005). Without this inclusion of Fe-bearing silicates the grain opacity is not high enough to efficiently absorb the stellar light at near-IR wavelengths (Tielens 1998; Woitke 2006), consequently radiative pressures are too low to generate the mass-loss rates observed. Micron-sized Fe-free silicate grains may provide a possible solution to the opacity problem in the winds of M-type stars; the high radiative scattering cross-section of these small grains compensates for their low absorption cross section (Höfner 2008; Norris et al. 2012) resulting in sufficient radiative pressure to drive an outflow. Other proposed solutions include the formation of small amounts of carbon based dust or solid iron condensates (Kemper et al. 2002; McDonald et al. 2010).

1.4   Infrared Studies of Dusty Evolved Stars

The cool photospheres (T ~ 2000 – 4000 K) of AGB stars emit the peak of their radiation in the near-IR portion (from about 0.8 to 2.5 μm) of the electromagnetic

spectrum. The dust shell around these stars also contributes to an IR excess, with dust absorbing UV and optical light and re-radiating it primarily in the infrared as either continuum emission or through the de-excitation of rotational and vibrational transitions in molecular bonds. Thus, to study dusty mass-losing evolved stars, we need telescopes capable of imaging and spectroscopy in wavelengths between $\sim 1\,\mu$m and a few hundred μm.

1.4.1 The detection of dust

Photometry

Broadband photometry can identify luminous objects with a flux excess above the photospheric emission in the IR, indicative of circumstellar dust, in a large number of objects through colour-magnitude diagrams. These diagrams have several distinct features, including branches that trace RGB stars, AGB stars, background galaxies and foreground objects. If these stars come from a single population then evolutionary models can be applied to derive the evolutionary history of the population (see Chapter 6). Otherwise applying a combination of near-IR and mid-IR colour cuts to the photometric data provides a means of classifying point sources and estimating the individual constituents of a galaxy (see Chapter 2). Photometric observations may also be used to construct spectral energy distributions (SEDs) to model mass-loss rates (see Chapter 3).

Spectroscopy

Quantitative analysis of the dust mineralogy requires detailed knowledge of the spectral features at wavelengths $> 2\,\mu$m, where the dominant solid state components exhibit resonances. The spectral signatures, due to the strong lattice vibrations of solid state grains, can be used to determine the composition, abundance, temperature, size and shape of the dust grain population, having more diagnostic power than that of photometric measurements, which provides information on the global properties of the

grains. IR spectroscopy also encompasses molecular and atomic emission and absorption lines, providing a diagnostic to determine physical parameters such as the temperature, density and radiation field in the wind.

1.4.2 Dust Mineralogy

As mentioned earlier (Section 1.1.1), there is a difference between the dust chemistry in O-rich and C-rich evolved stars, with the former mainly consisting of silicate dust species and metal oxides while the latter is comprised of carbonaceous species, such as amorphous carbon and polycyclic aromatic hydrocarbons (PAHs). The work presented in this thesis is predominantly dedicated to O-rich astrophysical environments, and we limit the discussion on mineralogy to those dust species which have been detected or are expected to form in O-rich envelopes.

Silicate dust dominates the IR spectra of the majority of dust-producing O-rich AGB stars, and can be found in either amorphous or crystalline form. The lattice structure of the particles dictates if a silicate grain is amorphous or crystalline. If there is a high degree of order in the lattice, the dust is crystalline, otherwise, it is in amorphous form. Amorphous silicates are most abundant, characterised by their broad, smooth features at 10 and 20 μm due to Si–O stretching and O–Si–O bending inside a lattice (Figure 1.7).

Depending on the optical properties of the envelope, the characteristic 10 μm and 20 μm silicate bands are seen in emission or absorption. For low mass-loss rates the envelope is optically thin and the bands appear in emission. As the optical depth of the dusty shell approaches unity the features become self-absorbed; this transition occurs first in the 10 μm feature (David & Papoular 1990). In optically thick shells the features appear in absorption.

Crystalline silicate features can be identified by their sharp narrow resonance features produced by lattice mode vibrations at wavelengths beyond 10 μm. The peak positions and shapes of these bands are dependent on the adopted Mg/(Mg+Fe) ra-
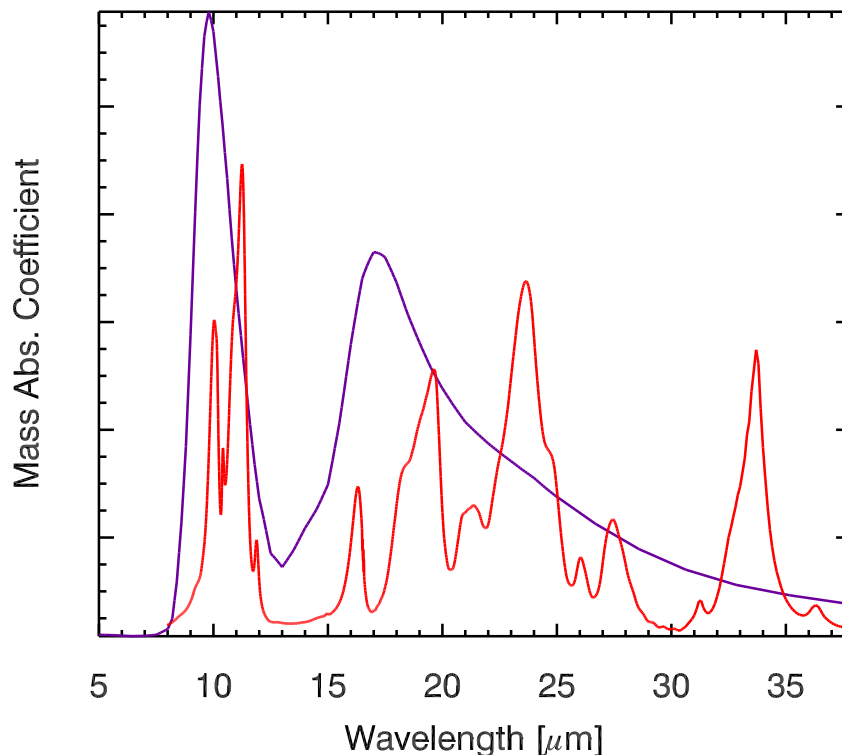
Figure 1.7: Mass absorption coefficients of amorphous (purple) and the crystalline (red) silicate forsterite. The amorphous silicates produce two broad bumps at 10 and 20 μm, while the spectra for crystalline silicates exhibits many sharp features.

tio, lattice structure, grain size and morphology (Molster et al. 2002b; Chihara et al. 2002; Koike et al. 2003; Min et al. 2003; Molster & Kemper 2005). From these variations in peak position and feature shape it is possible to constrain the minerals present. Comparisons with laboratory data have primarily identified these crystalline grains as Mg-rich olivines and pyroxenes (forsterite: Mg_2SiO_4 and enstatite: $MgSiO_3$) with little or no iron content (Molster et al. 1999b; de Vries et al. 2011). There is also evidence for Ca-rich pyroxenes such as diopside (Molster et al. 2002b).

The broad spectral features of amorphous silicates makes it harder to determine their exact mineralogical composition from spectroscopy. Both amorphous olivine
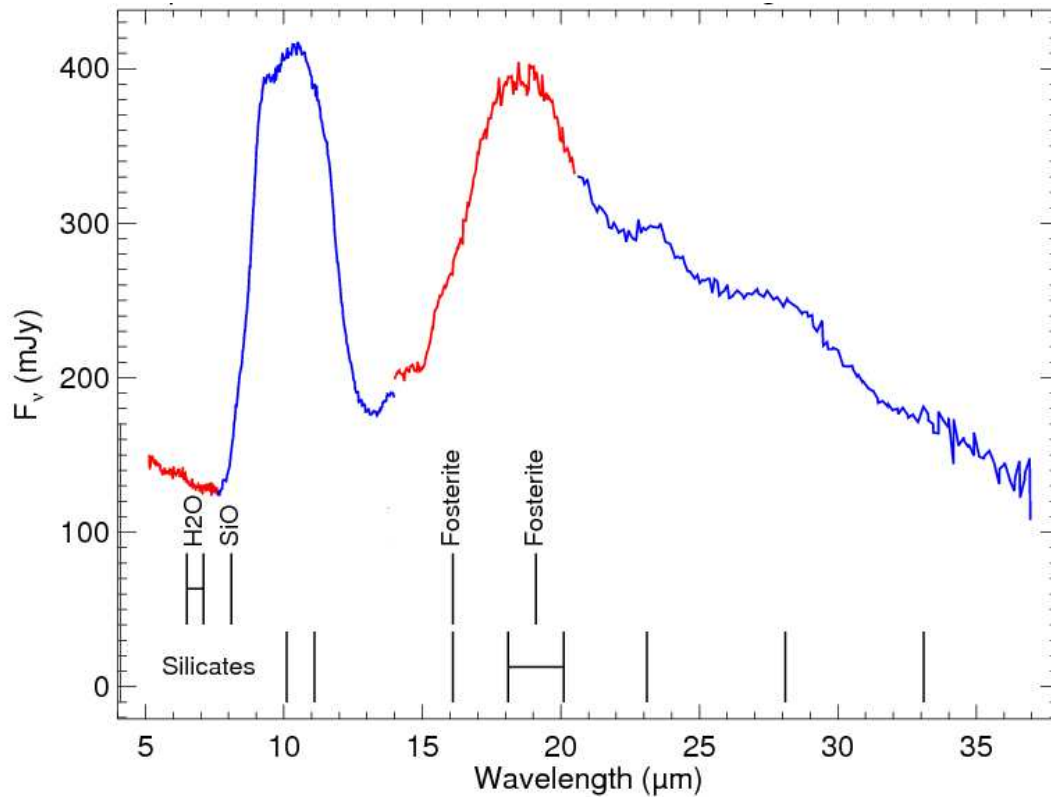
Figure 1.8: The Spectra of MSX SMC 018, a dust-enshrouded oxygen-rich AGB star in the SMC.

($Mg_{2x}Fe_{2-2x}SiO_4$) and amorphous pyroxene ($Mg_xFe_{1-x}SiO_3$) have similar shaped features, however the amorphous pyroxene features peak at a slightly shorter wavelength. Model spectra fits to this region show evidence for the presence of iron in the amorphous silicates either in the matrix or as a metal inclusion (Ossenkopf et al. 1992; Kemper et al. 2002; McDonald et al. 2010), this is in contrast to the crystalline silicates which are Fe-poor.

The difference in Fe content of the crystalline and amorphous silicates alters the grains near-IR absorptivity, resulting in a temperature differential between the grains (Woitke 2006; Höfner 2009). Thermodynamic calculations may in part explain this difference in composition, as forsterite and enstatite are among the first silicates to condense, while iron-containing silicates will form at significantly lower temperatures
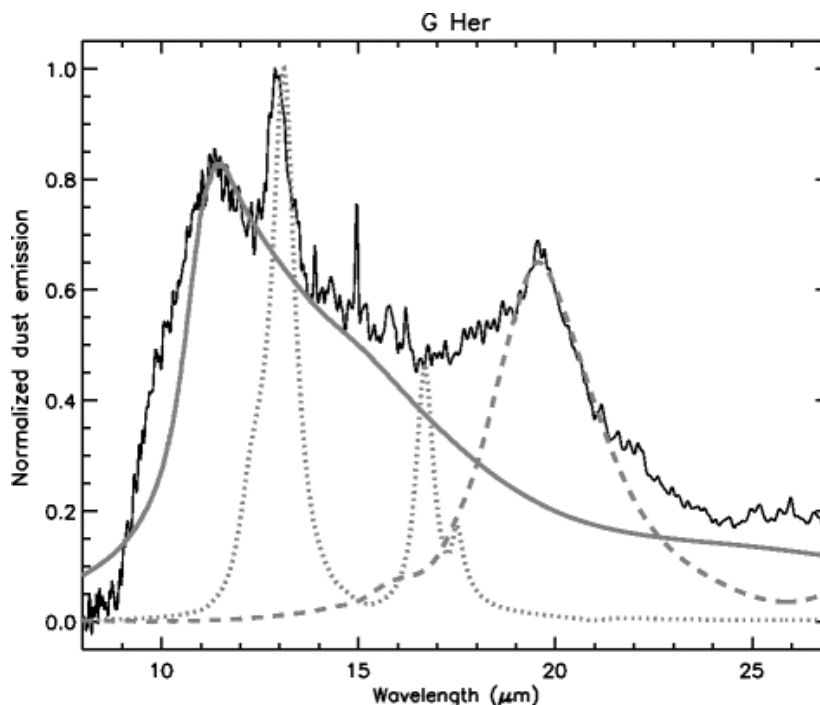
Figure 1.9: The continuum subtracted spectrum of G Her, compared to potential carriers for the emission bands. The grey solid line represents amorphous alumina (Al_2O_3), the dotted line spinel ($MgAl_2O_4$), and the dashed line $Mg_{0.1}Fe_{0.9}O$. Figure taken from Cami (2002).

(Gail & Sedlmayr 1999).

Crystalline silicates tend to be only a minor component comprising $\sim$ 10% of circumstellar dust shells (Kemper et al. 2001), yet some sources have been shown to have much higher abundances (Molster et al. 2001; Jiang et al. 2013). Molster et al. (1999b) identified a link between source morphology and crystallinity. Sources with circumstellar disks having a higher degree of crystallinity than spherical sources. In the same paper Molster et al. also noted compositional similarities between crystalline grains for both evolved and young stars, indicating that the same crystallisation process must be responsible in both cases. Waters et al. (1996) found crystalline features tend to be more prominent for stars with cooler dust shells, although this does not mean that crystalline silicates are indeed more abundant (Kemper et al. 2001).

Other dust species detected in oxygen-rich environments include: alumina (Al_2O_3), silica (SiO_2), spinel ($MgAl_2O_4$), metal oxides and metallic iron (see Figure 1.9). It should be noted that identification of these species is often based on a single (strong) feature, or the presence of a IR excess which cannot be reproduced by other more conventional species. For instance several different species have been proposed as the carrier of the narrow 13 μm dust feature detected in the spectra of oxygen-rich evolved stars. As this feature is predominately identified in SRb variable stars and RSGs with low infrared excesses and a narrow range of stellar photospheric and dust shell temperatures (Hron et al. 1997; Sloan et al. 2003a), the physical conditions of the shell must strongly influence its formation. Suggested carriers for this feature include spinel (Posch et al. 1999), corundum (Onaka et al. 1989) and silica (Speck et al. 2000). In order to provide a more reliable identification, attempts have been made to associate it with other emission features (Fabian et al. 2001; Sloan et al. 2003a), however, there is still dispute about any perceived correlations. For instance, other bands attributed to spinel around 16.8 and 32 μm have not been detected, indicating that spinel is an unlikely carrier of the 13 μm feature.

The emission feature at 20 μm also has a number of proposed carriers. Molster et al. (2002a) tentatively attributed this band to silica, while $Mg_xFe_{1-x}O$ may also be a potential carrier (Cami 2002). Depending on the Mg/Fe ratio, the band position can range from 16.5 to 19.5 μm, whereas its shape and strength are particularly sensitive to grain shape, making a definite identification challenging.

Iron is also an interesting case. In circumstellar environments it is highly depleted in the gas phase (Maas et al. 2005), thus must exist in solid form, either incorporated in other grains or as metallic iron grains. However, metallic iron has no IR vibrational modes and its presence can only be inferred from a featureless mid-infrared excess (McDonald et al. 2010).

1.4.3   Dust characteristics

From the relative strength and shape of the spectral bands it is possible to constrain the temperature of the dust and the grain size and shape (Bohren 1983; Fabian et al. 2001; Min et al. 2003; Voshchinnikov et al. 2006). Changes in grain size alter the width of the features because of differences in the resonances in the refractive indices of the grain material (Figure 1.10); as grains become larger the strength of the features weakens (particularly at shorter wavelengths) and the peak position will shift to slightly longer wavelengths (Min et al. 2004; Waters & Leinert 2008). Temperature changes alter the feature strengths, producing less distinct bands at cooler temperatures.

Grain-grain collisions in the outflows of evolved stars results in the fragmentation of large grains, limiting the maximum size of the dust grains. This tends to produce a power law size distribution (Biermann & Harwit 1980; Dominik et al. 1989). After numerous collisions the grains are assumed to be small compared to the wavelengths of interest ($a \ll \lambda/2\pi$), with a typical radius of 0.05 to 0.1 μm.

Grain shape is thought to be dependant on the temperature of formation, with grains forming in warm environments tending to be spherical, while those in cool regions have a more spheroidal formation (Voshchinnikov et al. 2006). Models of the spectral features tend to use either perfectly spherical grains or particles with a irregular structure (e.g. continuous distribution of ellipsoids). A homogeneous spherical compact grain is often assumed when performing radiative transfer calculations for ease of computation; as Mie theory (Mie 1908; Aden 1951; Toon & Ackerman 1981) can be applied to calculate the absorption co-efficients of the dust grain. A more realistic approach to modelling the dust structure is to used irregularly shaped particles. As observations include contributions from an ensemble of particles with various shapes, the shape of an individual grain is unimportant (Min et al. 2007). Only the average optical properties of the various shapes needs to be considered.
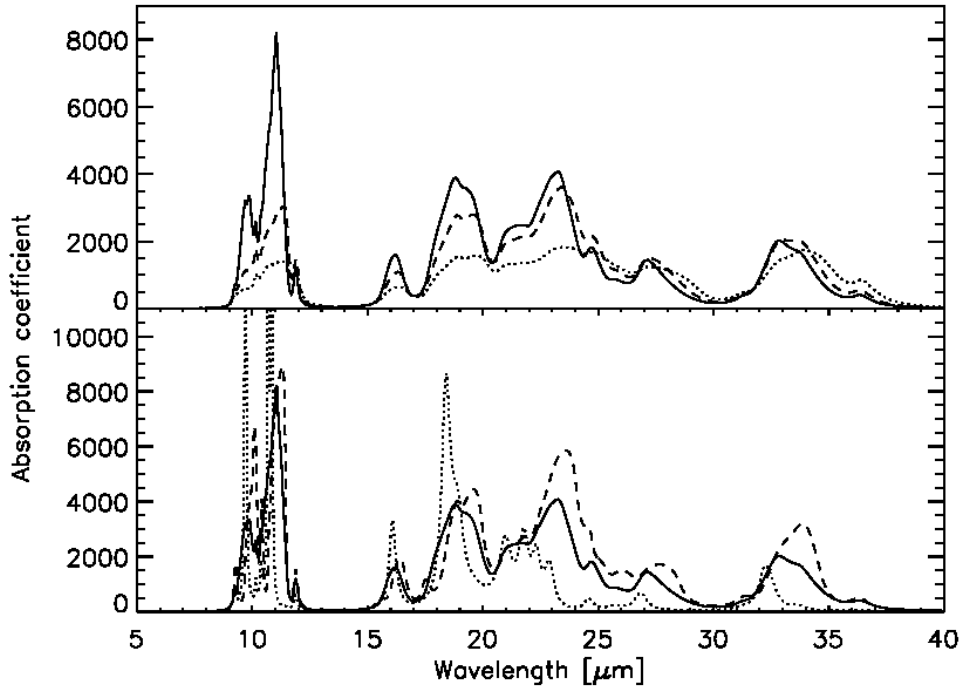
Figure 1.10: Mass absorption spectra of forsterite with different grain sizes and shapes. Top panel: forsterite grains of 0.1 μm (solid line), 2.0 μm (dashed line) and 4.0 μm (dotted line). Bottom panel: forsterite grains with Gaussian random field (solid line), distribution of hollow spheres (dashed line) and spherical Mie (dotted line) shape distribution, from Gielen (2009).

1.5   Effects of metallicity on AGB stars and dust

The chemical evolution of a galaxy refers to the changes in the abundances of chemical elements over time. As subsequent generations of stars are born they become more metal-enriched, as heavy elements manufactured by nuclear reactions in the stellar interiors of previous generations are returned to the ISM either through stellar winds or supernova explosions, modifying the composition of gas that stars are made from (Timmes et al. 1995; Travaglio et al. 1999; Pritzl et al. 2005).

The elemental abundance of AGB stars is reflected by its metallicity (defined as the ratio of a star's metal abundance relative to hydrogen compared to that of the Sun).

As dust grains are composed of metals, the number density of the grains, grain growth, and the grain size distribution could be sensitive to the abundances the star formed with. The chemical composition of the grain material will also be affected by metallicity, as different element mixtures alter the dust manufacturing processes. Observations of AGB stars in the Milky Way and Magellanic Clouds suggest the amount of dust produced by oxygen-rich AGB stars decreases as the metallicity of the star decreases, while the quantity of carbon-rich dust produced remains unchanged (Groenewegen et al. 2007; Sloan et al. 2008). The behaviour of the dust produced by carbon-rich AGB stars shows little dependence on metallicity since they self-synthesise the main constituents of the carbonaceous grains. For oxygen-rich stars, the dust requires metallicity-limited elements for both the nucleation seeds and molecular condensates (in particular, Si, Al, O, Fe, Ti).

In oxygen-rich environments a decline in metallicity results in a weakening of the circumstellar silicon monoxide (SiO) 8 μm absorption feature (Matsuura et al. 2005), emission from alumina-rich dust becomes negligible (Sloan et al. 2008), and there is a decline in the abundance of silicate dust. The reduction in both SiO molecular band strength and silicate dust abundance is consistent with the reduced silicon in a star's photosphere in a metal-poor system. However, the absence of amorphous alumina dust in the Magellanic Clouds is more surprising. It is expected that non-alpha-capture products like Al have a steeper falloff in elemental abundance with decreasing metallicity compared to elements like Mg and Si which are produced on shorter time-scales (Wheeler et al. 1989). Yet this should not be sufficient to fully explain the missing alumina dust in the Magellanic Clouds. Furthermore, alumina dust has been detected in oxygen-rich circumstellar envelopes of stars in the metal poor Galactic globular cluster 47 Tuc (Lebzelter et al. 2006; McDonald et al. 2011b). This suggests that under-abundance of alumina in the Magellanic Clouds samples is maybe due to an observational bias. We look at the alumina abundance in O-rich AGB stars in more detail in Chapter 5.

As you go to more metal-poor systems the fraction of 'naked' evolved stars (i.e.
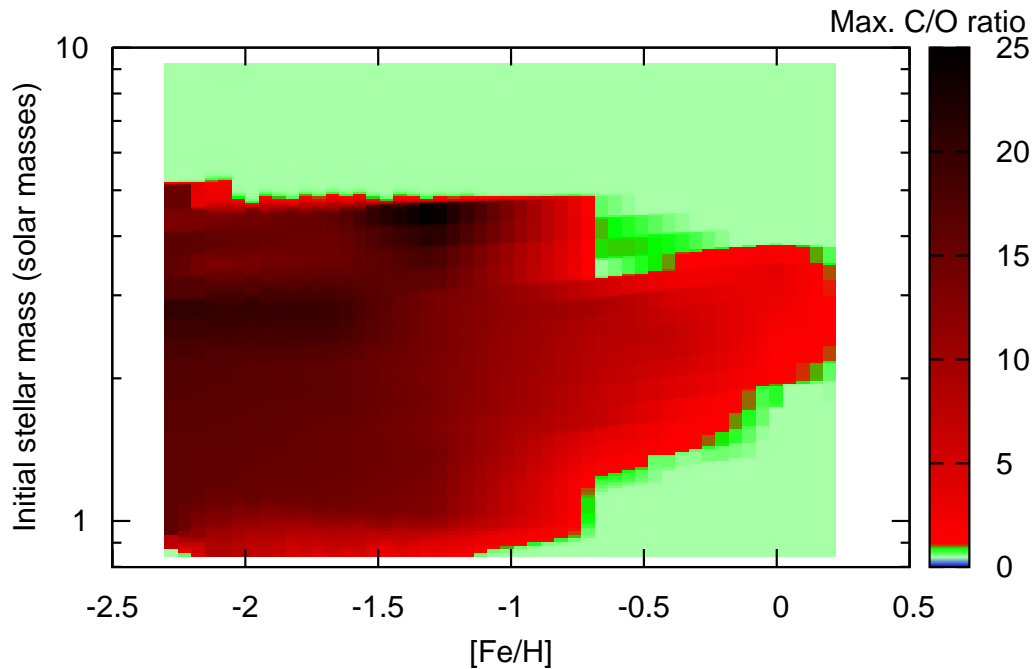
Figure 1.11: Maximum C/O ratio attained by stars at a given metallicity and initial mass, from McDonald et al. (2012) based on isochrones by Marigo & Girardi (2007).

those without an IR excess or dust features) increases (Sloan et al. 2008). Typically in Galactic sources with periods greater than 250 days, the amount of dust emission generally increases with increasing pulsation period and consequently with evolution along the AGB. In the Magellanic Clouds, oxygen-rich AGB stars with periods of less than 500 days generally have no associated dust shell, and SMC sources still tend to be naked up to periods of 700 days. This indicates a considerable lag in dust production compared to their Galactic counterparts (Sloan et al. 2008).

The fraction of carbon- to oxygen-rich AGB stars, and the mass range that the carbon stars encompass, depends on the metallicity of the host galaxy (Blanco et al. 1978, 1980; Groenewegen 1999; Cioni & Habing 2003). AGB stars with solar abundances will become carbon stars if their initial mass is in the region of $1.7 - 4$ $M_\odot$ (Straniero

et al. 1997; Marigo & Girardi 2007), this mass range increases to $1.2 - 4$ $M_\odot$ at metallicities comparable to the SMC (Zijlstra et al. 2006). This is due to the lower original oxygen abundances in the atmospheres of AGB stars at sub-solar metallicity; as such stars require less carbon to be dredged up to produce a C/O ratio greater than unity (Lattanzio & Wood 2004). Additionally, dredge-up is more efficient at lower metallicity (Vassiliadis & Wood 1993), adding greater amounts of carbon, thus the C/O ratio should be systematically higher in the Large and Small Magellanic Clouds (Marigo 2002).

Figure 1.11 shows the theoretical maximum C/O attained by stars at a given metallicity and mass. The exact limits where stars are expected to become carbon-rich depends on several parameters including the amount of dredge-up, mass-loss and hot bottom burning. Current models are not sufficiently accurate to state the boundary-region to a high degree of certainty, thus, observations of stellar populations are required to constrain the region in mass-metallicity space where stars are expected to become carbon-rich. Evidence of this enhanced C/O ratio in lower metallicity systems has been detected by Matsuura et al. (2005) who found that LMC carbon stars have a C/O of ≈ 1.5 compared to ≈ 1.1 in typical Galactic stars. This directly affects how much carbon-rich dust is returned to the interstellar medium at low metallicities.

The metallicity of an AGB star can affect its wind properties. Prior to the launch of *Spitzer* it was generally assumed that the superwind for all AGB stars would be weaker at lower metallicity, and below [Fe/H]= -1 the dust-driven wind would fail (Bowen & Willson 1991; Zijlstra 2004), requiring a pulsation-driven wind to drive the outflow. Instead, *Spitzer* observations indicate that high mass-loss rates can be achieved with dust-driven winds even at very low metallicity ([Fe/H] $\lesssim$ -1; Lagadec et al. 2008; Sloan et al. 2009; McDonald et al. 2011b).

Both dust and total mass-loss rates estimated for carbon stars show little dependence on metallicity, reaching rates comparable to Galactic stars (Groenewegen et al. 2007; Matsuura et al. 2007; Lagadec et al. 2009), however, the luminosity at which the superwind is observed decreases with metallicity (Lagadec & Zijlstra 2008). This can

be explained by the efficient formation of carbonaceous dust and the higher abundance of self-synthesised free carbon at low metallicity.

Oxygen-rich stars in the Milky Way and the Magellanic Clouds have similar total mass-loss rates at higher luminosities, but the dust mass-loss rates show a strong metallicity dependence (Wood et al. 1998; van Loon 2000; Lagadec et al. 2008). This is a consequences of the suppressed dust formation rate (due to the reduced SiO) in O-rich stars at sub-solar metallicity. This has implication for the onset of the superwind, which could be delayed until sufficient oxygen-rich dust has been produced (Lagadec & Zijlstra 2008; McDonald et al. 2012).

To characterise the total rate at which material is returned to the ISM by dusty evolved stars it is essential that the injection rate of gas and dust is correctly taken into account. This requires detailed knowledge of the outflow velocity and the dust-to-gas ratio in circumstellar envelopes. Observations of OH and H_2O maser emission in O-rich AGB stars indicate that the outflow velocity of the wind is slower for stars of the same luminosity or pulsation period at lower metallicity (Marshall et al. 2004; van Loon et al. 2001). This effect was first suggested by Wood et al. (1998) who realised that if the winds are driven by radiation pressure on the dust (and its coupling to the gas due to collisions), then the expansion velocity depends on both the dust-to-gas ratio (ψ) and luminosity.

It is expected that metal-deficient systems will have a lower dust-to-gas ratio in oxygen-rich stars, but for carbon-rich environments the dust-to-gas ratio may be similar to Galactic values (Habing 1996). Observational support for this hypothesis was found by van Loon (2000) who noted that the total (gas and dust) mass-loss rate is insensitive to the initial metallicity, but the dust-to-gas ratio has a linear dependence (Figure. 1.12).

Other properties of AGB stars also depend on metallicity. For instance, AGB stars in metal-deficient systems have warmer photospheres because the molecular opacities are smaller, since there is less heavy elements (e.g iron) in their mantles; this results in a more compact atmosphere. These stars will also have a larger dust-free inner cavity
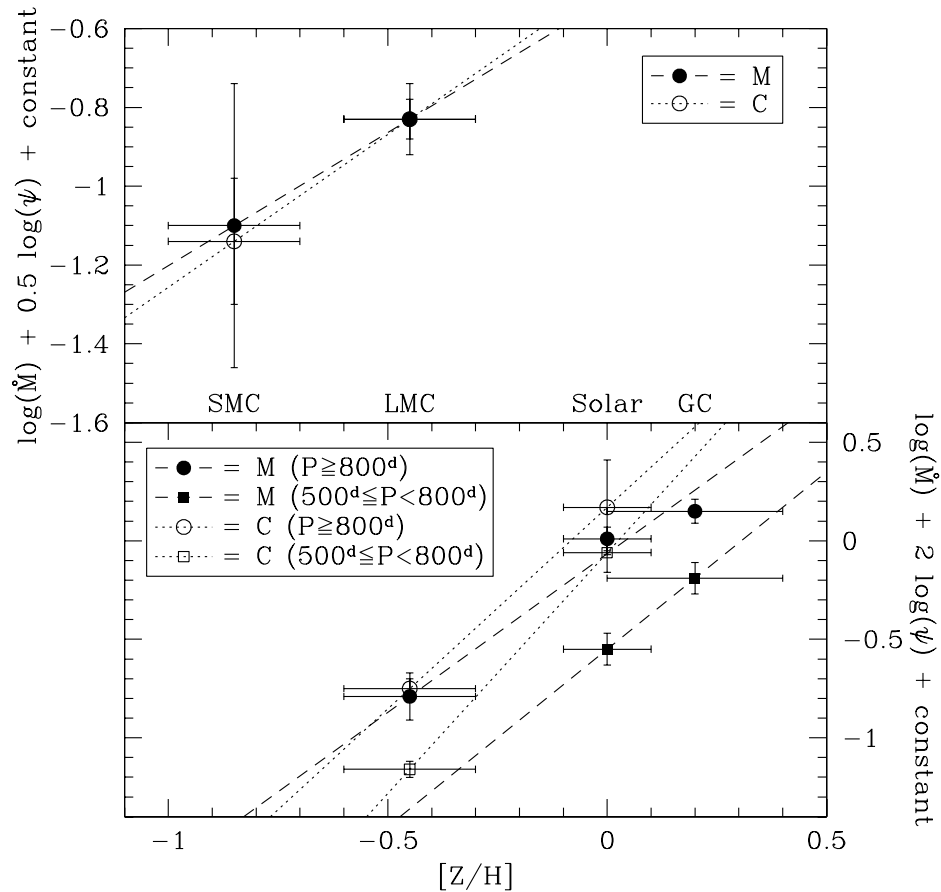
Figure 1.12: Mass-loss rates and dust-to-gas ratios for obscured AGB stars in the SMC, LMC, the Solar neighbourhood and Galactic centre as a function of their initial metallicities. The total (gas+dust) mass-loss rate ($\dot{M}$) only has a weak dependence on initial metallicity whilst the dust-to-gas ratio (ψ) has a linear dependence, from van Loon (2000).

(in terms of R_*), as the dust formation region will be further from the star due to the higher temperatures.

Contrary to theoretical predictions (Wood & Sebo 1996), the observed period–luminosity relation for Miras is not strongly dependent on metallicity (Whitelock et al. 2008). However, the pulsation amplitude may be affected by metallicity. The amplitude of the light-curve depends on the wavelength under consideration; at shorter wavelengths absorption by TiO (which varies strongly throughout the pulsation cycle)

causes large amplitude changes, at longer wavelengths this effect is not present and so the light curve amplitude is much smaller. As the abundance of TiO is metallicity dependant a low-metallicity environment may have weaker pulsation amplitudes for a given period in the visible. This may lead to a lower fraction of detected variables. This has been observationally confirmed by Frogel & Whitelock (1998).

1.6   Local Galactic Group

The Local Group of galaxies are our closest neighbours, located within ~ 1 Mpc of the Local Group baryonic centre. Their proximity allows us to obtain detailed views of the evolved stellar populations and their dust production. These nearby systems also allow us to analyse the global picture of the life cycle of matter at a particularly metallicity, representing a sample of galaxies that have elemental abundances much closer to the primordial abundances in the early Universe. The Local Group consists of three massive spiral galaxies (the Milky Way, Andromeda and M33) and more than 51 dwarf galaxies[1], which tend to be satellites of the spirals. Figure 1.13 shows the distribution of galaxies in the Local Group. The individual galaxies of the Local Group span a large range of basic properties; they are expected to show variations in gas-to-dust ratios, dust content and extinction curves due to the different compositions of the stellar populations which dominate the interstellar dust enrichment.

Infrared surveys on Local Group galaxies provide an ideal opportunity to investigate how the mineralogy and chemistry of dust produced by individual evolved stars depends on metallicity on a galactic scale. It also allows us to make accurate comparisons between stars as their distances are known, and hence their luminosities can be determined. For Milky Way sources, obtaining accurate measurement of stellar luminosities is problematic due to extinction and unknown/uncertain distances although, the launch of *GAIA* in late 2013 will soon provide precise distance measurements to

---

[1]The number of confirmed Local Group galaxies increases at the rate of about four per decade (van den Bergh 2000).

Figure 1.13: Map of the Local Group of Galaxies from Grebel (1999). The 1 Mpc boundary is indicated by the dashed line.

$\sim 10^5$ AGB stars in the Milky Way by measuring their parallaxes.

Currently, it is only possible see a global picture of the life cycle of dust in the galaxies closest to us, such as the Magellanic Clouds. This requires large surveys of the entire galaxy, with the ability to resolve evolved stars, supernova remnants, interstellar clouds, and star forming regions across a wide spectral range, i.e ultraviolet, optical, infrared, submm, and radio. Limited spatial resolution and sensitivity prevents the detailed study of the dust-life-cycle in the more distant galaxies in the Local Group, for instance Andromeda (M31). However, it is possible to resolve and obtain photometric measurements of the brightest, dustiest AGB stars in Andromeda and its satellite galaxies which will provide valuable clues in understanding the stellar population and dust input in other types of galaxies in the Local Group.

Table 1.1: LMC and SMC parameters

Parameter	LMC	Ref.	SMC	Ref.
Distance, d (kpc)	49.97 ± 0.17	1	61 ± 2	2, 3
Metallicity, [Fe/H] (dex)	-0.3	4, 5	-0.7	4, 5
Inclination angle (°)	34.7 ± 6.2	6	68 ± 2	7
Gas-to-dust ratio (Ψ)	200	. . .	500	. . .
E(B-V) (mag)	0.13	8	0.04	9

R   : (1) Pietrzyński et al. (2013); (2) Cioni et al. (2000); (3) Szewczyk et al. (2009); (4) Luck et al. (1998); (5) Meixner et al. (2010); (6) van der Marel & Cioni (2001); (7) Groenewegen (2000); (8) Massey et al. (1995); (9) Harris & Zaritsky (2004).

1.6.1   The Magellanic Clouds

Observations of evolved stars in the metal-poor environments of the Magellanic Clouds with the *Spitzer Space Telescope* provide an ideal opportunity to explore metallicity effects on the O-rich dust condensation sequence in AGB stars and to investigate how the dust mineralogy depends on the physical and chemical conditions of the envelope. Within the Large Magellanic Cloud (LMC) and Small Magellanic Cloud (SMC), we have a set of stars with similar characteristics: they are all at approximately the same distance from the Sun and are assumed to have a narrow range of metallicity within each galaxy. This allows us to measure luminosities and dust mass-loss rates from the observed spectral energy distributions. The parameters adopted in our calculations for the Magellanic Cloud stars are listed in Table 1.1. The dust-to-gas mass ratios of stars in the Magellanic Clouds are assumed to be lower than those of stars in the solar neighbourhood and to have a linear dependence with metallicity (van Loon 2000; Marshall et al. 2004; van Loon 2006), breaking the degeneracy between the dust column density and the gas density in the outflows of AGB stars.

LMC

The Large Magellanic Cloud (LMC) is a barred irregular galaxy and is the fourth largest galaxy within the Local Group. Studies of the resolved stellar populations combined with the global picture of the LMC is made possible because of its proximity (51 kpc; Feast 1999) and favourable viewing angle (35°; van der Marel & Cioni 2001) resulting in a low column density along the line of sight. Compared to the Sun the Magellanic environment is metal-poor, having a metallicity of [Fe/H] $\approx$ −0.3 dex (Westerlund 1997) which is similar to the mean metallicity of the Milky Way ISM during the epoch of peak star formation (Madau et al. 1996; Pei et al. 1999). The dust-to-gas mass ratio is also lower than that of the Solar neighbourhood, resulting in higher ambient ultraviolet fields (Gordon et al. 2003).

The LMC has been surveyed with many instruments; early surveys at optical and near-infrared wavelengths detected mainly AGB stars with optically thin dust shells (Westerlund et al. 1978; Blanco et al. 1980; Rebeirot et al. 1983; Frogel & Blanco 1990). It was not until the launch of the IR Astronomical Satellite (IRAS) in 1983 that the first IR images of AGB stars in the Magellanic Clouds were obtained (Frogel & Richer 1983), providing a new window in which to explore the sources of dust. The launch of *IRAS* also marked the beginning of galaxy-wide surveys in the IR, where large data sets are used provide insights to the properties of the host galaxy. Following the surveys of DENIS (1995-2001), MSX (1996-1997) and 2MASS (1997-2001) of the Magellanic Clouds in the near-IR, high-resolution photometry of almost the complete population of AGB stars with absent or optically-thin dust shells is available (Skrutskie et al. 2006). Obscured AGB stars with low near-IR flux levels present more of a problem as detectors were hampered by their sensitivity, limited to only the brightest sources (Cioni et al. 2000).

The *Spitzer Space Telescope* (*Spitzer*: Werner et al. 2004), launched in 2003, enabled IR imaging and spectroscopy of the Magellanic Clouds in exceptional detail. The high spatial resolution and unprecedented sensitivity of *Spitzer* in the mid-IR enabled
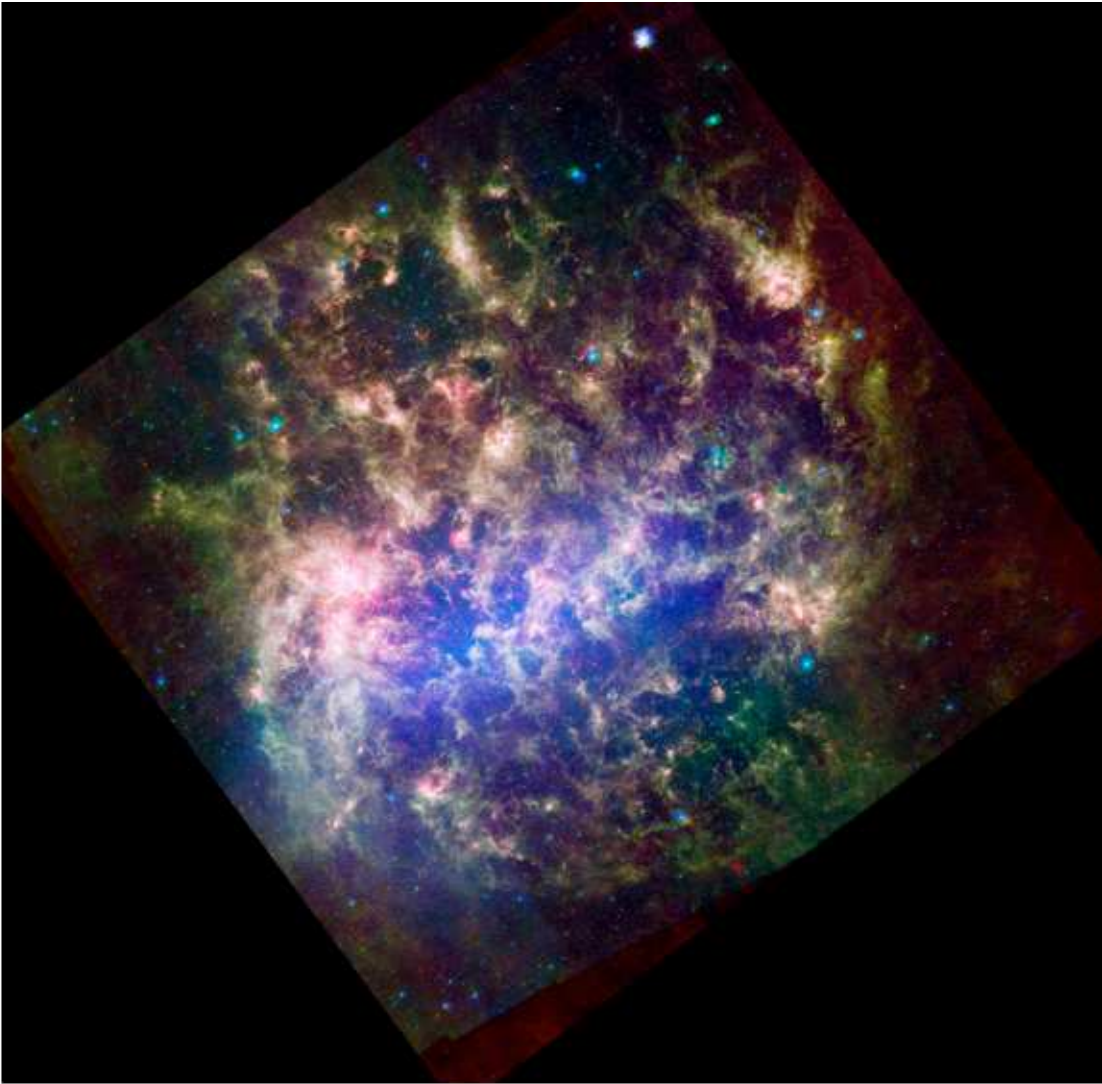
Figure 1.14: The Large Magellanic Cloud as imaged by *Spitzer* at 3.6 (blue), 8 (green), and 24 (red) μm, reproduced from Meixner et al. (2006).

a full census of all objects brighter than [8.0] = 15 mag in the LMC (Meixner et al. 2006). The project *Surveying the Agents of Galaxy Evolution* (SAGE) has produced a uniform and unbiased photometric survey of the LMC in all the IRAC (3.5, 4.5, 5.8, and 8.0 μm) and MIPS (24, 70, and 160 μm) bands (Figure 1.14), which complements the optical *Magellanic Clouds Photometric Survey* (MCPS) in the U, B, V, and I bands

and the *Two Micron All Sky Survey* (2MASS) in the near-infrared (J, H and Ks bands). *Herschel* has also targeted the Magellanic Clouds, probing the far-infrared (FIR) and submillimeter (submm) regime, detecting the emission from coldest dust grains. These surveys provide complete SED coverage and thereby trace the life cycle of baryonic matter that drives galactic evolution. A spectroscopic follow-up to the SAGE photometric survey; SAGE-Spec (Kemper et al. 2010) charts the life cycle of gas and dust in galaxies by observing a variety of circumstellar and interstellar environments, combining these results with the photometric data will provide a global view of the dust cycle in the Large Magellanic Cloud.

SMC

The Small Magellanic Cloud (SMC) is an irregular dwarf galaxy which shares a common envelope of neutral hydrogen with the LMC. The SMC has a lower mean metallicity ([Fe/H] $\approx$ −0.7) and a higher gaseous mass fraction compared to the LMC and the Milky Way (Bekki & Chiba 2007). This lower metallicity causes late-type stars of a given temperature to be bluer than similar stars in the LMC. The SMC's more primitive nature also means that it could be used as a crucial link for understanding high-redshift galaxies.

As with the LMC, the SMC has been surveyed by numerous instruments, particularly in the near-IR and mid-IR. These include *AKARI* and *Spitzer* surveys of the inner ~3 deg^2 bar region (Bolatto et al. 2007; Ita et al. 2010). In addition, the *Spitzer* SAGE-SMC (Surveying the Agents of Galaxy Evolution in the Tidally Stripped, Low Metallicity Small Magellanic Cloud; Gordon et al. 2011) *Spitzer* program has conducted a comprehensive survey of the entire SMC including the bar, wing and tail regions (Figure 1.15), providing a complete census of the evolved star population in the Magellanic Clouds.
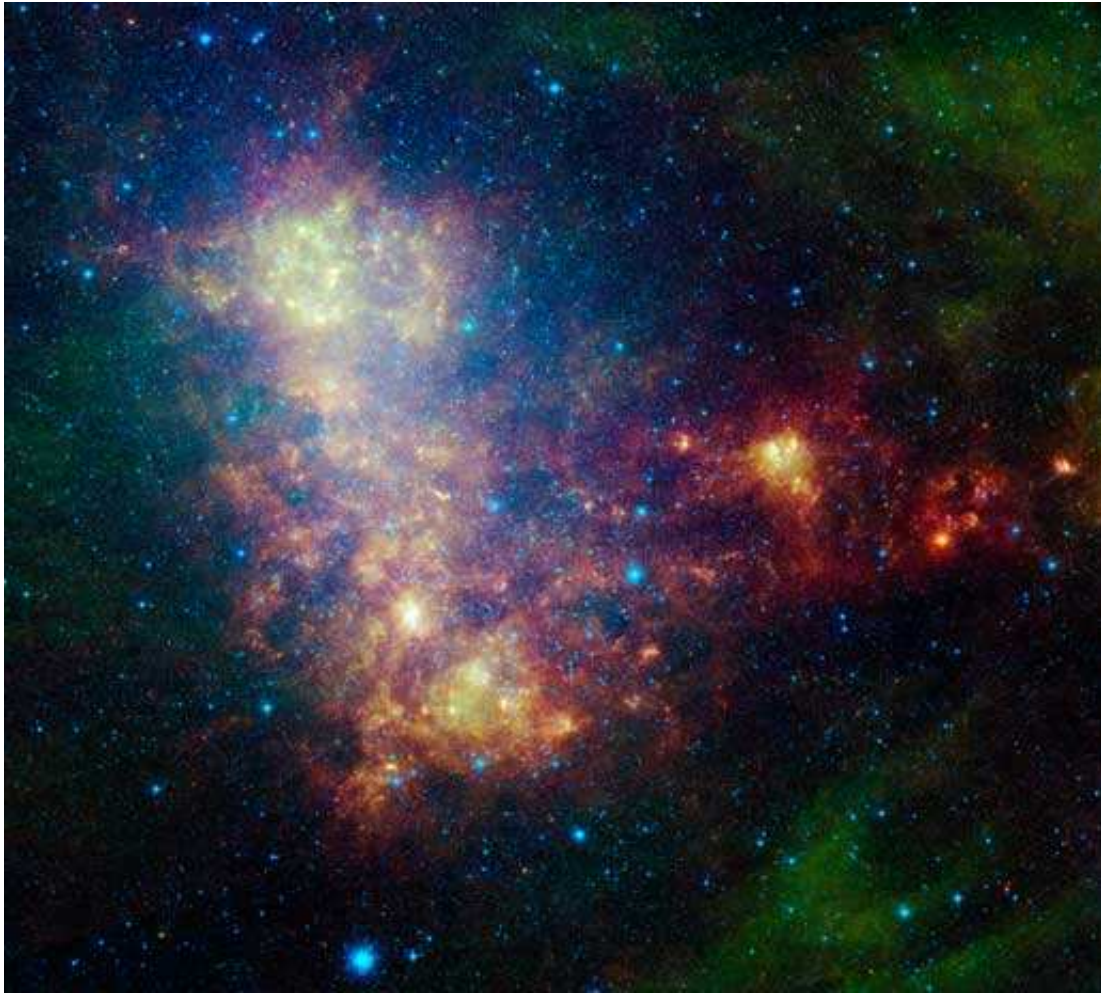
Figure 1.15: The Small Magellanic Cloud as imaged by *Spitzer* at 3.6 (blue), 8 (green), and 24 (red) μm, reproduced from Gordon et al. (2011).

1.6.2   M32

Messier 32 (M32) is a compact, low-luminosity elliptical (E2) galaxy and the closest companion to the Andromeda galaxy, with a projected separation of 22′ (5 kpc) from M31's centre (Howley et al. 2012). M32 is the only true elliptical galaxy in the Local Group, as such the galaxy is no longer undergoing star-formation. The morphology of M32 has been influenced by interactions with Andromeda; tidal stripping has removed M32's interstellar gas (Sage et al. 1998) and dust (Gordon et al. 2006), and interactions

may also explain the remarkable lack of globular clusters.

Due to its relative proximity (763 ± 24 kpc; Jensen et al. 2003), the bright stellar population of M32 can be resolved with both the *Hubble Space Telescope* and *Spitzer* in the bulge and outer halo (however, the extremely high surface brightness hinders detections in its central regions). M32 has been extensively studied, through both integrated light spectroscopic studies and photometric studies of resolved stars (e.g. Baade 1944; Rose 1985; Grillmair et al. 1996; Worthey et al. 2004; Sarajedini et al. 2012). These indicate a complex star formation history, and incite much debate about the nature and spatial distribution of M32's stars.

1.6.3 Globular Clusters

Galactic globular clusters are also ideal environments in which to study low-metallicity evolved stars. These systems contain approximately 10^4 to 10^6 metal-poor old stars, which formed during a single star-forming event (Benacquista 2002). The majority of globular clusters are comprised of a single stellar population (ω Centauri being a notable exception: McDonald et al. 2011b) and have roughly the same mass and metallicity. Estimated metallicities for Galactic globular clusters range from [Fe/H] = −2.3 to Solar (Harris 1996), while their ages range from 10 to 15 Gyr (Ashman & Zepf 1998). Unlike the galaxies in the Local Group, globular clusters are not undergoing star formation, and have virtually no emission from cold ISM dust (van Loon et al. 2006; Matsunaga et al. 2008).

1.7 Overview

Within the wider framework of understanding the life-cycle of dust on a galaxy-wide scale, this work aims to investigate the effects of metallicity on circumstellar dust produced by evolved stars. This is accomplished with *Spitzer* observations of a large sample of evolved stars in the Local Group. Low-resolution infrared spectroscopic

observations are used to characterise dust composition whereas photometric measurements provide information on individual circumstellar environments and the stellar populations in each galaxy.

Chapter 2 focuses on the classification of point sources observed with *Spitzer* in the Magellanic Clouds. Chapter 3 details work detecting crystalline silicates in oxygenrich evolved stars across a range of metallicities and mass-loss rates while the mineralogy of these crystalline silicates is investigated in Chapter 4. A grid of radiative transfer models for O-rich AGB stars with a range of dust compositions is presented in Chapter 5, which we apply to AGB stars in the LMC to investigate the relative contribution from amorphous silicate and amorphous alumina dust. Chapter 6 analyses the stellar content of M32 using photometric data taken with *Spitzer*. Finally, I summarise the main findings of this thesis in Chapter 7 and draw some general conclusions. Details of some potential avenues for future work are also given.

2

Point Source Classification

The work presented in this chapter was published as part of the SAGE-Spec collaboration in Woods et al. (2011), Woods et al. (in prep.) and Ruffle et al. (in prep.).

Contribution: As a member of the SAGE-Spec collaboration I contributed to the testing and refinement of the decision-tree. I also derived bolometric magnitudes for the point sources and identified the spectroscopic pointings which fell within the SAGE-SMC footprint. I have assisted in forming a consensus classification of sources; for a source to be assigned a classification it is required that three people independently come to the same classification. Independently, I also contributed to the documentation for the *SPICA*-MCS instrument by modelling colours of stellar populations with the proposed filter sets.

In order to gain a better understanding of how the mineralogy and formation of oxygen-rich dust depends on metallicity, the following chapters (Chapters 2 to 5) focus on infrared spectroscopic studies of a sample of O-rich AGB stars and RSGs in the Milky Way and the Magellanic Clouds. This chapter describes how the oxygen-rich AGB stars and RSGs were identified from a large spectral survey of IR point sources in the Magellanic Clouds. It also details how SAGE-Spec mid-infrared spectroscopy was used to calculate the spectral energy distributions of dusty point sources using

a proposed set of *SPICA*-MCS filters and their resulting magnitudes and colours, in preparation for potential legacy surveys of nearby galaxies with *SPICA*.

2.1   Introduction

The SAGE-LMC, SAGE-SMC and HERITAGE surveys have mapped the Magellanic Clouds in the infrared using the *Spitzer* and *Herschel* Space Telescopes. These surveys have detected approximately 8.5 million point sources in the LMC (Meixner et al. 2006) and 2.5 million point sources in the SMC (Gordon et al. 2011). Of these ~22000 LMC sources and ~7000 LMC sources were classified as evolved, oxygen-rich stars (Blum et al. 2006; Boyer et al. 2011).

A spectroscopic follow-up to the SAGE photometric surveys, SAGE-Spec (Kemper et al. 2010), targeted point sources in the LMC using *Spitzer's* Infrared Spectrograph (IRS; Houck et al. 2004). These observations cover the full luminosity and colour range found in the SAGE-LMC photometric survey. One of the goals of the SAGE-Spec program is to develop a comprehensive classification scheme for point sources based on the mid-IR spectra. These classifications improve our understanding of the stellar populations of the Magellanic Clouds and allow verification of the photometric classifications (i.e, the colour-colour and colour-magnitude cuts) used by the SAGE and HERITAGE surveys.

The SAGE-Spec collaboration has compiled a complete, homogeneously-reduced catalogue of infrared ($\lambda = 5.2 - 38\ \mu$m) spectra (within the SAGE footprint) taken by the IRS on board *Spitzer*. This data archive contains over 1000 staring-mode observations of sources within the LMC (including 197 from the SAGE-Spec legacy program itself) and ~ 250 pointings in the SMC. Approximately 90 per cent of these IRS staring mode targets are unique point sources, which encompass a wide variety of circumstellar and interstellar environments. For a full description of the original target selection, observing strategy and the techniques used in the data reduction for the SAGE-Spec legacy program the reader is referred to Kemper et al. (2010).

2.2   The Classification Method

The 197 objects targeted by the SAGE-Spec legacy program were classified according to their *Spitzer* IRS spectrum and existing broad-band photometry, including optical *UBVI* photometry from the Magellanic Clouds Photometric Survey (Zaritsky et al. 2004), 2MASS *JHK$_s$* photometry (Skrutskie et al. 2006), mid-IR photometry (IRAC 3.6, 4.5, 5.8, 8.0 and MIPS 24 μm) and far-IR photometry (MIPS 70 and 160 μm), from the SAGE catalogue (Meixner et al. 2006). These targets provide an inventory of dusty point sources in the Magellanic Clouds.

For the purposes of classification, objects in the sample with similar spectral characteristics were identified. These objects were grouped together and compared to expected spectral characteristics for the individual categories. Objects were classified according to their evolutionary stage and chemistry (e.g, oxygen or carbon rich). For instance, O-rich post-AGB stars can be identified by their double-peaked SED and strong silicate features at 10 and 20 μm, while embedded YSOs can be recognised by oxygen-rich dust features superimposed on a red continuum and distinguished from other YSOs by ice absorption features at 15 μm. A selection of the rich and spectrally diverse point sources in the Magellanic Clouds are shown in Figures 2.1 and 2.2.

From these initial classifications by the SAGE-Spec collaboration, a decision-tree algorithm (Fig. 2.3) for object classification was developed by Woods et al. (2011). This system classifies point sources according to their infrared spectral features, continuum and SED shape, bolometric luminosity, variability and other ancillary data. For a source to be assigned a classification it is required that three people independently reach the same classification; this rigorous approach minimises spectral identification errors particularly in low-contrast spectra, and provides additional checks for contamination from by nearby objects or from spurious features introduced in the data reduction.

This spectral classification method can also be applied to globular clusters, Galactic point sources and even other external galaxies. With some modification (allowing for
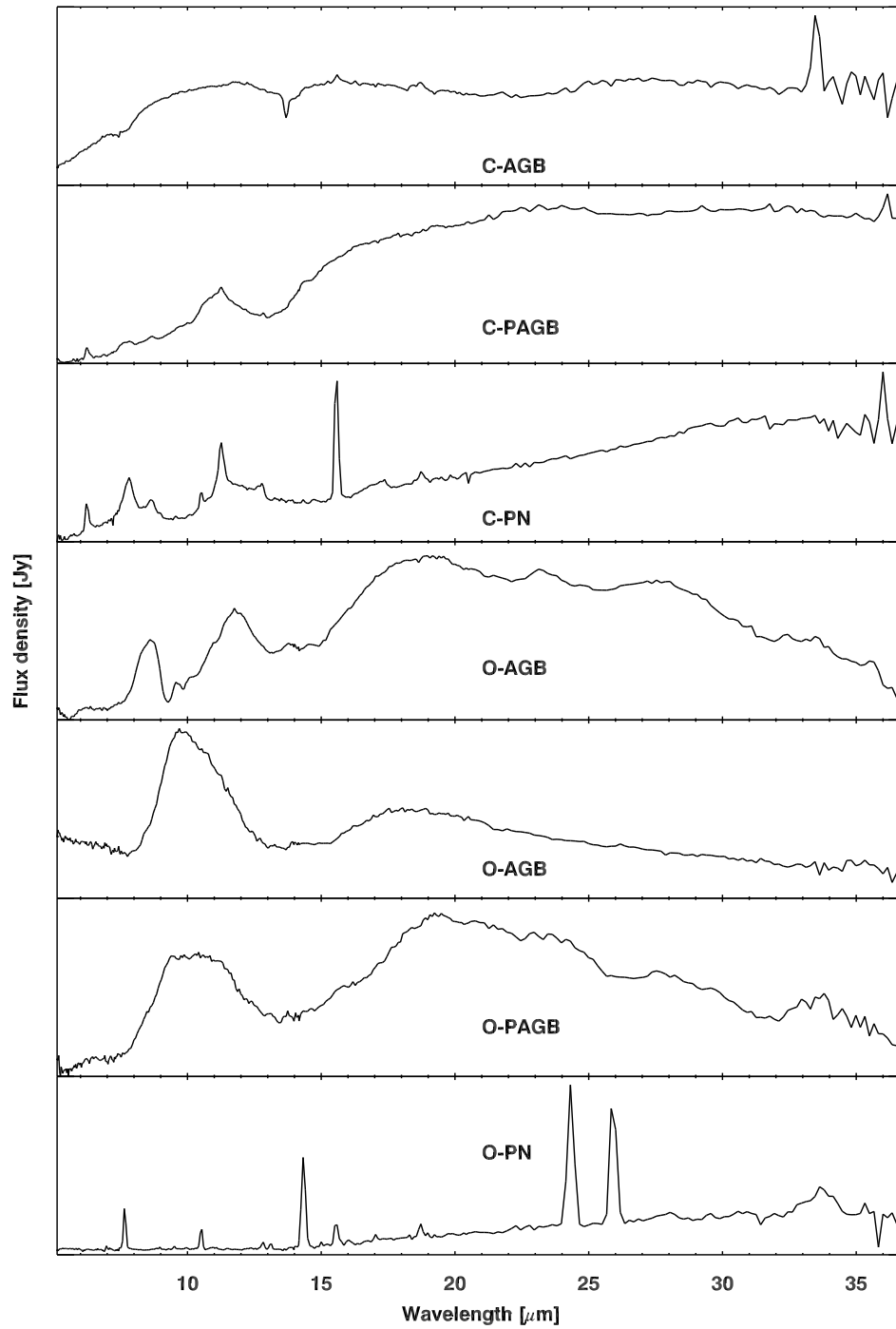
Figure 2.1: A selection of *Spitzer* spectra illustrating the rich spectral diversity in the Magellanic Clouds.
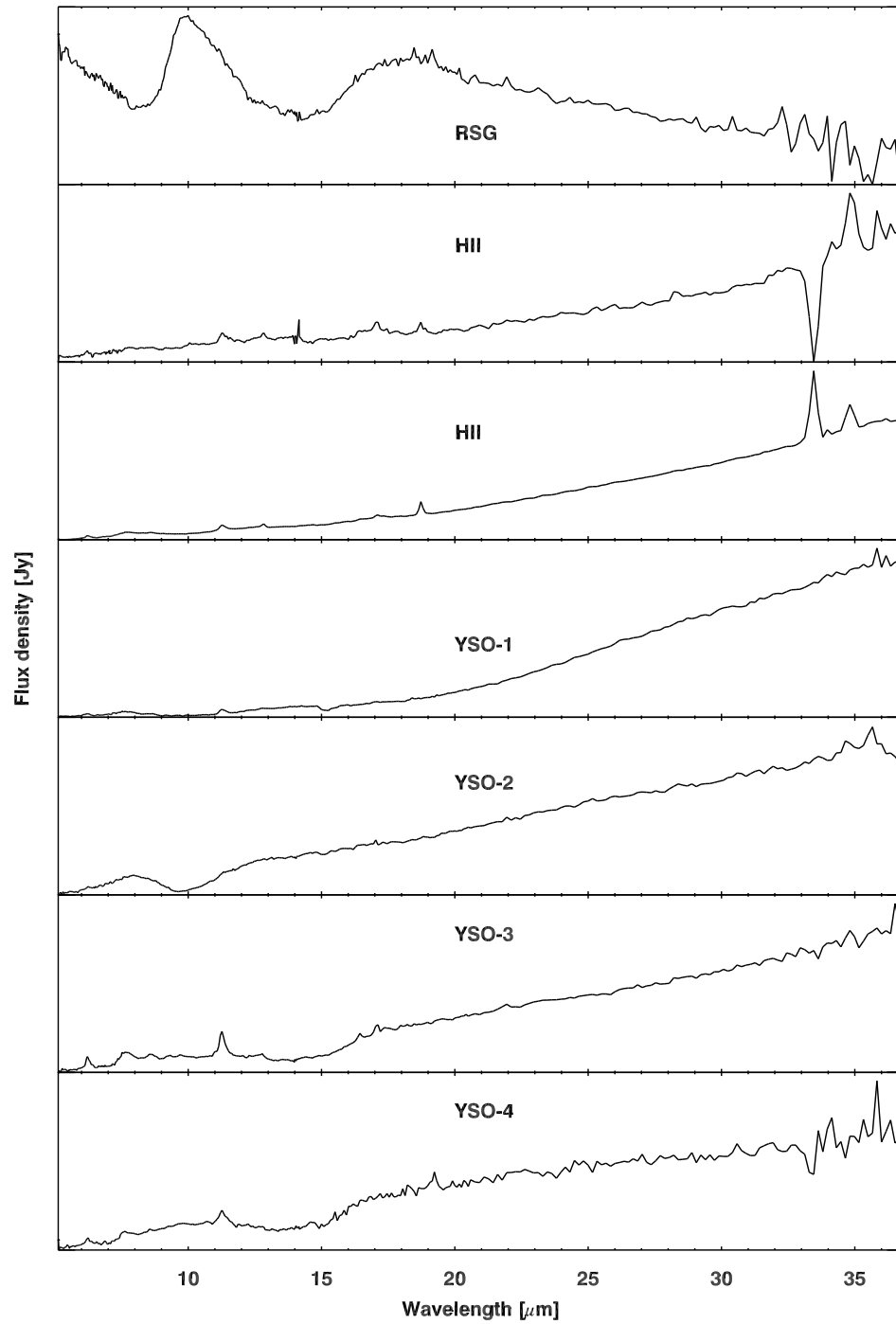
Figure 2.2: A selection of *Spitzer* spectra illustrating the rich spectral diversity in the Magellanic Clouds.

Figure 2.3: The decision tree for the classification of infrared point sources using spectra, associated photometry, luminosity and variability. Image reproduced from Ruffel et al. (in prep.); after Woods et al. (2011).

differing resolutions and signal-to-noise) it can also be applied to data from the *IRAS* and *ISO* satellites and future missions such as *JWST* and *SPICA*. This may also provide additional information for classifying sources; for instance, the extended coverage at short wavelengths (λ = 2.38 - 45.2 μm) of *ISO* SWS (Short Wavelength Spectrometer; de Graauw et al. 1996) spectra allows C-rich AGB stars to be identified via the C_2H_2 bands near 3 μm.

2.3 Bolometric Magnitudes

Spectroscopically, it can often be challenging (if not impossible) to distinguish between O-AGB stars and their more massive ($>8\,M_\odot$) counterparts, RSGs. Three methods commonly employed to discriminate between these classes are luminosity, pulsation amplitude and age. The known distance to sources in the Magellanic Clouds makes luminosity the more logical discriminant. The 'classical' upper luminosity limit for AGB stars, based on the core-mass–luminosity relationship, is $M_{\rm bol}$ = −7.1 (Wood et al. 1983). This is not an absolute limit: a few low-mass AGB sources occasionally traverse this limit during thermal pulses (Wood et al. 1992), while more massive AGB stars are brighter due to hot-bottom burning (Blöcker et al. 2000). Other authors have put forward their own luminosity cut-offs: van Loon et al. (1999) uses a limit of $M_{\rm bol}$ = −7.5 to distinguish between the RSGs and O-AGBs, whereas Groenewegen et al. (2009), who allow for hot-bottom burning, uses a value of $M_{\rm bol}$ = −8.0 as the divider. For the classification scheme employed, the classical limit of $M_{\rm bol}$ = −7.1 was used as the discriminant between the RSGs and the O-AGBs in our sample, unless the star resides in a cluster too young for a low-mass star to have reached the AGB or there is good evidence in the literature to support a different classification (for instance optical spectra with lithium absorption or OH maser emission would suggest the object is an O-AGB star).

The bolometric magnitudes ($M_{\rm bol}$) of our sources in the LMC and SMC samples were calculated via a simple trapezoidal integration of the IRS spectrum and opti-
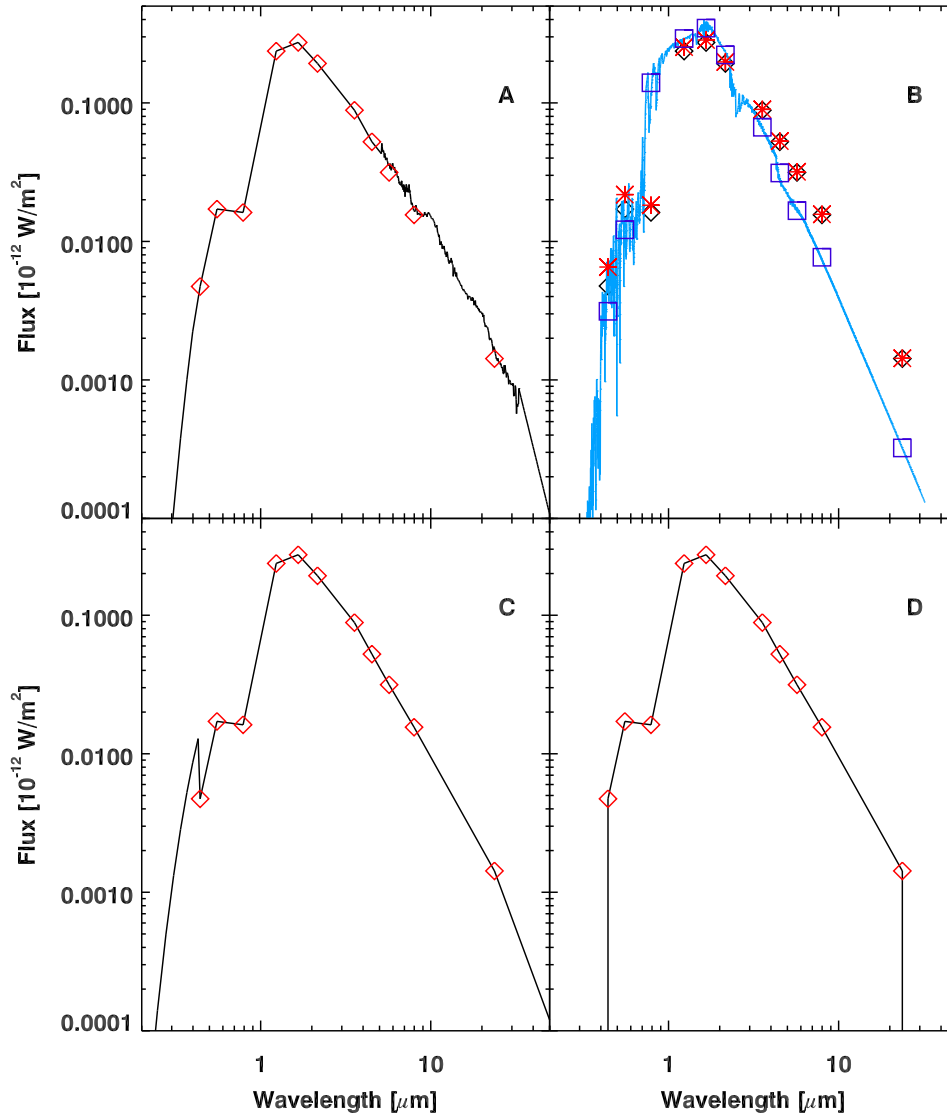
Figure 2.4: Comparison of methods used to calculate Bolometric magnitudes for the SAGE-Spec sample: The trapezoidal integration method is shown in panel A; SED fitting McDonald et al. (2009) method: in panel B; Sloan et al. (2008) method: in panel C and Srinivasan et al. (2009) method: in panel D.

cal/infrared photometry, to which a Wien tail was fitted in the optical, while a Rayleigh-Jeans tail was fitted to the long-wavelength data. For stellar photospheres, and O-AGB/RSG stars with little infrared excess, bolometric magnitudes were also calculated using the SED-fitting code described by McDonald et al. (2009). This code performs a χ^2-minimisation between the observed SED (corrected for interstellar reddening) and a grid of - stellar atmosphere models (Allard et al. 2011) which are scaled in flux to derive a bolometric luminosity. This provided a better χ^2 fit to the optical and near-IR photometry than fitting a Planck function. For the most-enshrouded stars, fitting the SED with 'naked' stellar photosphere models leads to a under-estimation of the temperature and luminosity due to circumstellar reddening and hence this method is not preferred for very dusty sources. The distances and $E(B - V)$ values adopted in our calculations are listed in Table 1.1.

For the initial SAGE-Spec sample, bolometric magnitudes were also calculated using the method described by Sloan et al. (2008). This technique involves fitting a $3\,600\,$K Planck function to the optical photometry and integrating over the spectrum and photometry. This is most appropriate for AGB stars and RSGs where a $3\,600\,$K Planck function is realistic, and for dusty sources where most of the emission is longward of the J band. Luminosities have also been derived for a colour-selected sample of LMC AGB stars via trapezoidal integration of the photometric data, however, this method assumes that there is zero flux outside the first and last photometric points (Srinivasan et al. 2009).

The methods used to calculate the bolometric luminosity for an O-rich evolved star is shown in Figure 2.4 and a comparison of the luminosities calculated for the entire SAGE-Spec sample are shown in Fig. 2.5. In general, there is good agreement between the different methods, however, there is a systematic offset in the values of Srinivasan et al. (2009) which are typically brighter by $\sim 0.15\,$mag; this is due to the use of a different zero-point flux (S. Srinivasan, priv. comm). The derived bolometric magnitudes show the greatest divergence when there is limited photometric coverage. For these cases the trapezoidal integration of the IRS spectra and photometry provides
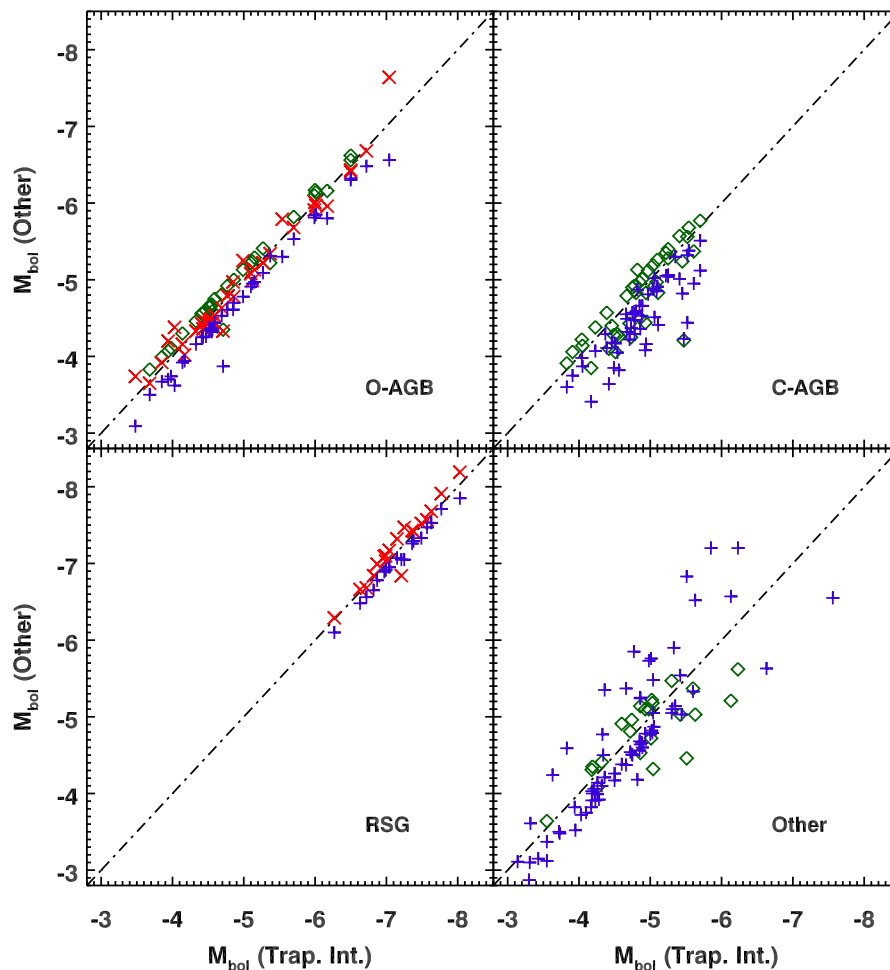
Figure 2.5: Bolometric magnitudes for the SAGE-Spec sample: The trapezoidal integration method (dashed line) is compared to the McDonald et al. (2009) method: red crosses, Sloan et al. (2008) method: purple plus signs and Srinivasan et al. (2009) method: green diamonds.

the most reliable estimate of the bolometric luminosity, however this may slightly overestimate the flux for bluer objects since it neglects molecular absorption.

Figure 2.6 compares the bolometric magnitudes for O-AGB stars and RSGs in the Magellanic Clouds and the Galactic globular cluster sources considered in this work. In the LMC we probe the full AGB luminosity range, however, in the SMC the observed
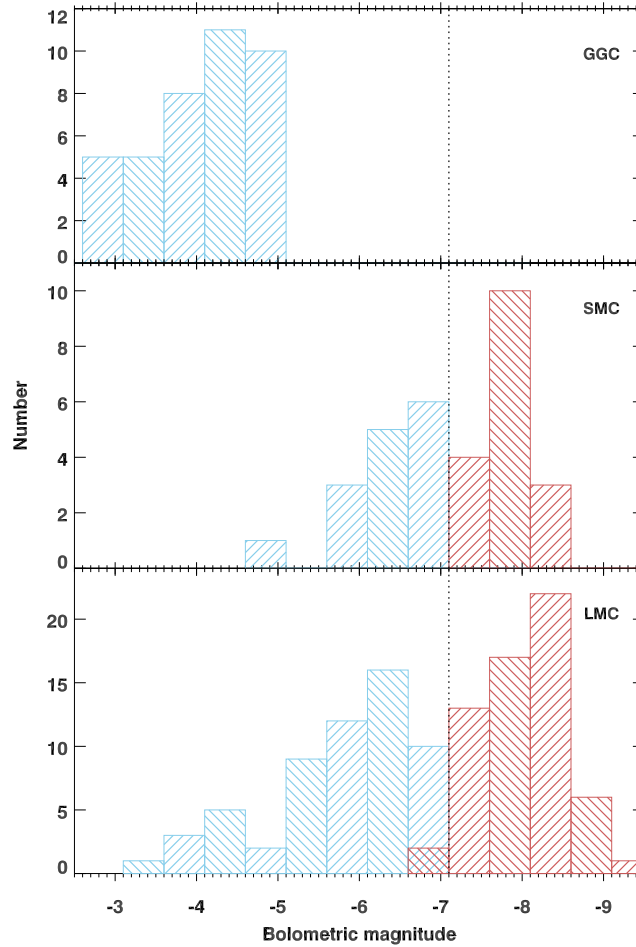
Figure 2.6: Comparison of the bolometric magnitudes in the LMC, SMC and globular cluster samples. The 'classical' luminosity limit for AGB stars is indicated by the dotted line. Sources to the left of the line are AGB stars (blue) and to the right RSGs (red).

sample is biased to the brightest AGB sources and supergiants. The double-peaked distribution for the O-AGB stars in LMC indicates that we are sensitive to both the low mass AGB population and an intermediate mass population, which are currently undergoing hot bottom burning. In the LMC sample a small number of sources classified as RSG fall below the 'classical' lower luminosity limit of RSGs. These sources are members of young clusters, where evolutionary time-scales are insufficient for low-

mass stars to have reached the AGB. Since RSGs are more massive than AGB stars ($>8\,M_\odot$) and thus evolve more rapidly, we consider a suitable O-rich star to be a RSG if it resides in a young cluster.

One limitation of using luminosity as the discriminant between O-rich AGB stars and RSGs is the potential contamination of the RSGs by foreground oxygen-rich RGB and AGB stars. This contamination may be mitigated via radial velocity measurements.

2.4 Spectral Classifications for the Magellanic Cloud

We applied the decision-tree classification methodology of Woods et al. (2011) to all the archival IRS observations of point sources within the SAGE-LMC (Woods et al., in prep.), and SAGE-SMC footprints (Ruffle et al., in prep.). A summary of the classification of IRS staring mode point sources within the SAGE-LMC footprint is given in Table 2.1, and classifications of point sources within the SAGE-SMC footprint are given in Table 2.2. Based on these classifications, a sample of O-AGB and RSG sources in the Magellanic Clouds was compiled.

Table 2.1: Summary of classifications for LMC point sources.

Type	Count	Agreement with Photometric Class (%)	Type	Count
YSO	325	...	C-PAGB	21
Star	33	...	O-PAGB*	34
C-AGB	150	60.6	(*inc. RV Tau)	10
O-AGB	86	57.8	C-PN	15
RSG	78	42.3	O-PN	28
H	80	...	Galaxies	8
Other	41	...	Unknown	8

Table 2.2: Summary of classifications for SMC point sources.

Type	Count	Agreement with Photometric Class (%)	Type	Count
YSO	54	...	C-PAGB	3
Star	11	...	O-PAGB*	2
C-AGB	39	84.6	(*inc. RV Tau)	0
O-AGB	22	68.1	C-PN	19
RSG	23	86.9	O-PN	5
H	16	...	Galaxies	1
Other	18	...	Unknown	7

2.4.1 Comparison of Spectroscopic and Photometric Classifications

By relating the spectroscopically identified O-rich and C-rich evolved stars, and the YSO spectral classes to regions in colour-magnitude space, the accuracy of the photometric classifications can be tested. Near-IR to mid-IR colour–magnitude diagrams (CMDs) for the SMC and the LMC are presented in Figures 2.7–2.12. The photometry presented here is from the *Spitzer* SAGE-LMC and SAGE-SMC archive catalogue, and the photometric classifications are based on the colour cuts from Boyer et al. (2011).

Photometrically, RSGs, C-AGB and O-AGB stars that have not yet reached the 'superwind' phase of evolution are predominantly separated using colour-magnitude cuts in the $J - K_s$ versus K_s CMD. While extreme AGB stars (X-AGB) which are heavily dust-enshrouded are often obscured at optical and near-IR wavelengths are selected via their mid-IR colours.

IR colours are generally a good indicator of the stellar characteristics and dust properties of large stellar populations. However, inaccuracies in the classifications often occur due to the overlap of different classifications in colour–magnitude and colour–colour space. The cuts used by Boyer et al. (2011) to select AGB stars and to separate O-AGB stars and RSGs from C-AGB stars (in $J - K_s$) shows good agreement (better than 85 per cent) with the spectroscopic classifications. Oxygen-rich stars (O-AGB and RSGs) and S-AGB stars are the primary contaminants in the C-AGB class; while contamination between O-AGBs and RSG stars is the main source of error when separating these sources and requires additional (non-photometric) information to make a cleaner cut. Very dusty C-AGB, O-AGB and RSGs are not included in these classifications and are instead included in the extreme AGB star (X-AGB) classification.

The X-AGB class is predominantly composed of C-rich AGB stars (~56 per cent). Surprisingly, massive O-rich AGB stars only make up a small fraction of this class (~8 per cent). The biggest contaminants are YSOs (~20 per cent) and H regions (~9.5 per cent). This large overlap of YSOs and evolved carbon stars in colour-magnitude space leads to conflicting photometric classifications; these categories would benefit
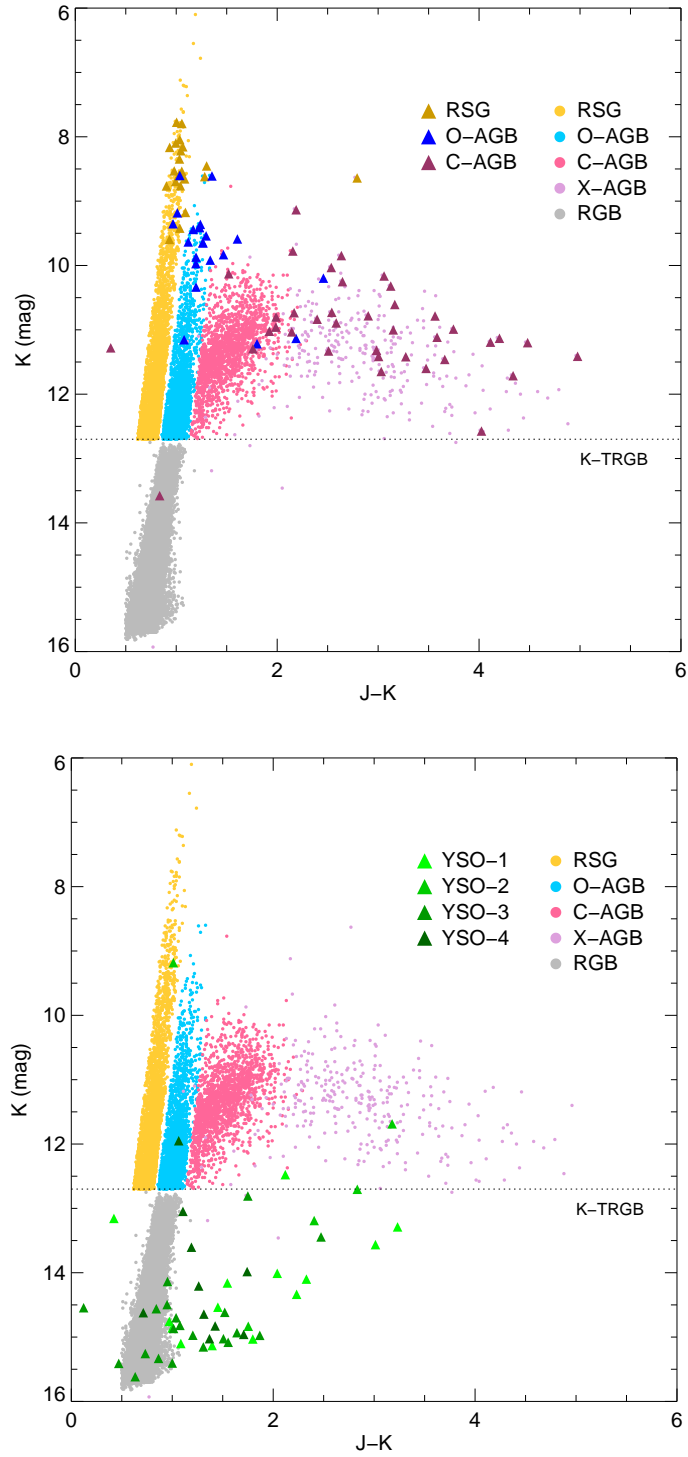
Figure 2.7: $J - K_s$ vs. K_s colour magnitude diagram for the SMC showing the spectrally classified O-AGB, RSG and C-AGB plotted over the SAGE-SMC evolved star photometric classifications of Boyer et al. (2011). In the bottom panel the YSO spectral classes are shown as green points.
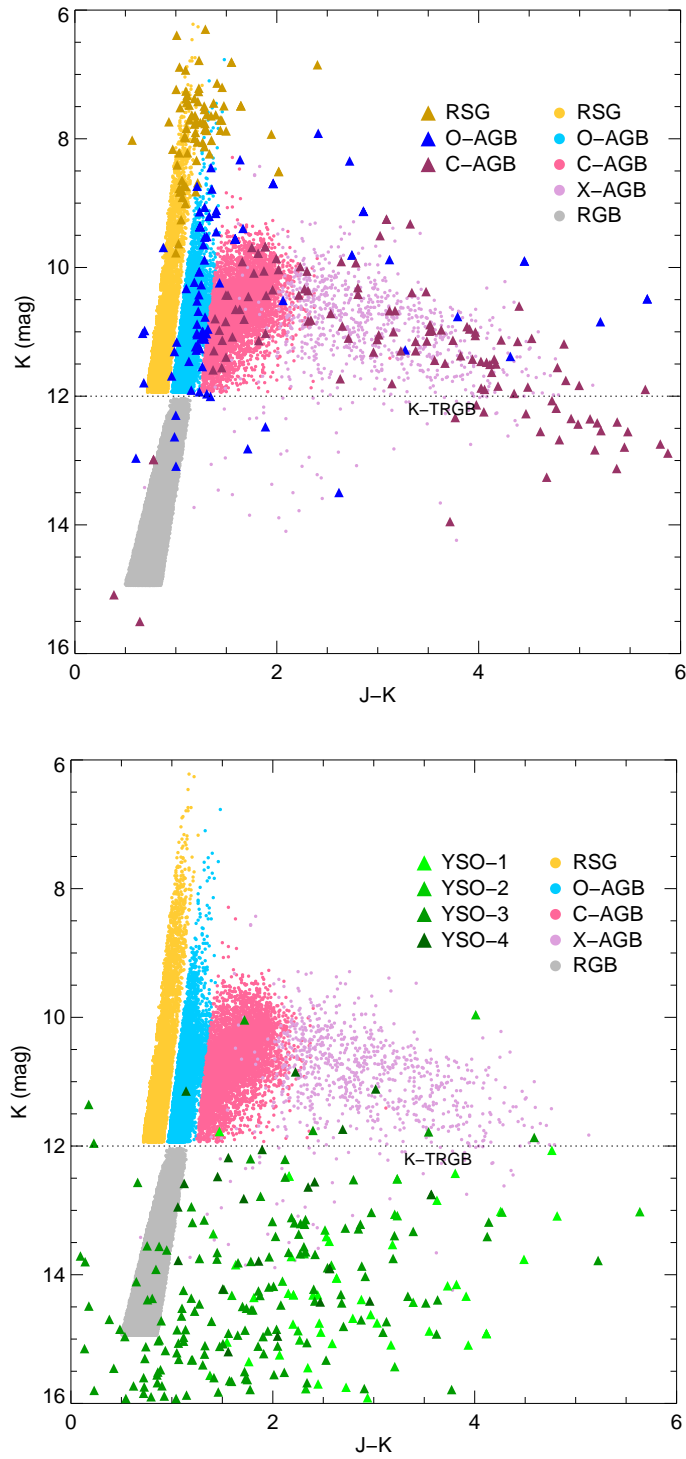
Figure 2.8: $J - K_s$ vs. K_s colour magnitude diagram for the LMC. In the bottom panel the evolved star photometric selection criteria from Cioni et al. (2006) and Boyer et al. (2011) is indicated.
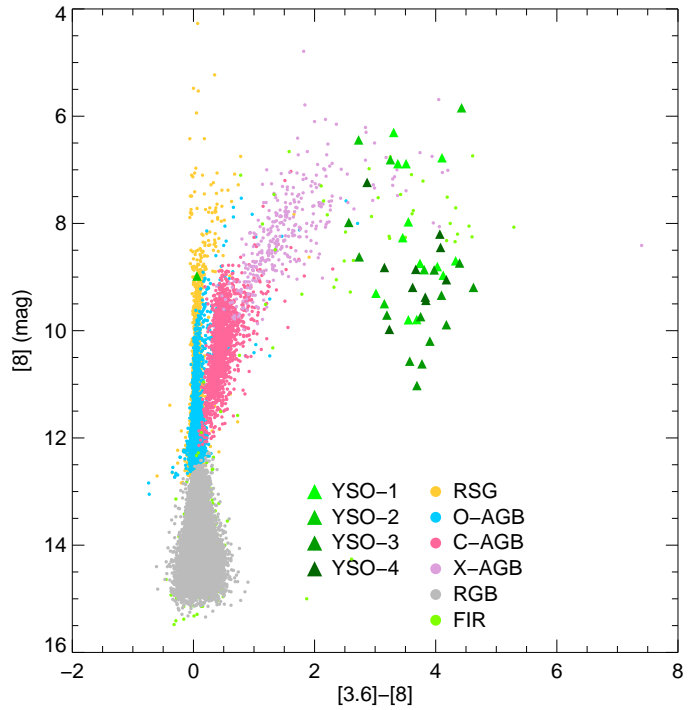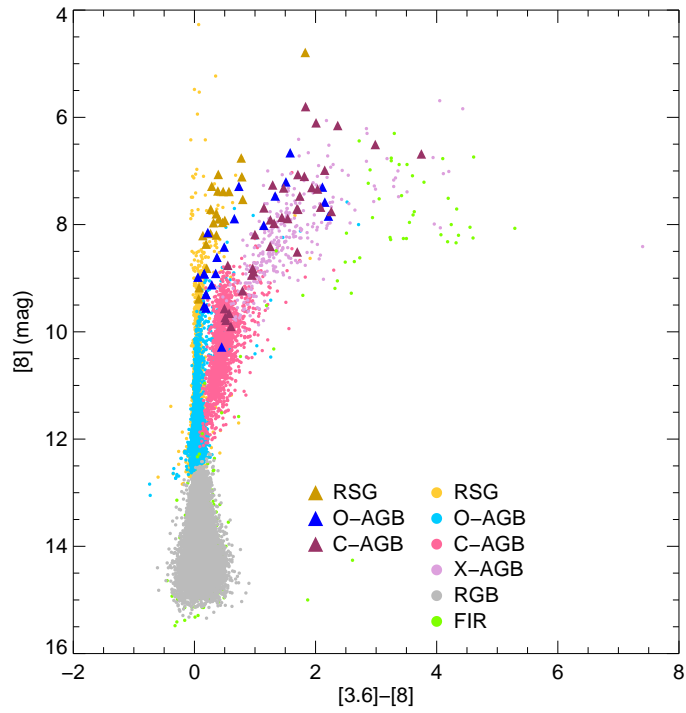
Figure 2.9: [3.6] − [8] vs. [8] colour magnitude diagram for the SMC. Due to circumstellar dust extinction, many dust-enshrouded X-AGB stars are only discernible by their mid-IR colours.
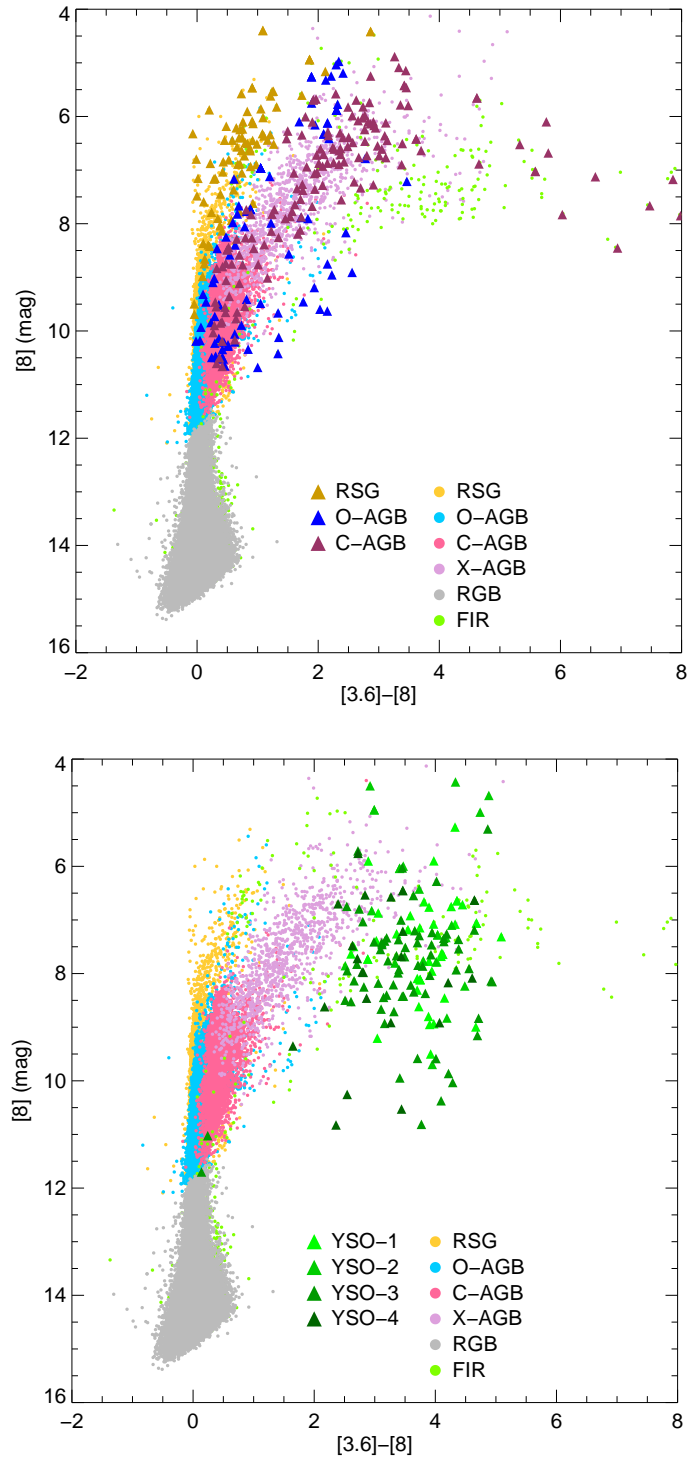
Figure 2.10: [3.6] − [8] vs. [8] colour magnitude diagram for the LMC.
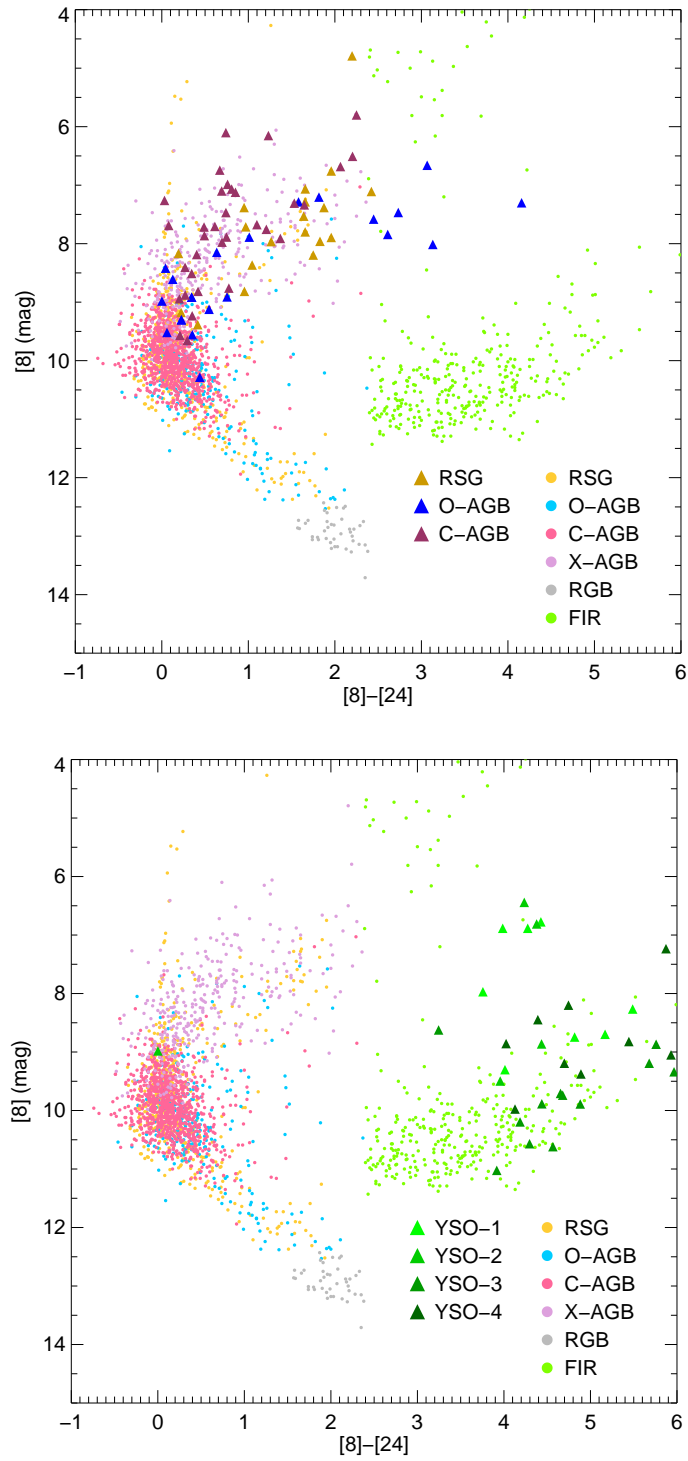
Figure 2.11: $[8] - [24]$ vs. $[8]$ colour magnitude diagram for the SMC. In this case, the YSOs are cleanly separated from the evolved star population.
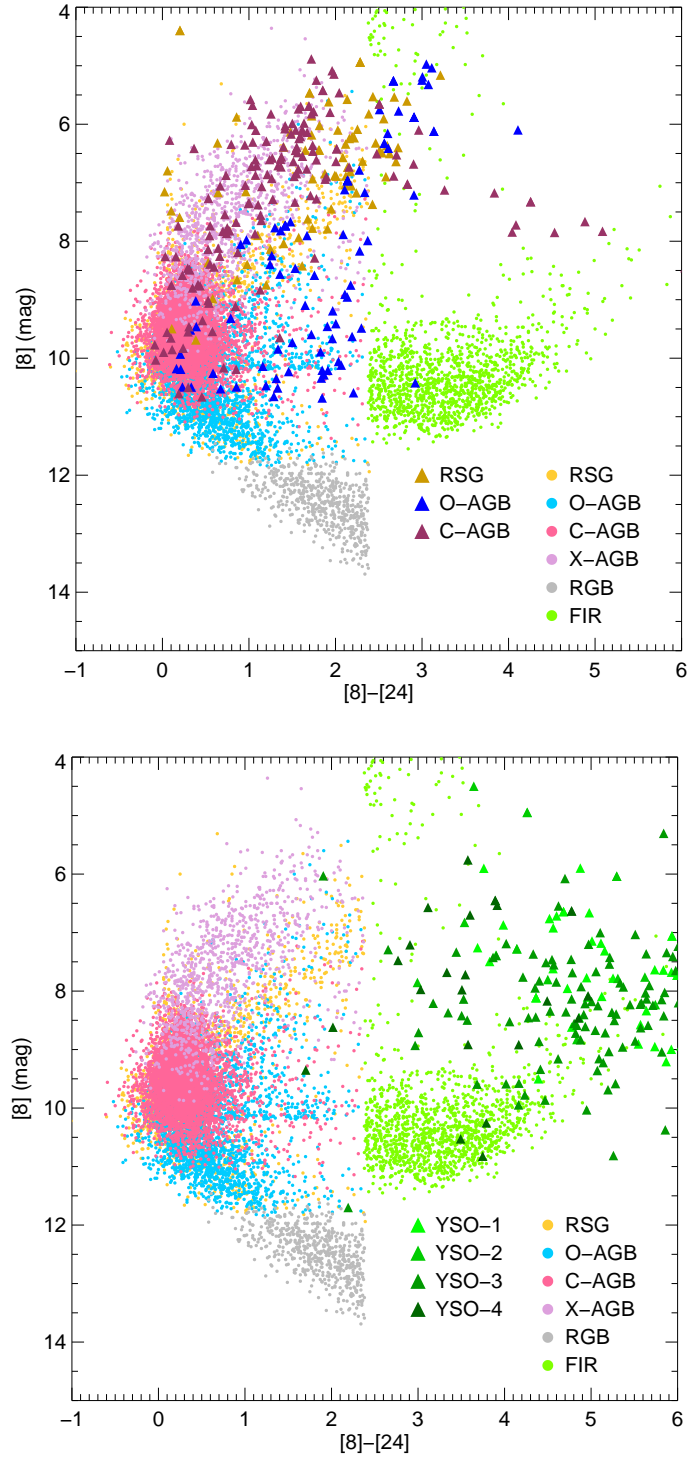
Figure 2.12: [8] − [24] vs. [8] colour magnitude diagram for the LMC.

from additional filters in the mid-IR to aid identification (See Section 2.5.1).

In general, the more massive O-AGB stars are photometrically classified as Far-IR Objects (FIR). This class encompasses sources with rising spectral energy distributions (SEDs) and are selected on the basis that the 24-μm flux density is greater than the 8-μm flux density. Sources with a rising spectrum toward longer wavelengths are typically YSOs (~47 per cent), however, O-AGBs and RSGs can show a strong IR excess at 8 and 24 μm due to silicate features. These O-rich evolved sources have similar photometric characteristics to evolved YSOs with silicate features in emission superimposed on a hotter dust continuum, limiting photometric selection. In the FIR category, ~20 per cent of the sources are spectroscopically classified as O-rich stars (O-AGB and RSGs), and ~8 per cent of the sources are matched to C-AGB stars.

2.5 *SPICA*

The Space Infrared Telescope for Cosmology and Astrophysics (*SPICA*) is a proposed medium-to far-infrared (5 – 210 μm) space telescope, whose science objectives include understanding the formation and evolution of baryonic matter (dust and gas) in galaxies. *SPICA* will have 3.5-metre mirror (comparable to that of *Herschel*) that will be cooled to cryogenic temperatures to achieve a high sensitivity and spatial resolution. The instruments on board *SPICA* will have both spectroscopic and imaging capabilities; the wide field of view enables large photometric surveys of crowded regions in M31 to the depth reached by SAGE for the LMC. *SPICA* is expected to be launched in the early 2020s and its mission is scheduled to last for a minimum of 3 years.

2.5.1 Synthetic colour-colour cuts for the proposed *SPICA* bands

The large point-source spectroscopic sample and associated spectral classifications of the *Spitzer* IRS staring mode targets in the Magellanic Clouds can be used to develop synthetic colour-colour cuts for the proposed *SPICA* Mid-infrared Camera and Spec-
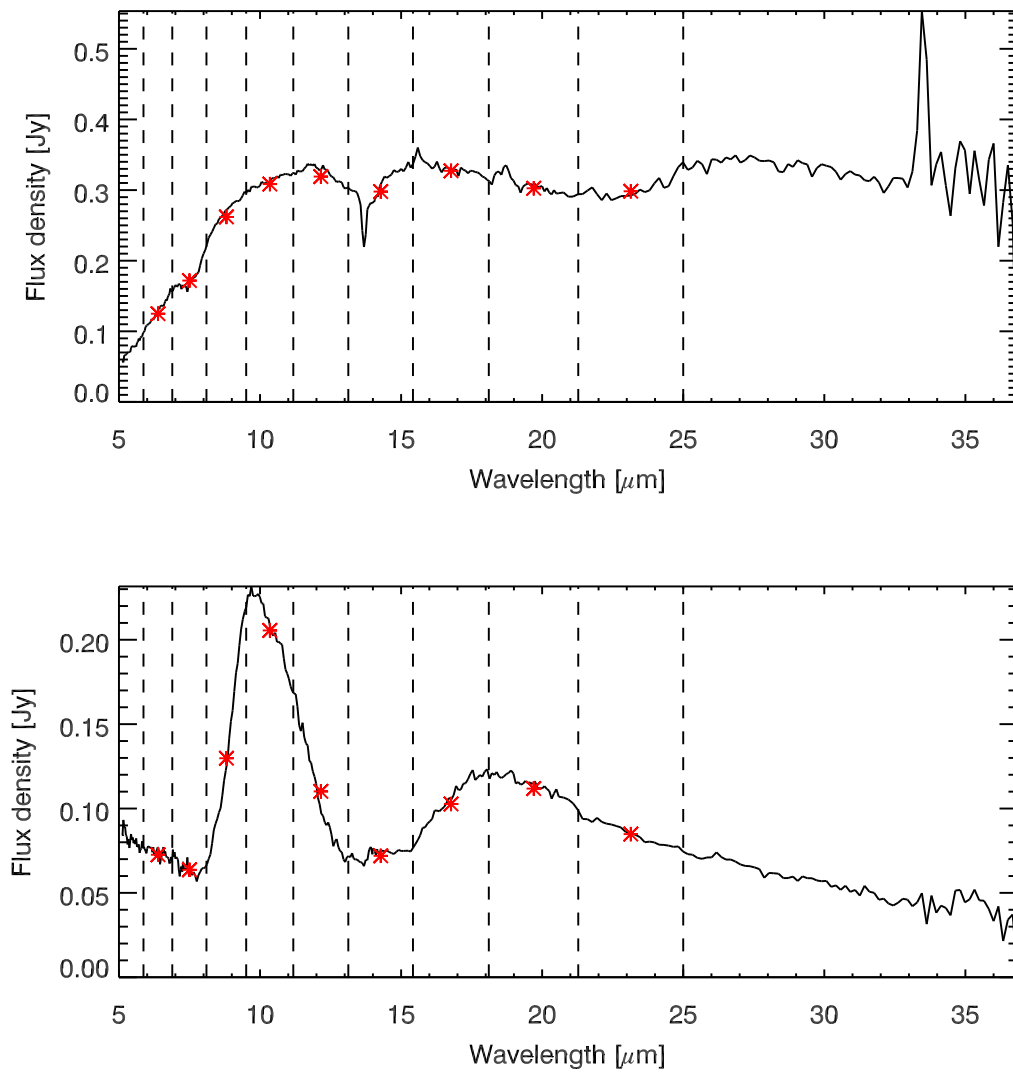
Figure 2.13: Example of 'typical' *Spitzer* spectra for a C-AGB (top) and an O-AGB (bottom) with the proposed *SPICA* transmission curves superimposed. The synthetic flux in each band is indicated by an asterisk.

Table 2.3: Proposed filter bands for *SPICA* WFC-S.

Channel Number	Central wavelength (μm)	Wavelength range (μm)	Interpolated zero magnitude (mag)
1	5.43	5.00 − 5.87	17.9
2	6.38	5.87 − 6.89	17.6
3	7.50	6.89 − 8.10	17.3
4	8.81	8.10 − 9.51	16.6
5	10.34	9.51 − 11.18	15.6
6	12.15	11.18 − 13.13	14.5
7	14.27	13.13 − 15.42	13.1
8	16.77	15.42 − 18.11	11.5
9	19.70	18.11 − 21.28	9.7
10	23.14	21.28 − 25.00	7.5

trometer (MCS) bands (see Kataza et al. 2012). The MCS instrument will have a wavelength coverage of 5-25 μm, and a $5' \times 5'$ field of view. The ten filters in the camera are expected to have continuous wavelength coverage over the *SPICA* spectral range and each will cover equal widths in logarithmic wavelength. Table 2.3 lists the proposed *SPICA* filters and bandpasses. Based on these specifications and assuming a rectangular filter function with equal width in log space, synthetic fluxes for the proposed *SPICA* bands can be calculated for typical objects (i.e. evolved stars and YSOs) from the SAGE-Spec catalogue.

Synthetic fluxes at the effective central wavelength in each *SPICA* band were obtained by convolving the preliminary *SPICA* filter transmission curves with *Spitzer* spectra. Figure 2.13 shows the spectra of a C-AGB and a O-AGB star with the *SPICA*-MCS bandpasses superimposed; the synthetic flux density for each band is also indicated. These estimates of the flux density can then be converted to colours using zero
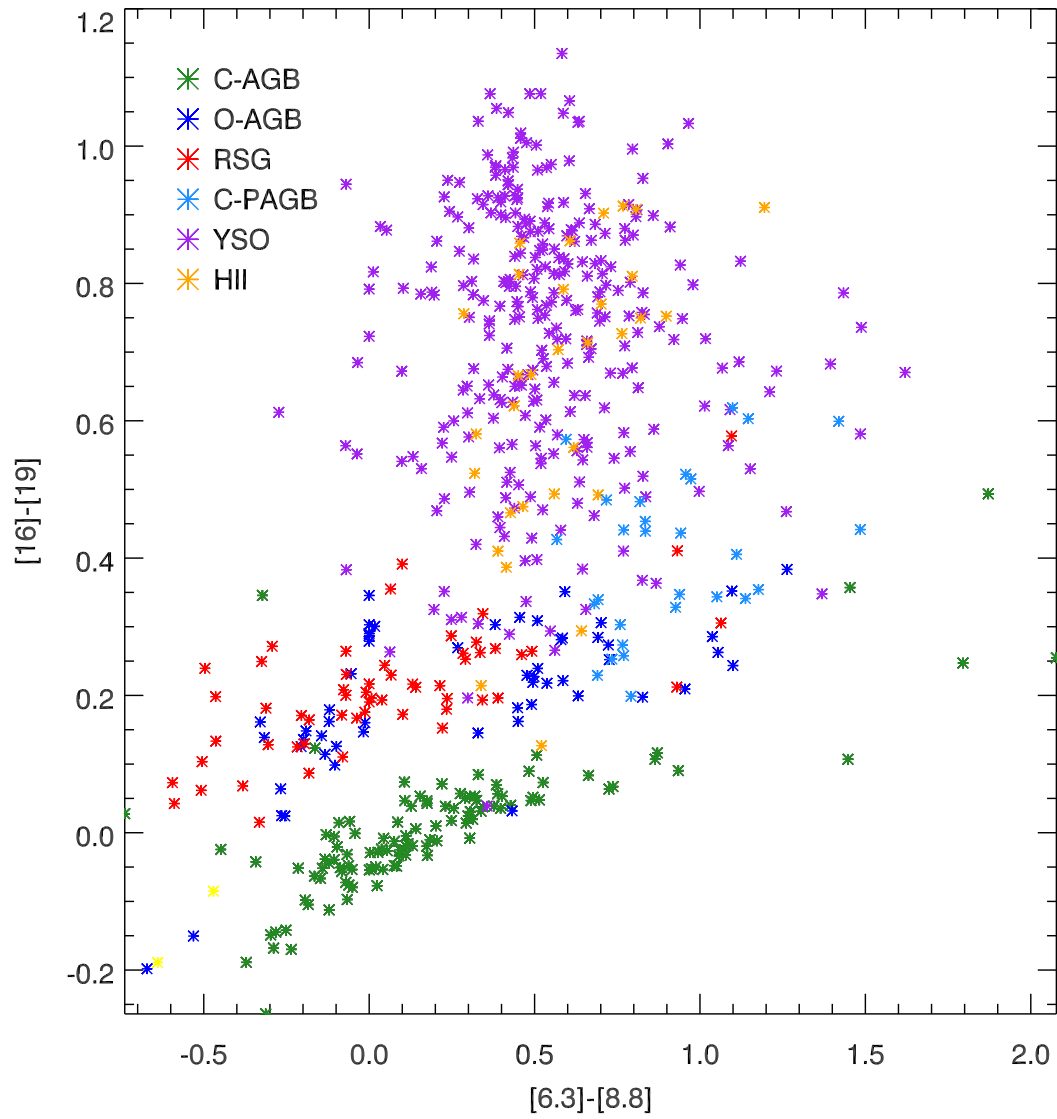
Figure 2.14: Colour–colour diagram using proposed *SPICA*-MCS filters convolved with the SAGE-Spec and archival spectra.

point magnitudes. These were interpolated from the zero points for the *Spitzer* bands; all reported magnitudes are in the Vega System (see Rieke et al. 2008, and references therein).

By relating the spectral classifications of typical objects in the SAGE-Spec catalogue to their predicted colours in the *SPICA*-MCS filters the region each object class will occupy in colour-magnitude space can be determined and a photometric colour-classification scheme can be developed. Figure 2.14 shows an example colour–colour diagram for the LMC using the proposed *SPICA*-MCS filters; the [6.6]–[8.8] versus [16]–[19] colour–colour cut is a good diagnostic for separating carbon-rich AGB stars from other cool evolved stars. The distinction between C-AGB stars and YSOs can also clearly be seen in this figure. These colour indices are based on the 'Manchester Method' for analysing carbon stars in the Magellanic Clouds (Sloan et al. 2006; Zijlstra et al. 2006). The [6.6]–[8.8] colour indicates the temperature of the carbon-rich dust and the [16]–[19] colour estimates the contribution from cool dust from the underlying the MgS feature.

The additional mid-IR photometric information provided by *SPICA* will break the degeneracy in the overlapping region of colour space covered by dusty evolved stars (X-AGB and FIR classes) and YSOs. Resolving conflicting classifications will enable accurate population characteristics and the dust-production rates by chemical type to be determined.

The exact specifications for the *SPICA*-MCS filters have not yet been finalised. The filters currently proposed have yet to be optimised for the detection of the most relevant molecular species and mineral components in evolved stars, the ISM and star forming regions. By adjusting the band centre positions and also by taking account of the technical constraints a revised filter set can be developed. This will better discriminate the emission and absorptions features from different dust species and improve photometric colour-classification schemes.

2.6 Summary

In this chapter, we apply a decision tree spectral classification diagnostic to all the archival *Spitzer* IRS observations of point sources within the Magellanic Clouds. The classification criterion is primarily based on the spectral features present and SED characteristics. The large data-set enables us to compile a statistically significant sample of O-AGBs and RSGs with sub-solar metallicity. Bolometric magnitudes were used as a determinant between these two objects classes which otherwise have indistinguishable spectral characteristics. This sample forms the basis of this work, and will be studied in detail in the following chapters.

The spectral classification of point sources in the Magellanic Clouds allow us to improve existing colour classifications, and to predict colours of stellar populations with the proposed filter sets for the *SPICA*-MCS instrument. These MCS colour-magnitude diagrams provides clearer separation between key populations, minimising contamination between stellar types and unresolved background galaxies. The improved SED coverage also enables the dust features to be better sampled.

3

Crystalline Silicate Formation

The work presented in this chapter was published in Jones et al., 2012, MNRAS, 427, 3209.

3.1 Introduction

The formation of crystalline silicates in the wind of evolved stars is not well understood: crystalline structures are the energetically more favourable atomic arrangement for silicates yet, in most cases, crystalline silicate dust is only a minor component of the circumstellar dust shell. The transition from amorphous to crystalline silicate grains is a thermal process, requiring temperatures in the region of 1040 K (Hallenbeck et al. 1998; Fabian et al. 2000; Speck et al. 2011). However, there is little consensus on how silicates in stellar outflows gain sufficient energy for this transition to occur. In order to determine the physical conditions under which crystalline silicates form we require a better understanding of the conditions surrounding the star (e.g. wind densities). The formation process of crystalline grains can be constrained by correlating the crystalline fraction with the dust or gas column density. A correlation with dust density suggests that annealing of amorphous silicate grains heated by radiation is probably the dominant means by which crystals are manufactured (Sogawa & Kozasa 1999), while a correlation with gas density would suggest that direct condensation of crystalline silicates in the wind will dominate (e.g. Tielens 1998; Gail & Sedlmayr 1999).

In *Infrared Space Observatory* (*ISO*) spectra of Milky Way (MW) giant stars, the spectral features due to the crystalline silicates forsterite (Mg_2SiO_4) and enstatite ($MgSiO_3$) typically only appear around evolved stars if their mass-loss rate is higher than a threshold value of $\sim 10^{-5}$ $M_\odot$ yr^{-1} (Cami et al. 1998; Sylvester et al. 1999). For example, the high-density winds of heavily enshrouded OH/IR stars have measured crystalline fractions of up to ~ 20 per cent of the silicate mass (Kemper et al. 2001; de Vries et al. 2010). Conversely, lower mass-loss rate AGB stars, such as Miras, normally lack crystalline silicate dust features in their spectra. This suggests a correlation between lattice order and wind density (e.g. Cami et al. 1998; Speck et al. 2008). Alternatively, contrast effects between amorphous and crystalline silicate grains at different temperatures can mask the characteristic spectral features of the crystalline material (up to the 40 per cent mass fraction level) in infrared spectra of low mass-loss rate AGB stars (Kemper et al. 2001). If the crystalline and amorphous silicates are in thermal contact with each other, contrast improves, and the detection of smaller amounts (< 40 per cent) of crystalline silicates in low mass-loss rate AGB stars becomes possible. This could explain detections of crystalline silicates in lower mass-loss rate objects, such as the recent observations of low-metallicity, low mass-loss rate evolved stars in Galactic globular clusters that show crystalline silicates (Sloan et al. 2010; McDonald et al. 2011a; Lebzelter et al. 2006).

Observations of evolved stars in the metal-poor environments of the Magellanic Clouds with the *Spitzer Space Telescope* provide an ideal opportunity to explore the occurrence of crystallinity and investigate how the O-rich dust condensation depends on the physical and chemical conditions of the envelope. The dust-to-gas mass ratios of stars in the Magellanic Clouds are assumed to be lower than those of stars in the Solar neighbourhood and have a linear dependence with metallicity (van Loon 2000; Marshall et al. 2004; van Loon 2006), breaking the degeneracy between the dust column density and the gas density in the outflows of AGB stars. By carefully studying the dependence of crystallinity on the dust and gas mass-loss rate, we address the influences of dust density and gas density on the formation of crystalline grains.

3.2   The sample

Our sample contains 69 oxygen-rich AGB stars (O-AGB) and 76 RSG stars in the Magellanic Clouds which were observed spectroscopically with *Spitzer*, and 131 Galactic field O-AGBs and RSGs observed with either *Spitzer* or *ISO*. The *Spitzer* spectra cover a wavelength range of 5.2–37.2 μm while *ISO* spectra cover the 2.38–45.2 μm part of the spectrum. We combine this sample with 39 spectra from 14 Galactic globular clusters to extend the low end of the metallicity range.

3.2.1   LMC sample

The LMC sample comprises 54 O-AGB and 60 RSG stars selected based on the decision-tree classification scheme developed by Woods et al. (2011). Within the SAGE-Spec catalogue, 197 objects have been classified according to their *Spitzer* IRS spectrum and SED with associated *U, B, V, I, J, H, K_s*, IRAC and MIPS photometry. From this we found 40 O-AGB stars and 19 RSGs. To supplement this LMC sample, we applied the decision-tree classification methodology of Woods et al. (2011) to all the archival IRS observations of point sources within the SAGE-LMC footprint (Woods et al., in prep.), resulting in a further 148 sources. As this work is primarily concerned with crystalline silicates, which become prominent at longer wavelengths ($\lambda > 20$ μm), for inclusion in the sample we require that the sources were observed with the Long-Low (14.5–37.2 μm) module on IRS. We limit our study to those spectra which were visually deemed to have a sufficient signal-to-noise for the identification of crystalline silicate features. Thus we arrive at a total of 114 sources. Table 3.1 lists the sources in the LMC sample, along with SAGE-Spec identification (SSID) (see Kemper et al. 2010), coordinates, Astronomical Observation Request (AOR), bolometric magnitudes (M_{bol}), periods and mass-loss rates determined from SED fitting with the 'Grid of Red supergiants and Asymptotic giant branch ModelS' (; see Section 3.3.1).

Table 3.1: Details of the sources in the LMC sample. For each source the SAGE-Spec identification (SSID), coordinates, Astronomical Observation Request (AOR), classification, bolometric magnitudes (M_{bol}), period and dust mass-loss rate ($\dot{M}_{dust}$) is given.

SSID	RA (J2000)	Dec (J2000)	AOR	Class	$M_{bol}{}^{a}$	Period (d)	$\dot{M}_{dust}$ (M$_\odot$ yr^{-1})
4007	04 40 28.49	−69 55 12.70	6077440	O-AGB	−6.68	1179[b]	3.61E−08
4	04 47 18.63	−69 42 20.53	22400256	RSG	−6.81	...	5.01E−09
4022	04 49 22.46	−69 24 34.90	10958336	RSG	−7.97	361[d]	1.19E−08
6	04 49 34.38	−69 05 49.17	24318720	O-AGB	−5.54	...	2.59E−09
4024	04 49 41.38	−68 37 51.00	6076672	RSG	−7.86	1280[d]	5.43E−08
4031	04 50 40.43	−69 17 31.70	6022400	RSG	−7.51	1292[d]	2.85E−09
8	04 51 28.58	−69 55 49.90	22400768	O-AGB	−3.82	884[b]	2.09E−08
4038	04 51 28.94	−68 57 49.50	6020096	O-AGB	−5.48	1090[d]	5.12E−09
4054	04 52 43.18	−70 47 37.80	33283584	O-AGB	−4.22	...	7.90E−11
4077	04 54 14.26	−68 44 14.20	11220224	O-AGB	−5.96	694[b]	7.87E−10
4076	04 54 14.26	−68 44 13.60	11220480	O-AGB	−5.96	694[b]	7.40E−09
4078	04 54 14.29	−68 44 14.40	11219456	O-AGB	−6.06	694[b]	7.09E−09
4079	04 54 14.30	−68 44 14.00	11219712	O-AGB	−5.96	694[b]	2.00E−09
4081	04 54 14.36	−68 44 14.30	11219200	O-AGB	−5.96	694[b]	8.37E−09
4086	04 55 03.01	−69 29 13.10	10958848	RSG	−8.53	...	2.27E−09
4090	04 55 10.17	−68 20 34.90	5056256	RSG	−8.54	856[d]	5.45E−07
4091	04 55 10.47	−68 20 29.80	10973952	RSG	−9.07	886[b]	8.18E−08
4092	04 55 16.03	−69 19 12.00	10959104	RSG	−8.39	512[d]	1.42E−08
4095	04 55 21.58	−69 47 16.80	10959360	RSG	−8.12	...	1.63E−09
4098	04 55 33.44	−69 24 58.90	11239168	RSG	−7.22	683[d]	1.05E−08
22	04 56 23.26	−69 27 48.00	22404096	O-AGB	−4.62	20[b]	9.06E−08
4131	04 57 43.21	−70 08 50.40	10959872	RSG	−8.52	830[d]	2.67E−07
4149	05 00 19.10	−67 07 58.20	10960128	O-AGB	−5.50	911[b]	1.72E−08
4159	05 01 43.48	−69 40 48.50	33287680	O-AGB	−4.25	...	1.05E−08
27	05 02 21.52	−66 06 37.98	22406144	RSG	−8.19	...	3.64E−08
4187	05 04 14.19	−67 16 14.10	6015488	RSG	−9.05	418[f]	5.94E−09
38	05 04 28.91	−67 41 23.43	22408704	O-AGB	−6.17	577[b]	3.35E−08

EVOLVED STARS IN THE LOCAL GROUP

Table 3.1 – continued from previous page

SSID	RA (J2000)	Dec (J2000)	AOR	Class	$M_{bol}{}^a$	Period (d)	$\dot{M}_{dust}$ (M$_\odot$ yr^{-1})
4199	05 05 33.49	−70 33 46.70	10960896	RSG	−8.04	. . .	2.60E−09
4205	05 06 27.72	−68 12 03.90	6014976	O-AGB	−6.35	598^b	1.18E−08
54	05 07 59.36	−68 39 25.71	22412032	O-AGB	−3.98	150^b	1.37E−07
61	05 10 59.06	−68 56 13.82	22414336	O-AGB	−5.97	169^b	1.96E−08
4245	05 11 59.36	−69 25 32.80	33292800	O-AGB	−6.00	. . .	3.61E−08
4254	05 13 04.57	−64 51 40.30	6024192	O-AGB	−5.48	708^d	1.72E−08
4267	05 13 33.75	−66 34 19.30	33283328	O-AGB	−6.77	. . .	9.89E−09
4277	05 13 54.41	−69 31 45.80	27575808	RSG	−8.44	. . .	3.16E−08
4283	05 14 49.75	−67 27 19.50	10962688	RSG	−8.48	806^d	1.38E−07
82	05 18 11.05	−67 26 48.92	22419456	O-AGB	−6.43	. . .	1.96E−08
4323	05 19 53.38	−69 27 34.10	25688064	RSG	−7.80	475^c	4.39E−09
4324	05 20 01.45	−67 34 42.30	11218944	O-AGB	−6.32	602^c	1.51E−08
4325	05 20 01.45	−67 34 42.30	11217920	O-AGB	−6.32	602^c	6.03E−09
4326	05 20 01.55	−67 34 41.90	11218176	O-AGB	−6.32	602^c	9.78E−10
4327	05 20 01.62	−67 34 41.40	11218432	O-AGB	−6.32	602^c	1.54E−07
4328	05 20 01.68	−67 34 42.40	11218688	O-AGB	−6.32	602^c	8.34E−09
4329	05 20 01.71	−67 34 42.40	11217664	O-AGB	−6.32	602^c	1.58E−08
4335	05 20 23.61	−69 33 27.40	25688320	RSG	−7.41	451^c	8.29E−09
93	05 21 01.71	−69 14 17.07	22421760	O-AGB	−5.10	92^b	1.58E−08
96	05 22 06.91	−71 50 17.89	22422528	O-AGB	−4.47	81^b	1.96E−08
4368	05 22 21.14	−65 55 51.80	33284352	O-AGB	−4.47	. . .	8.07E−09
4393	05 23 43.60	−65 42 00.40	10963200	RSG	−8.04	313^d	1.42E−08
4418	05 25 44.78	−69 04 49.20	25687552	RSG	−7.86	199^e	5.14E−09
4427	05 26 11.35	−66 12 11.30	10963968	RSG	−7.98	597^d	6.01E−09
4434	05 26 22.20	−66 21 28.60	11239680	RSG	−8.39	475^d	6.48E−08
4441	05 26 34.88	−68 51 40.20	10964224	RSG	−8.91	. . .	2.74E−10
4080	05 27 10.24	−69 36 26.60	6022144	O-AGB	−5.96	694^b	1.04E−08
4449	05 27 10.24	−69 36 26.60	6022144	O-AGB	−6.40	529^c	2.78E−09
4452	05 27 34.36	−66 53 30.10	11239680	RSG	−8.04	600^d	3.60E−08
116	05 27 38.76	−69 28 45.57	22427392	RSG	−7.52	. . .	1.60E−08

Table 3.1 – continued from previous page

SSID	RA (J2000)	Dec (J2000)	AOR	Class	$M_{bol}{}^a$	Period (d)	$\dot{M}_{dust}$ (M$_\odot$ yr^{-1})
4454	05 27 40.19	−69 08 04.60	6077952	RSG	−8.77	...	4.67E−07
4464	05 28 22.19	−69 08 32.90	19151104	RSG	−7.16	...	7.09E−08
4466	05 28 28.89	−68 07 08.30	10964480	RSG	−8.45	479^d	4.09E−09
4467	05 28 32.11	−69 29 09.40	6020864	O-AGB	−5.61	50^b	7.90E−11
4468	05 28 36.73	−69 20 03.80	6014208	O-AGB	−6.98	605^b	2.49E−09
4480	05 28 48.23	−71 02 29.30	10964992	O-AGB	−6.21	1137^b	2.11E−08
4483	05 28 59.96	−67 45 00.80	17399552	O-AGB	−5.35	387^c	3.60E−08
4486	05 29 03.14	−69 48 06.30	6014720	O-AGB	−6.83	453^d	7.09E−08
4487	05 29 03.49	−69 06 46.40	11238912	RSG	−7.88	363^d	1.46E−08
121	05 29 24.61	−69 55 14.19	27084288	O-AGB	−7.04	...	1.63E−08
4490	05 29 42.22	−68 57 17.70	10965248	RSG	−8.94	765^d	8.03E−09
122	05 29 54.80	−69 04 15.73	22428672	RSG	−7.42	...	1.82E−08
123	05 30 04.67	−68 47 29.08	22428928	RSG	−7.14	...	3.83E−07
4494	05 30 10.33	−69 09 34.00	11238912	O-AGB	−5.39	...	4.39E−09
4496	05 30 20.57	−66 53 02.30	10965504	RSG	−8.28	...	4.67E−07
128	05 30 48.40	−67 16 45.88	22430208	RSG	−7.30	...	2.92E−09
129	05 30 52.25	−67 17 34.22	22430464	RSG	−7.35	...	1.20E−08
4508	05 31 04.18	−69 19 03.20	10965760	RSG	−8.16	644^d	3.06E−07
4509	05 31 10.67	−66 35 31.70	11239680	RSG	−8.23	426^d	3.33E−09
130	05 31 28.43	−70 10 27.65	22430720	O-AGB	−5.26	393^b	1.70E−08
4512	05 31 36.75	−66 30 08.30	10966016	RSG	−8.48	616^d	3.84E−09
135	05 32 19.31	−67 31 20.34	22432000	RSG	−7.78	...	5.78E−08
4529	05 32 35.63	−67 55 08.80	6015744	RSG	−8.36	872^d	5.95E−09
4530	05 32 37.12	−67 06 56.90	10966784	O-AGB	−6.08	...	5.17E−09
4535	05 32 51.74	−67 06 50.20	6023168	O-AGB	−6.70	1260^d	5.45E−07
4547	05 33 36.48	−69 23 13.00	27985408	O-AGB	−6.63	13^b	9.34E−08
4555	05 34 14.13	−69 47 20.50	5056512	RSG	−8.49	...	3.06E−07
4566	05 35 14.17	−67 43 55.90	10967552	RSG	−8.00	590^d	5.43E−08
147	05 35 19.01	−67 02 19.50	22434816	RSG	−7.57	...	1.06E−08
4569	05 35 24.53	−69 04 03.60	11238912	RSG	−7.48	436^d	8.03E−09

Table 3.1 – continued from previous page

SSID	RA (J2000)	Dec (J2000)	AOR	Class	M_{bol}[a]	Period (d)	$\dot{M}_{dust}$ ($M_\odot$ yr^{-1})
4583	05 35 28.30	−66 56 02.80	10967808	RSG	−8.60	798[d]	5.14E−09
4595	05 36 05.95	−69 58 02.50	33291520	O-AGB	−5.26	. . .	3.60E−08
4618	05 38 20.15	−69 37 32.40	11239424	RSG	−9.16	112[d]	1.19E−08
4622	05 38 33.94	−69 20 31.70	6076416	RSG	−8.17	944[d]	4.12E−08
4670	05 39 44.80	−69 55 18.10	6020608	O-AGB	−6.85	1393[d]	3.96E−09
4718	05 40 24.37	−69 21 17.00	11239424	RSG	−7.97	. . .	3.89E−09
4724	05 40 43.76	−69 21 58.10	10969600	RSG	−8.21	. . .	3.84E−09
4730	05 40 48.49	−69 33 36.20	10970112	RSG	−8.12	473[d]	4.12E−08
4733	05 40 55.27	−69 23 25.40	25688576	RSG	−8.12	. . .	3.33E−09
4739	05 40 59.12	−69 18 36.20	11239424	RSG	−8.24	424[d]	8.07E−09
165	05 41 02.04	−70 43 10.90	22440192	O-AGB	−6.64	709[b]	1.03E−08
4740	05 41 06.83	−69 17 14.80	25688832	RSG	−7.67	. . .	5.95E−09
4742	05 41 10.64	−69 38 04.20	10970368	RSG	−8.05	552[d]	5.17E−09
166	05 41 14.58	−71 32 36.01	22440448	O-AGB	−4.20	583[c]	1.87E−09
169	05 41 57.43	−69 12 18.61	22440960	RSG	−7.47	. . .	1.22E−07
170	05 42 03.91	−69 13 07.64	22441472	RSG	−7.47	. . .	9.85E−09
171	05 42 06.76	−69 12 31.35	22441728	RSG	−7.82	. . .	1.41E−08
172	05 42 09.98	−69 13 28.76	22441984	RSG	−6.96	. . .	3.35E−09
4752	05 42 35.46	−69 08 48.10	25689344	RSG	−7.89	. . .	3.96E−09
180	05 44 06.10	−68 37 53.68	22444288	O-AGB	−6.57	239[b]	2.62E−09
4760	05 44 13.82	−66 16 44.90	10970880	RSG	−8.28	. . .	9.89E−09
182	05 44 40.08	−69 11 49.11	22444800	O-AGB	−3.85	99[b]	3.45E−09
185	05 45 46.35	−67 32 39.16	22445824	O-AGB	−3.28	484[c]	2.65E−09
4777	05 49 13.42	−70 42 40.10	6015232	O-AGB	−5.72	666[d]	9.34E−08
4784	05 52 27.78	−69 14 10.00	6016512	O-AGB	−6.46	621[d]	8.29E−09
4791	05 55 21.11	−70 00 02.10	6077184	O-AGB	−6.40	1220[d]	3.16E−08

(a) Bolometric magnitudes are calculated as described in Sec. 2.3.

R   : (b) Soszyński et al. (2008, 2009); (c) Fraser et al. (2005, 2008);

(d) Groenewegen et al. (2009); (e) Pojmanski (2002).

3.2.2   SMC sample

The SMC sample of 15 O-AGB and 16 RSG stars was compiled from IRS staring mode observations for which Long-Low data was available within the SAGE-SMC (Gordon et al. 2011) spatial coverage. Again, these were supplemented with optical, 2MASS, IRAC and MIPS photometry from the SAGE-SMC catalogue (Gordon et al. 2011), and the S^3MC catalogue (Bolatto et al. 2007). Evolved stars were identified from the SAGE-SMC mid-IR classifications of Boyer et al. (2011), with 57 candidate evolved stars found. IR photometry alone is insufficient to accurately separate the dusty O-AGB and RSG stars from contamination by young stellar objects (YSOs) with strong oxygen-rich dust features, in particular those with a 10-μm silicate absorption feature. As with the LMC sample, we classify each object according to its *Spitzer* IRS spectrum based on its spectral features, SED, calculated bolometric luminosity, variability information and additional information from the literature, returning 27 O-AGB stars and 18 RSGs. Again, sources observed solely with the IRS Short-Low setting or with a poor signal-to-noise ratio were excluded from the sample. A summary of the SMC sample can be found in Table 3.2.

3.2.3   Galactic field sample

To provide a solar metallicity comparison, our sample also includes *ISO* Short Wavelength Spectrometer (SWS; de Graauw et al. 1996) spectra of 79 O-AGB, 9 probable O-AGBs and 22 RSG stars in the Milky Way, covering a wavelength range of 2.38–45.2 μm. This Galactic field sample was compiled from the ISO/SWS database,[1] which contains 1271 observations in full-scan mode. This database contains observations obtained for a wide range of individual observing projects, which have been uniformly reduced by Sloan et al. (2003b) and classified based on the overall shape of the SED and their IR spectral features (such as oxygen- or carbon-rich dust emission, etc.) by Kraemer et al. (2002). From this database, we selected those sources with optically-

---

[1] `http://isc.astro.cornell.edu/~sloan/library/swsatlas/aot1.html`

Table 3.2: Details of the sources in the SMC sample. For each source the name, coordinates, Astronomical Observation Request (AOR), classification, bolometric magnitudes (M_{bol}), period and dust mass-loss rate ($\dot{M}_{dust}$) is given.

Name	RA	Dec	AOR	Class	M_{bol}	Period	$\dot{M}_{dust}$
	(J2000)	(J2000)				(d)	($M_\odot$ yr^{-1})
HV 11223	00 32 01.90	−73 22 34.00	6019584	O-AGB	−6.21	407[a]	1.16E−10
HV 1366	00 42 49.90	−72 55 10.00	6017024	O-AGB	−4.90	305[a]	3.92E−11
MSX SMC 024	00 42 52.23	−73 50 51.70	10663169	O-AGB	−6.64	418[a]	1.02E−08
MSX SMC 018	00 46 31.59	−73 28 46.50	10668800	O-AGB	−6.09	915[a]	5.46E−08
SMC010889	00 48 27.02	−73 12 12.30	25689600	RSG	−8.58	...	1.75E−09
SMC011709	00 48 46.32	−73 28 20.70	25689856	RSG	−7.99	...	4.95E−10
PMMR 24	00 48 51.79	−73 22 39.90	17409024	RSG	−7.62	231[b]	2.59E−09
MSX SMC 096	00 50 06.40	−73 28 11.10	10667008	RSG	−7.93	...	7.86E−10
MSX SMC 055	00 50 07.19	−73 31 25.20	10657536	RSG	−7.91	1749[a]	3.26E−08
MSX SMC 134	00 50 44.39	−72 37 39.00	10665216	O-AGB	−5.68	248[a]	5.96E−08
MSX SMC 109	00 51 29.68	−73 10 44.30	10667520	RSG	−8.35	...	2.60E−09
HV 11303	00 52 09.00	−71 36 22.00	6017536	O-AGB	−7.07	534[a]	4.07E−10
BMB−B 75	00 52 12.87	−73 08 52.70	17409280	O-AGB	−6.74	760[c]	2.95E−08
HV 11329	00 53 39.40	−72 52 39.20	6017280	O-AGB	−6.40	377[a]	3.27E−10
MSX SMC 000	00 55 18.10	−72 05 31.00	10666240	RSG	−7.10	544[a]	2.77E−10
MSX SMC 168	00 55 26.76	−72 35 56.10	10668288	RSG	−8.00	...	1.76E−09
HV 838	00 55 38.30	−73 11 42.00	6017792	RSG	−7.21	654[a]	9.49E−11
HV 11366	00 56 54.80	−72 14 07.00	6018304	O-AGB	−6.27	183[a]	4.23E−11
HV 12149	00 58 50.30	−72 18 34.00	6019328	O-AGB	−7.04	745[a]	1.88E−09
SMC046662	00 59 35.04	−72 04 06.20	25690112	RSG	−8.07	321[b]	3.10E−09
MSX SMC 181	01 00 48.18	−72 51 02.10	10665728	RSG	−7.28	1062[a]	8.85E−09
HV 11423	01 00 54.80	−71 37 55.00	25691136	RSG	−7.78	...	2.94E−09
SMC052334	01 01 54.16	−71 52 18.80	25690368	RSG	−7.68	...	3.42E−10
SMC055188	01 03 02.38	−72 01 52.90	27603200	RSG	−7.54	530[c]	3.91E−09
SMC55681	01 03 12.98	−72 09 26.50	25687808	RSG	−7.79	...	2.96E−09
MSX SMC 234	01 03 42.35	−72 13 42.80	27522048	O-AGB	−6.49	...	4.05E−08
HV 1963	01 04 26.80	−72 34 40.00	6018048	O-AGB	−6.74	330[a]	7.28E−11
IRAS F01066	01 08 10.27	−73 15 52.30	17409536	O-AGB	−5.64	882[c]	3.35E−08
HV 12956	01 09 02.25	−71 24 10.20	27528960	O-AGB	−6.27	523[c]	5.79E−08
MSX SMC 149	01 09 38.24	−73 20 02.40	10668032	RSG	−7.98	...	5.18E−09

R : (a) Groenewegen et al. (2009); (b) Pojmanski (2002); (c) Soszyński et al. (2011).

thin, oxygen-rich dust emission (group 2.SE) sources dominated by emission from warm silicate dust (groups 3.SE and 3.SB) and the optically-thick sources with cool silicate dust (groups 4.SA, 4.SB, 4.SC and 4.SE) which have a sufficient signal-to-noise ratio to distinguish the solid state features. Sources which have no significant dust emission (only SiO absorption at 8 μm), incomplete spectra and those which did not fulfil the criteria to be classed as an O-AGB or RSG by the Woods et al. (2011) decision-tree were eliminated from the sample. We also require the spectra to show the amorphous silicate features in order to fit their spectral energy distribution using the   model grid (see Section 3.3.1). We verified in the literature that the selected sources were classified as either an O-AGB or a RSG. The resulting list of 110 spectra is shown in Table 3.3. In instances where a source was observed by the SWS on multiple occasions, we analyse each spectrum independently. The TDT (Target Dedicated Time) number is used to identify the particular spectra for each source.

Since both RSGs and O-AGB stars are red, luminous and exhibit similar dust emission characteristics, confusion exists between these two types of sources. Sources for which reliable estimates for the distance are available or are known OH masers are further sub-divided into O-AGB and RSG stars. We consider distances from the revised *Hipparcos* catalogue (van Leeuwen 2007) to be reliable if the relative error is less than 20 per cent. The variability types have been taken from the Combined General Catalogue of Variable stars (GCVS; Kholopov et al. 1998; Samus et al. 2004).

Table 3.3: Details of the sources in the Galactic *ISO* SWS sample. For each source the name, coordinates, TDT (Target Dedicated Time) number, classification, distance, period and dust mass-loss rate ($\dot{M}_{\mathrm{dust}}$) is given.

Name	RA (J2000)	Dec (J2000)	TDT	Class	Distance (pc)	Ref.	Period[a] (d)	$\dot{M}_{\mathrm{dust}}$ ($M_\odot$ yr^{-1})
S Scl	00 15 22.18	−32 02 43.4	37102018	O-AGB	430	16	363	1.35E−09
S Scl	00 15 22.18	−32 02 43.4	73500129	O-AGB	430	16	363	1.13E−09
WX Psc	01 06 25.96	12 35 53.1	39502217	O-AGB	833	4	660	1.92E−07
WX Psc	01 06 25.96	12 35 53.1	76101413	O-AGB	833	4	660	1.92E−07
OH 127.8	01 33 50.60	62 26 47.0	44301870	O-AGB	…	…	…	2.36E−06
OH 127.8	01 33 50.60	62 26 47.0	78800604	O-AGB	…	…	…	6.25E−07
SV Psc	01 46 35.30	19 05 04.0	80501620	O-AGB	380	14	102	3.08E−09
Mira	02 19 20.78	−02 58 36.2	45101201	O-AGB	128	8	332	1.18E−08
SU Per	02 22 06.93	56 36 15.1	43306303	RSG	1900	10	533	1.22E−08
S Per	02 22 51.70	58 35 14.1	43306550	RSG	1900	10	822	4.84E−08
UU For	02 37 23.60	−26 58 39.0	44202463	O-AGB	…	…	…	2.38E−08
YZ Per	02 38 25.33	57 02 46.2	47301604	RSG	1900	10	378	1.22E−08
W Hor	02 44 14.70	−54 18 04.0	17902728	O-AGB	…	…	137	5.20E−09
W Hor	02 44 14.70	−54 18 04.0	75600502	O-AGB	…	…	137	5.17E−09
W Per	02 50 37.90	56 59 00.7	63702662	RSG	1900	10	485	1.28E−08
RV Cam	04 30 41.70	57 24 41.8	83801807	O-AGB	350	14	101	2.59E−09
RV Cam	04 30 41.70	57 24 41.8	86202101	O-AGB	350	14	101	2.58E−09
TX Cam	05 00 50.39	56 10 52.6	69501070	O-AGB	390	13	557	4.23E−08
IRC +50137	05 11 19.45	52 52 33.7	86201803	O-AGB	1200	3	635	1.92E−07
α Ori	05 55 10.39	07 24 25.5	69201980	RSG	130	1	335	2.37E−10
V348 Vel	10 26 15.71	−53 53 29.9	25400410	O-AGB	…	…	…	3.76E−09
RT Car	10 44 47.23	−59 24 48.0	25901312	…	…	…	…	8.79E−09
S Vir	13 33 00.05	−07 11 41.3	25302224	O-AGB	328	11	375	2.60E−09
W Hya	13 49 02.07	−28 22 02.8	8902004	O-AGB	114	14	361	3.27E−09
W Hya	13 49 02.07	−28 22 02.8	41800303	O-AGB	114	14	361	2.26E−09
θ Aps	14 05 19.93	−76 47 47.9	7901809	O-AGB	110	14	119	2.55E−09
RX Boo	14 24 11.63	25 42 13.8	8201905	O-AGB	155	14	340	3.72E−09

Name	RA (J2000)	Dec (J2000)	TDT	Class	Distance (pc)	Ref.	Period[a] (d)	$\dot{M}_{dust}$ ($M_\odot$ yr^{-1})
RV Boo	14 39 15.90	32 32 22.3	8202437	O-AGB	393	14	137	3.14E−09
RV Boo	14 39 15.90	32 32 22.3	39401737	O-AGB	393	14	137	2.13E−09
RW Boo	14 41 13.41	31 34 19.9	42800541	O-AGB	293	1	209	1.54E−09
X Her	16 02 39.78	47 14 21.7	8001921	O-AGB	137	1	...	4.42E−09
V Nor	16 10 01.80	−49 14 12.3	45901136	O-AGB	...	...	156	9.31E−10
U Her	16 25 47.70	18 53 33.0	43402028	O-AGB	234	1	406	5.11E−09
α Sco	16 29 24.42	−26 25 54.1	8200369	RSG	185	1	...	3.93E−10
IRAS 16350	16 38 48.10	−48 00 10.0	45901249	...	...	...	...	1.06E−07
IRAS 17004	17 03 55.90	−41 24 02.2	28901123	O-AGB	...	...	...	1.12E−06
IRAS 17010	17 04 28.30	−38 44 23.0	45901669	O-AGB	...	...	...	1.05E−06
AH Sco	17 11 17.02	−32 19 30.9	8403013	RSG	2260	2	714	3.85E−08
V438 Oph	17 14 39.80	11 04 10.0	11601203	O-AGB	416	3	170	1.69E−09
V438 Oph	17 14 39.80	11 04 10.0	81001108	O-AGB	416	3	170	1.55E−09
TY Dra	17 36 59.99	57 44 25.0	46600803	O-AGB	430	14	...	6.20E−09
TY Dra	17 36 59.99	57 44 25.0	74102309	O-AGB	430	14	...	6.19E−09
AFGL 1992	17 39 15.50	−30 14 24.0	28700701	O-AGB	2200	9	...	5.05E−08
AFGL 5379	17 44 22.53	−31 55 43.4	9402123	O-AGB	1190	15	...	6.14E−07
AFGL 5379	17 44 22.53	−31 55 43.4	13601695	O-AGB	1190	15	...	1.57E−06
AFGL 5379	17 44 22.53	−31 55 43.4	32200779	O-AGB	1190	15	...	2.45E−06
AFGL 5379	17 44 22.53	−31 55 43.4	84300128	O-AGB	1190	15	...	2.52E−06
AFGL 2019	17 53 18.80	−26 56 37.0	84900929	O-AGB	...	...	928	1.36E−07
AU Her	17 57 19.50	29 46 32.0	45401501	...	...	...	399	1.22E−08
VX Sgr	18 08 04.00	−22 13 26.8	9900171	RSG	1570	2	732	5.22E−08
OH 21.5+0.5	18 28 30.90	−09 58 16.0	87200833	O-AGB	2500	7	...	2.60E−06
AFGL 2199	18 35 46.80	05 35 47.0	71200120	O-AGB	2480	3	...	1.93E−07
OH 26.5+0.6	18 37 32.49	−05 23 59.3	33000525	O-AGB	1370	16	...	1.43E−06
X Oph	18 38 21.10	08 50 02.3	47201847	O-AGB	270	18	329	2.98E−09
OH 26.2−0.6	18 41 13.80	−06 15 01.0	86901013	O-AGB	1070	17	...	1.87E−07
FI Lyr	18 42 04.80	28 57 29.0	82700735	O-AGB	358	1	146	3.84E−09
AFGL 5535	18 48 41.90	−02 50 28.2	30801670	O-AGB	1770	5	...	1.41E−06

Name	RA (J2000)	Dec (J2000)	TDT	Class	Distance (pc)	Ref.	Period[a] (d)	$\dot{M}_{dust}$ (M$_\odot$ yr^{-1})
OH 32.8−0.3	18 52 22.23	−00 14 10.4	32001560	O-AGB	. . .	. . .	. . .	2.50E−06
EIC 722	18 58 03.90	08 15 28.0	47801654	. . .	. . .	. . .	. . .	1.15E−07
R Aql	19 06 22.19	08 13 47.3	12200329	O-AGB	220	16	284	1.17E−08
R Aql	19 06 22.19	08 13 47.3	32000318	O-AGB	220	16	284	1.14E−08
R Aql	19 06 22.19	08 13 47.3	47801417	O-AGB	220	16	284	1.12E−08
R Aql	19 06 22.19	08 13 47.3	53400105	O-AGB	220	16	284	7.70E−09
R Aql	19 06 22.19	08 13 47.3	67600406	O-AGB	220	16	284	1.17E−08
AFGL 2374	19 21 36.32	09 27 51.5	35001427	O-AGB	1130	15	. . .	1.93E−07
AFGL 2403	19 30 29.50	19 50 42.0	32000603	O-AGB	2300	15	. . .	1.30E−06
AFGL 2403	19 30 29.50	19 50 42.0	50200604	O-AGB	2300	15	. . .	2.14E−06
GY Aql	19 50 07.00	−07 36 54.0	34401040	. . .	. . .	. . .	204	1.12E−08
NR Vul	19 50 11.50	24 55 20.0	53701751	RSG	2300	10	. . .	6.30E−09
RR Aql	19 57 36.00	−01 53 10.4	53400809	O-AGB	403	11	395	1.27E−08
Z Cyg	20 01 27.56	50 02 31.0	37400126	O-AGB	. . .	. . .	264	3.86E−08
Z Cyg	20 01 27.56	50 02 31.0	43402401	O-AGB	. . .	. . .	264	3.52E−08
V1943 Sgr	20 06 55.20	−27 13 29.0	85700514	O-AGB	197	1	. . .	1.54E−09
V584 Aql	20 10 29.70	−01 37 39.9	73200811	O-AGB	390	14	. . .	3.17E−09
X Pav	20 11 45.91	−59 56 13.0	14401801	O-AGB	270	11	199	6.32E−09
BI Cyg	20 21 21.75	36 55 55.4	38101617	RSG	1580	10	. . .	2.33E−08
BC Cyg	20 21 38.49	37 31 58.4	35201201	. . .	. . .	. . .	700	2.32E−08
KY Cyg	20 25 57.30	38 21 10.6	12700917	RSG	1580	10	. . .	1.68E−08
RW Cyg	20 28 50.60	39 58 54.0	12701432	RSG	1320	10	550	1.60E−08
NML Cyg	20 46 25.50	40 06 59.4	5200726	RSG	1740	12	. . .	1.89E−07
NML Cyg	20 46 25.50	40 06 59.4	34201224	RSG	1740	12	. . .	1.89E−07
NML Cyg	20 46 25.50	40 06 59.4	74103105	RSG	1740	12	. . .	1.89E−07
FP Aqr	20 46 36.60	−00 54 11.0	51801556	O-AGB	. . .	. . .	. . .	1.92E−08
RX Vul	20 52 59.80	03 22 16.3	53502929	O-AGB	710	16	457	4.73E−09
μ Cep	21 43 30.40	58 46 48.1	5602852	RSG	870	10	730	8.38E−09
μ Cep	21 43 30.40	58 46 48.1	8001274	RSG	870	10	730	8.85E−09
μ Cep	21 43 30.40	58 46 48.1	39802402	RSG	870	10	730	7.86E−09

Table 3.3 – continued from previous page

Name	RA (J2000)	Dec (J2000)	TDT	Class	Distance (pc)	Ref.	Period[a] (d)	$\dot{M}_{dust}$ ($M_\odot$ yr^{-1})
EP Aqr	21 46 31.89	−02 12 45.9	38600922	O-AGB	135	14	...	4.86E−09
EP Aqr	21 46 31.89	−02 12 45.9	53501243	O-AGB	135	14	...	3.83E−09
SV Peg	22 05 42.10	35 20 53.0	17301206	O-AGB	196	14	145	5.00E−09
SV Peg	22 05 42.10	35 20 53.0	74500605	O-AGB	196	14	145	5.19E−09
OH 104.91	22 19 26.38	59 51 23.0	28300921	O-AGB	2300	15	...	5.46E−07
RW Cep	22 23 06.97	55 57 48.0	57401207	...	...	...	346	4.25E−08
CD Gru	22 26 10.50	−45 14 13.0	53904667	...	...	...	...	2.48E−08
U Lac	22 47 43.39	55 09 31.0	41400406	RSG	3470	6	...	1.19E−08
BU And	23 23 39.90	39 43 38.4	38201201	O-AGB	...	...	382	4.42E−09
V582 Cas	23 30 27.33	57 58 34.5	38501620	O-AGB	...	...	300	1.34E−08
V582 Cas	23 30 27.33	57 58 34.5	42300804	O-AGB	...	...	300	1.84E−08
PZ Cas	23 44 03.30	61 47 22.3	9502846	RSG	2400	10	925	4.93E−08
PZ Cas	23 44 03.30	61 47 22.3	42604702	RSG	2400	10	925	4.90E−08
Z Cas	23 44 31.49	56 34 52.6	10101714	O-AGB	...	...	496	6.14E−09
R Cas	23 58 24.77	51 23 18.7	24800223	O-AGB	190	16	430	8.56E−09
R Cas	23 58 24.77	51 23 18.7	26301524	O-AGB	190	16	430	1.11E−08
R Cas	23 58 24.77	51 23 18.7	38300825	O-AGB	190	16	430	8.56E−09
R Cas	23 58 24.77	51 23 18.7	38302016	O-AGB	190	16	430	8.77E−09
R Cas	23 58 24.77	51 23 18.7	39501330	O-AGB	190	16	430	8.79E−09
R Cas	23 58 24.77	51 23 18.7	42100215	O-AGB	190	16	430	8.56E−09
R Cas	23 58 24.77	51 23 18.7	44301926	O-AGB	190	16	430	9.44E−09
R Cas	23 58 24.77	51 23 18.7	62702122	O-AGB	190	16	430	8.28E−09

(a) Periods are taken from the GCVS (Kholopov et al. 1998; Samus et al. 2004)

R   : (1) van Leeuwen (2007); (2) Chen & Shen (2008); (3) De Beck et al. (2010);

(4) Decin et al. (2007); (5) Herman et al. (1986); (6) Humphreys (1978); (7) Justtanont et al. (2006);

(8) Knapp & Bowers (1988); (9) Le Sidaner & Le Bertre (1996); (10) Levesque et al. (2005);

(11) Loup et al. (1993); (12) Massey & Thompson (1991); (13) Olivier et al. (2001);

(14) Olofsson et al. (2002); (15) van Langevelde et al. (1990); (16) Whitelock et al. (2008);

(17) Xiong et al. (1994); (18) Young (1995).

Spitzer P1094 Galactic sample

Spitzer low-resolution spectra of 21 faint Galactic O-AGB stars were observed as part of Program 1094. Spectral data reduction was done in (Higdon et al. 2004) in a manner similar to that summarised by Furlan et al. (2006) and Sargent et al. (2009). Many of these sources are not well known in the literature and ancillary data including photometry, periods, variability type and distance indicators were difficult to find in the literature. As before we classify these sources using the decision tree, however, these classifications may be less robust than the other samples due to uncertainty in the SED shape. This means our sample may suffer some contamination by oxygen-rich post-AGB sources. The Galactic *Spitzer* sources are listed in Table 3.4.

3.2.4 Globular cluster sample

To complement these sources, *Spitzer* IRS observations of oxygen-rich sources in 14 Galactic globular clusters (GGC) allow the metallicity range we investigate to be extended to lower metallicities. The globular cluster sample consists of 39 O-AGB stars (observed in the Short- and Long-Low) which are discussed by Sloan et al. (2010) and McDonald et al. (2011b). Both these studies compute bolometric luminosities, periods and dust mass-loss rates for each object allowing a ready comparison to the Magellanic Cloud stars, however, it should be noted that the mass-loss rates are obtained via an alternative method to that discussed in Section 3.3.1. For consistency we recalculate the mass-loss rates using the models to obtain a uniform treatment of the mass-loss rates and directly compare the globular cluster sources to the other samples. Table 3.5 lists the sources considered in this work.

Table 3.4: Details of the sources in the Galactic *Spitzer* IRS sample. For each source the name, coordinates, Astronomical Observation Request (AOR), classification, period and dust mass-loss rate ($\dot{M}_{dust}$) is given.

Name	RA	Dec	AOR	Class[a]	Period[b]	$\dot{M}_{dust}$
	(J2000)	(J2000)			(d)	($M_\odot$ yr^{-1})
IRAS 00534+6031	00 56 28.41	60 47 09.25	6082816	O-AGB	410.0	5.44E−09
IRAS 00589+5743	01 01 58.43	57 59 47.86	6083072	. . .	188.0	5.07E−08
IRAS 03434+5818	03 47 31.26	58 28 10.41	6082304	. . .	. . .	1.14E−07
IRAS 05314+2020	05 34 26.48	20 22 53.78	6083584	. . .	240.0	2.99E−09
IRAS 08425−5116	08 44 04.77	−51 27 43.74	6078976	O-AGB	. . .	4.65E−07
IRAS 13581−5444	14 01 28.90	−54 59 00.08	6081536	O-AGB	. . .	3.05E−07
IRAS 16523+0745	16 54 46.42	07 40 27.07	6083328	. . .	274.0	5.71E−09
IRAS 17030−3053	17 06 14.07	−30 57 38.83	6084864	O-AGB	. . .	6.58E−07
IRAS 17276−2846	17 30 48.30	−28 49 02.39	6080768	. . .	. . .	7.06E−07
IRAS 17304−1933	17 33 22.13	−19 35 51.75	6084352	O-AGB	. . .	1.16E−07
IRAS 17338−2140	17 36 52.23	−21 42 41.08	6085632	O-AGB	. . .	1.89E−07
IRAS 17347−2319	17 37 46.29	−23 20 53.48	6080000	O-AGB	. . .	4.48E−07
IRAS 17413−3531	17 44 43.45	−35 32 35.28	6081280	. . .	. . .	1.91E−07
IRAS 17513−3554	17 54 42.02	−35 54 51.38	6080256	O-AGB	. . .	3.68E−07
IRAS 18195−2804	18 22 40.17	−28 03 07.61	6079744	O-AGB	. . .	4.16E−07
IRAS 18231+0855	18 25 33.36	08 56 46.62	6082560	. . .	. . .	1.76E−08
IRAS 18279−2707	18 31 03.68	−27 05 40.93	6085376	O-AGB	. . .	2.97E−08
IRAS 18291−2900	18 32 19.55	−28 58 09.81	6084096	. . .	. . .	4.17E−08
IRAS 19256+0254	19 28 08.39	03 00 25.32	6081792	O-AGB	. . .	1.14E−07
IRAS 19456+1927	19 47 49.65	19 35 22.67	6081024	O-AGB	. . .	1.92E−07
GX Tel	20 11 48.22	−55 25 26.65	6082048	O-AGB	340.8	1.63E−08

(a) The available data were insufficient for determining whether some sources were an O-AGB or RSG; these sources are not assigned a classification.

(b) Periods are taken from the GCVS (Kholopov et al. 1998; Samus et al. 2004).

Table 3.5: Details of the sources in the globular cluster sample. Distances, [Fe/H] values, periods and bolometric magnitudes for NGC 5139 (ω Cen) were taken from McDonald et al. (2011b); values for these parameters for all other clusters are from Sloan et al. (2010).

Cluster	Star name	RA (J2000)	Dec (J2000)	AOR	Distance (kpc)	[Fe/H]	Period (d)	M_{bol}	$\dot{M}_{dust}$ (M$_\odot$ yr^{-1})
NGC 362	V16	01 03 15.10	−70 50 32.3	21740800	9.25	−1.20	138	−4.10	1.84E−09
NGC 362	V2	01 03 21.85	−70 54 20.1	21740800	9.25	−1.20	89	−3.50	5.80E−10
NGC 5139	61015	13 25 21.33	−47 36 53.9	27854592	5.30	−1.71	…	−3.29	7.92E−11
NGC 5139	42044	13 26 05.35	−47 28 20.6	27854848	5.30	−1.37	0.3	−3.01	1.30E−10
NGC 5139	33062	13 26 30.19	−47 24 27.8	27856128	5.30	−1.08	110	−3.61	4.36E−09
NGC 5139	44262	13 26 46.36	−47 29 30.4	27852800	5.30	−0.80	149.4	−3.27	6.25E−10
NGC 5139	44262	13 26 46.36	−47 29 30.4	21741056	5.30	−1.63	149	−3.88	1.30E−09
NGC 5139	44277	13 26 47.72	−47 29 29.0	27855104	5.30	−1.37	124	−3.19	2.40E−10
NGC 5139	56087	13 26 48.05	−47 34 56.8	27853824	5.30	−1.84	…	−3.08	1.38E−10
NGC 5139	43351	13 26 55.02	−47 28 45.9	27854336	5.30	−0.98	…	−2.79	7.39E−11
NGC 5139	55114	13 26 55.55	−47 34 23.4	27854080	5.30	−1.45	…	−3.16	1.59E−10
NGC 5139	41455	13 27 15.82	−47 27 54.6	27855360	5.30	−1.22	90	−3.05	1.64E−10
NGC 5139	35250	13 27 37.73	−47 25 17.5	27855872	5.30	−1.06	65	−3.05	4.28E−10
NGC 5927	V3	15 28 00.13	−50 40 24.6	21741824	7.76	−0.35	297	−4.64	1.10E−08
NGC 5927	V1	15 28 15.17	−50 38 09.3	21741568	7.76	−0.35	202	−4.13	6.21E−09
NGC 6356	V5	17 23 17.06	−17 46 24.5	21743104	15.35	−0.50	220	−4.61	1.47E−09
NGC 6356	V3	17 23 33.30	−17 48 07.4	21743104	15.35	−0.50	223	−4.06	1.19E−09
NGC 6356	V1	17 23 33.72	−17 49 14.8	21743104	15.35	−0.50	227	−4.54	1.33E−08
NGC 6356	V4	17 23 48.00	−17 48 04.5	21743104	15.35	−0.50	211	−4.42	9.85E−10
NGC 6352	V5	17 25 37.52	−48 22 10.0	21742848	5.89	−0.69	177	−4.27	3.20E−09
NGC 6388	V4	17 35 58.94	−44 43 39.8	21743360	12.42	−0.57	253	−4.68	6.21E−09
NGC 6388	V3	17 36 15.04	−44 43 32.5	21743360	12.42	−0.57	156	−3.83	3.55E−10
Terzan 5	V7	17 47 54.33	−24 49 54.6	21744128	6.64	−0.08	377	−4.98	1.88E−08
Terzan 5	V2	17 47 59.46	−24 47 17.6	21743872	6.64	−0.08	217	−4.41	4.87E−09
Terzan 5	V5	17 48 03.40	−24 46 42.0	21744128	6.64	−0.08	464	−5.09	2.27E−08
Terzan 5	V8	17 48 07.18	−24 46 26.6	21744128	6.64	−0.08	261	−5.04	2.68E−09

Table 3.5 – continued from previous page

Cluster	Star name	RA (J2000)	Dec (J2000)	AOR	Distance (kpc)	[Fe/H]	Period (d)	M_{bol}	$\dot{M}_{dust}$ ($M_\odot$ yr^{-1})
Terzan 5	V6	17 48 09.25	−24 47 06.3	21744128	6.64	−0.08	269	−4.72	2.31E−08
NGC 6441	V2	17 50 16.16	−37 02 40.5	21744384	13.00	−0.56	145	−3.98	1.31E−09
NGC 6441	V1	17 50 17.09	−37 03 49.7	21744384	13.00	−0.56	200	−4.26	1.38E−09
IC 1276	V3	18 10 50.79	−07 13 49.1	21742080	5.40	−0.69	300	−4.72	1.24E−08
IC 1276	V1	18 10 51.55	−07 10 54.5	21742080	5.40	−0.69	222	−4.60	1.57E−09
NGC 6637	V4	18 31 21.88	−32 22 27.7	21745664	8.95	−0.66	200	−4.44	1.04E−08
NGC 6637	V5	18 31 23.44	−32 20 49.5	21745664	8.95	−0.66	198	−4.44	2.22E−09
NGC 6712	V7	18 52 55.38	−08 42 32.5	21745920	7.05	−0.97	193	−4.34	2.01E−09
NGC 6712	V2	18 53 08.78	−08 41 56.6	21745920	7.05	−0.97	109	−3.91	2.59E−09
NGC 6760	V3	19 11 14.31	01 01 46.6	21746176	8.28	−0.48	251	−4.71	6.50E−09
NGC 6760	V4	19 11 15.03	01 02 36.8	21746432	8.28	−0.48	226	−4.34	6.40E−09
Palomar 10	V2	19 17 51.48	18 34 12.7	21746944	5.92	−0.10	393	−4.96	8.85E−09
NGC 6838	V1	19 53 56.10	18 47 16.8	21746944	3.96	−0.73	179	−4.00	2.32E−09

3.3 Analysis

3.3.1 Determining the gas and dust mass-loss rates

We derive individual dust mass-loss rates ($\dot{M}_{dust}$) of O-AGB and RSG stars by fitting their infrared SEDs with the oxygen-rich subset of the 'Grid of Red supergiants and Asymptotic giant branch ModelS' (; Sargent et al. 2011). This approach avoids the onerous task of determining these quantities by individually modelling via radiative transfer (RT) the nuances of the IRS and SWS spectra. The coverage of the oxygen-rich   models has been compared to the observed colours and magnitudes of the SAGE-Spec sample and was found to be in good agreement (see figs. 2–7 from Sargent et al. 2011). Gas mass-loss rates can be obtained by scaling the dust mass-loss rates using an assumed gas-to-dust-ratio (Ψ) based on the metallicity. Table 3.6 lists the

Table 3.6: Summary of adopted gas-to-dust-ratios.

Environment	Gas-to-dust ratio (Ψ)
MW	100
LMC	200
SMC	500
NGC 362	1500
NGC 5139	4000
NGC 5927	200
NGC 6356	300
NGC 6352	500
NGC 6388	400
Terzan 5	100
NGC 6441	400
IC 1276	500
NGC 6637	500
NGC 6712	900
NGC 6760	300
Palomar 10	100
NGC 6838	500

values of Ψ adopted in our calculations. We assume that the field stars in the Milky Way come from a single solar metallicity population with $\Psi_\odot = 100$ (Knapp et al. 1993). For the globular clusters, the gas-to-dust-ratio was determined from the metallicity listed in Table 3.5 using the following relation: $\Psi = 100 \times 10^{-[\mathrm{Fe/H}]}$. However, it should be noted that the gas-to-dust-ratio metallicity dependence is only weakly constrained and thus the adopted gas-to-dust ratios are highly uncertain.

The optical/infrared broad-band photometry for all sources in the Magellanic Clouds, were combined with 'synthetic' *IRAS* 12-μm fluxes obtained by convolving the spectrum with the 12-μm *IRAS* band profile[2]. In instances where there was more than one

---

[2]The *IRAS* filter bandpasses and zero points can be found in Neugebauer et al. (1984).

epoch of data for a band, the photometry was averaged to minimise variability effects (due to pulsations) in the fitting. Additionally, if a source was missing photometric data at [5.8], [8.0], [12] or [24], the IRS spectrum was convolved with the appropriate broadband photometric filter and included in the SED, to better constrain the fit parameters and prevent the fit being limited by a lack of data points in a given region.

The SEDs for the Milky Way sources were constructed using 2MASS *JHK_s* photometry combined with *IRAS* 12, 60 and 100 μm data from the Point Source Catalogue (Beichman et al. 1988), and the Faint Source Catalogue (Moshir, M. 1989). To obtain a uniform data set we supplemented the SED with convolved photometry from the *ISO* spectra in the IRAC and MIPS 24 μm bands to obtain synthetic fluxes. These were calculated using the IDL routine _____, which is available from the Spitzer Science Centre. Synthetic photometry was also derived for desired photometric bands from the O-rich models according to the convolution method outlined above.[3]

Variable AGB stars can show large absolute magnitude amplitudes in the optical, typically in the range of $\Delta M_V \lesssim 11$ mag (Samus et al. 2004). Infrared amplitudes are less than this with *K*-band amplitudes usually $\Delta M_K \lesssim 2.3$ mag and IRAC 3.6 μm $\Delta M_{3.6} \lesssim 2.0$ mag (McQuinn et al. 2007; Vijh et al. 2009). Due to the large variability in optical *UBVI* data we chose to exclude these points from the SED fitting.

Long-period Mira variables can also show significant variation in the mid-IR due to pulsations: multi-epoch *ISO*-SWS spectral studies of the variable stars T Cep, R Aql and R Cas covering minimum to post-maximum pulsation phases over a single pulsation cycle allow us to characterise the variations in amplitude at longer wavelengths ($\lambda > 8.0\,\mu$m). Synthetic photometry was obtained from the spectra at each epoch for the *IRAS* [12] and MIPS [24] bands, and the difference in magnitude between photometric maximum and minimum was used as a measure of the amplitude. We found that $\Delta M_{12} \lesssim 0.4$ mag and $\Delta M_{24} \lesssim 0.6$. For all sources the photometric uncertainties in these bands were modified to account for this change in magnitude during a pulsation cycle. At near-IR wavelengths we also account for changes in magnitude due to pulsa-

---

[3]In the case of 2MASS relative spectral response curves are provided by Cohen et al. (2003).

tions by adjusting the photometric uncertainties to reflect the differences in magnitude across a pulsation cycle.

We do not correct the SEDs for interstellar reddening. Due to the close proximity ($d \lesssim 4$ kpc) of the Galactic sources and the low column densities along each line-of-sight to the Magellanic Clouds the dereddening correction in the infrared is negligible compared to the uncertainty in the photometric measurements if variability is considered.

A χ^2–minimisation analysis was used to fit the convolved model fluxes to the observed SEDs. As the grid is calculated for sources at 50 kpc, we scale the convolved model fluxes to match those of the star before commencing the χ^2 fitting. The scaling factor was calculated such that it minimised the difference between the source and the model, this allows the distance d to be a free parameter (within set reasonable boundaries; see Table 3.7).

The reduced χ^2, weighted by photometric uncertainties is given by:

$$\chi^2 = \frac{1}{N} \sum_{i=1}^{N} \left(\frac{(\log_{10}[\lambda F_\lambda(i)] - \log_{10}[\lambda M_\lambda(i)])^2}{\sigma(\log_{10}[\lambda F_\lambda(i)])^2} \right), \tag{3.1}$$

where λF_λ is the observed broadband photometry with errors,

$$\sigma(\log_{10}[\lambda F_\lambda]) = \frac{1}{\ln(10)} \frac{\sigma(\lambda F_\lambda)}{\lambda F_\lambda}, \tag{3.2}$$

and λM_λ is the scaled model fluxes for N measurements. This fitting process is repeated for each model SED with a scaling factor and χ^2 value returned for each model. Determining accurate dust mass-loss rates is vital in order to investigate the onset of crystallinity. By fitting in the $\log_{10}[\lambda F_\lambda]$ plane we effectively give more weight to the longer wavelength bands where the dust grains emit most of their flux and obtain a better fit to the shape of the SED. This method relies upon the source being well sampled across a range of photometric bands, however there are some sources where there is no 2MASS *JHKs*, IRAS [60] or MIPS [70], so the overall fit is not as well constrained.

For the LMC and SMC we assume the star lies at a distance d between $d_{\min}$ and $d_{\max}$ to account for variations in distance across each galaxy due to its inclined geome-
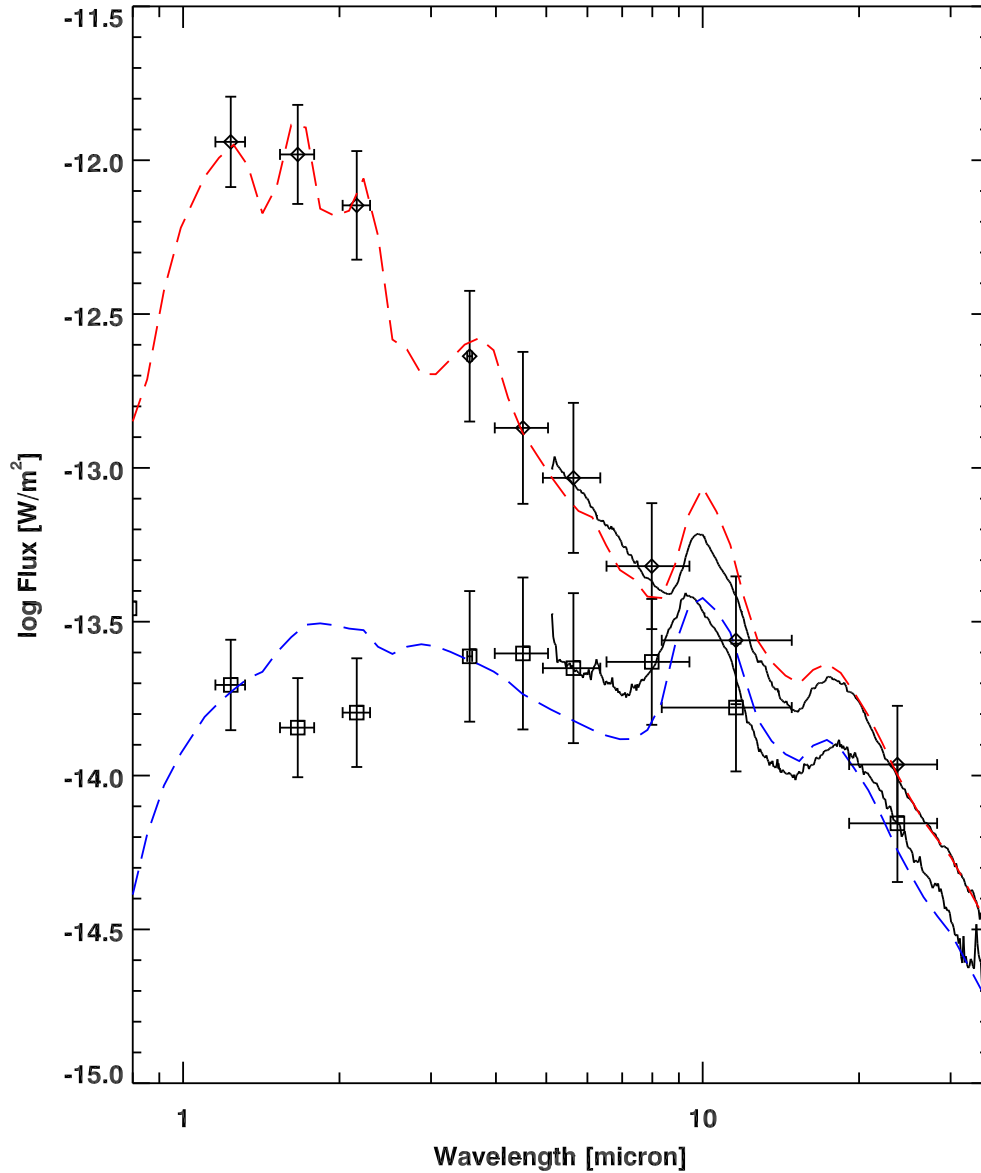
Figure 3.1: Best-fitting models to the broadband photometry for a RSG (MSX SMC 234; dashed red) and an O-AGB star (MSX SMC 149; dashed blue) in the SMC. The solid line is the observed spectra for each star. Similarly the square and diamond points are the respective observed photometry for the O-AGB and RSG sources. The photometric errors have been estimated based on the variability.

Table 3.7: The scale factor range.

Galaxy	Distance (kpc)	Scale factor
LMC	51 ± 3	$0.86 - 1.09$
SMC	61 ± 3	$0.61 - 0.74$
Milky Way	< 4	> 156

try (van der Marel & Cioni 2001) which corresponds to a range of allowed luminosity scale factors for each population. For the globular clusters the allowed range in the scale factor for each source was determined, using the distances and associated error listed in Table 3.5. Where possible the scale factor used for Galactic sources corresponds to its *Hipparcos* distance if the relative errors are less than 20 per cent, otherwise we adopt a distance range of $d < 4$ kpc. Table 3.7 lists the distance range and scaling factor allowed for each galaxy. As the luminosity is a fitting parameter to the distance, we attribute no significance to its best-fit values.

To prevent any over-interpretation of the best fit parameters, we consider all sets of model parameters that produce a good fit to the source, with $\chi^2 - \chi^2_{\text{best}} < 3$, where χ^2_{best} is the reduced χ^2 value of the best-fitting model for each source, following the method employed by Robitaille et al. (2007). For each parameter we find the average value and its standard deviation from the range of acceptable fits. Fig. 3.1 shows an example best-fitting model to the SEDs of an O-AGB and a RSG in the SMC. The error bars are an indication of the expected change in flux due to variability. The IRS spectrum for each source is plotted to illustrate that a good fit has been achieved. These are not included in the fitting as the mineralogy is a fixed parameter in the   model grid.

The dust mass-loss rates determined through the spectral fitting of the SEDs with the   model grid are listed in Tables 3.1–3.5. In principal, the fitting routine also provides uncertainties for the individual dust mass-loss rates, of order 10 to 55 per cent, however, in absolute terms, the errors are much greater than this due to the inherent uncertainties and assumptions in the model.

In order to assess the accuracy of the absolute values derived in the   fitting, we compare our derived dust mass-loss rates to those determined by Groenewegen et al. (2009) and McDonald et al. (2011b) for common sources between the data sets. The   dust mass-loss rates are systematically greater by a factor of 3–8. This is predominantly due to a difference in the choice of optical constants and grain shape. The   grid uses the astronomical silicates of Ossenkopf et al. (1992), while both Groenewegen et al. (2009) and McDonald et al. (2011b) use a combination of silicates, metallic iron and aluminium oxide. Different physical parameters used in modelling the dust envelope and central star also contribute to this discrepancy. For more details on how the   models compare to other modelling efforts we refer the reader to Sargent et al. (2011).

Our analysis regarding the onset of crystallinity is very sensitive to the uncertainties in the dust and gas mass-loss rates, thus it is important to account for the possible sources of error and caveats used in the modelling to prevent misinterpretation. The   models assume that all outflows have the same constant velocity of 10 kms^{-1}, whereas in reality they may have expansion velocities between ~5 and ~25 kms^{-1}, even within the same galaxy. However, by assuming a constant velocity the dust and gas mass-loss rates obtained in the fitting can be used as a proxy for the gas and dust column densities. As we have been consistent in our treatment of the samples and in the determination of the dust mass-loss rates, the relative uncertainty between the sources is small compared to the absolute uncertainties, allowing comparisons to be drawn across the sample. The derived gas mass-loss rates have an additional uncertainty because of the adopted scaling relation between dust and gas in circumstellar environments. For oxygen-rich evolved stars, this relation depend strongly on metallicity, however, it is not well constrained. As such, the absolute values for the gas mass-loss rate should be treated with a degree of caution, nevertheless, we expect the assumed gas-to-dust ratios to provide a reasonable first order approximation of the relative gas mass-loss rates.

Table 3.8: Wavelength intervals for extracting crystalline silicate emission features.

Feature (μm)	Continuum interval (μm)
23.6	22.3 - 24.6
28.1	26.0 - 31.1
33.6	31.5 - 35.0

3.3.2 Measuring the crystalline silicate features

Narrow spectral features due to crystalline silicates tend to cluster in well-defined complexes, found near 10, 18, 23, 28, 33, 40 and 60 μm (Molster et al. 2002b). We do not extract information for the features near 10 and 18 μm as it is impossible to cleanly separate them from the broader, underlying amorphous silicate features.

In order to determine the properties of crystalline silicate emission features across a range of metallicities, we have defined a continuum representing a featureless thermal dust component, which we used as a baseline to obtain an enhanced view of the spectral features beyond 20 μm. To produce a smooth continuum, a 5-pixel boxcar smoothing algorithm was applied to the IRS spectra to reduce the noise fluctuations between each data point (while preserving the resolution). However, it is possible that this results in any low-contrast, broad dust features being treated as continuum. The continuum was determined by applying a cubic spline fit in F_ν-space for $\lambda > 19.5\,\mu$m. Spline points were fitted to the spectra at 19.8, 21.3, 25.5, 31.3, 35.6 μm where the continuum is well defined and no strong spectral features are present. Examples of the spline fitting procedure can be seen in Fig. 3.2, while Fig. 3.3 presents the resulting continuum-divided spectra. In instances where a 'noise spike' is present in a spectrum at a standard spline point (for example SSID130), the spline point was moved to the closest alternative wavelength where no feature could be visually identified. A similar procedure was applied to the *ISO* SWS spectra after regridding to the *Spitzer* IRS resolution.

We prefer the above method compared to the alternate approach used by some
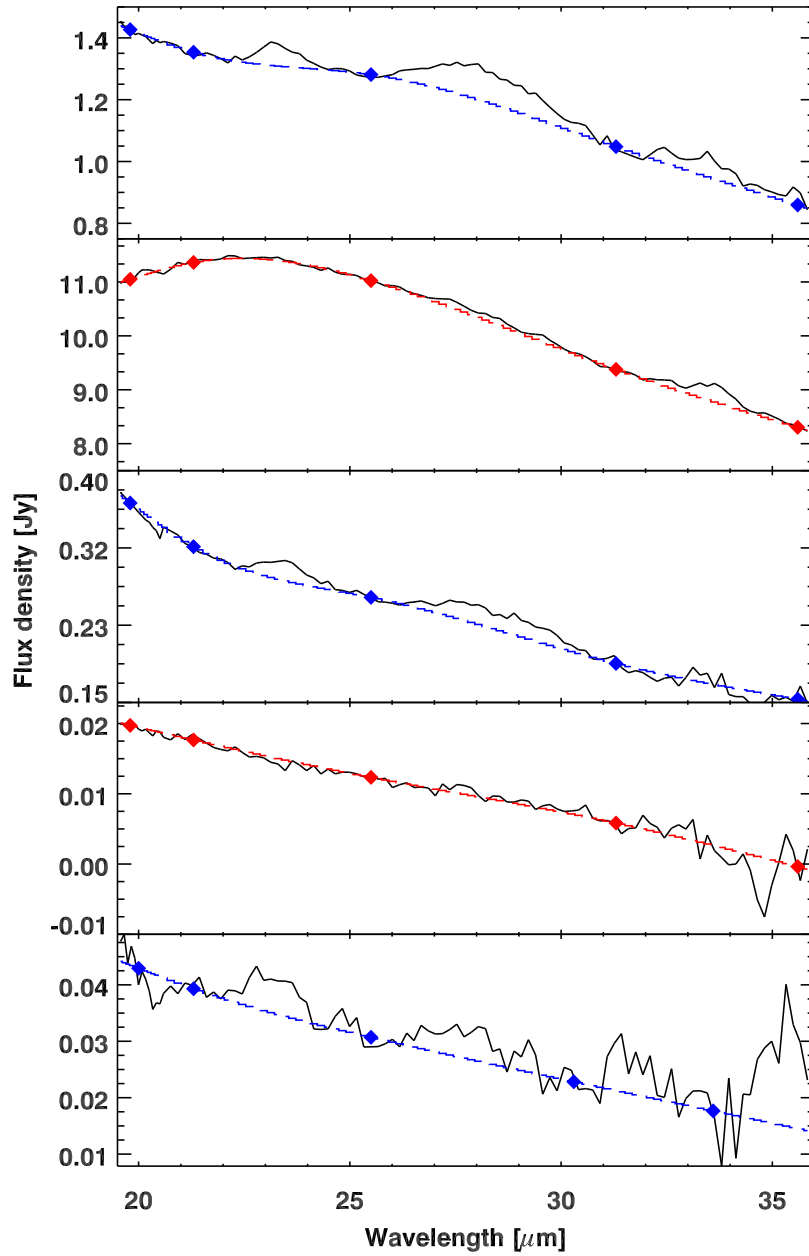
Figure 3.2: Example of the spline fitting for an LMC O-AGB (top), LMC RSG (2nd panel), SMC O-AGB (3rd panel), SMC RSG (4th panel). The spline (dashed line) is fitted to the spectra at the marked wavelengths. The top three spectra show crystalline emission features, while the spectrum in the 4th panel does not. The bottom panel shows SSTISAGEMC J053128.44−701027.1 (SSID 130), where alternative spline points were selected in order to produce a smooth continuum.
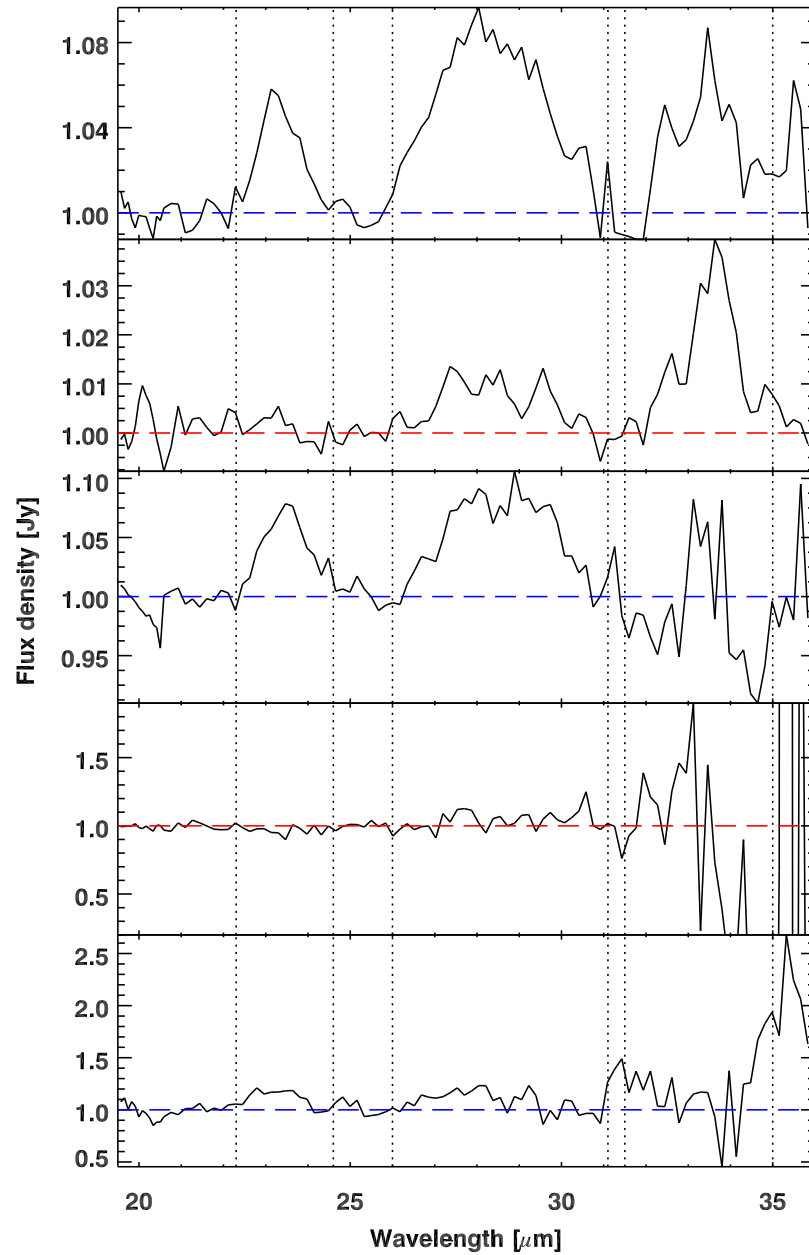
Figure 3.3: Continuum-divided spectra from the sources shown in Fig. 3.2. The dotted vertical lines mark the regions within which the complex strength was measured.

authors (e.g. de Vries et al. 2010; Gielen et al. 2011), in which a local continuum is defined for each feature via linear interpolation between flux densities in a given wavelength range on either side of the feature. As slight variations in the position of the feature and noise in the spectra all have strong effects on the determination of the continuum because the fitting region is small. Also the dust continuum is inherently non-linear, with changes in curvature, producing a non-systematic offset between sources.

We determine equivalent widths of the 23-, 28- and 33-μm features in each spectrum to provide a quantitative measure of their strengths. These are calculated with respect to the underlying continuum as determined by the aforementioned spline fitting process. The equivalent widths (W_{eq}) can then be determined by:

$$W_{eq} = \sum_{\lambda} \left(1 - \frac{F_{obs}}{F_{cont}} \right) d\lambda, \tag{3.3}$$

where F_{obs} and F_{cont} are the observed flux and the flux of the spline-fitted continuum. The wavelengths used to define the blue and red sides of each feature are given in Table 3.8. An example of the feature extraction process is given in Fig. 3.3.

If a feature is particularly weak compared to the continuum, its strength may be influenced by how the continuum is fitted. To quantify this effect, we also determined equivalent widths using linear interpolation to approximate the continuum under the features. For spectra with high contrast features or with a good S/N ratio the difference in strength is of the order of $\lesssim$ 15 per cent, however, there is a large disparity (up to ~65 per cent) in strengths for low contrast features.

Both the spline and linear interpolation methods will underestimate the total contribution from the crystalline silicate components to the total flux. These methods fit the continuum under each crystalline silicate emission feature, however, the crystalline silicates grains will also contribute some flux to the underlying continuum, which is composed of contributions from all dust species of varying mineralogy, lattice structure, temperature and size and shape distributions.

3.4 Results

3.4.1 Mass-loss rates within populations

We have separated the O-AGB and RSGs stars in each galaxy in order to examine the influence of the mass-loss process on the dust production in these two classes of object separately. Furthermore, we distinguish between sources in which crystalline silicates are visually apparent and those whose silicates appear to be solely amorphous. For each population we determine the mean $\log \dot{M}_{\rm dust}$ and $\log \dot{M}$. In general, the dust mass-loss rate for the sources with only amorphous silicates increases as the metallicity of the sample increases. Thus, the SMC and globular cluster sources have low dust mass-loss rates while the Galactic field sources have the largest dust mass-loss rates. The individual objects within a galaxy encompass a range of mass-loss rates as indicated in Fig. 3.4. An overview of $\langle \log \dot{M}_{\rm dust} \rangle$ and $\langle \log \dot{M} \rangle$ for each population is presented in Table 3.9.

In each instance the mean dust and gas mass-loss rates are higher for the sources which exhibit crystalline silicate features compared to those that do not. Also, while a low mass-loss rate is no guarantee that the silicates will be entirely amorphous, it is evident that high mass-loss rate sources have a greater disposition to exhibit crystalline silicate features. The mean dust mass-loss rates for the sources with crystalline silicates do not show the same metallicity dependence as the sources with only amorphous silicates. As these objects have different gas densities but similar dust column densities this may indicate that crystallinity depends on the dust density in the wind. The mass of the central star may also be significant: a greater fraction of O-AGB stars (56 per cent) display crystalline bands compared to the RSGs (24 per cent) and, as the metallicity decreases, the proportion of RSGs with crystalline features also drops. This may be due to differences in the silicate dust composition of RSG and O-AGB stars, with the former exhibiting amorphous Ca-Al-rich silicates before forming Mg-rich silicates (Speck et al. 2000; Verhoelst et al. 2009).

Table 3.9: Summary of mean mass-loss rates.

Population		Sources with only amorphous silicates			Sources with crystalline silicates		
		$\langle \log \dot{M}_{\mathrm{dust}} \rangle$	$\langle \log \dot{M} \rangle$	N	$\langle \log \dot{M}_{\mathrm{dust}} \rangle$	$\langle \log \dot{M} \rangle$	N
MW	O-AGB	−8.07	−6.07	59	−6.87	−4.87	50
MW	RSG	−7.95	−5.95	15	−7.41	−5.41	7
LMC	O-AGB	−8.19	−5.89	36	−7.20	−4.90	18
LMC	RSG	−8.21	−5.91	49	−7.53	−5.23	11
SMC	O-AGB	−9.18	−6.49	10	−7.42	−4.72	5
SMC	RSG	−8.83	−6.13	15	−7.49	−4.78	1
Terzan 5	O-AGB	−8.06	−5.98	4	−7.64	−5.56	1
Palomar 10	O-AGB	−8.05	−5.95	1	. . .	. . .	0
NGC 5927	O-AGB	−7.96	−5.61	1	−8.21	−5.86	1
NGC 6760	O-AGB	−8.19	−5.71	2	. . .	. . .	0
NGC 6356	O-AGB	−8.66	−6.16	4	. . .	. . .	0
NGC 6441	O-AGB	−8.87	−6.31	2	. . .	. . .	0
NGC 6388	O-AGB	−8.83	−6.26	2	. . .	. . .	0
NGC 6637	O-AGB	−8.32	−5.66	2	. . .	. . .	0
NGC 6352	O-AGB	. . .	. . .	0	−8.49	−5.80	1
IC 1276	O-AGB	−8.36	−5.67	2	. . .	. . .	0
NGC 6838	O-AGB	−8.63	−5.90	1	. . .	. . .	0
NGC 6712	O-AGB	−8.64	−5.67	2	. . .	. . .	0
NGC 362	O-AGB	−8.99	−5.79	2	. . .	. . .	0
NGC 5139	O-AGB	−9.66	−6.03	10	−8.36	−4.73	1

(a) $\dot{M}_{\mathrm{dust}}$ distribution
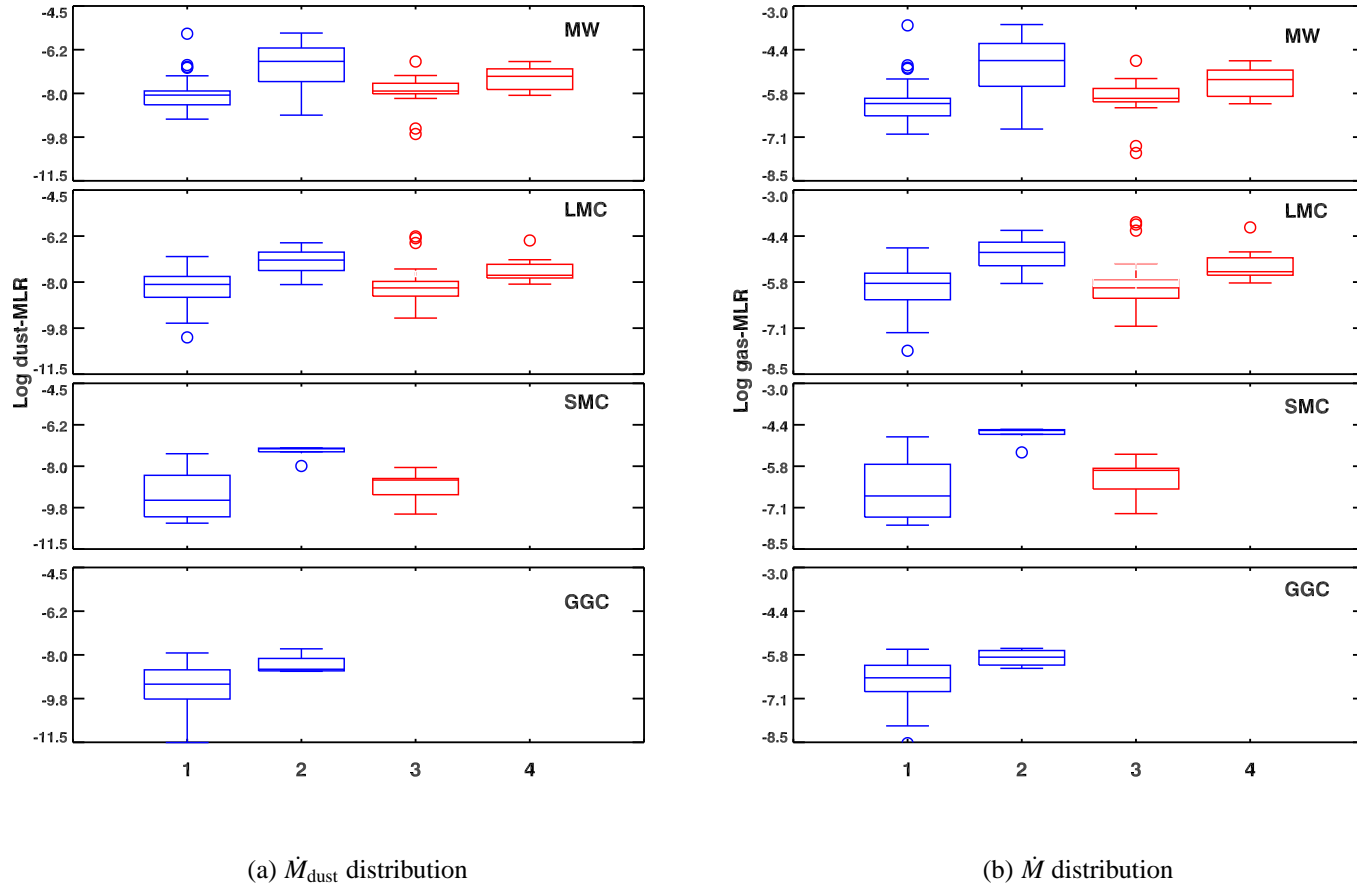
(b) $\dot{M}$ distribution

Figure 3.4: Overview of the dust and gas mass-loss rate distributions for each population. Column 1: O-AGBs with solely amorphous silicates, column 2: O-AGBs with crystalline silicates, column 3: RSGs with only amorphous silicates, column 4: RSGs with crystalline silicates. The box encloses the inter-quartile range, the whiskers extend out to 1.5 times the lower or upper quartile or to the maximum or minimum value of the data (if smaller). Outliers are indicated by circles.
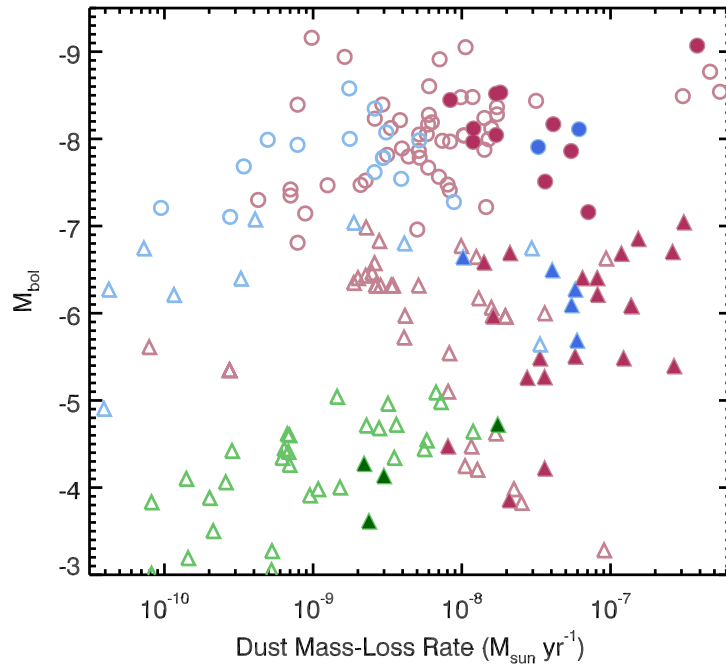
Figure 3.5: Bolometric luminosity versus dust mass-loss rate for the LMC (red colours), SMC (blue) and globular cluster (green) sources. O-AGB stars are plotted as triangles and RSG as circles. Objects with crystalline silicates are plotted with closed symbols. Milky Way sources are not included because of distance uncertainties.

Fig. 3.5 shows the bolometric magnitude as a function of dust mass-loss-rate. We detect crystalline silicates across the full AGB and RSG luminosity range, from the early AGB to the most luminous RSGs. This indicates that we are sensitive to crystalline features down to a low luminosity limit, not just in the brightest sources where there is better contrast between the feature and the noise. For the Magellanic Clouds our sample is biased towards the brightest AGBs and RSGs or dusty sources with high mass-loss rates. Here the threshold density for the onset of crystallinity is greater than that of the Galactic field stars and globular cluster sources. As such, the detection of crystalline features in the Magellanic Clouds may be limited by the signal-to-noise ratio.

3.4.2   Mass-loss rates and crystalline feature strength

The strengths of the 23-, 28- and 33-μm features are shown against the dust mass-loss rate (Fig. 3.6) and total mass-loss rate (Fig. 3.7). In both instances, objects with crystalline silicate features are represented by filled symbols, while open ones represent sources where crystalline silicates are not visually apparent. It is interesting to compare and contrast the behaviour of the crystalline features at the different wavelengths, in particular the 23- and 33-μm features, which have the same principal carrier, forsterite. At 33 μm, features due to the crystalline silicate grains only become apparent at the highest mass-loss rates, where the majority of the sources display some crystallinity. This is usually interpreted as evidence that there is a threshold value in the mass-loss rate at which crystalline silicates can form (Cami et al. 1998; Sylvester et al. 1999). We observe, however, that the forsterite feature at 23 μm paints a different picture. Here, the transition between sources that exhibit a feature and those that do not is blurred, indeed at the highest mass-loss rates ($\dot{M} > 10^{-4}\,\mathrm{M}_\odot\,\mathrm{yr}^{-1}$) the detection rate of the 23-μm feature drops: this may be a consequence of the forsterite grain temperature or it may indicate that the 23-μm band is going into absorption due to high column density. An example of the changing relative strengths of the two forsterite features as the optical depth of the shell increases is plotted for three MW stars in Fig. 3.8. Like the 23-μm forsterite feature, the 28-μm enstatite feature spans a wider mass-loss rate range than the 33-μm feature. However, in all three cases no evidence for crystallinity is seen in the lowest mass-loss rate sources.

The sources where no feature is visually apparent are well described by a Gaussian distribution around a strength/continuum ratio of zero. This implies that the spread is due to stochastic noise in the spectra and that we can trust systematics in the crystalline silicate detections. For the 23- and 33-μm bands there is a slight positive skew, this is probably due to real features that we are unable to visually identify in the data as a consequence of substantial noise in the *Spitzer* spectra at these wavelengths. The 33-μm band can be susceptible to contamination from diffuse [S III] and [Si II] emission

lines, which may be improperly subtracted due to their non-uniform variation across the slit. We have taken care to minimise this contamination by excluding this region from our analysis if we detect the presence of sky lines. Consequently, the detection rate of the complexes represents a lower limit.
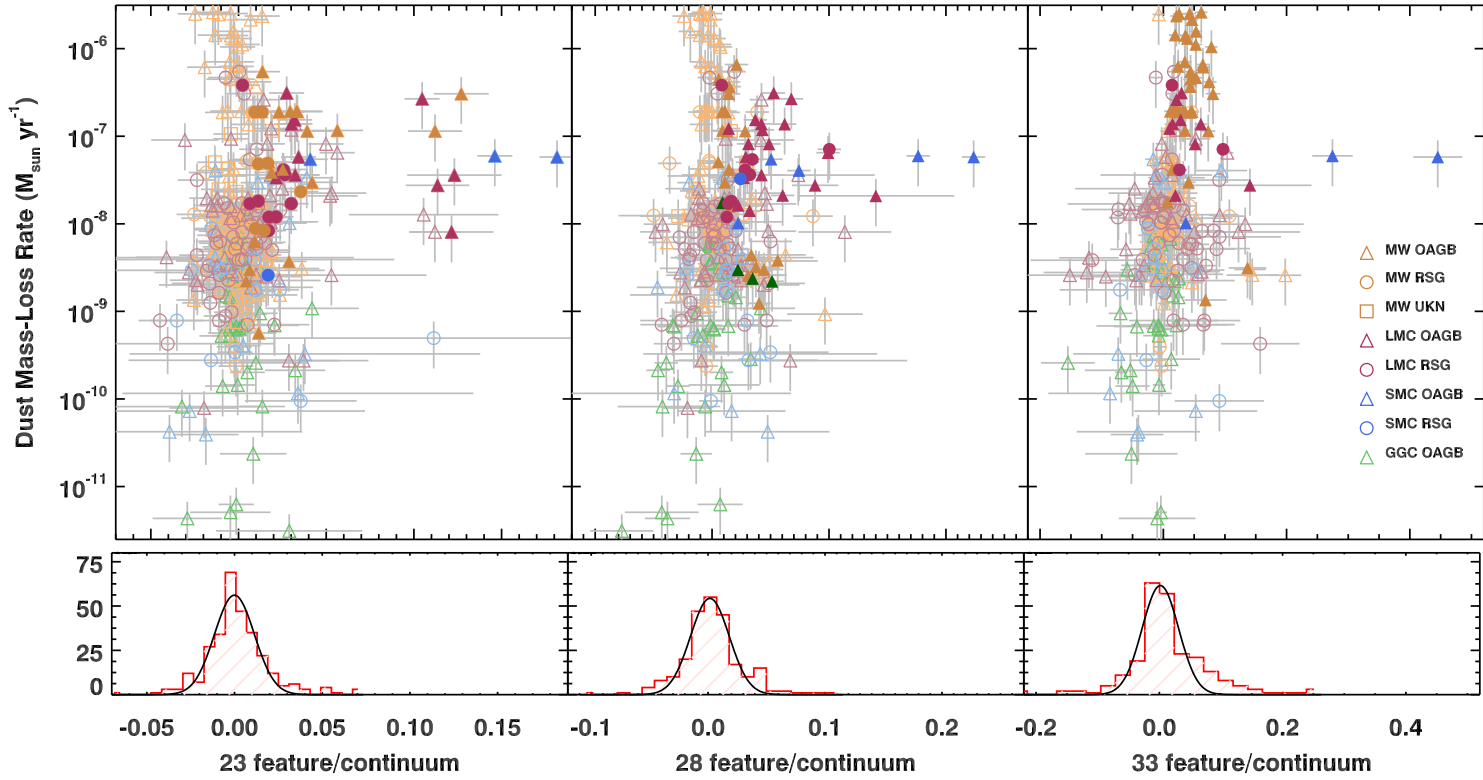
Figure 3.6: The strength of the 23-, 28- and 33-μm features versus $\dot{M}_{\mathrm{dust}}$, the dust mass-loss rate. O-AGB stars are represented by triangles, RSG as circles and sources which cannot be distinguished as either O-AGB or RSG are indicated by squares. The LMC sources are plotted in red; SMC: blue; MW: orange; and the globular clusters: purple. Filled symbols indicate that a crystalline feature can be visually identified. For sources where no feature is detected, a Gaussian is fitted to the distribution of feature strength/continuum.
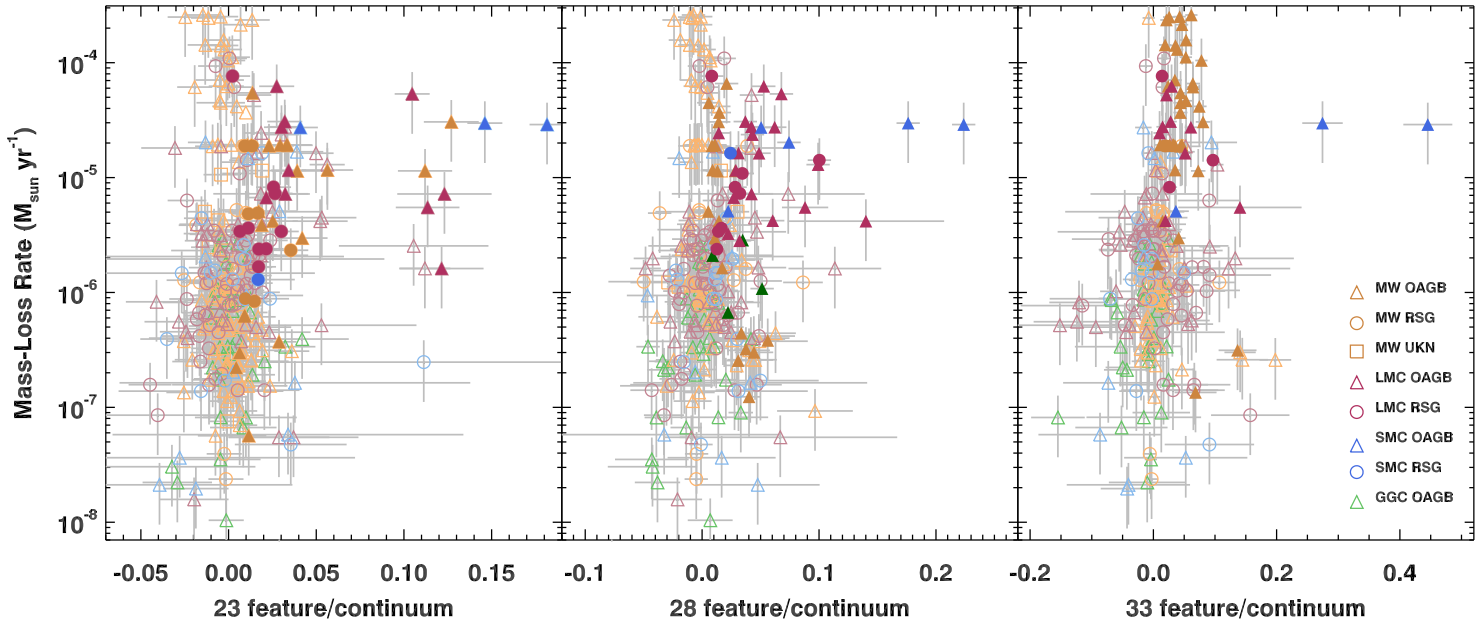
Figure 3.7: The strength of the 23-, 28- and 33-μm features versus $\dot{M}$, the total mass-loss rate. As with the dust mass-loss rates there is no apparent threshold value between sources with and without 23- and 28-μm silicate features. Symbols are the same as Fig. 3.6.

3.4.3   Dust temperature

The strengths of individual bands are affected by the abundance of each species, and by grain shape and temperature. By eliminating the former two parameters, we can derive the temperature of the emitting grains. We can eliminate the need to parametrise the abundance by taking the strength ratio of features that have the same carrier: in the case of forsterite, we can use the ratio of the 23- and 33-μm features.

Eliminating the effects of grain shape is more difficult, as these are further confounded by the choice of laboratory optical constants used to create the feature shapes. Emission models for the forsterite grains were computed from laboratory data (Jäger et al. 1998; Koike et al. 1998). Both these datasets give a good match to the observed feature profiles and do not differentiate different crystallographic axes, reducing the number of parameters which we must fit. From these, we use three sets of absorption efficiencies ($Q_{\text{fors}}(\nu)$). The first comes directly from Koike et al. (1998). The second is derived from the optical constants of Jäger et al. (1998), using homogeneous spherical particles with radii of 0.01 μm via Mie theory. The third is similarly calculated using a continuous distribution of ellipsoid grains with equivalent volumes.

Assuming that the long wavelength ($\lambda > 21$ μm) forsterite features are formed in an optically-thin region of the outflow then the crystalline forsterite spectrum can be approximated by:

$$F(\nu)_{\text{fors}} \sim B(T_{\text{fors}}, \nu) \times Q(\nu)_{\text{fors}} + F_{\text{cont}} \tag{3.4}$$

where $B(T_{\text{fors}}, \nu)$ is a blackbody of temperature T_{fors}, $Q(\nu)_{\text{fors}}$ is the forsterite absorption efficiency, and F_{cont} represents the sum of the featureless thermal dust component and stellar continuum. This component is effectively removed from the spectra by subtracting the spline-fitted continuum we use in Section 3.3.2. We therefore also subtract an identically-fitted spline from the modelled forsterite spectrum to ensure consistency.

These continuum-subtracted forsterite absorption efficiencies were then multiplied by blackbody functions corresponding to temperatures between 30 and 1000 K at 5 K intervals. The strengths of each feature were then determined by summing the remain-
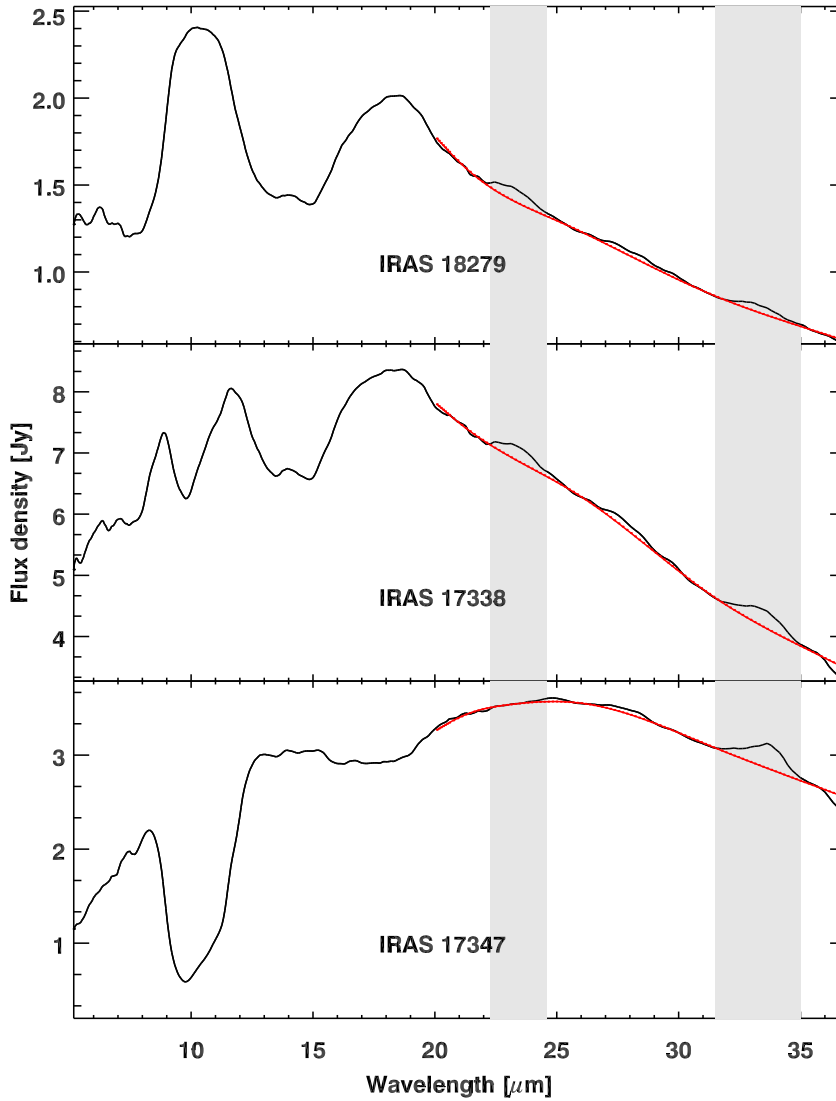
Figure 3.8: Three *Spitzer* spectra ordered in terms of the 10 μm optical depth. The shaded regions indicate the wavelengths where the 23- and 33-μm features were measured. As the dust shell becomes optically thick the 23-μm feature strength becomes suppressed. The smooth red lines show the adopted continua (spline).
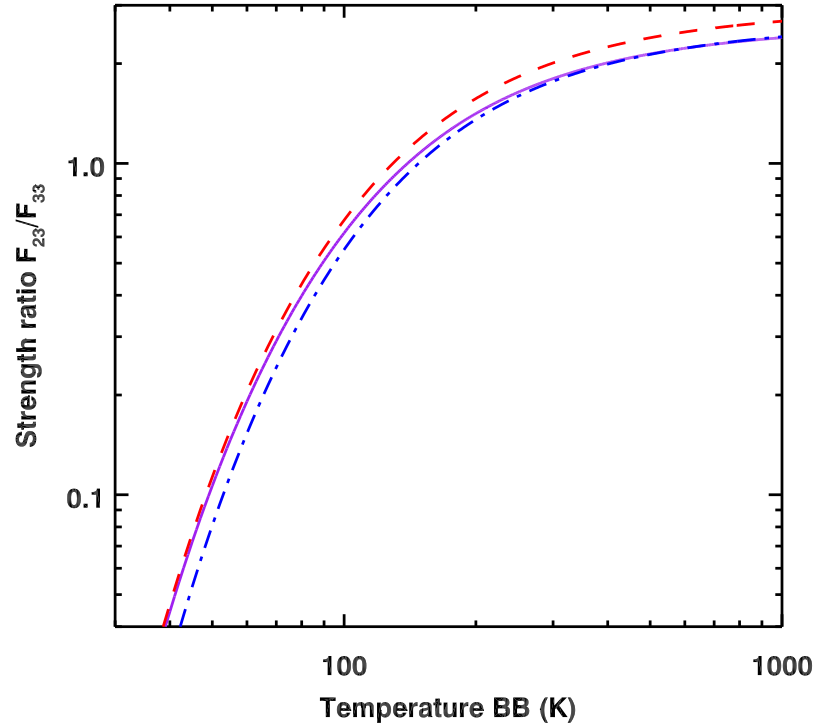
Figure 3.9: The ratio of relative peak strengths above continuum for the 23- and 33-μm forsterite bands as a function of the forsterite dust grain temperature. The different curves represent the different forsterite laboratory data: solid purple: (Koike et al. 1998); dashed red: (Jäger et al. 1998) continuous distribution of ellipsoids shape distribution (CDE); and dash dot blue: (Jäger et al. 1998) homogeneous spherical particle shape distribution (Mie).

ing flux over the wavelength intervals given in Section 3.3.2, and a ratio of the 23-to 33-μm features was determined. Fig. 3.9 shows how this ratio changes with temperature, allowing direct comparison to observed band strengths. An average of the resulting forsterite temperatures are given in Table 3.10. In sources where there is no 23-μm feature detection, T_{fors} may be incorrect due to self-absorption. This approach relies on the ratio of features' strengths, it is not greatly affected by the change in feature position due to temperature, and can therefore be treated as a robust estimate of

temperature once one takes into account the above caveats regarding grain shape and self-absorption.

In the 23-μm wavelength regime, the suppression of the forsterite feature for the majority of the sources where crystallinity is present is probably a consequence of the poor contrast of the cool grains above the amorphous dust continuum and, as such, they are indiscernible with *Spitzer* and *ISO*. For the sources with extremely high mass-loss rates we believe the absence of the 23-μm forsterite feature is due to self-absorption. Fig. 3.10 shows the spectra of four Galactic O-AGB stars undergoing intense mass-loss rates. In these sources, amorphous silicate absorption features are seen at 10 and 20 μm; OH 32.8−0.3, OH 26.5+0.6 and IRAS 17276−2846 also clearly exhibit crystalline silicate absorption features up to 33 μm where the feature appears in emission. The extreme OH/IR star IRAS 16342−3814 is also known to have some crystalline silicate features in absorption (Dijkstra et al. 2003). This object is undergoing an intense mass-loss of $\sim 10^{-3}$ M$_\odot$ yr^{-1}, which is approximately an order of magnitude greater than the highest mass-loss rates determined in this work. This behaviour is similar to that modelled by de Vries et al. (2010), who found that at mass-loss rates greater than 10^{-5} M$_\odot$ yr^{-1} even the 33-μm band becomes self-absorbed in some lines of sight. These results show that there is a limit to the strength of the crystalline silicates in AGB stars.

3.4.4 Pulsation period and crystalline feature strength

In general, as an AGB star evolves, the stellar radius increases, it becomes brighter, and its pulsation period increases. A similar period–luminosity relation exists for RSGs, although they often have smaller amplitudes and less regular periodicities. Fig. 3.11 compares the crystalline band strength with pulsation period. Care needs to be taken when comparing trends with pulsations across a metallicity range, since a star's effective temperature is metallicity-dependent and hence so are radius and pulsation period (Wood 1990). We therefore consider each population separately. We find that the frac-
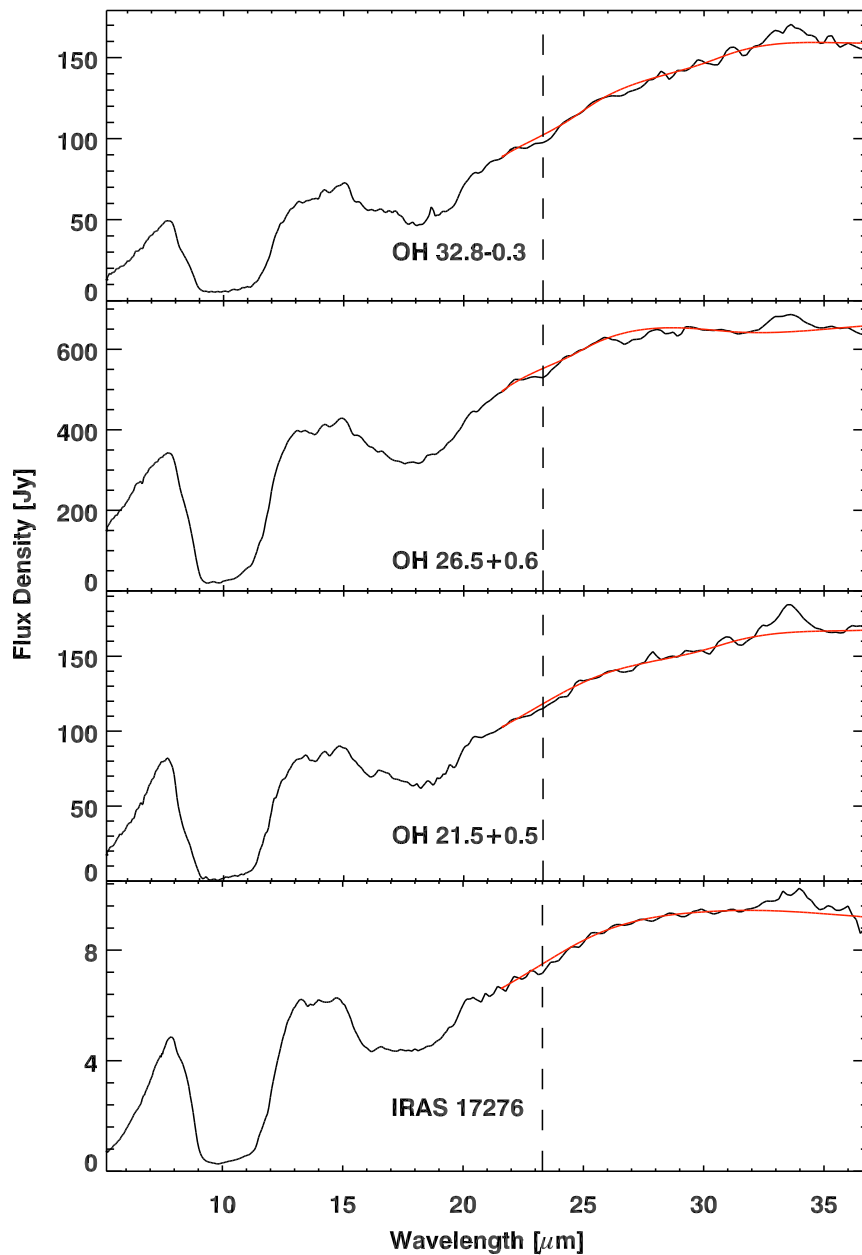
Figure 3.10: Spectra showing crystalline silicate absorption and emission features. To enhance the visibility of the crystalline features in the spectra the adopted continua are shown (smooth red lines). The position of the 23-μm feature is indicated by a dashed line.

Table 3.10: Derived forsterite temperatures for stars with a 33-μm feature. In sources where there is no 23-μm feature detection, T_{fors} may be incorrect due to self-absorption.

Star	23 μm Ft.	T_{fors} (K)	Star	23 μm Ft.	T_{fors} (K)
NML Cyg	Y	88 ± 10	MSX LMC 807	N	≤ 150
NML Cyg	Y	121 ± 23	S Scl	N	≤ 64
WX Psc	Y	89 ± 10	HD 269599	N	≤ 66
WX Psc	Y	89 ± 10	AFGL 2199	N	≤ 70
IRC +50137	Y	170 ± 47	AFGL 2403	N	≤ 53
HV 12956	Y	102 ± 13	AFGL 2403	N	≤ 68
OH 104.91+2.41	Y	67 ± 6	AFGL 2374	N	≤ 89
IRAS 03434+5818	Y	458 ± 365	AFGL 5379	N	≤ 47
IRAS 04553−6825	Y	73 ± 7	AFGL 5379	N	≤ 46
IRAS 04545−7000	Y	88 ± 10	AFGL 5535	N	≤ 50
IRAS 05402−695	Y	98 ± 12	OH 21.5+0.5	N	≤ 52
IRAS 05298−6957	Y	108 ± 15	OH 26.2−0.6	N	≤ 43
IRAS 05389−6922	Y	498 ± 390	OH 26.5+0.6	N	≤ 63
IRAS 135811−5444	Y	193 ± 63	OH 32.8−0.3	N	≤ 45
IRAS 17304−1933	Y	321 ± 190	OH 127.8 +0.0	N	≤ 84
IRAS 17338−2140	Y	169 ± 46	OH 127.8 +0.0	N	≤ 56
IRAS 17413−3531	Y	158 ± 39	IRAS 05128−6455	N	≤ 70
IRAS 18279−2707	Y	507 ± 385	IRAS 04407−7000	N	≤ 122
IRAS 18291−2900	Y	245 ± 108	IRAS 08425−5116	N	≤ 56
IRAS 19256+0254	Y	546 ± 364	IRAS 05329−6708	N	≤ 206
IRAS 19456+1927	Y	267 ± 130	IRAS 05558−7000	N	≤ 153
MSX SMC 134	Y	117 ± 19	IRAS 17004−4119	N	≤ 56
IRAS 17010−3840	N	≤ 51	IRAS 17513−3554	N	≤ 84
IRAS 17030−3053	N	≤ 53	IRAS 18195−2804	N	≤ 60
IRAS 17276−2846	N	≤ 54	IRAS 18231+0855	N	≤ 513
IRAS 17347−2319	N	≤ 47	MSX SMC 024	N	≤ 84

tion of sources showing crystalline silicate features is greater for sources with pulsation period longer than 700 days than for sources with short pulsation periods. Furthermore, in these long period pulsators the strength of the crystalline features appears to be increasing with period. This effect is strongest for the 28 μm feature in Fig. 3.11. These stars are typically more evolved with higher dust mass-loss rates than the sources with periods less than 700 days.
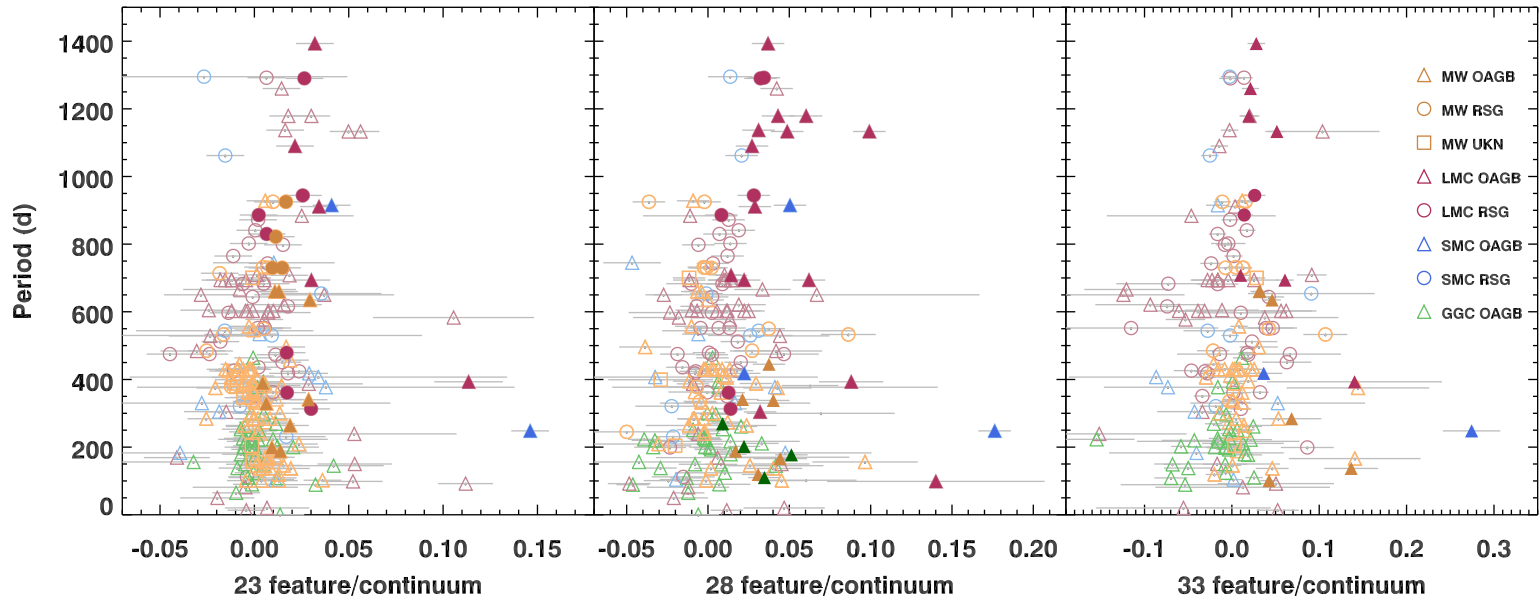
Figure 3.11: Comparison between pulsation period and the crystalline silicate feature strength. Symbols are the same as Fig. 3.6.

Probable disc sources

Fig. 3.12 shows three sources that exhibit unusually strong crystalline silicate features in their spectra. Strong crystalline silicate features such as these are often found in long-lived circumstellar discs where dust processing creates very high abundances of crystalline silicates (Molster et al. 1999b; Gielen et al. 2008, 2011). We propose that HD 269599 (SSID 4464), MSX SMC 134 and HV 12956 have a stable disc-like geometry, which invalidates the assumption of a spherically-symmetric outflow for the SED fitting. HD 269599 is a member of the young (16 ± 2 Myr) cluster NGC 1994 (Kumar et al. 2008) which contains B and B[e] stars. Because of its large infrared excess it is probable that HD 269599 is also a relatively massive, relatively young star with a disc. Optical spectroscopy confirms that HD 269599 is a B[e] supergiant (Lamers et al. 1998; Kastner et al. 2010).

MSX SMC 134 is RAW 631, an optically identified carbon star. Optical and near-infrared spectroscopy confirm its carbon-rich nature (Sloan et al. in prep, van Loon et al. 2008). The combination of a carbon-rich photosphere and oxygen-rich dust is the hallmark of a silicate carbon star (first discovered by Little-Marenin 1986). The leading explanation for these sources is that the silicate dust was trapped in a disc in a binary system before the mass-losing star evolved into a carbon star (Lloyd Evans 1991; Barnbaum et al. 1991).

We could find nothing in the literature that signifies the presence of a disc around HV 12956, but postulate the presence of a disk is required to show these high-contrast crystalline silicate features.

3.5 Discussion

3.5.1 Mass-loss rates

Determining total mass-loss rates requires an assumption about the scaling relation between the dust and gas in the envelope of AGB stars; this correction factor is not
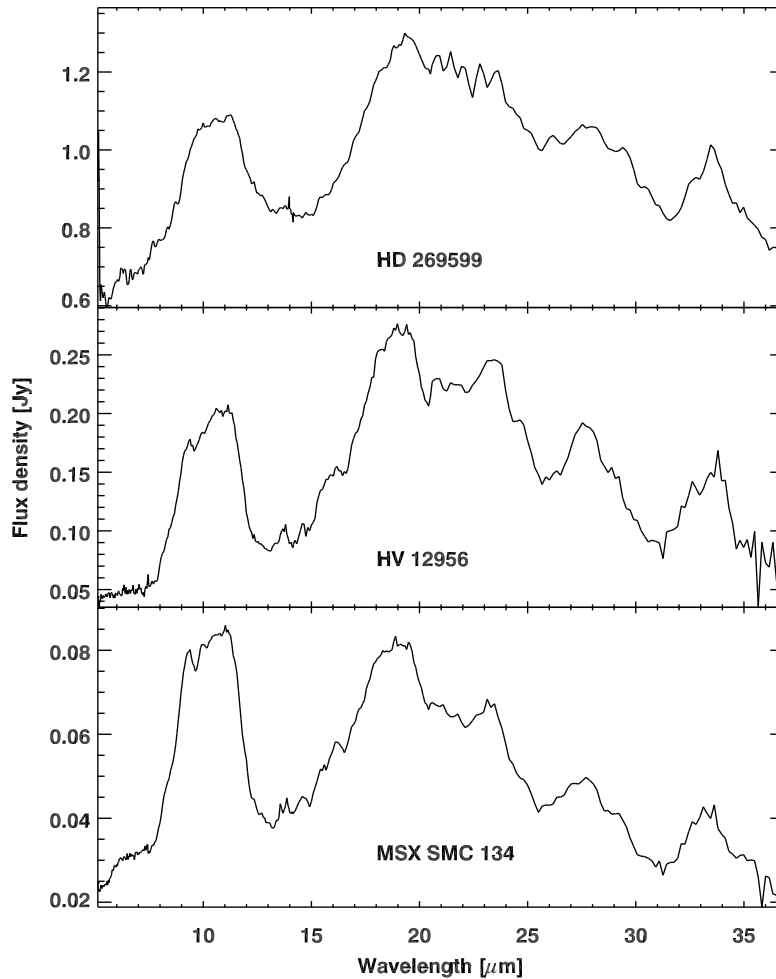
Figure 3.12: *Spitzer* spectra of three sources which display very strong crystalline features. We postulate that these sources have a stable disc-like geometry.

well known, even for Milky Way sources. It was proposed by van Loon (2000) that the gas-to-dust ratio for O-rich sources scales with the initial metallicity. Although this relation has an inherent scatter, it is commonly applied when deriving gas mass-loss rates. Our estimates for the total mass-loss rates are similarly affected by the large uncertainties in the correction factor, which may blur the effects of the gas density on the onset of crystallinity in the envelopes of evolved stars. Furthermore, the precision of the individual gas mass-loss rates will be affected by the assumption that objects

in each galaxy are of the same metallicity. Total mass-loss rates, determined from CO emission, may provide a better constraint of the gas density. This would require observations with the full ALMA array for objects at the distance of the Magellanic Clouds (Woods et al. 2012), however, the correlation between CO and total gas mass is also uncertain.

3.5.2 Onset of crystallinity

Theoretical dust condensation studies predict that the dust (Sogawa & Kozasa 1999) or gas (Tielens 1998; Gail & Sedlmayr 1999) column density in the circumstellar envelope is critical for the formation of crystalline silicates. Our observations show that, at high dust densities ($\dot{M}_{\mathrm{dust}} > 3 \times 10^{-8}\,\mathrm{M_\odot\,yr^{-1}}$), the majority of the sources in our sample exhibit silicate grains with a crystalline component. However, we first detect evidence for crystallinity at a low dust column density corresponding to $\dot{M}_{\mathrm{dust}} \sim 5 \times 10^{-10}\,\mathrm{M_\odot\,yr^{-1}}$. Approximately 10 per cent of the sources with dust mass-loss rates between $10^{-9.3}$ and $10^{-8}\,\mathrm{M_\odot\,yr^{-1}}$ show the distinctive structure of crystalline silicate bands. A transition in the silicate structure is seen when dust mass-loss rates of 10^{-8} to $10^{-7}\,\mathrm{M_\odot\,yr^{-1}}$ are reached. Here, the silicate grains undergo a transition from only a few per cent of sources displaying crystallinity to over 80 per cent of the sources, in less than 1 dex in dust mass-loss rates. This transition appears to be sharper for the dust mass-loss rates compared to the gas mass-loss rates, although the uncertainties are greater for the gas mass-loss rates. Although tentative, this suggests that crystallinity is predominantly correlated to the dust mass-loss rate, and thus annealing of amorphous silicate grains by radiation is probably the primary formation mechanism for crystalline silicates in the outflows of AGB and RSG stars.

Alternatively, Sloan et al. (2008) argue that in low-density winds grain growth occurs over a long period, allowing the atoms to arrange themselves in the most energetically-favourable lattice structure before being locked in place as the grain accumulates more layers. At higher densities grains will accrete material faster, preventing the migra-

tion of atoms. If this was the case one would most likely expect to see a bimodal distribution of crystalline sources, which is not supported by our results.

For sources undergoing the most extreme mass-loss rates a combination of crystallisation processes may be in effect. Here conditions are favourable for both thermal annealing of the amorphous grains and crystalline grains forming by direct condensation from the gas phase, where the higher densities in the dust-formation zone raise the silicate condensation temperature above the glass temperature (Lodders & Fegley 1999; Gail & Sedlmayr 1999). This combined effect may in part explain why the sources with high mass-loss rates tend to have stronger crystalline features.

3.6   Conclusions

We have analysed *Spitzer* and *ISO* infrared spectra of 217 O-AGB and 98 RSG stars in the Milky Way, Magellanic Clouds and Galactic globular clusters, to explore the onset of crystallinity. Dust mass-loss rates were established through spectral energy distribution fitting with the   model grid and the strength of the crystalline features determined from the spectra. The main results of this study are summarised as follows:

- We detect crystalline silicates over 3 dex in dust mass-loss rate down to rates of $\sim 10^{-9}$ $M_\odot$ yr^{-1}.

- Crystalline silicates are more prevalent in higher mass-loss rate objects, though sources undergoing the highest mass loss do not show the 23-μm forsterite feature. This is due to the poor contrast of the low temperature of the forsterite grains above the continuum and in some cases (self-)absorption of the short wavelength ($\lambda < 25\mu$m) crystalline silicate features.

- The dust mass-loss rate appears to have a greater influence on the crystalline fraction than the gas mass-loss rate. This may suggest that the annealing of amorphous silicate grains by radiation is probably the primary formation mechanism for crystalline silicates in the outflows of AGB and RSG stars.

4

Crystalline Silicate Mineralogy

The work presented in this chapter expands upon the work published in Jones et al., 2012, MNRAS, 427, 3209.

4.1   Introduction

In this chapter, we will present a mineralogical analysis of the crystalline silicate features detected in the *Spitzer* and *ISO* SWS spectra between 22 and 35 μm. The dust characteristics in this sample of O-rich AGB stars and RSG in the Galaxy and the Magellanic Clouds are of particular interest because of the different metal content in the dust-forming region of their circumstellar envelopes. This may affect the dust condensation sequence and hence the composition of the crystalline silicate dust.

The first step towards understanding the dust condensation sequence of these stars is the identification of the dust emission features in the infrared spectra. Crystalline silicates in the outflows of AGB stars and RSGs exhibit sharp resonance features at wavelengths beyond 10 μm. The peak positions and shapes of these bands depend on the adopted Mg/(Mg+Fe) ratio, lattice structure, grain size and morphology (Molster et al. 2002b; Chihara et al. 2002; Koike et al. 2003; Min et al. 2003). From these variations it is possible to determine the minerals present, by comparing the observed spectral features to laboratory spectra of different dust species.

4.2   Feature identification

To compare the crystalline silicate features across the Milky Way, Magellanic Clouds and the Galactic globular clusters we derive mean continuum-subtracted spectra for the complexes at 23, 28 and 33 μm. The emission from the crystalline silicate features can be isolated from the observed spectrum by subtracting a continuum according to Equation 3.4. Emission features were extracted from the resulting continuum-subtracted spectra over the wavelength ranges specified in Table 3.8, and averaged using a weighting factor (calculated from the point-to-point RMS) to account for the varying signal-to-noise in each region. The mean spectral complexes for the MW, LMC and SMC sources are shown in Fig. 4.1. In the globular cluster sample only the 28-μm spectral complex is present. These are compared to laboratory spectra of crystalline olivine and pyroxene with varying Fe/(Mg+Fe) ratios. Average feature shapes for the O-AGB stars and RSGs in our sample are presented in Fig. 4.2.

The precise shape and position of the continuum-subtracted features will depend on the spline-fitted continuum. In order to evaluate how sensitive a feature is to the defined continuum, we also computed average profiles using a linear continuum. The central wavelength of the 23-μm feature (measured by finding the wavelength which bisects the integrated flux of the feature) has a mean variation of 0.08 μm when a linear continuum was fitted, a mean change in position of 0.19 μm was recorded for the 28-μm feature and the 33-μm feature had a 0.17 μm change. In extreme cases where the features are weak compared to the continuum, or the spectra have a low signal-to-noise the central wavelength may move by 0.43 μm. For most cases the change in wavelength is relatively minor. Figure 4.3 shows the influence of the continuum on a source with strong features, MSX SMC 134, and a source with weaker features, IRAS 18279. The average feature shape is remarkably insensitive to the method of continuum fitting, due in large part to the weighting factor and normalisation.
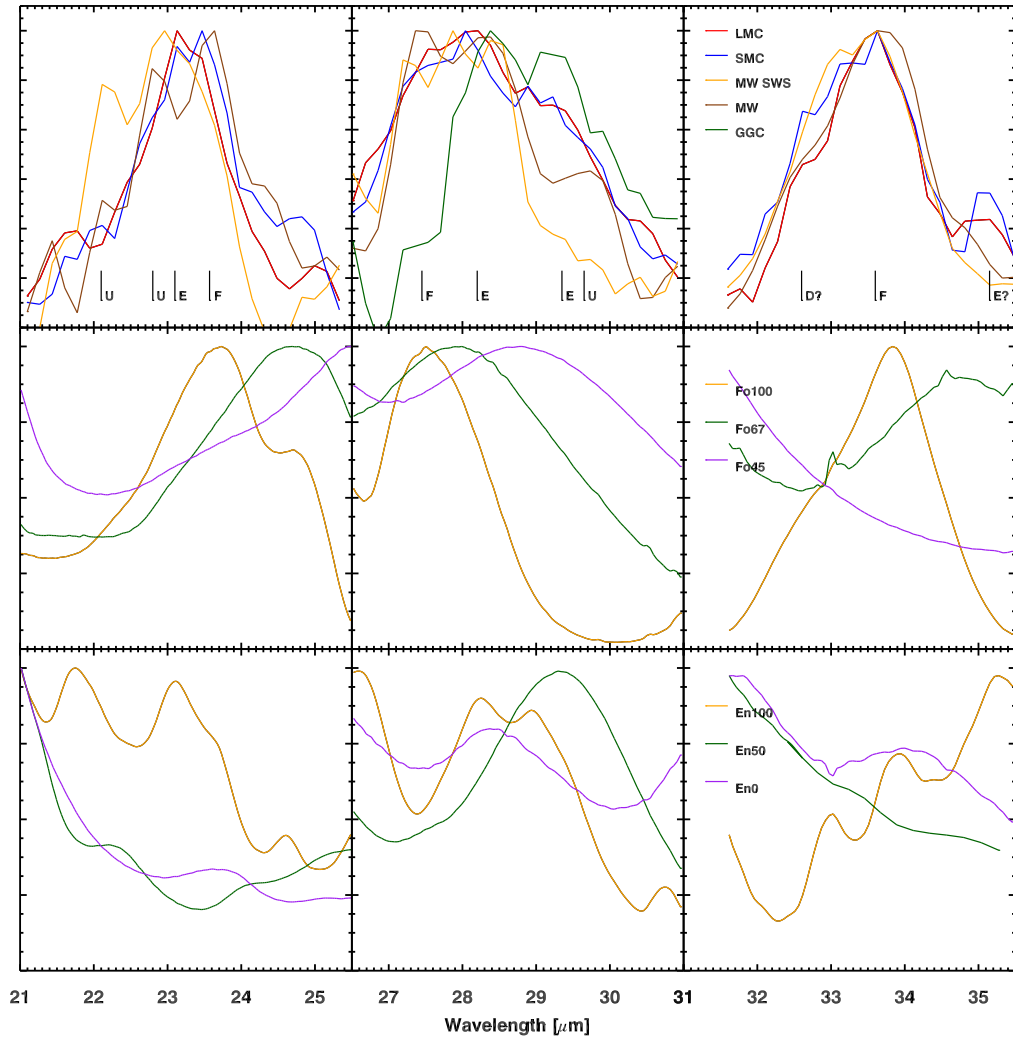
Figure 4.1: Overview of the normalised mean continuum-subtracted 23-, 28- and 33-μm complexes. *Top*: the LMC, SMC, globular cluster and MW *Spitzer* complexes are plotted in blue, red, green and brown respectively, while the MW spectra from the SWS re-gridded to IRS resolution are plotted in orange. The tick marks indicate the wavelengths where crystalline silicate features are found in the observed spectra. The crystalline species are indicated by a F (forsterite), E (enstatite), D (diopside), while a U indicates an unidentified species. *Middle row*: Laboratory spectra of crystalline olivine with Mg/(Mg+Fe) ratios of: 45% (purple), 67% (green) and 100% (yellow). *Bottom*: Laboratory spectra of crystalline pyroxene with Mg/(Mg+Fe) ratios of: 0% (purple), 50% (green) and 100% (yellow).
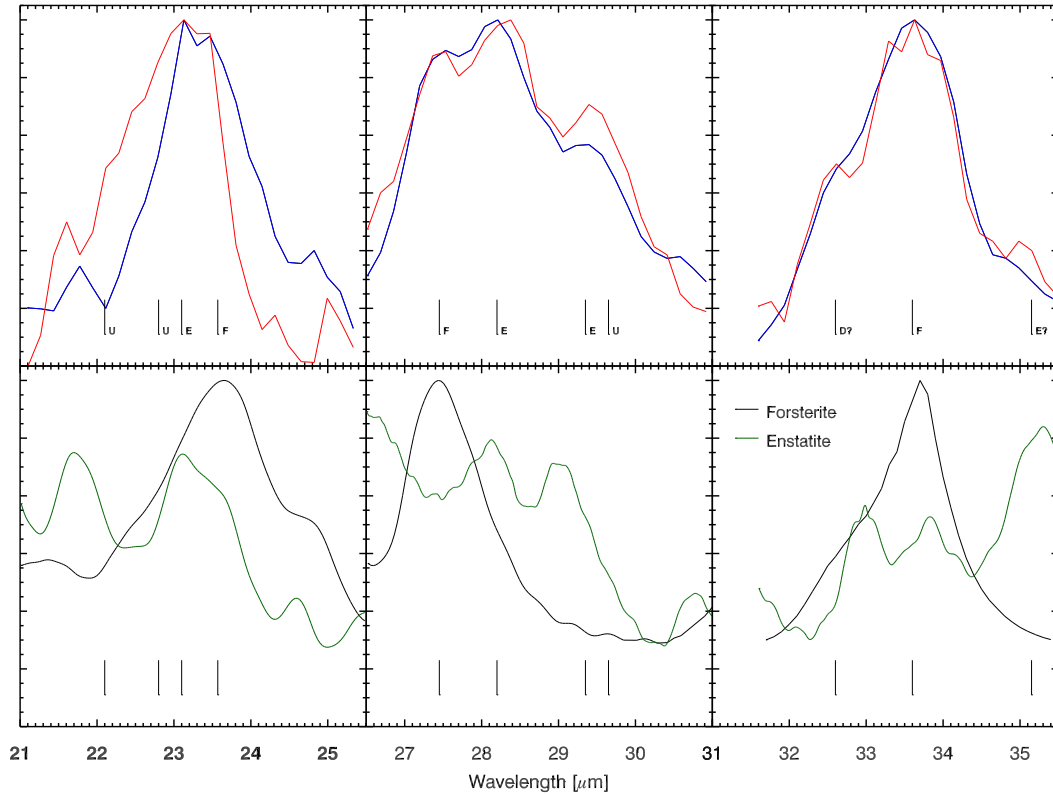
Figure 4.2: Overview of the normalised mean continuum-subtracted 23-, 28- and 33-
μm complexes. *Top*: The combined mean complex spectrum of O-AGB (blue) and
RSG (Red) sources. The tick marks indicate the wavelengths where crystalline fea-
tures are found in the observed spectra. The crystalline species are indicated by a F
(forsterite), E (enstatite), D (diopside), while a U indicates an unidentified species.
Bottom: Laboratory spectra of forsterite (black) and enstatite (green) are plotted for
comparison (Koike et al. 1998).
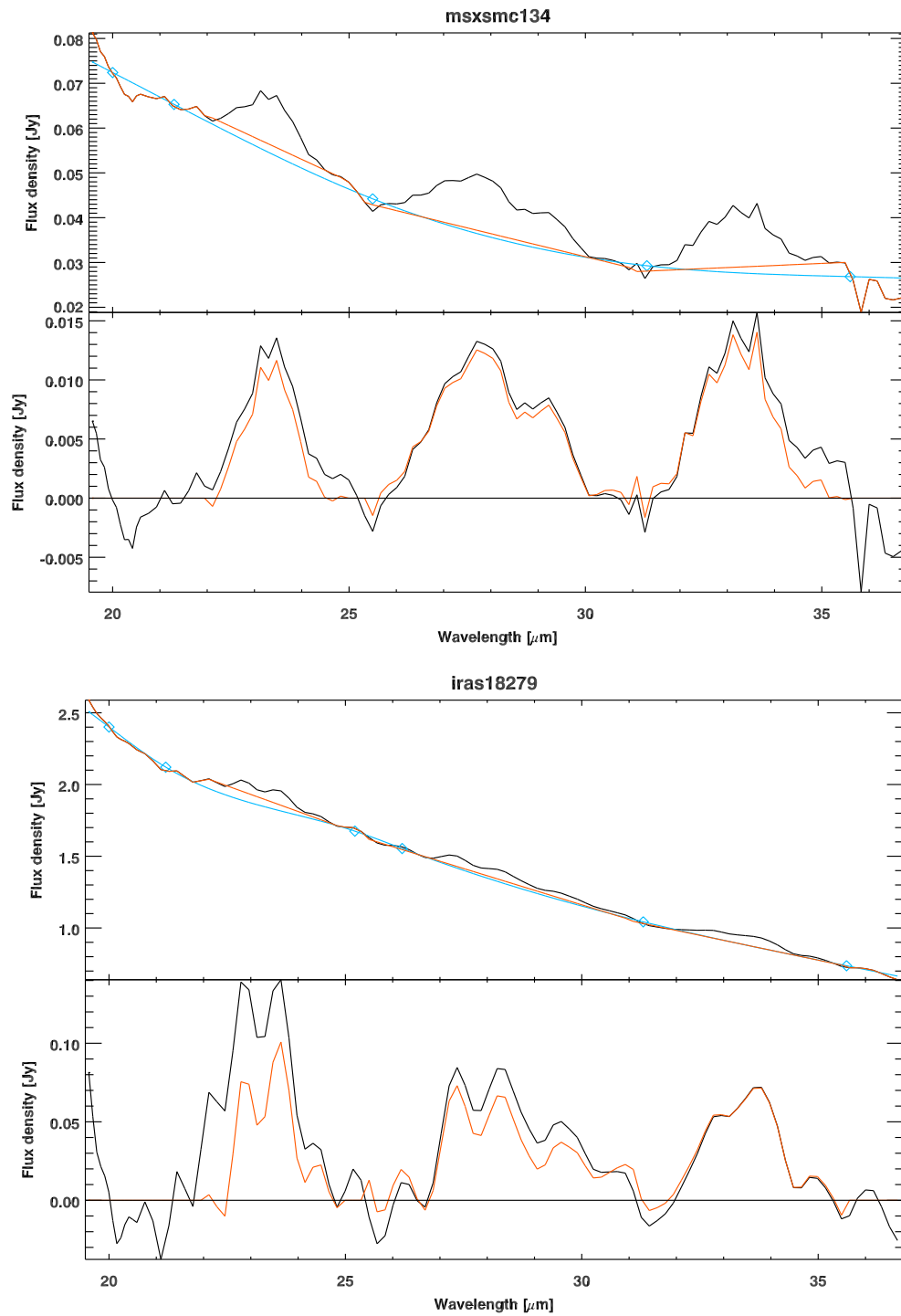
Figure 4.3: The effects of the continuum fitting method on the continuum-subtracted feature profile. For each star, the top panel shows a spline-fitted continuum (blue) and a linear continuum (red), while the bottom panel shows the residual features from the spline fit (black) and linear fit (red).
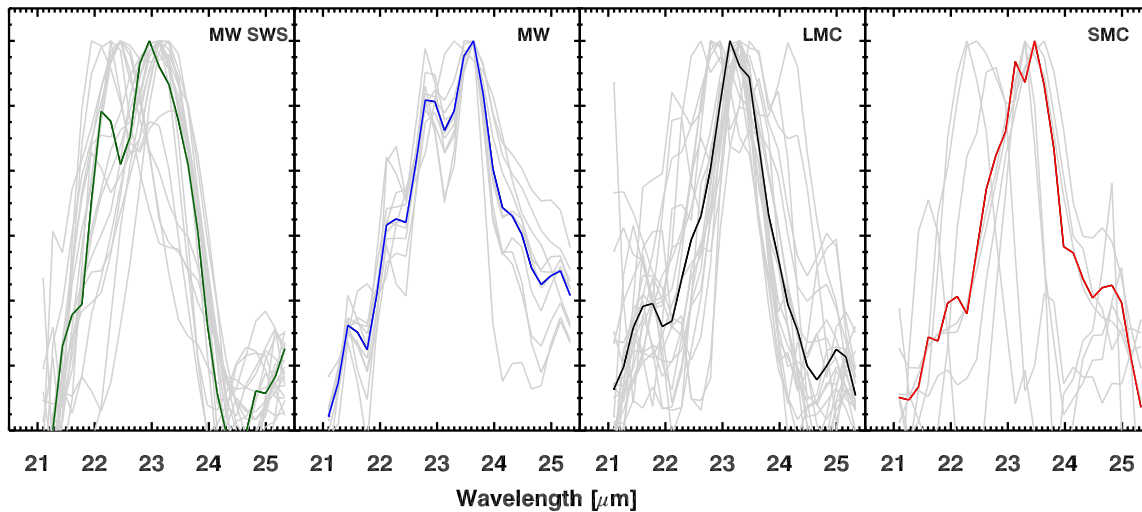
Figure 4.4: The normalised continuum-subtracted 23 μm features (grey lines) compared to the mean 23 μm complex.

4.2.1 The 23-μm complex

The 23-μm complex is clearly seen in several of the stars across a wide range of dust mass-loss rates. However, it becomes less prominent and even absent in the highly-enshrouded sources. This band is entirely absent in the globular cluster sources across all mass-loss rates. The complex is thought to be dominated by forsterite emission (Molster et al. 2002b; Sloan et al. 2008), with its peak fitting the dust spectra better than Fe-rich members of the olivine series.

To study the systematics between features in the spectra we compare them to the mean spectra. Figures 4.4 shows the normalised continuum-subtracted features compared to the mean spectral complex. The average central wavelength of the complex for each population is around 23.35 μm, however, the variations between samples and individual sources is larger than that of the 33-μm feature.

The complex is comprised of several blended features at 22.3, 22.8, 23.0 and 23.7 μm whose relative strengths provide the main difference between the samples. While the 22.3, 23.0 and 23.7 μm features have previously been reported by Molster et al. (2002b), this is the first-time the 22.8 μm component is seen. The complex is domi-
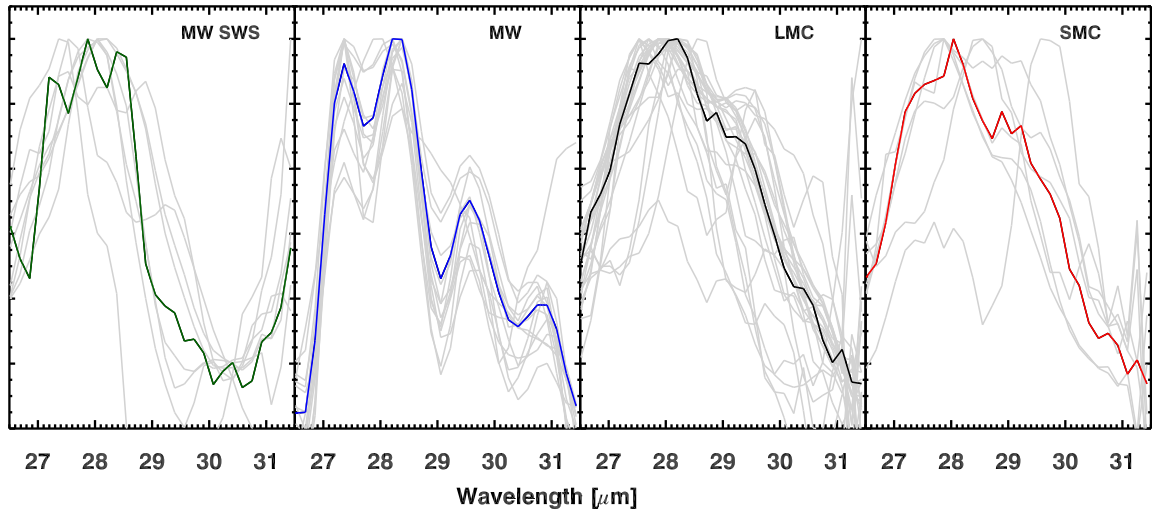
Figure 4.5: The normalised continuum-subtracted 28 μm features (grey lines) compared to the mean 28 μm complex.

nated by the 23.7-μm forsterite band, with the 23.0-μm enstatite feature also contributing to the substructure. The 22.3-μm and the newly discovered 22.8 μm bands have yet to be attributed to a dust species.

The strength of the 23.0-μm feature compared to the 23.7-μm feature provides the main difference between the Magellanic Cloud mean profiles and the MW profiles. The mean profile of the SWS Galactic sources exhibits the largest deviation from the other mean spectra: this mean spectrum shows prominent 22.3- and 22.8-μm features which are more subdued in the other profiles. Furthermore, the mean SWS Galactic spectrum is shifted towards the blue. The mean profile of the RSGs has a similar shift to shorter wavelengths with a central wavelength of ~23.0 μm (compared to the O-AGB sources at 23.4 μm), as seen in the top left panel of Fig. 4.2.

4.2.2   The 28-μm complex

The 28-μm complex shows clear variations in the spectra with metallicity. Although the samples show a similar peak position around 27.8 μm, the spectral shape is different for the Magellanic Cloud, globular cluster and Galactic sources. This complex is

comprised of several blended features of which the 27.5-μm forsterite feature, combined with the 28.2- and 29.4-μm enstatite features, are the main components (Molster et al. 2002b). In the Magellanic Cloud profiles, the broader feature may indicate an enhanced enstatite contribution compared to forsterite. There may also be a significant contribution from the unidentified 29.6 μm feature, which is especially pronounced in the MW *Spitzer* mean complex. Unlike the MW and the Magellanic Cloud profiles, the mean spectrum for the globular clusters does not show a forsterite component; here, the complex is dominated by enstatite. There is no discernible difference between the O-AGB stars and the RSGs.

Determining an average profile for the MW SWS spectra was hampered by the troublesome boundary between bands 3D, 3E and 4 in this region, where known light leaks and spectral response calibration problems result in large uncertainties in the flux (Sloan et al. 2003a). Several SWS spectra show a broad plateau extending from $\sim 27.5-32.2 \, \mu$m. We could find no evidence for a similar feature shape in any of the *Spitzer* spectra and we conclude that this plateau is probably an instrumental artifact. We have taken care to exclude any sources where this artifact may be present in the *ISO* SWS data before determining a mean spectrum for this sample.

It is clear from Figure 4.6 that there is a large discrepancy between these mean profiles and the 28 μm outflow complex determined by Molster et al. (2002b). That complex shows a sharp rise across the band, furthermore the red-edge of the complex has a strong relatively flat component with few peaks, which is not seen in any of the *Spitzer* spectra. The *Spitzer* Galactic and extragalactic post-AGB disc emission complexes calculated by Gielen et al. (2011) also show no evidence for a plateau in the 28-μm complex. Thus, we believe that our 28-μm profiles provide a more accurate/reasonable reflection of the crystalline features present in outflows, as these are not affected by the problematic SWS 3D and 3E bands.
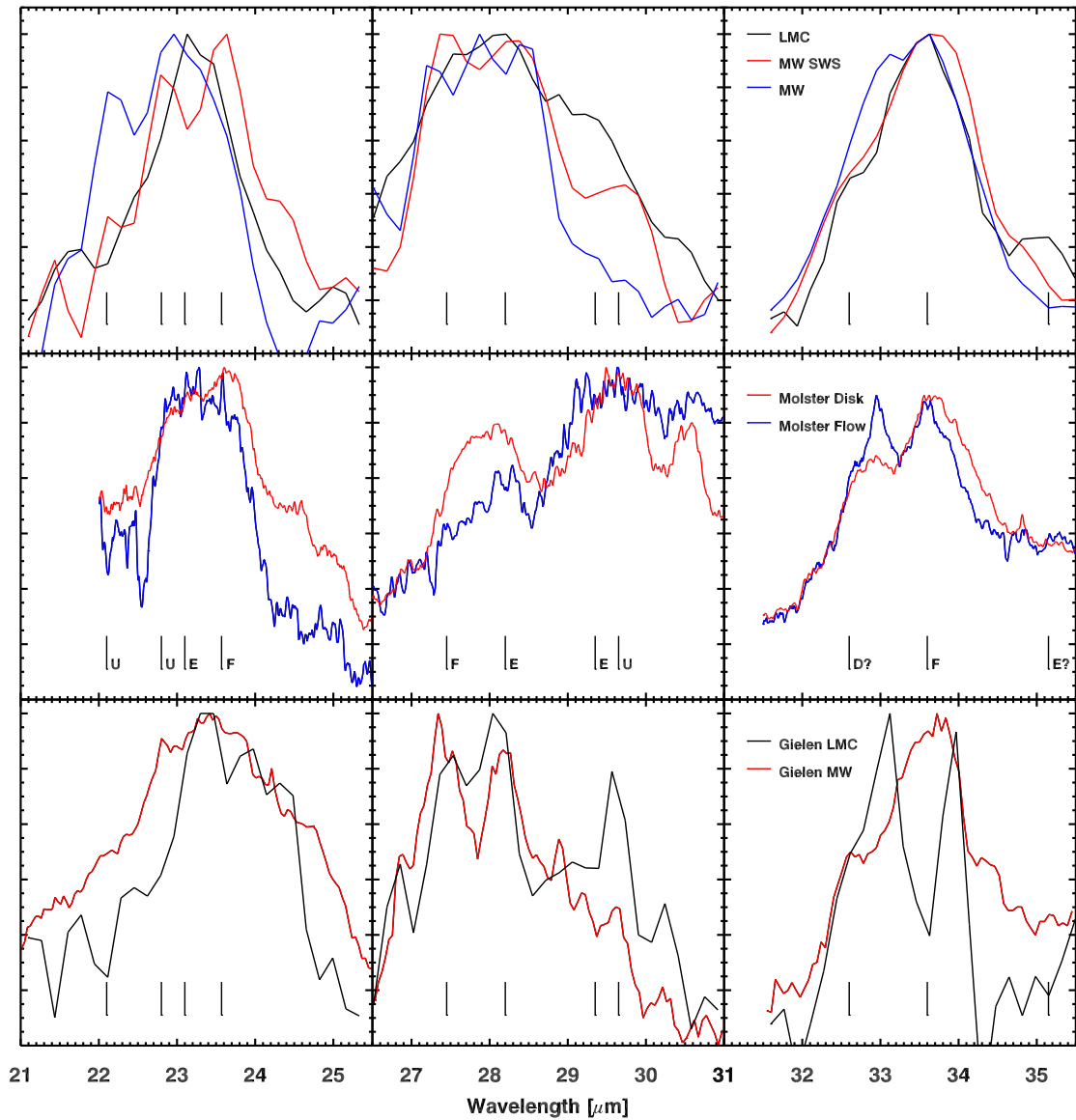
Figure 4.6: A comparison of the mean crystalline silicate complexes determined for the sources in our sample and the calculated mean complexes of Molster et al. (2002b) and Gielen et al. (2011). The tick marks indicate the wavelengths where crystalline features are found in observed spectra.
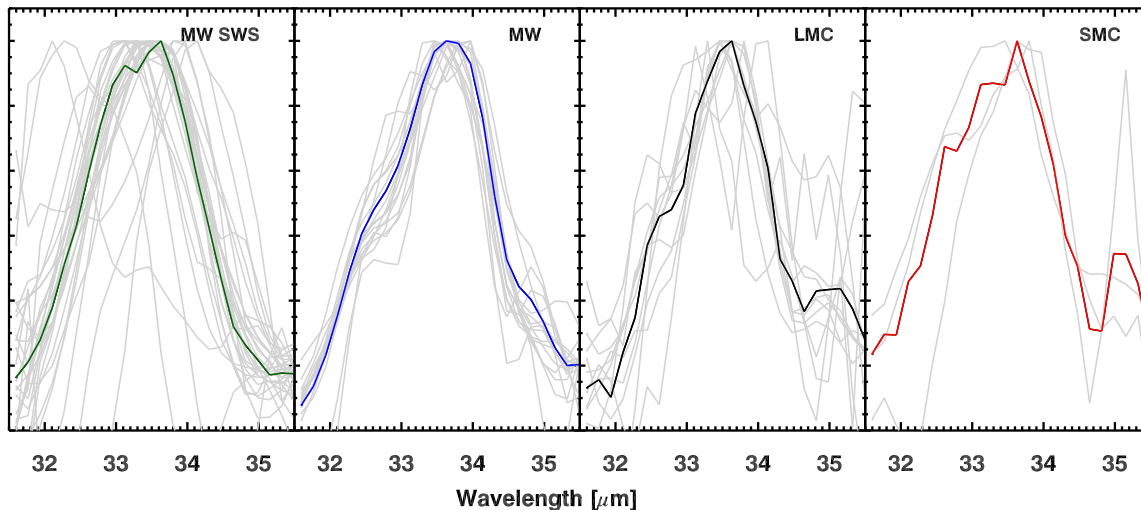
Figure 4.7: The normalised continuum-subtracted 33 μm features (grey lines) compared to the mean 33 μm complex.

4.2.3 The 33-μm complex

The 33-μm complex is dominated by the strong forsterite feature at 33.6 μm, and is particularly prominent in sources with high mass-loss rates. In both the LMC and SMC samples, strong noise around 33 μm complicates the identification and extraction of features, thus the detection rate may be lower than expected compared to the MW sample. The 33-μm complex is not seen in the globular cluster stars. The complex shows remarkably little variance with metallicity, both in terms of the shape, mean wavelength and FWHM. The mean wavelength of the extracted feature is 33.54 μm, varying by 0.13 μm across the three galaxies. The position of the 33.6-μm feature is consistent with cool Mg-dominated crystalline olivine grains. If the grains contained iron inclusions then the peak of the feature would be shifted to the red (Koike et al. 2003; Pitman et al. 2010). Warmer grains would also result in a shift in band position to longer wavelengths (Koike et al. 2006). The 33-μm complex also exhibits some less prominent sub-structure. There is a weak feature on the left shoulder of the complex at 32.2 μm, tentatively identified as diopside ($MgCaSi_2O_6$) by Molster et al. (2002b). At the red edge of the band we note the presence of an enstatite feature at 35.3 μm.
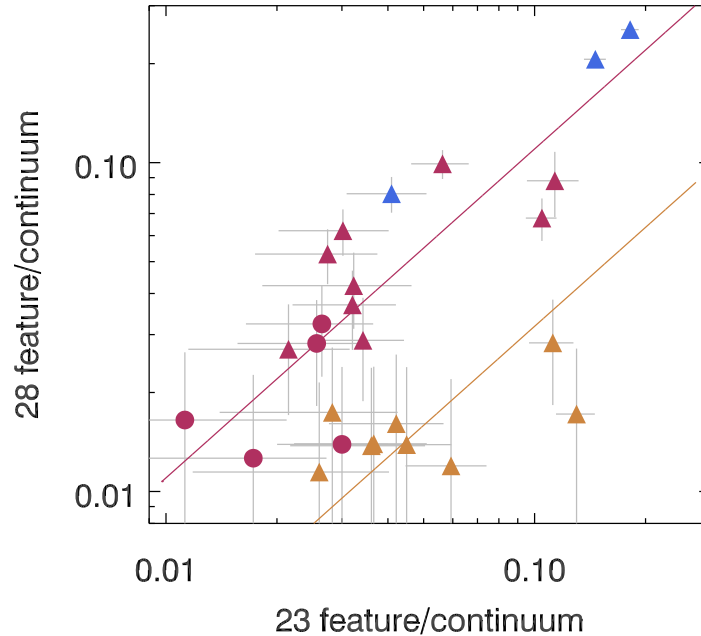
Figure 4.8: Correlation between the strength of the 23-μm feature and the 28-μm feature. The symbols and colours are as defined in Fig. 3.6, except the filled symbols represent the presence of both a 23- and a 28-μm feature. The lines show the least square fit to the LMC (red) and MW (orange) features.

4.3 The olivine-to-pyroxene ratio

The variation in spectral shape and the differences between individual bands present in the 28-μm complexes for the Milky Way, Magellanic Clouds and globular clusters, may indicate a change in the crystalline silicate dust mineralogy with metallicity. As the metallicity increases, the enstatite substructure at 28.2 and 29.4 μm becomes less pronounced, whereas the forsterite substructure at 27.5 μm becomes more distinct. This dichotomy between the Magellanic Clouds and the Galaxy can be clearly seen in Figs. 4.8 and 4.9, which show the relations between the 23- and 33-μm forsterite features and the 28-μm enstatite feature strength (measured according to Sec. 3.3.2). The separation between the populations, as indicated by the difference between the
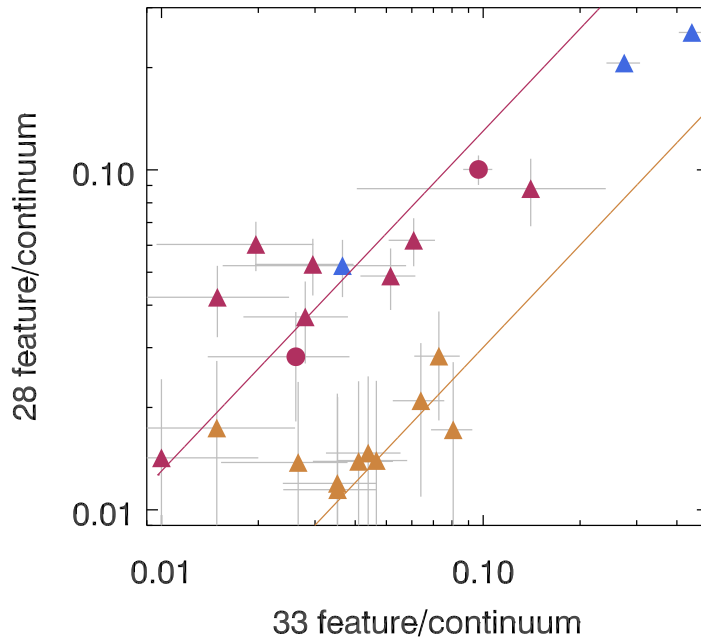
Figure 4.9: Correlation between the strength of the 33-μm feature and the 28-μm feature, with best-fit line for each population. The symbols and colours are as defined in Fig. 3.6, except the filled symbols represent the presence of both a 33- and a 28-μm feature.

lines of best fit to the crystalline silicate features in each galaxy, suggests a change in crystalline dust composition with metallicity, with enstatite seen increasingly at low metallicity, while forsterite becomes depleted. A line of best fit is not plotted for the SMC sources due to there being insufficient data points. Note that the globular cluster sources do not feature in these plots as they only exhibit the 28-μm enstatite feature, also indicating a change in dust composition with metallicity. This trend is almost certainly a metallicity effect, and not due to changes in mass-loss rate or luminosity, as we are sensitive to crystalline silicate features in AGB and RSG sources across several dex in both luminosity and mass-loss rate.

Figure 4.10 shows the relation between the 23- and 33-μm features that have the
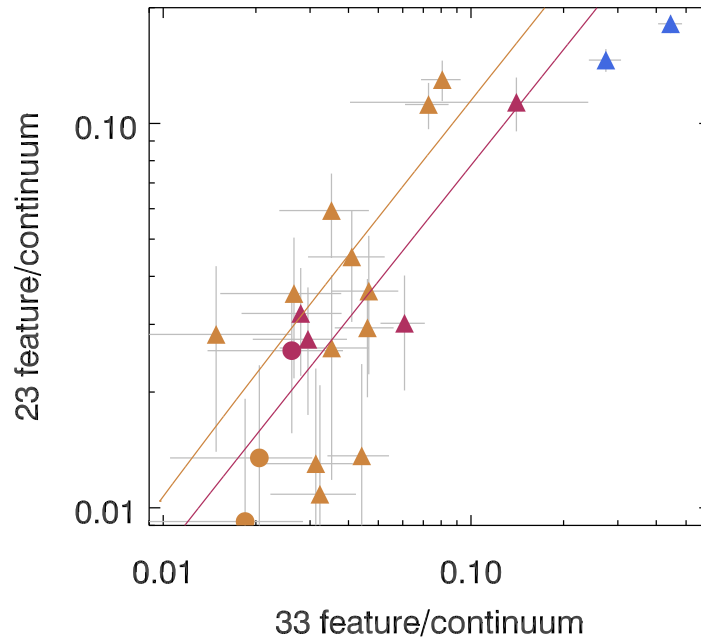
Figure 4.10: Correlation between the strength of the 23-μm feature and the 33-μm feature. The symbols and colours are as defined in Fig. 3.6, except the filled symbols represent the presence of both a 23- and a 33-μm feature.

same primary carrier (forsterite). There is no clear separation between the different metallicity populations. However, several of the Milky Way sources are not very well represented by the best fit line. These sources are experiencing intense mass-loss rates, consequently the 23-μm feature might be experiencing self-absorption.

We detect a change in the crystalline silicate mineralogy with metallicity, with enstatite seen increasingly at low metallicity, while forsterite becomes depleted. This variation in the olivine-to-pyroxene ratio can be explained by a number of possible mechanisms.

4.4 Mineralogy and metallicity

Our results provide strong evidence for a change in crystalline silicate production with metallicity; here we explore some of the possible reasons for these differences.

The molecules available for dust production in O-rich stars are limited by the abundances of heavy elements that are not produced on the AGB. The abundance of Mg, Si, Ca, Al, and Fe in the photosphere reflect the initial abundances of the molecular cloud from which the star formed, while the surface abundances of C and O are altered by dredge-up and hot bottom burning. Dredge-up only increases the [O/H] abundance by small amounts. However efficient hot bottom burning in low-metallicity, high-mass AGB stars may result in [O/H] depletion (Ventura et al. 2002). For stars with solar-like abundances, both Mg and Fe are more abundant than Ca and Al (Mg/Fe being approximately unity). These abundances change with overall metallicity. For non-α-capture products like Al, this effect is even more severe (Wheeler et al. 1989).

For solar-metallicity stars, the classical dust condensation sequence in the outflows of O-rich evolved stars predicts that aluminium- or calcium-rich dust grains form first, at temperatures around 1400 K, before silicon and magnesium condense into silicates at slightly lower temperatures (Tielens 1990; Lodders & Fegley 1999; Gail & Sedlmayr 1999). A parallel condensation sequence, involving magnesium and silicon, starts with the direct condensation of forsterite from the gas phase at temperatures around 1050 K. This is subsequently transformed into enstatite through reactions between forsterite and SiO_2 gas, according to the equilibrium reaction:

$$2MgSiO_3 \rightleftharpoons Mg_2SiO_4 + SiO_2. \tag{4.1}$$
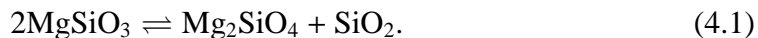
The condensation sequence in O-AGB stars is slightly different from that of supergiants (Speck et al. 2000; Verhoelst et al. 2009), however, the end-point for both sequences results in the formation of magnesium-rich silicates. The lower detection rate of crystalline features in RSGs may be a consequence of this alternate condensation pathway, due to the delayed production of Mg-rich amorphous silicates. We

speculate that this production is a necessary precursor for the formation of forsterite and enstatite, as it provides suitable material from which to anneal crystalline silicates.

4.4.1 Fe-content of crystalline silicates

The crystalline silicates in our sample are comprised of Mg-rich olivines and pyroxenes (forsterite: Mg_2SiO_4 and enstatite: $MgSiO_3$). Recently, the crystalline features in the *ISO* spectra of RX Lac, T Cep, T Cet and R Hya were found to be better matched with the iron-rich silicate: $Mg_{0.18}Fe_{1.82}SiO_4$ (Pitman et al. 2010; Guha Niyogi et al. 2011). These sources occur early on in the silicate emission sequence (which characterises the shape of the 10 μm complex; see Sloan & Price 1995) and lack the classical emission/absorption features that have been attributed to amorphous silicate dust; they also tend to have optically thinner dust shells. However, *Herschel* observations of the 69 μm crystalline silicate band in more evolved AGB stars do not find evidence for iron in the lattice structure of the crystalline olivine (de Vries et al. 2011). The sources in our sample tend to have optically thicker shells and a greater abundance of amorphous silicates. Consequently, Fe-rich crystalline silicates may only form early on in the AGB, in low-density winds.

4.4.2 Forsterite-to-Enstatite ratio

At solar metallicities, forsterite is the dominant crystalline species, but as the metallicity drops enstatite becomes preferentially formed. We consider five possibilities for this difference below.

1. The elemental abundance of Mg, Si and O during dust condensation will also influence the forsterite-to-enstatite ratio. If either Mg or O are depleted then enstatite could preferentially form. One might expect the abundances of Si and Mg to scale from the solar values by the same amount, in which case a lower relative abundance of O would be required for enstatite production. This could be due to water formation locking up free oxygen, changes in the natal C/O ratio

with metallicity, or efficient hot bottom burning in low-metallicity high-mass AGB stars.

In more metal-poor galaxies, dredge-up of newly produced carbon has a greater effect on the C/O ratio in the photosphere of the star (Lattanzio 2003). A higher abundance of CO reduces the amount of free oxygen available for dust production, which might result in the preferential formation of grains with a pyroxene stoichiometry as they require less oxygen.

The chemical abundances in massive AGB stars can also be modified by hot bottom burning. If the temperatures are high enough ($T > 3 \times 10^6$ K) for the NO cycle and Ne-Na cycle to become active, oxygen will become depleted and sodium should be enhanced (Caciolli et al. 2011). Oxygen depletion (and associated sodium enhancement) has been observed in several low metallicity globular cluster stars (Kraft et al. 1997; Gratton et al. 2001). These stars have insufficient mass to have undergone hot bottom burning, however, it may be possible that the abundances of the primordial gas was enriched in He, C, N and Na, but depleted in O by an early population of massive AGB stars (Ventura et al. 2001; Decressin et al. 2007).

2. Differences in the temperature gradient in the outflows of O-AGB and RSG stars in the Galaxy, Magellanic Clouds and Galactic globular clusters will alter the position of equilibrium in the forsterite/enstatite reaction. As the temperature of the circumstellar envelope decreases, the position of equilibrium in Eq. 4.1 will shift to favour the exothermic reaction, in this case the production of enstatite. Consequently the $MgSiO_3/Mg_2SiO_4$ ratio would increase. This reaction requires that equilibrium is reached.

3. Alternatively, non-equilibrium conditions during dust condensation may alter the order that olivines and pyroxenes form. In denser environments, the dust shells are more likely to reach equilibrium due to the increased probability of interactions with other atoms/molecules, thus for Galactic sources where the partial

pressure of dust is greatest, the circumstellar envelopes are more likely to reach equilibrium than sources at lower metallicities. Under equilibrium conditions it is predicted that forsterite will form before enstatite. If forsterite condenses first then Mg will deplete at twice the rate of Si. Conversely, if enstatite condenses first the [Mg/Si] ratio will remain constant until the Si is exhausted.

4. Furthermore, the higher partial pressure of dust-forming elements in the envelopes of Milky Way sources likely results in the growth of larger grains. The size of forsterite grains may also be an important factor in enstatite production: for large grains the surface area per unit volume decreases, reducing available reaction sites for the infusion of SiO_2 in the crystalline lattice. This curtails the amount of forsterite available for conversion to enstatite, and may result in large forsterite grains coated by a enstatite mantle.

5. Nucleation of Mg, SiO and H_2O in the conditions relative to stellar outflows could also plausibly form enstatite (Goumans & Bromley 2012). For silicates to nucleate from gas phase molecules, they must follow a series of thermodynamically-favourable reaction pathways, resulting in a small metastable silicate cluster with an enstatite stoichiometry. Once a cluster has formed these must grow under appropriate temperature conditions to become macroscopic particles (Gauger et al. 1990). The subsequent growth of this cluster is extremely exothermic; this increase in internal grain temperature may be sufficient for the partial crystallisation of the forming dust particle. Why this nucleation pathway would be favoured in the metal-poor environments of the Magellanic Clouds remains unclear.

4.5 Conclusion

The sample of O-rich AGB stars and RSG in the Galaxy and the Magellanic Clouds observed by the IRS on *Spitzer* was analysed in order to investigate how the mineralogy depends on the physical and chemical conditions of the star's envelope. The results of the survey indicate that:

- O-AGB stars have a higher proportion of sources with crystalline silicates features than RSGs, however, there is little variation in the structure of the crystalline silicate dust for O-AGB and RSG stars.

- We report the presence of a newly detected 22.8 μm emission feature in the spectra of Milky Way AGB and RSG stars.

- We detect a change in the crystalline silicate mineralogy with metallicity, with enstatite seen increasingly at low metallicity, while forsterite becomes depleted. This variation in the olivine-to-pyroxene ratio can be explained by a number of possible mechanisms.

5

Modelling the Alumina Abundance in O-AGB stars

The work presented in this chapter has been submitted to MNRAS for publication.

5.1 Introduction

Although not understood in detail, the thermodynamic condensation sequence for oxygen-rich outflows (C/O < 1) predicts that refractory oxides such as alumina (Al_2O_3) would be the first astrophysically significant species to form. These grains can exist relatively close to the star ($T_{cond} \sim 1400$ K at pressures relevant to stellar outflows) and may act as seed nuclei for other grains (e.g. Onaka et al. 1989; Stencel et al. 1990; Sogawa & Kozasa 1999). At larger radii, where the temperature is lower ($T \sim 1000$ K) silicate grains form.

It is well established that the dust in oxygen-rich outflows consists mainly of silicates (Woolf & Ney 1969; Hackwell 1972; Treffers & Cohen 1974). However, alumina dust has been detected in the spectra of some low mass-loss rate ($\dot{M}$) O-rich AGB stars in the Milky Way (Onaka et al. 1989; Speck et al. 2000; Dijkstra et al. 2005). These stars show a broad low-contrast emission feature in the $7 - 14$ μm region which is best fit with a blend of amorphous alumina and amorphous silicates. As the star evolves

along the AGB the shape and peak position of this feature changes; silicate dust becomes more important and dominates the 10-μm emission (Little-Marenin & Little 1990; Sloan & Price 1995). At high mass-loss rates the 10-μm feature is only due to silicates. This sequence has been quantified by Sloan & Price (1995, 1998) using flux ratios in the 9–12 μm region.

The *Spitzer* Space Telescope has taken spectra of a large number of individual evolved stars in the Large and Small Magellanic Clouds, covering a wide range of colours and magnitudes (Kemper et al. 2010). Although the mineralogy of the oxygen-rich AGB stars in the Magellanic Clouds is dominated by amorphous silicates both at low and high mass loss rates (Sargent et al. 2010; Riebel et al. 2012) some sources also contain a small fraction of crystalline silicates (Jones et al. 2012). There is an apparent absence of Al_2O_3 in the *Spitzer* spectra of O-AGB stars in the Magellanic Clouds (Sloan et al. 2008), with the 10-μm feature of low density (low $\dot{M}$) winds better reproduced by amorphous silicate grains than the expected mixture of Al_2O_3 and silicates. This implies that either alumina dust is depleted in the LMC or that observational biases hinder its detection. However, an extensive systematic study into the Al_2O_3 content of evolved stars in the LMC has not yet been carried out.

In this study we evaluate the alumina content of oxygen-rich AGB stars in the Magellanic Clouds, by creating a grid of radiative transfer models that explores a range of physical parameters relevant to evolved stars.

5.2   Modelling the circumstellar dust shell

To determine the relative contributions of alumina dust from the spectra of O-rich AGB stars in the LMC, radiative transfer modelling is required to calculate detailed spectra of circumstellar dust shells. In this paper we use the one-dimensional radiative transfer code   (Bouwman et al. 2000, 2001; Kemper et al. 2001) to evaluate the emergent spectrum from a central star surrounded by a spherically-symmetric dust shell.
solves the transfer equations for the basic free parameters such as stellar temperature,

chemical composition, grain size distribution, etc. under the constraint of radiative equilibrium, using a Feautrier-type method (Feautrier 1964). It also allows the user to implement multiple dust shells, each consisting of different dust components with an independent grain-size distribution function. In the following sub-sections we will describe the selection of the input parameters adopted in the modelling.

5.2.1 Model input

Photospheres

The models have been calculated using three different synthetic stellar photospheres for O-rich stars of solar-metallicity taken from Fluks et al. (1994). The spectral types of the central star used in the model grid are: M1 with an effective stellar temperature (T_{eff}) of 3715 K, M5 (T_{eff} = 3396 K) and M9 (T_{eff} = 2667 K). These were chosen to reproduce the range of values expected for O-AGB stars. As luminosity only acts as a scaling factor for the emission and does not affect the spectral shape (Ivezic & Elitzur 1997), a typical luminosity for AGB stars of 7000 $L_{\odot}$ was assumed, resulting in stellar radii ($R_{\star}$) for the central star of 202.3, 242.1 and 392.5 $R_{\odot}$ (respectively).

Dust shell geometry

The dust is assumed to be distributed in a spherical shell with an r^{-2} density distribution, giving rise to a spherically-symmetric, time-independent stellar wind with a constant outflow velocity. The lack of silicate absorption features in the spectra of O-rich AGB stars in the LMC sample and the relative weakness of the mid-IR flux compared to the flux at 1 μm (Sargent et al. 2010) indicates that these stars typically have optically-thin dust shells in the mid-IR, thus limiting the column density along the line of sight. In optically-thin dust shells the geometry of the circumstellar shell has little influence on the appearance of the spectral features, as all grains receive approximately the same amount of (near-IR) stellar photons, and absorption of scattered or emitted radiation is minimal due to the decreasing extinction efficiency of the

Table 5.1: Model Parameters

Parameter	Range of Values
Star	
Spectral type	M1, M5, M9
$L_\star$ ($L_\odot$)	7000
T_{eff} (K)	3715, 3396, 2667
$R_\star$ ($R_\odot$)	202.3, 242.1, 392.5
Dust Shell Properties	
R_{in} ($R_\star$)	2.5, 3, 5, 7.5 and 15
$R_{\text{out}}/R_{\text{in}}$	200
v_{exp} (kms^{-1})	10
Dust-to-gas ratio (Ψ)	1/200
Density profile	$\rho(r) \sim r^{-2}$
$\dot{M}$ ($M_\odot$ yr^{-1})	10^{-10}–10^{-5}
Dust Grain Properties	
Size distribution	MRN
Grain shape	CDE
a_{min} (μm)	0.01
a_{max} (μm)	1.00
q	3.5
Dust Species	**Reference**
Amorphous Mg_2SiO_4	Dorschner et al. (1995)
Amorphous Al_2O_3	Begemann et al. (1997);
	Koike et al. (1995)
Fe	Ordal et al. (1988)

oxygen-rich dust at longer wavelengths. However, the density profile of the dust shell determines the dust mass distribution over temperature, thus affecting the continuum emission levels and feature strengths. For optically-thick dust shells the geometry of the circumstellar dust would significantly influence the shape of the spectral features and would require a more complex treatment of the density distribution.

The inner radius of the dust shell (R_{in}) is determined assuming that the dust temperature at this radius is equal to the condensation temperature of the dust species, and that

$$T_d(r) = T_\star \left(\frac{R_\star}{2r} \right)^{2/(4+s)}, \tag{5.1}$$

with $s \approx 1$ (Olofsson 2004). For amorphous silicates the condensation temperature is $T_{cond} \sim 1000$ K (Gail & Sedlmayr 1999), however alumina is expected to condense at higher temperatures $T_{cond} \sim 1400$ K. To be consistent with other modelling efforts (e.g. Heras & Hony 2005; Groenewegen 2006; Sargent et al. 2011; Srinivasan et al. 2011) we do not include multiple dust shells with separate dust components, each with its own temperature distribution. Instead, to account for this range in condensation temperature, and for dynamical effects such as pulsations, R_{in} is varied for a best fit. We calculate models for $R_{in} = 2.5, 3, 5, 7.5$ and 15 $R_\star$. These are similar to the range of R_{in} values explored by the O-rich models (Sargent et al. 2011), based on estimates for the condensation radius by Höfner (2007).

In some instances a given set of model parameters may result in dust temperatures at the inner regions of the shell that are in excess of the condensation temperature. We deem these models to be unphysical and eliminate them from our grid.

The outer radius (R_{out}) determines the duration of the mass loss and hence the total shell mass, and increases the amount of cold dust. In order to accurately determine the thickness of the shell, far-IR data is required. The dust temperatures at the outermost regions of the wind only contribute slightly to the mid-IR flux and hence cannot be constrained by our models. For instance, for the M9III model with $R_{in} = 7.5$ and a total mass-loss rate of 1×10^{-6} M$_\odot$ yr^{-1}, the 24-μm flux was only ~ 4.8 per cent higher

for $R_{\rm out} = 1000\,R_{\rm in}$ as compared to $R_{\rm out} = 200\,R_{\rm in}$. Thus we used a fixed value of $R_{\rm out} = 200\,R_{\rm in}$ as a lower limit for the shell thickness, as this is computationally less expensive.

The outflow dynamics, and in particular the density and velocity of the wind, play an important role in the emergent spectra. Typical wind velocities derived from observations of Galactic AGB stars range from 10 to 20 kms^{-1} (Vassiliadis & Wood 1993; Bloecker 1995; Habing & Olofsson 2003). In the lower-metallicity environments of the LMC and SMC it is expected that the wind speed in O-AGB stars is smaller compared to their Galactic counterparts (Marshall et al. 2004). We adopt a constant outflow velocity for the dust of $v_{\rm exp} = 10$ kms^{-1} for all the Magellanic Cloud object (Wood et al. 1992; van Loon et al. 2001). For the assumptions adopted in the present paper, the mass-loss rate is linearly related to the actual individual expansion velocity via $\dot{M} \propto v_{\rm exp}/(10\,{\rm km\,s^{-1}})$.

Total mass-loss rates are varied from 10^{-10} to 10^{-5} M$_\odot$ yr^{-1} and the dust-to-gas ratio is taken to be $\Psi = 0.005$ which is typically used for O-AGB stars in the LMC (Groenewegen 2006; Sargent et al. 2011; Srinivasan et al. 2011). This enables us to encompass a large range of spectral morphologies, from 'naked' (dust-free) stars to the 'extreme' evolved stars with very large infrared excesses. However, caution must be taken when comparing models with low dust-production rates ($\dot{D}$) to observations, as it is very difficult to differentiate stellar photospheres from sources with very low-contrast dust features below $\dot{D} \approx 10^{-11}$ M$_\odot$ yr^{-1} (Riebel et al. 2012), since the dust-emission contrast is proportional to the dust-production rate.

For all our models a distance of 49.97 kpc to the LMC is assumed (Pietrzyński et al. 2013).

Dust grain properties

The circumstellar envelopes of O-AGB stars are mineralogically complex. For stars with low mass-loss rates ($\dot{M} < 10^{-7}$M$_\odot$ yr^{-1}) simple metal oxides are the most abundant species (Cami 2002; Posch et al. 2002); at greater mass-loss rates silicates (in
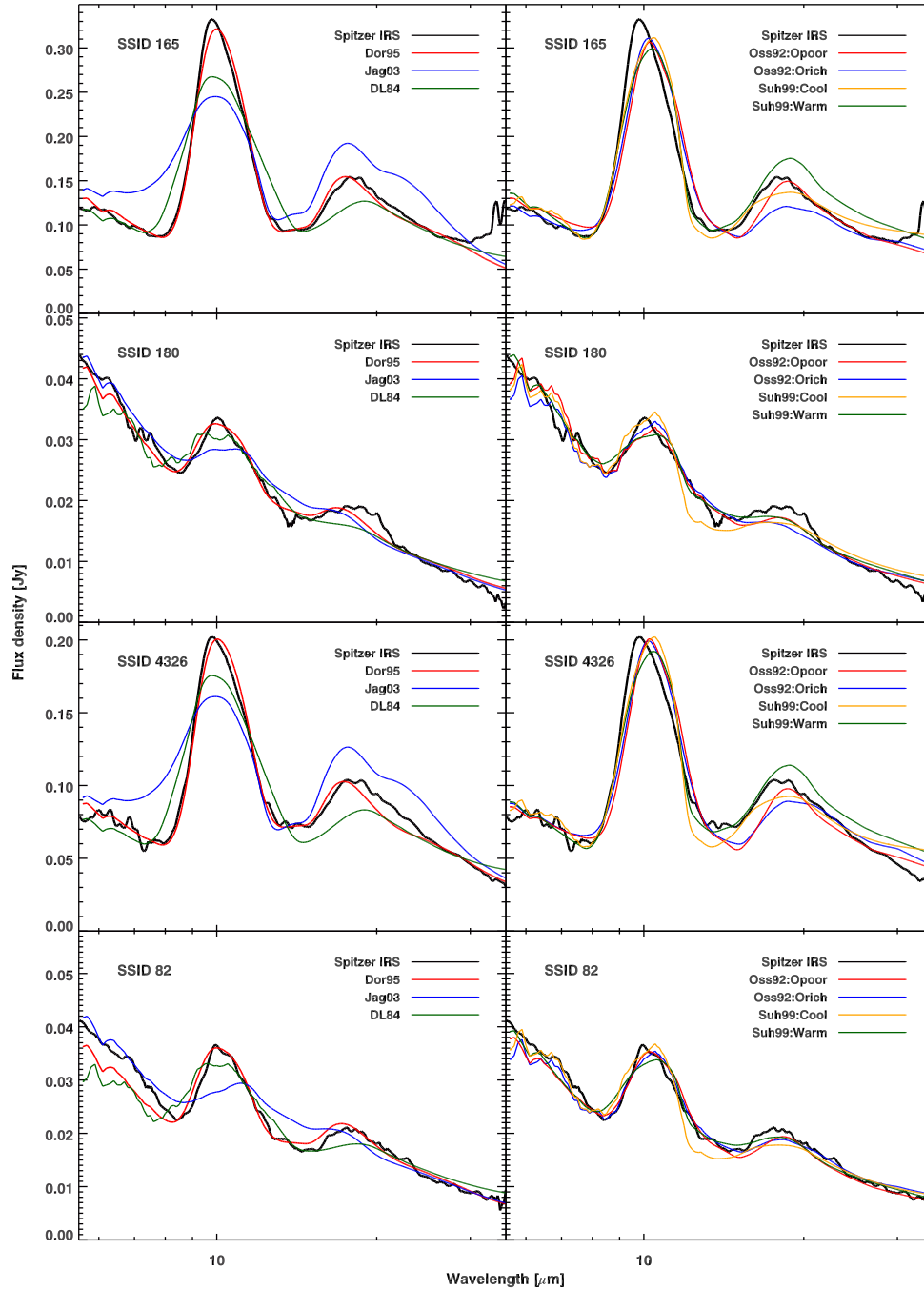
Figure 5.1: Comparison of astronomical and laboratory silicates to *Spitzer* IRS observations of O-rich AGB stars in the LMC. The optical constants derived by Dorschner et al. 1995 provide the best overall fit to the spectra.

both amorphous and crystalline form) become the dominant dust component. Metallic iron grains are thought to also contribute to the infrared emission around oxygen-rich AGB stars (Kemper et al. 2002; Verhoelst et al. 2009; McDonald et al. 2010), and iron may be incorporated in other dust grains, for example in amorphous silicates (Gail & Sedlmayr 1999).

The chemical composition of amorphous silicate grains is not well known, and previous studies of oxygen-rich AGB stars have considered a wide range of dust compositions with varying success. In Figure 5.1 we compare five sets of 'astronomical silicates' and two dust compositions obtained from laboratory measurements to *Spitzer* IRS observations of O-rich AGB stars in the LMC. The astronomical silicates we consider are the oxygen-deficient (Opoor) and oxygen-rich (Orich) silicates from Ossenkopf et al. (1992), the 'warm' and 'cool' silicates from Suh (1999), and the (Draine & Lee 1984, hereafter DL84) astronomical silicates derived from ISM lines-of-sight. For the laboratory measured dust species we consider the amorphous olivine refractory indices from Jäger et al. (2003) and Dorschner et al. (1995).

We find that the pure amorphous olivine from Dorschner et al. (1995) best reproduce the position and relative strengths of the $10\,\mu$m and $20\,\mu$m features in the infrared spectrum of O-rich AGB stars in the LMC. We assume that the stoichiometric composition of the amorphous silicate dust grains is not dependent on the mass-loss rate of the AGB star.

To increase the opacity in the near-IR region, we also include metallic iron, using laboratory data from Ordal et al. (1988). We adopt a metallic iron abundance of 4 per cent by mass with respect to the amorphous silicates, following Kemper et al. (2002); de Vries et al. (2010).

For the refractive indices of amorphous alumina dust, we use the optical constants for porous alumina grains measured by Begemann et al. (1997), which are extended to shorter wavelengths ($\lambda < 7.8\,\mu$m) by concatenation with optical constants from Koike et al. (1995).

For all dust species modelled we adopt a standard Mathis-Rumpl-Nordsieck (MRN)
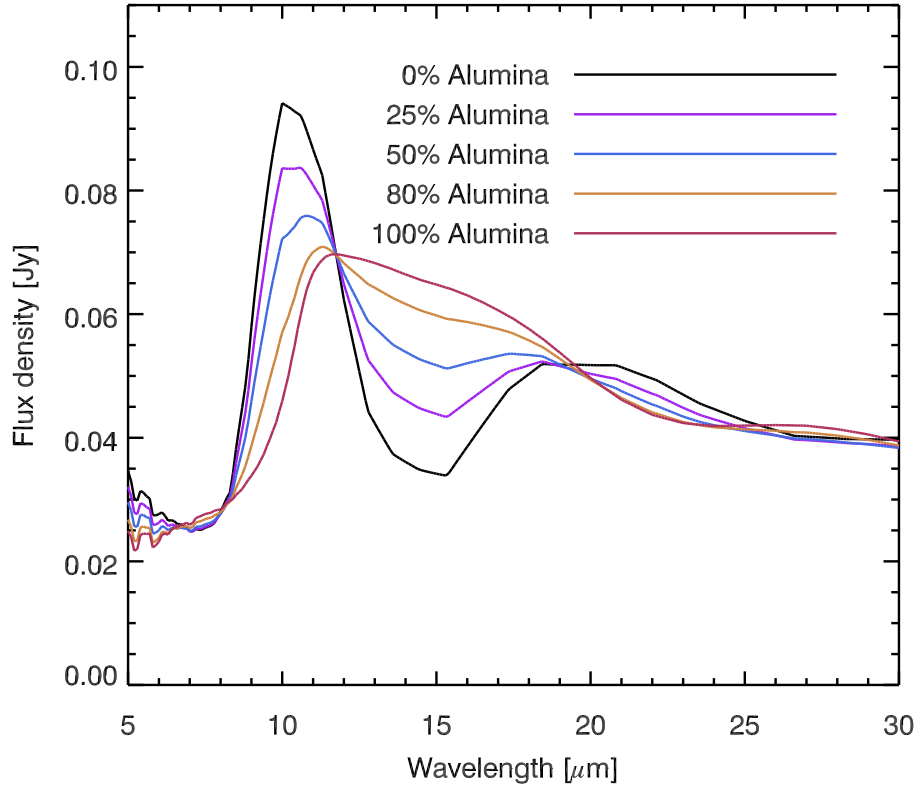
Figure 5.2: Five spectra with different alumina abundances are shown, for $\dot{M} = 7.5 \times 10^{-7}$ M$_\odot$ yr^{-1}. All other model parameters are constant.

grain size distribution (Mathis et al. 1977), given by $N(a) \propto a^{-q}$, with q= 3.5, for a grain size range of $a = 0.01 - 1\mu$m. To calculate the absorption and scattering coefficients of the dust grains from the complex refractive indices measured in the lab, an assumption about the grain shape distribution needs to be made; we adopt a continuous distribution of ellipsoids (CDE) for the particle shape (Bohren & Huffman 1983). This is preferred over homogeneous spherical grains as regularly-shaped particles introduce resonance effects resulting in unrealistic feature shapes (Min et al. 2003).

The alumina abundance was varied in increments of 5 per cent for 0–40 per cent, and increased in steps of 10 per cent for 40–100 per cent. Spectra with different alumina abundances are shown in Figure 5.2; there is a clear change in the shape and

strength of the 10- μm feature as the alumina abundance is increased.

5.3 Model results

From our models we compute expected flux densities for the broad-band filters of 2MASS, *Spitzer*, *WISE* and *AKARI* by convolving the   spectral output with the relative spectral response curves[1]. The calculated fluxes are further converted into Vega magnitudes, which can be directly compared to catalogue values.

5.3.1 Colour–colour diagrams

In this section we show examples of the colour–colour space occupied by our grid of models and compare our synthesised photometry to observations of evolved stars. Since our models are created for dusty O-rich AGB stars we focus on mid-IR colours, where molecular and dust spectral features cause distinct photometric signatures and the central star's effective stellar temperature has little influence on the flux.

Mid-IR colour–colour diagrams (CCD) for the model grid are presented in Figures 5.3–5.5. For comparison, we also include LMC point sources from the SAGE-Spec survey, which were identified as O-rich AGB stars and RSGs using *Spitzer* IRS spectra and ancillary photometry (Kemper et al. 2010; Woods et al. 2011; Jones et al. 2012). These were cross-identified with the *AKARI* LMC point source catalogue (Ita et al. 2008; Kato et al. 2012) and the *WISE* all-sky catalogue (Wright et al. 2010).

In general, our models are consistent with the range of observed colours for oxygen-rich stars in the colour-colour diagrams considered here, especially when the contribu-

---

[1]Filtercurves were obtained from the official websites:

http://www.ipac.caltech.edu/2mass/releases/allsky/doc/sec6_4a.html;

http://ssc.spitzer.caltech.edu/irac/spectral_response.html;

http://ssc.spitzer.caltech.edu/mips/spectral_response.html;

http://www.astro.ucla.edu/~wright/WISE/passbands.html

and http://www.ir.isas.jaxa.jp/ASTRO-F/Observation/RSRF/IRC_FAD/index.html
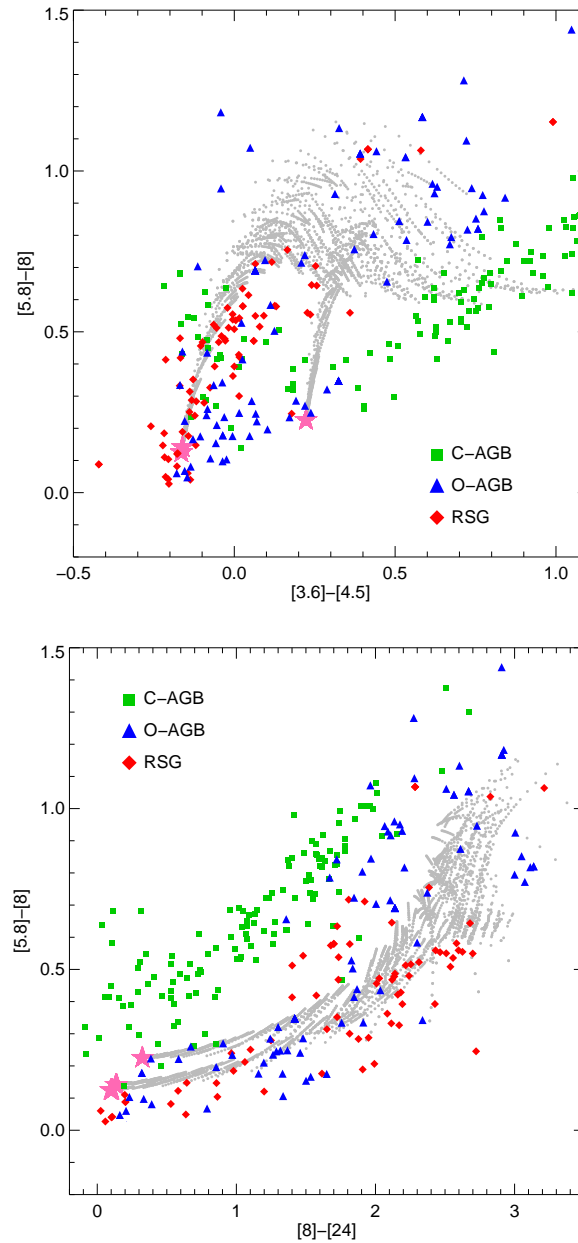
Figure 5.3: *Spitzer* IRAC/MIPS colour-colour diagrams for two combinations of colours. Small, grey dots denote the models from our O-rich grid. Also shown are the Fluks et al. (1994) photospheres (pink stars) used to generate the grid. To illustrate the model grid coverage, the evolved sources in the SAGE-Spec sample are overlaid: O-rich AGB stars are represented by blue triangles, RSGs by red diamonds and C-rich AGB stars by green squares.
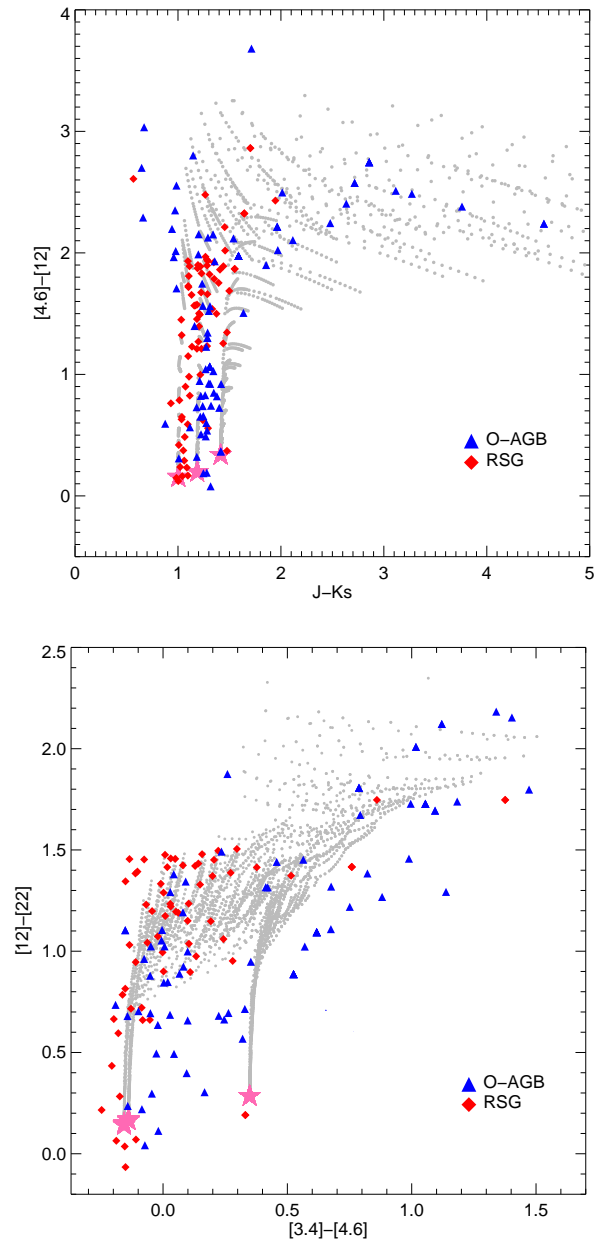
Figure 5.4: 2MASS–*WISE* J-K$_s$ vs. [4.6] − [12] colour-colour diagram (top) and *WISE* [12] − [22] vs. [3.4] − [4.6] colour-colour diagram (bottom) of the known O-AGB and RSG stars in the SAGE-Spec sample. Symbols are as in Figure 5.3.
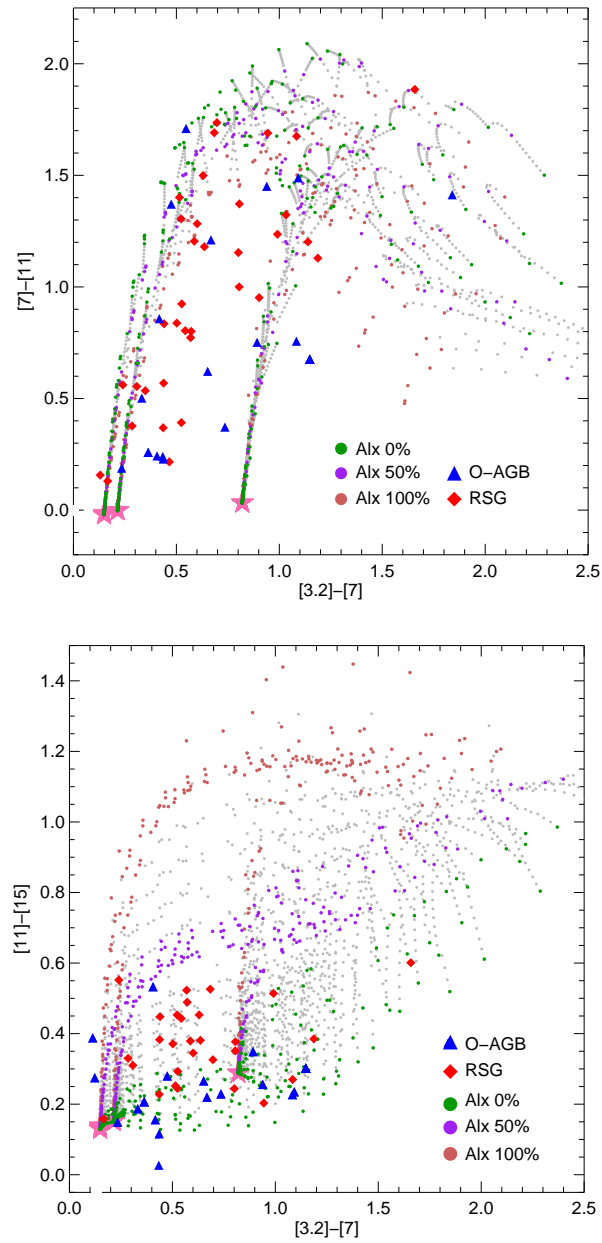
Figure 5.5: *AKARI* colour-colour diagrams for two combinations of colours. Models with pure amorphous silicates (green), pure alumina (brown) and an equal blend between alumina and silicates (purple) are highlighted. All other symbols are as in Figure 5.3.
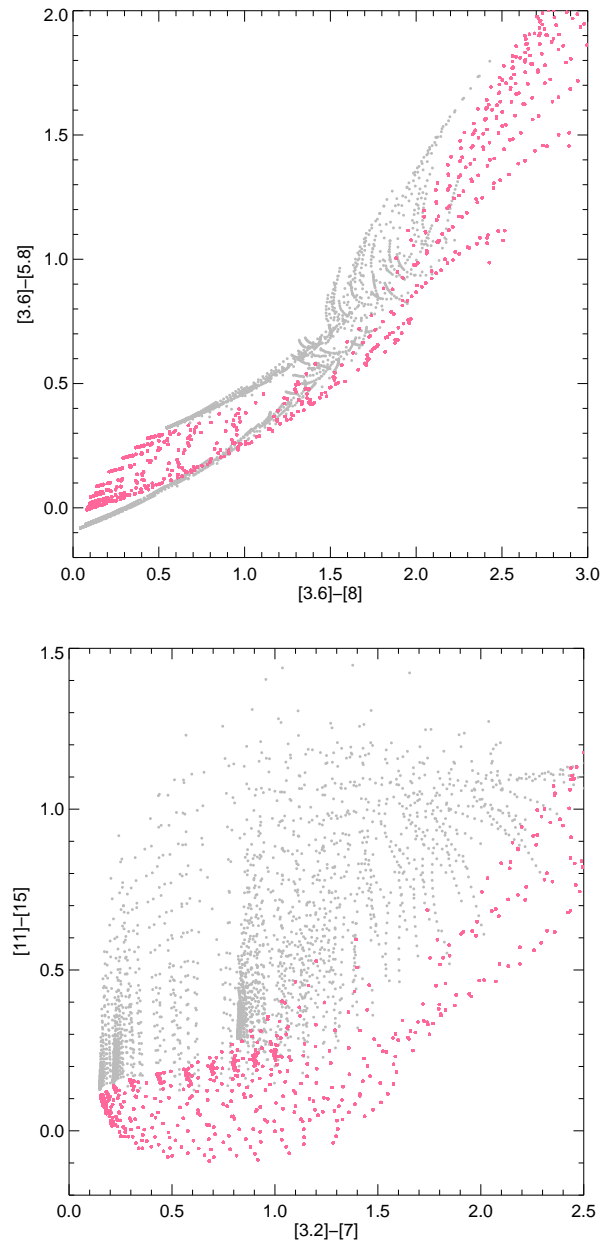
Figure 5.6: Comparison of the coverage of the model grid described in this work with the oxygen-rich   models (pink points).

tions from circumstellar dust becomes significant in describing the observed photometry. However, the resolution of the grid before dust production begins is limited to narrow columns in colour-colour space (Figure 5.4), corresponding to sets of models with low optical depths derived from the three input stellar photospheres. The sparse grid coverage for the dust-free sources reflects the compromise between the accuracy of the model fit and the required computational time, with emphasis placed on the fine sampling of model AGB stars with apparent dust excesses.

The IRAC [5.8]−[8.0] versus [3.6]−[4.5] colour-colour diagram, shown in the top panel of Figure 5.3, traces the photospheric temperature of the central star and continuum emission from the circumstellar dust shell. At these wavelengths O-rich dust has no distinguishable signatures, unless it contains a significant fraction of iron or has a strong 10-μm silicate feature, both of which affect the 8-μm flux. The IRAC colours are insufficient to distinguish between carbon-rich AGB stars, oxygen-rich AGB stars and RSGs, as such there is a significant overlap between the carbon-rich dust sources and our oxygen-rich models. The largest discrepancy between our model grid and observations is for sources that lie in the largely-dustless region below [5.8]−[8.0] < 0.6 mag. These sources have little circumstellar excess, and may be better represented by photospheres with a larger range of stellar effective temperatures, metallicity and surface gravity. With the onset of mass-loss, the dust emission increases and the model colours provide better coverage of the observed data.

Moving to longer wavelengths, the [5.8]−[8] versus [8]−[24] CCD (Figure 5.3; bottom panel) is an effective tracer of stars with significant amounts of circumstellar dust. It is often used to distinguish oxygen-rich from carbon-rich stars as there is little overlap between the populations (Kastner et al. 2008; Boyer et al. 2012). Our models on the whole show a considerable overlap with the colours of the O-rich AGB stars from SAGE-Spec sample but are well seperated from the region occupied by the C-rich AGB stars.

The top panel in Figure 5.4 shows a colour-colour diagram incorporating both near- and mid-IR data. This essentially compares the model photospheres via the J−K$_s$

colour to the dust excess, traced by the *WISE* [4.6]−[12] colour. In the diagram the different stellar types are reasonably well separated (due to differences between the stars effective temperature), until the stars become heavily dust-enshrouded at [4.6]−[12] > 1.6. The observed RSGs, with bluer (J−K$_s$) colours, are generally traced by models with an M1 photosphere, while the O-AGB stars that have slightly redder J−K$_s$ colours are represented by the cooler M5 and M9 photospheres. The models reproduce the range of observed colours quite well, except for sources which lie off to the left of the model grid. This discrepancy is most likely due to an enhanced scattering by dust in an asymmetric shell or due to pulsations which can significantly effect the near-IR flux of AGB stars (Whitelock et al. 2003).

The *WISE* [12]−[22] versus [3.4]−[4.6] CCD shown in the bottom panel of Figure 5.4 has a similar model coverage to the *Spitzer* [5.8]−[8.0] versus [3.6]−[4.5] CCD. The *WISE* [3.4]−[4.6] colour is comparable to the *Spitzer* IRAC [3.6]−[4.5] colour and is a good indicator of the emission from the warmest regions of the dust shell, while the 12- and 22-μm filters measure the emission from the silicate features at 10 and 20 μm and thus this colour is a good tracer of oxygen-rich dust. As before a number of the O-rich AGB and RSG stars which contain little or no dust around them are not covered by the model grid. Additionally, some sources with [3.4]−[4.6] > 0.5 mag and [12]−[22] < 1.5 mag fall outside the region covered by our model grid; these sources may be better represented by models with a higher percentage of metallic iron grains in the circumstellar shell, which would increase the [3.4]−[4.6] colour.

Figure 5.5 shows two-colour diagrams using *AKARI* colours of [7]−[11] versus [3.2]−[7] and [11]−[15] versus [3.2]−[7]. The models with pure amorphous silicates, pure alumina and an equal blend between alumina and silicates are highlighted. While there is considerable degeneracy in the [7]−[11] colour, which measures the 10-μm feature irrespective of the Al$_2$O$_3$ content, the [11]−[15] colour provides a measurement of the change in strength/shape of the 10-μm dust feature. This diagram separates the different dust types well, in sources with a reasonable dust excess. It can therefore be used as a diagnostic to derive the fractional abundance of alumina (Alx). The sources

in the SAGE-Spec sample occupy a region in colour-colour space corresponding to an alumina fraction of less than 50 per cent (we return to this in Section 5.4).

Comparison to the   model grid

In a recent similar study, Sargent et al. (2010) and Srinivasan et al. (2011) developed the Grid of RSG and AGB ModelS (   ) to reproduce the range of observed infrared colours of LMC red supergiant (RSG) and AGB stars, and to measure their luminosities and dust production rates. The   grid consists of models for oxygen-rich as well as carbonaceous chemistries; the O-rich models (Sargent et al. 2010) consist of oxygen-deficient silicate grains from Ossenkopf et al. (1992), while the carbon-star dust (Srinivasan et al. 2011) is composed of a mixture of amorphous carbon and silicon carbide, the latter making up 10 percent of the mass. The authors used the **2D**ust code (Ueta & Meixner 2003) to solve the radiative transfer problem for a dust shell of given inner and outer radius and optical depth around a central star that was represented by a model photosphere. They chose the range of input parameters (inner radii, optical depths) to cover the expected and observed values for LMC evolved stars.

We compare our model output to the O-rich   models in Figure 5.6. Overall, there is good agreement between the sets of models, particularly in the IRAC bands at shorter wavelengths ($\lambda < 8\mu$m). In the near-IR the   grid agrees better with the bluer stellar sequences where stellar temperature has a greater influence on the colour, however, in the mid-IR our models span a wider range of colour space due in part to the inclusion of alumina and the choice of optical constants for the amorphous silicates. It should also be noted that two models that overlap in colour-colour space may not necessarily have the exactly the same input parameters.

5.3.2 SE index

The silicate emission (SE) index is a spectral classification system developed by Sloan & Price (1995, 1998) to measure the variation in the shape/strength of the emission

feature at about 8–12 μm in oxygen-rich AGB stars. The observed spectra are divided into eight categories (SE 1–8) based on the ratios of narrow-band fluxes at 10, 11 and 12 μm (F10, F11 and F12). These classes are designed to reflect the progression from the broad oxygen-rich dust emission features with little structure (SE 1–3) to the classic narrow 9.7-μm silicate features (SE 7–8).

The change in spectral features represents the dust formation process along the AGB, which depends strongly on $\dot{M}$ (Dijkstra et al. 2005). We would therefore expect the SE index to reflect the mass-loss rate, the chemical composition of the dust grains (i.e. the relative abundances of silicates and amorphous alumina), and variations in the temperature of the dust shell (Ivezic & Elitzur 1995; Hron et al. 1997; Egan et al. 2001).

To investigate the parameter space covered by each SE class we apply the spectral classification procedure of Sloan et al. (2003a) to each optically thin model in our grid. To isolate the dust emission we subtract the appropriate stellar photosphere used in constructing the model. Each model's dust excess was quantified via the dust emission contrast (DEC), defined as the ratio of dust emission to stellar emission between 7.67 and 14.03 μm (Sloan et al. 2008). In keeping with observations, and to prevent any over-interpretation of models with no significant dust excess, we do not ascribe an SE class to models with DEC ≤ 0.10. This corresponds to all models with a mass-loss rate below $\dot{M} \sim 3 \times 10^{-9}$ M$_\odot$ yr^{-1}.
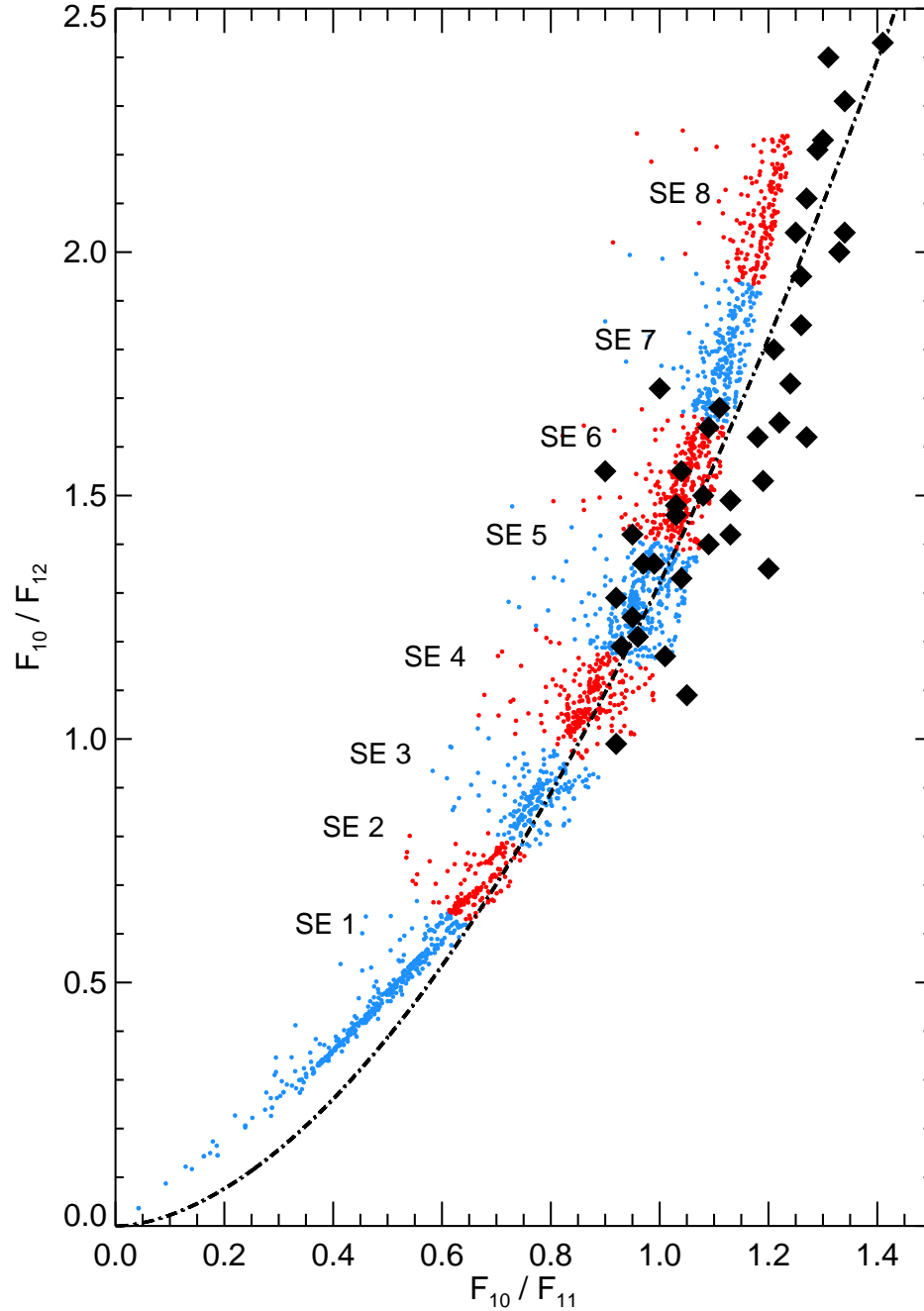
Figure 5.7: The silicate dust sequence power law: $F_{10}/F_{12} = 1.32(F_{10}/F_{11})^{1.77}$ (dotted black line; from Sloan & Price 1995), and the flux ratios for the individual models. For comparison the filled black diamonds show the flux ratios of LMC O-AGB sources.
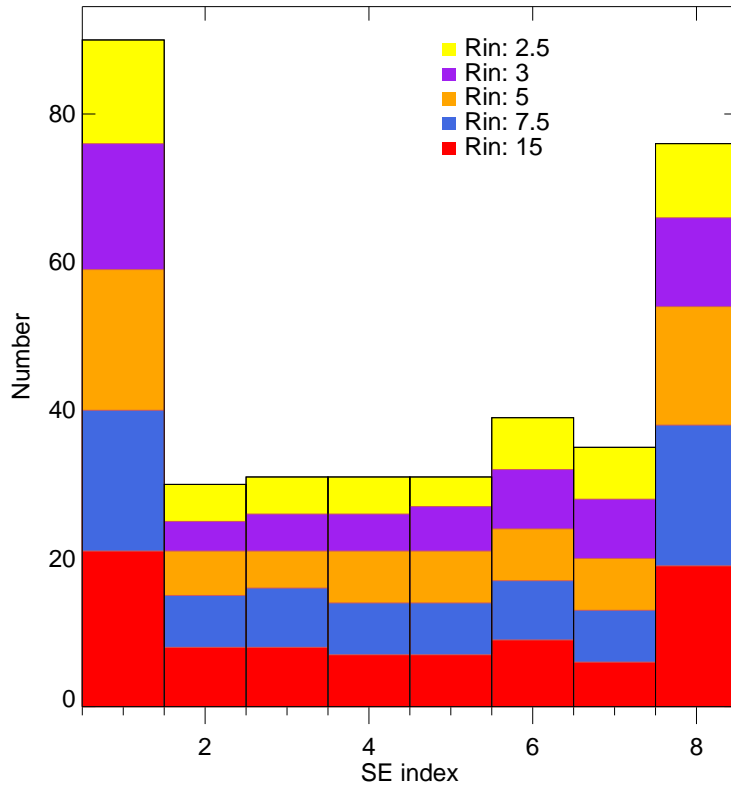
Figure 5.8: Distribution of the model grid silicate emission index. Each colour represents a dust shell inner radius explored by the grid for models with an M9 stellar photosphere. The even distribution between R_{in} models suggests that the SE index is independent of the dust temperature.
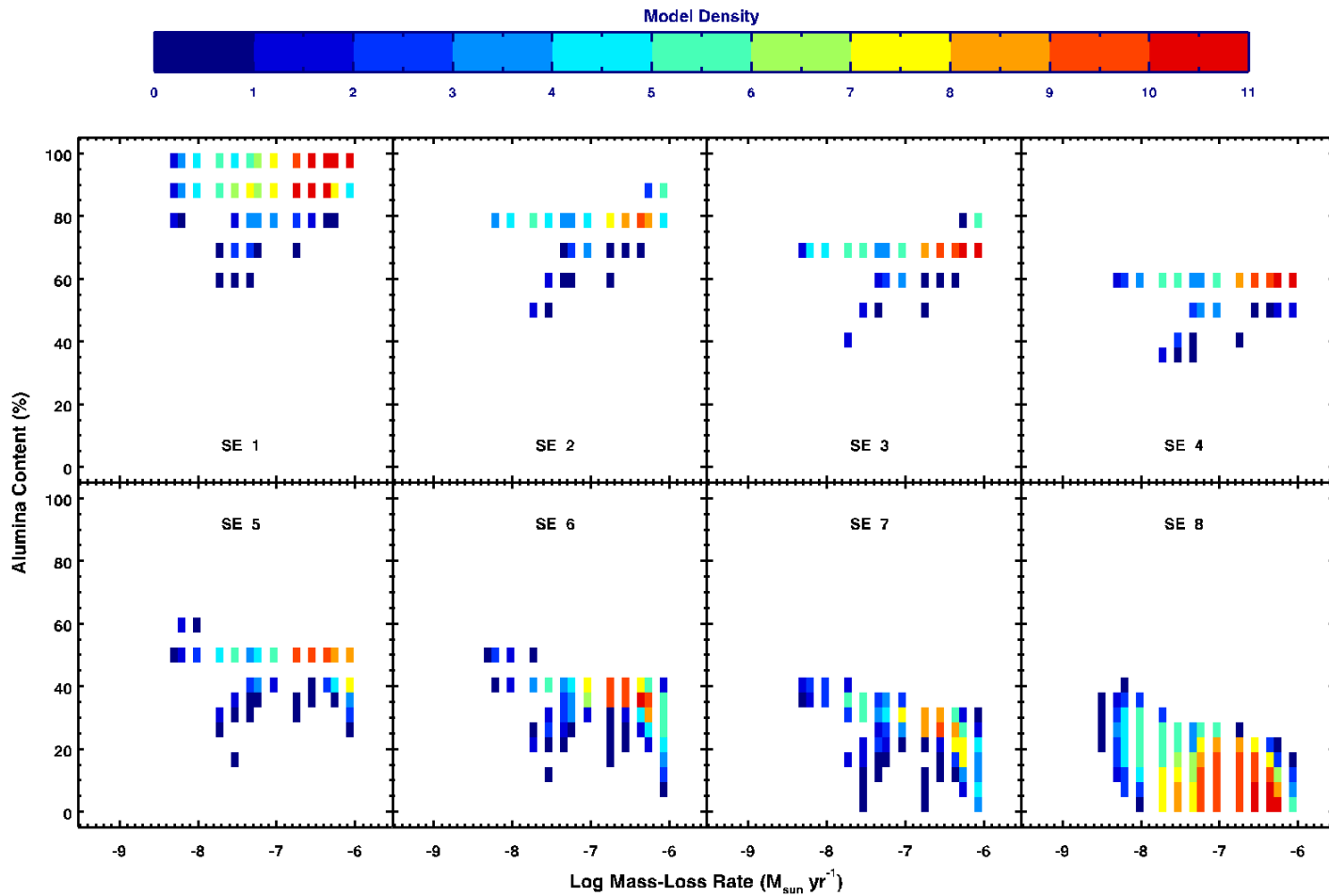
Figure 5.9: The relationship between the alumina content and total mass-loss rate for the models in our grid with a dust excess, separated according to the silicate emission index.

Figure 5.7 shows the F10/F12 versus F10/F11 model flux ratios and the empirically derived silicate dust sequence power law: $F_{10}/F_{12} = 1.32(F_{10}/F_{11})^{1.77}$ (Sloan & Price 1995), which forms the basis for the SE index classification. Our models reproduce each of the eight SE indices along the silicate dust sequence; SE classes one and eight contain the largest numbers of models, with the remainder equally distributed across SE indices 2–7. This due to sources falling outside the SE1–8 range being classified as either SE1 or SE8.

The slight deviation from the silicate dust sequence power law at SE8 maybe a consequence of the grain size distribution used in the modelling. Observationally, sources in the Milky Way tend to occupy a region to the right of the silicate dust sequence for SE8, while stars from low-metallicity Galactic globular clusters populate a region to the left of the sequence (Sloan et al. 2008, 2010). At the other end of the SE sequence, we suspect the curvature arises due to the models in our grid with high mass-loss rates combined with a high fractional abundance of alumina (Alx).

The distribution of SE classes for our model grid is shown in Figure 5.8. Segregating the models according to the inner radius of the dust shell has no significant effect upon the SE index distribution, which suggests that the SE index is independent of the dust temperature. This is not surprising as the SE index is calculated using flux ratios across the 10 μm feature of a given temperature, effectively eliminating the grain temperature parameter. Since we have isolated the dust emission, the SE index is also independent of the spectral type and the effective temperature of the central star.

Figure 5.9 illustrates the range in mass-loss rate and alumina abundance covered by each SE class. Increasing the density of the shell leads to models moving upward and to the right along the SE sequence, however, changes in position are generally to small to move a model to a higher SE class. For models dominated by either pure alumina or silicates, the shell density may have a greater influence as it determines when the emission from the dust shell becomes significant compared to that of the stellar photosphere.

The composition of the dust has a more substantial effect on the SE index than
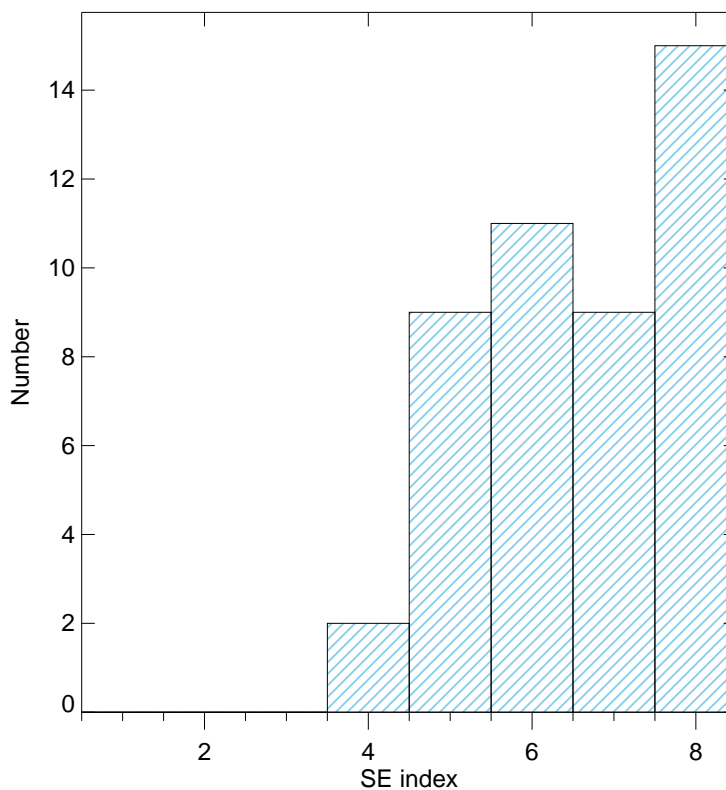
Figure 5.10: Distribution of the O-rich AGB stars in the LMC with silicate emission index.

the mass-loss rate. For a given mass-loss rate, a blend of alumina and silicates can reproduce the full silicate dust sequence. SE classes 1–3 are successfully reproduced by shells dominated by alumina dust (Alx $\gtrsim$ 70 per cent), while classes SE 6–8 are populated by models dominated by amorphous silicates (Alx $\lesssim$ 50 per cent).

The distribution of the O-rich AGB stars in the LMC with silicate emission index is shown in Figure 5.10. This suggests that the dust in the LMC is primarily silicate-rich, whilst alumina is largely absent, in agreement with the alumina dust abundances derived from *AKARI* photometric colours in Figure 5.5. However, our spectroscopic sample only includes relatively bright AGB stars in the LMC, which have sufficient signal-to-noise in their IRS spectra to quantify the dust excess. Thus, the lack of sources with a low SE index could be due to an observational bias.

5.4 Measuring the alumina fraction

To estimate the alumina content of AGB stars in the LMC, we apply our model grid to the sample of 54 O-rich AGB stars described by (Jones et al. 2012, Chapter 3) taken from the *Spitzer* SAGE-Spec sample of Kemper et al. (2010) and the archival IRS spectra in the LMC. As alumina has not been observed in optically-thick AGB envelopes, we excluded the sources where the 10-μm feature is in self absorption from our analysis. Also excluded are sources that essentially appear as stellar photospheres with no significant infrared excess due to dust emission, but have been classified as AGB stars due to molecular absorption features and photometric variability. From this we are left with 37 sources.

To model the AGB stars we have scaled the IRS spectrum to match the IRAC 5.8- and MIPS 24-μm fluxes to enable an accurate comparison to photometry. For each star we fitted the models to the observed broadband *JHK*$_\mathrm{s}$, IRAC and MIPS 24-μm photometric data and the flux measured over set wavelength intervals (line segments) from the spectra. This allows us to achieve a good fit to both the SED and the observed spectrum. The line segments have continuous wavelength coverage over the full *Spitzer* spectral range and each of the nine bands cover equal widths in logarithmic wavelength. An additional six narrow bands (0.38 μm wide) over the 8–13 μm interval provide detailed measurements of the 10-μm feature. An example of the regions used to measure the spectral flux is shown in Figure 5.11. These 15 bands measure the spectral flux and place a strong constraint on the individual dust species present in the IR-spectrum. This is essential, as fits based only on the photometric data points poorly constrain the relative strengths of the dust features.

Comparisons between the models and the data were made with an automated fitting routine and the best fit was selected based on a chi-square (χ^2) minimisation technique. The quality of the best-fit model was defined by:

$$\chi^2 = \frac{1}{N} \sum_i \frac{(f_{\mathrm{obs}_i} - f_{m_i})^2}{\sigma_i^2},$$

(5.2)

where f_{obs_i} and f_{m_i} are the observed and model flux in the ith band with error bar σ_i
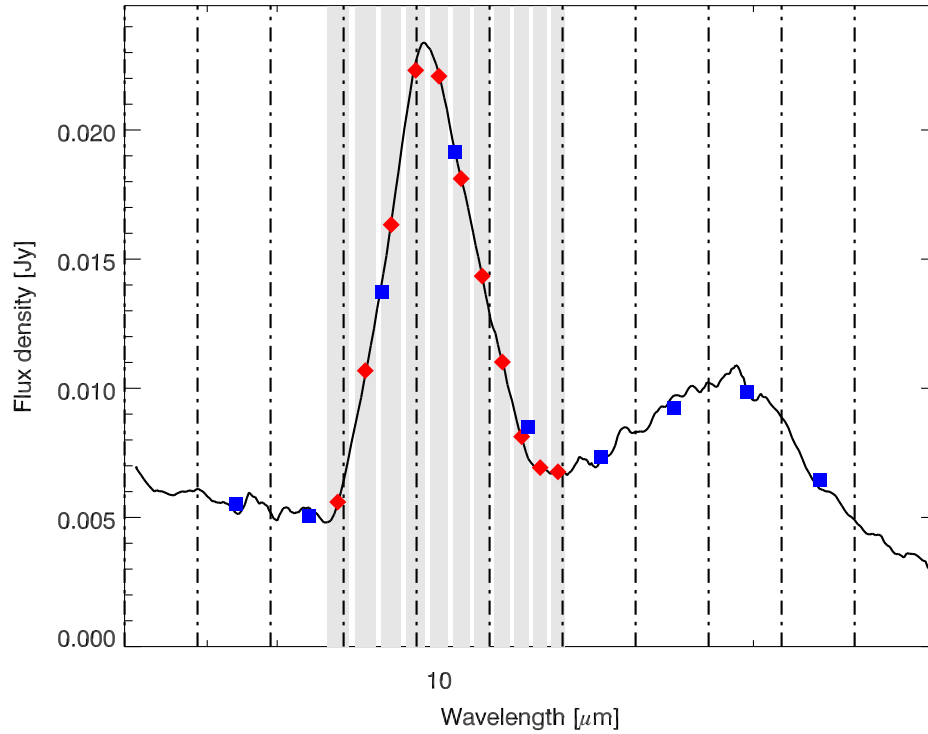
Figure 5.11: Example of the method used to measure the spectral flux from the spectrum of SSID 96 using line segments. The shaded regions show the wavelength ranges over which we determine the narrow-band flux and the vertical dashed lines show the wavelength ranges used to measure the broad-band flux.

and N is the total number of data points being fitted. Uncertainties in the photometric data were modified to account for variability across a pulsation cycle (see Riebel et al. 2012; Jones et al. 2012), and uncertainties in the spectroscopic data were inflated by a factor of five (see Groenewegen et al. 2009).

Our models are computed for a single luminosity, therefore they must be scaled to match the luminosity of the source in question before performing the χ^2 fitting. The luminosity (L) of the source can be computed from this scaling factor (η) via $\eta = (L/7000 \, L_\odot)(d/49.97 \, \text{kpc})^2$, where the distance ($d$) is assumed to be 49.97 kpc for the LMC. As the luminosity is scaled, so too must the wind parameters be scaled

appropriately. Following equation (2) of Groenewegen (2006), the stellar radius and the mass-loss rate must scale by the factor $\sqrt{\eta}$. The other model parameters and outputs are independent of this scaling.

Several models may provide a good fit to a source (defined arbitrarily by $\chi^2 - \chi^2_{min} <$ 3). To gauge the range a parameter could vary for a given source, we calculate its median absolute deviation; this is more resilient to outliers than the standard deviation and thus provides a more robust estimator of the uncertainty. The SEDs and spectra for all the O-AGB stars in our sample (identified by the SAGE-Spec designation; SSID) along with best-fitting model for each source are shown in Figure 5.12. The modelling results are summarised in Table 5.2.

All the O-AGB stars in our sample exhibit significant dust emission. Although the 10-μm feature is apparent in each spectrum, it exhibits a considerable variation in shape and there is a broad variety in the other spectral features between individual stars. At this stage, it is worth remembering that the model grid is intended to provide an initial estimate to the fitting parameters and that each best model fit can be optimised by fine-tuning the model values on an individual basis.

In general the fitting of the models to the spectra plus the spectral energy distribution (SED) is of a high quality for an automated routine (c.f. Sargent et al. 2011; Riebel et al. 2012) and the model grid is very successful at reproducing the observed shape of the 10-μm feature.

At longer wavelengths ($\lambda > 16\ \mu$m) the models are less successful in reproducing the broad emission feature at 18 μm and the slope of the continuum in the observed spectra. This discrepancy is due in part to the choice of optical constants; in laboratory silicates the 18-μm emission feature peaks at too short a wavelength compared to observations and its strength is often too strong with respect to the observed 10-μm feature. Conversely, astronomical silicates provide a better fit to the 20-μm region, however, the shape is broader than observed and they over-predict the flux in the 10-μm region and cannot reproduce its shape and position. More complicated situations are not considered in the model such as: different spatial density distributions of the
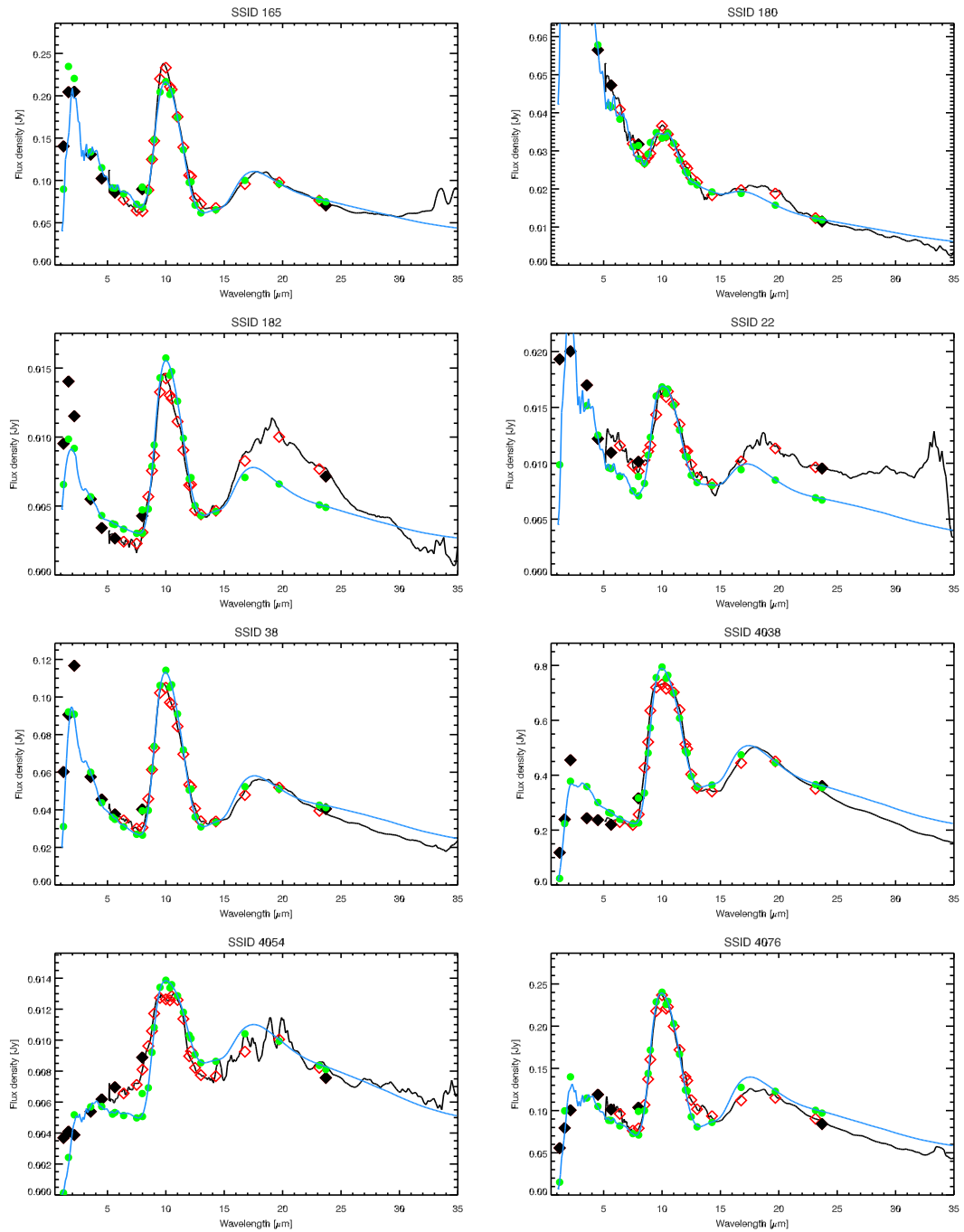
Figure 5.12: The observed *Spitzer* spectra of O-rich AGB stars (black) and the corresponding best-fit model (blue). The photometric points are shown as black diamonds, the flux from the spectral segments as red diamonds and the synthetic flux from the models are green circles. The least-square fit is performed by matching the green model points to the red/black data points.

Figure 5.12: — Continued.

Figure 5.12: — Continued.

Figure 5.12: — Continued.

EVOLVED STARS IN THE LOCAL GROUP
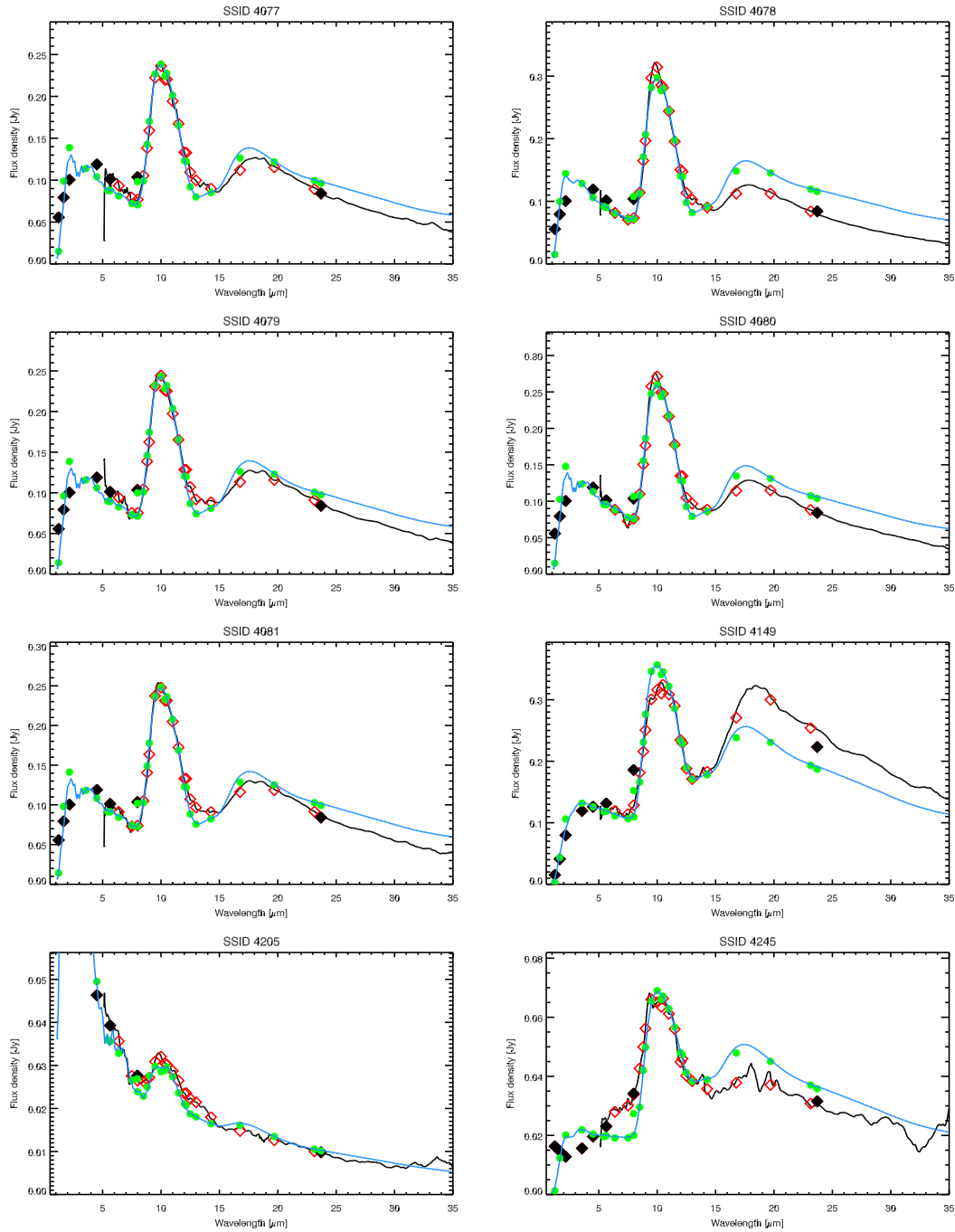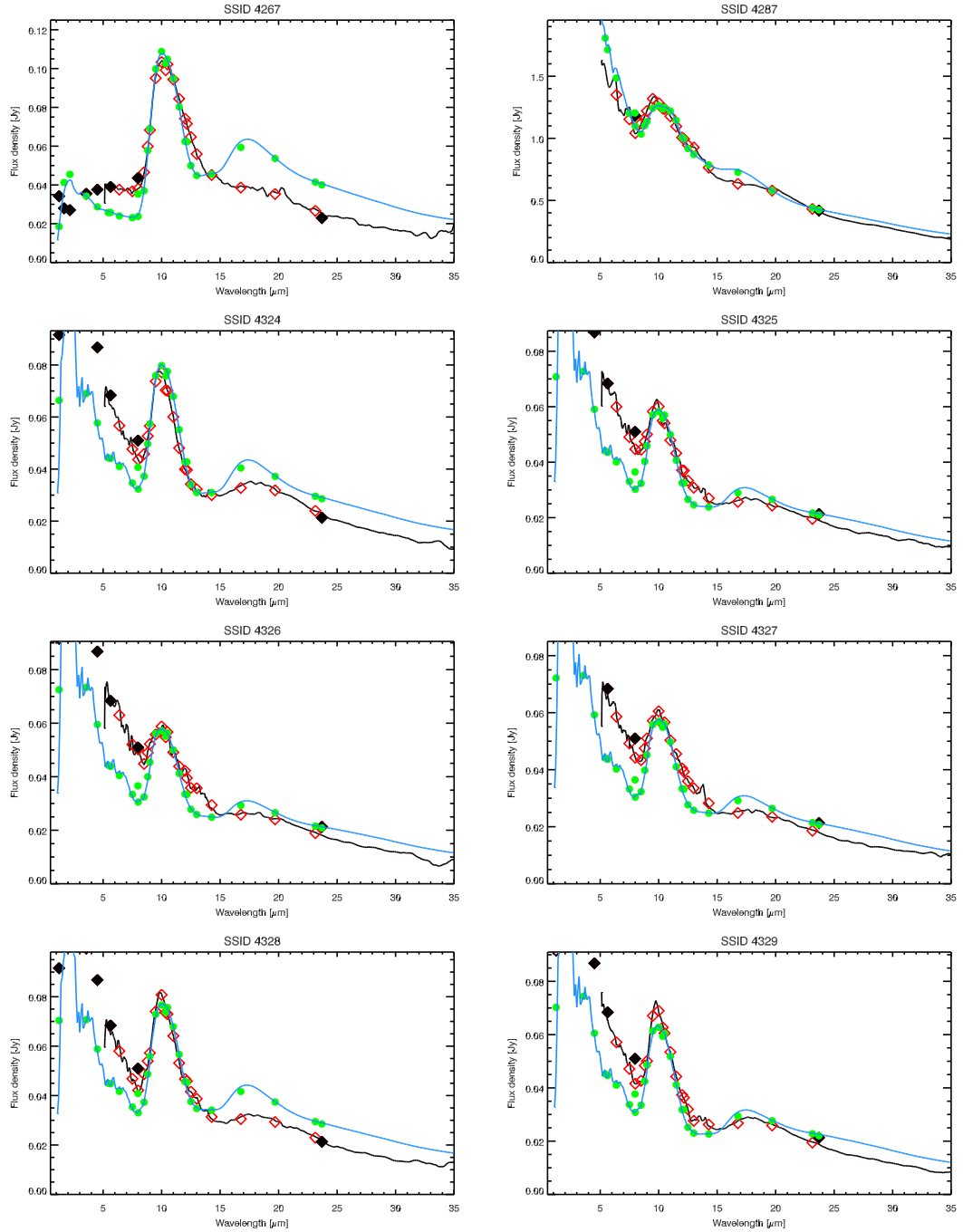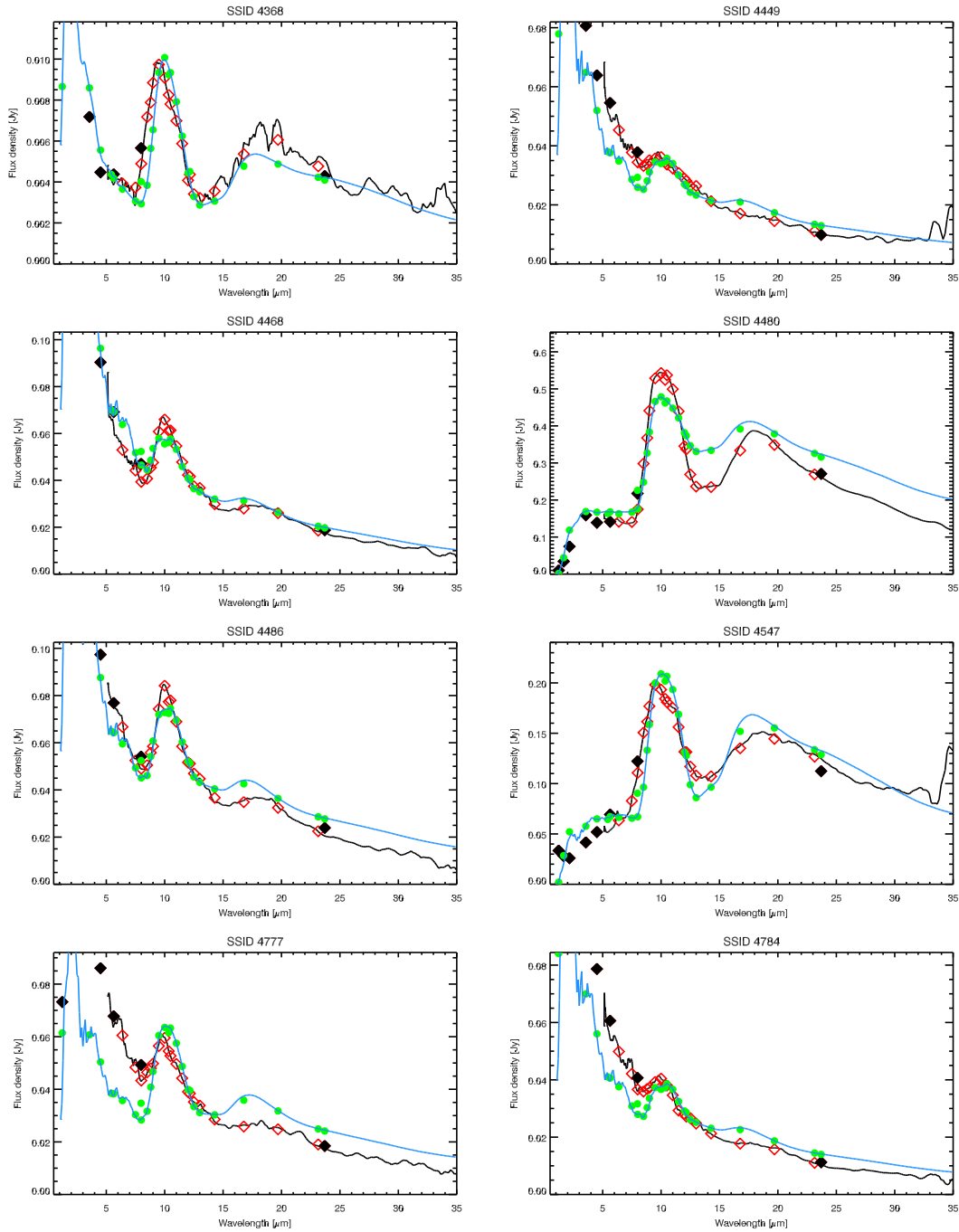
Table 5.2: The best-fit model parameters.

SSID	Spectral type	M_{bol}	R_{in} (R$_{star}$)	$\dot{M}$ (M$_\odot$ yr^{-1})	Alx. (%)	χ^2
6	M1	-4.69 ± 0.43	15 ± 2.5	$(2.77 \pm 0.74) \times 10^{-7}$	15 ± 10	85
22	M9	-4.10 ± 0.26	2.5 ± 0.5	$(1.41 \pm 0.52) \times 10^{-7}$	30 ± 10	9
38	M5	-5.45 ± 0.36	5.0 ± 0.5	$(3.92 \pm 0.39) \times 10^{-7}$	5 ± 10	5
61	M9	-5.59 ± 0.19	3.0 ± 0.5	$(1.40 \pm 0.28) \times 10^{-7}$	35 ± 10	8
82	M9	-5.99 ± 0.22	7.5 ± 2.5	$(1.26 \pm 0.28) \times 10^{-7}$	40 ± 15	7
93	M1	-4.97 ± 0.07	15 ± 2.5	$(1.05 \pm 0.11) \times 10^{-7}$	0 ± 10	8
96	M5	-4.03 ± 0.22	7.5 ± 2.5	$(1.36 \pm 0.37) \times 10^{-7}$	5 ± 5	12
165	M9	-6.43 ± 0.11	5.0 ± 2.0	$(6.17 \pm 1.13) \times 10^{-7}$	0 ± 10	6
180	M9	-6.01 ± 0.28	2.5 ± 2.0	$(8.48 \pm 4.08) \times 10^{-8}$	40 ± 20	4
182	M1	-3.24 ± 0.31	15 ± 0.5	$(1.42 \pm 0.41) \times 10^{-7}$	10 ± 10	22
182*	M5	-3.29 ± 0.11	5.0 ± 2.5	$(1.45 \pm 0.50) \times 10^{-7}$	15 ± 15	11
4038	M5	-6.96 ± 0.74	7.5 ± 2.5	$(2.63 \pm 0.52) \times 10^{-6}$	20 ± 10	8
4054	M9	-2.57 ± 0.83	7.5 ± 2.5	$(6.94 \pm 0.43) \times 10^{-7}$	30 ± 10	19
4076	M9	-5.92 ± 0.10	5.0 ± 2.0	$(1.22 \pm 0.10) \times 10^{-6}$	5 ± 10	6
4077	M9	-5.91 ± 0.10	5.0 ± 2.0	$(1.22 \pm 0.11) \times 10^{-6}$	5 ± 10	6
4078	M5	-5.91 ± 0.10	7.5 ± 2.5	$(1.21 \pm 0.10) \times 10^{-6}$	0 ± 10	13
4079	M9	-5.91 ± 0.10	5.0 ± 2.0	$(1.22 \pm 0.24) \times 10^{-6}$	0 ± 10	5
4080	M9	-5.98 ± 0.13	5.0 ± 2.5	$(1.26 \pm 0.22) \times 10^{-6}$	0 ± 10	8
4081	M9	-5.93 ± 0.11	5.0 ± 2.5	$(1.23 \pm 0.24) \times 10^{-6}$	0 ± 10	6
4149	M1	-5.76 ± 0.13	15 ± 0.5	$(3.02 \pm 0.97) \times 10^{-6}$	15 ± 25	8
4205	M9	-5.84 ± 0.26	2.5 ± 2.0	$(7.85 \pm 3.76) \times 10^{-8}$	40 ± 20	5
4245	M5	-4.02 ± 0.99	15 ± 0.5	$(1.36 \pm 0.39) \times 10^{-6}$	30 ± 20	20
4267	M1	-4.80 ± 0.99	15 ± 2.5	$(7.30 \pm 0.96) \times 10^{-7}$	25 ± 10	37
4287	M5	-10.78 ± 0.38	5.0 ± 2.5	$(3.05 \pm 1.64) \times 10^{-7}$	60 ± 10	2
4324	M9	-5.85 ± 0.24	5.0 ± 0.5	$(3.15 \pm 1.36) \times 10^{-7}$	15 ± 10	15
4325	M9	-5.92 ± 0.20	2.5 ± 2.5	$(1.63 \pm 0.41) \times 10^{-7}$	15 ± 15	17
4326	M9	-5.94 ± 0.19	2.5 ± 0.5	$(1.64 \pm 0.42) \times 10^{-7}$	20 ± 15	20
4327	M9	-5.93 ± 0.20	2.5 ± 2.0	$(1.64 \pm 0.41) \times 10^{-7}$	20 ± 15	18
4328	M9	-5.89 ± 0.22	5.0 ± 2.5	$(3.21 \pm 1.26) \times 10^{-7}$	25 ± 10	17
4329	M9	-5.94 ± 0.19	2.5 ± 2.0	$(1.64 \pm 0.42) \times 10^{-7}$	5 ± 10	15
4368	M5	-3.67 ± 0.40	2.5 ± 2.5	$(5.79 \pm 1.08) \times 10^{-8}$	5 ± 10	17
4449	M9	-5.88 ± 0.26	3.0 ± 0.5	$(1.20 \pm 0.38) \times 10^{-7}$	50 ± 20	13
4468	M9	-6.56 ± 0.21	2.5 ± 2.5	$(1.09 \pm 0.11) \times 10^{-7}$	40 ± 15	8
4480	M5	-6.11 ± 0.11	15 ± 0.5	$(5.32 \pm 1.20) \times 10^{-6}$	35 ± 25	25
4486	M9	-6.40 ± 0.22	3.0 ± 0.5	$(2.03 \pm 0.35) \times 10^{-7}$	40 ± 15	6
4547	M9	-5.24 ± 0.70	15 ± 0.5	$(3.56 \pm 1.04) \times 10^{-6}$	0 ± 20	23
4777	M9	-5.73 ± 0.10	5.0 ± 0.5	$(2.98 \pm 1.27) \times 10^{-7}$	30 ± 15	28
4784	M9	-5.96 ± 0.25	3.0 ± 0.5	$(1.24 \pm 0.40) \times 10^{-7}$	50 ± 20	17

Note: The best-fit obtained without a metallic iron component is indicated by an *.
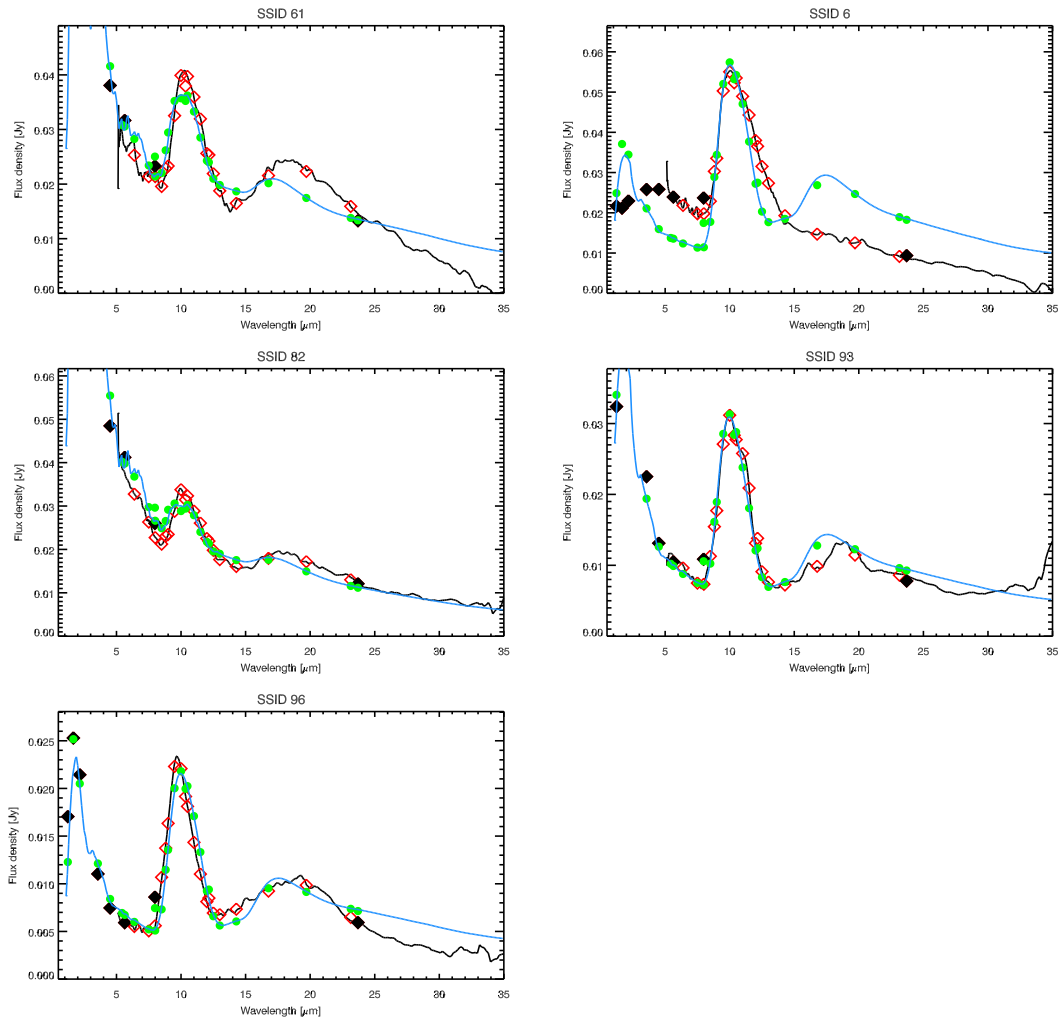
Figure 5.12: — Continued.

dust; deviations from spherical symmetry; or a steeper density profile may also causes for deviations between the model and the observations at longer wavelengths.

In some stars (for example, SSID 4329), there is a small discrepancy between the models and the spectra in the 4–8-μm wavelength region. The inclusion of iron grains is necessary to reproduce the general slope of the SED and explain excess emission in the spectra up to 8 μm, as laboratory silicates provide too little opacity in the near-IR (Kemper et al. 2002; Verhoelst et al. 2009; McDonald et al. 2010). Other proposed

sources of this excess continuum emission includes amorphous carbon (Demyk et al. 2000) or micron-sized O-rich dust grains (Höfner 2008; Norris et al. 2012). In these cases the metallic iron abundances may need to be increased in order to reproduce the observed profiles. In this study we use an iron abundance of 4 per cent with respect to the amorphous silicates, however Groenewegen et al. (2009) find a value of 5 per cent provides the best fit.

While the adoption of iron grains has generally worked well, in one instance (SSID 182) its inclusion proves detrimental to the fit. Figure 5.13 shows the best-fitting models to SSID 182. The total mass-loss rate for both models was $\sim 1.4\times10^{-7}$ M$_\odot$ yr^{-1}, and the alumina mass fraction $\sim$ 15 per cent. The inclusion of metallic iron has a greater influence on the dust shell inner radius, which determines the temperature of the hottest dust.

The aim of the models presented here is to understand the 10 μm feature; consequently, some other features are not well fitted by our models. In our modelling we only use three dust components: amorphous silicates, amorphous alumina and metallic iron; this grain mixture is successful at reproducing the observed shape of the 10-μm feature. The profile of the 18-μm feature shows considerable variation between spectra. This is not well constrained using any set of the available optical constants for silicates. Thus, the fits to the observations with the current dust model place a strong weight on the 10-μm feature, and very little weight on the 18-μm feature. Other dust components that may be present but are not taken into account include crystalline silicates, gehlenite ($Ca_2Al_2SiO_7$) and spinel ($MgAl_2O_4$). Three spectra (SSID 22, 182 and 419) have strong crystalline silicate complexes near 23, 28 and 33 μm, which will contribute some flux to the underlying continuum. A more detailed description of the crystalline silicate features in the present sample can be found in (Jones et al. 2012, Chapters 3 and 4).

Previously, calcium-aluminium-rich silicates, such as gehlenite ($Ca_2Al_2SiO_7$) have been detected in significant amounts (25–50 per cent) around O-rich evolved stars with low mass-loss rates (Mutschke et al. 1998; Speck et al. 2000; Heras & Hony 2005; Ver-
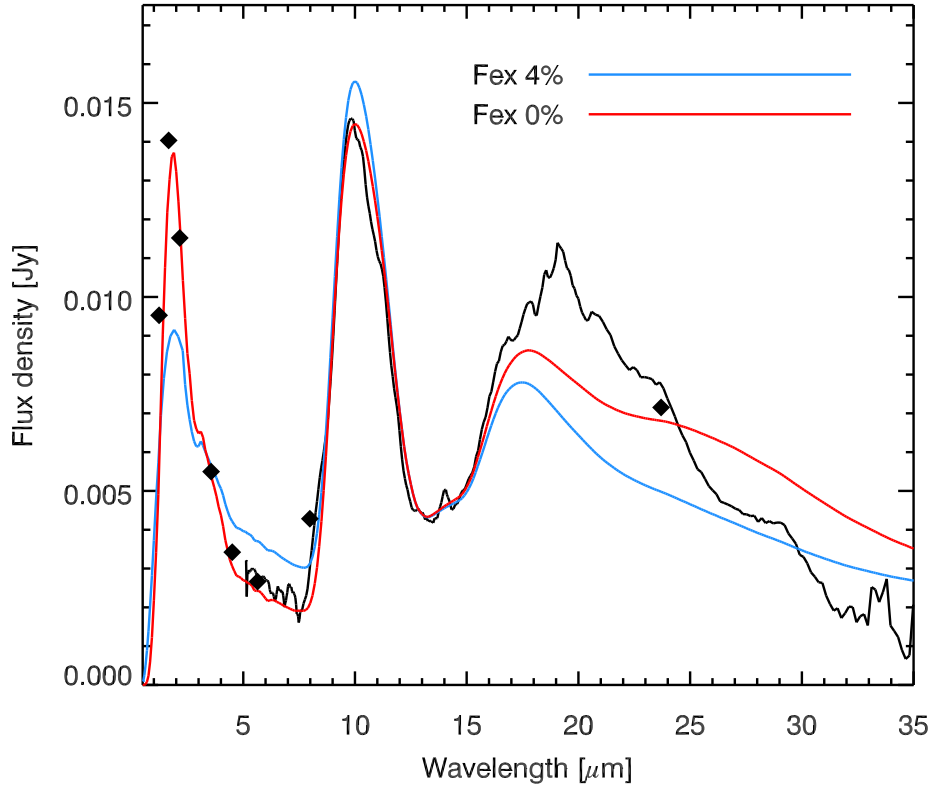
Figure 5.13: Fits to the SEDs and IRS spectra of SSID 182, using metallic iron (blue) and without iron (red). This is the only source where the fit is not improved with an iron component. The best-fit model obtained from our grid with 4 per cent iron grains has a χ^2 of 23, while the best-fit without iron had a χ^2 of 11.

hoelst et al. 2009). In these models gehlenite was included to fit the short-wavelength component of the 10-μm feature and to provide additional flux in the 19-μm region. We find that the 10-μm feature in our sample is fit reasonably well using a combination of Mg-rich silicates and alumina; thus the contribution from other dust species can only be small. This discrepancy may be due to the choice of optical constants use for the amorphous silicates.

Two sources in our sample, IRAS 04544−6849 (SSID 4076–4081) and HV 2446 (SSID 4324–4329), have been observed with the IRS at different epochs over one vari-
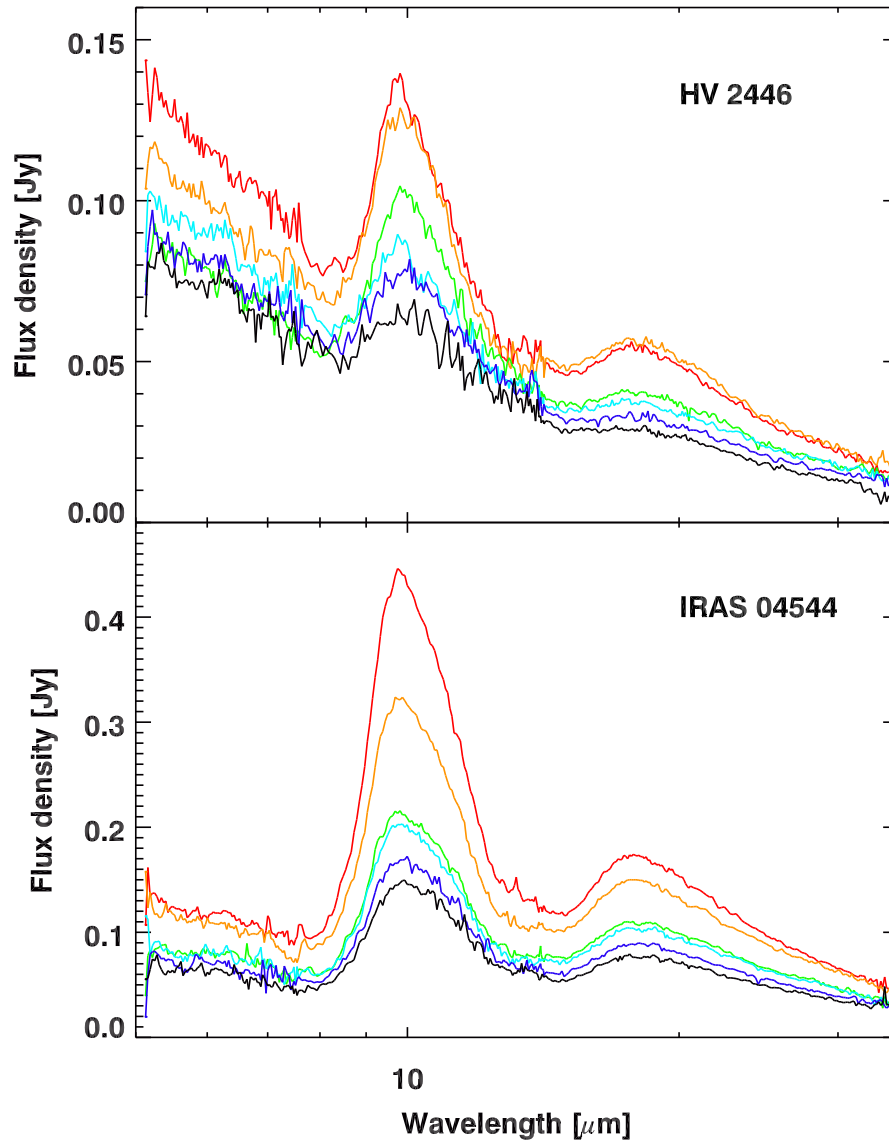
Figure 5.14: Observed spectral variations for HV 2446 (SSID 4324–4329) and IRAS 04544−6849 (SSID 4076–4081).

ability cycle. The SED for each source includes photometry from multiple epochs, while the spectra represent an instantaneous view of the star at a precise phase of the pulsation cycle. In both these stars the strength ratio of the 10- to 20-μm silicate emission features varies with pulsation phase (Figure 5.14). This is due to changes in the dust temperature, which is directly related to the luminosity of the star (Monnier et al. 1998). For both these sources the stellar and dust-shell parameters of our best-fit models are consistent across the pulsation cycle, as to some extent temporal variations are minimised. However, our models are sensitive to the change in dust optical properties, as the peak wavelength and width of the 10-μm feature in the spectra shows discernible variations between maximum and minimum light in the pulsation cycle; this indicates that the dust properties in the shell vary with pulsation phase. Furthermore, it will introduce some scattering in our model results when comparing between stars.

The brightest star in the sample, RS Men (SSID 4287), has a bolometric magnitude in excess of -10.78 if it was at the distance of the LMC, which is significantly above the luminosity expected for a bright RSG. This star has been identified as a foreground Mira variable with a distance of 4.75 kpc and radial velocity of 140 km s^{-1} (Buchanan et al. 2006; Whitelock et al. 1994). Incidentally, this source also has the highest alumina fraction in our sample of 60 per cent.

SSID 6 along with SSID 4267 are not well described by our models and their fits are the least satisfactory. These spectra are unusual as they exhibit a strong 10-μm silicate feature but no 18-μm feature. One possible explanation is that the silicates have recently formed and the 18-μm feature has a low contrast ratio with respect to the 10-μm feature. Alternatively this may be explained by a lack of cooler dust, or the dust may be composed only of small 0.1 μm Mg-rich olivine and alumina grains (Gielen et al. 2011).

5.5 Discussion

Using the dust-shell models presented here, we are able to constrain both the mass-loss rate and the fractional abundance of alumina. Based on the best-fitting models the mass-loss rates range from $\sim 8 \times 10^{-8}$ to 5×10^{-6} $M_\odot$ yr^{-1}, and the alumina fraction ranges from 0 to 50 per cent. We compare our derived mass-loss rates to those determined from SED fitting with the   model in Riebel et al. (2012) and to values listed in Groenewegen et al. (2009). The agreement is generally quite good between our mass-loss rates and the literature values, however, our mass-loss rates are slightly lower than the   fits, predominantly due to the inclusion of metallic iron grains and alumina in our models.

To have a better understanding of the mass-loss rates and dust abundances derived by this fitting, some limitations of the models must be kept in mind. The photospheric models used are appropriate for solar metallicities, and may not be entirely representative of the molecular abundances typical of AGB stars in the Magellanic Clouds. This is more significant for stars with a very low contrast dust excess, where there is a strong photospheric contribution and molecular absorption features due to CO, H$_2$O, and SiO are prominent. Observing the CO emission lines in the submillimetre (due to rotational transitions) for a number of Magellanic Cloud sources would also be beneficial to constrain the mass-loss parameters. This would enable us to have a better understanding of the expansion velocity and gas-to-dust ratios in the envelopes of evolved stars. The fits to the sources may also be improved by including a finer grid spacing, for instance, the iron abundance could be incremented in one percent intervals (up to abundances of 10 per cent) to improve the fit to the stars in the near-IR region.

In our sample, the dust composition is best fit by amorphous silicates, with appreciable amounts of amorphous alumina and additional, small contributions from metallic iron. Alumina is detected in most sources, however, in all cases its fractional abundance is less than 50 per cent. The alumina fractions we have obtained are consistent with those estimated using other methods (see Sections 5.3.1 and 5.3.2).
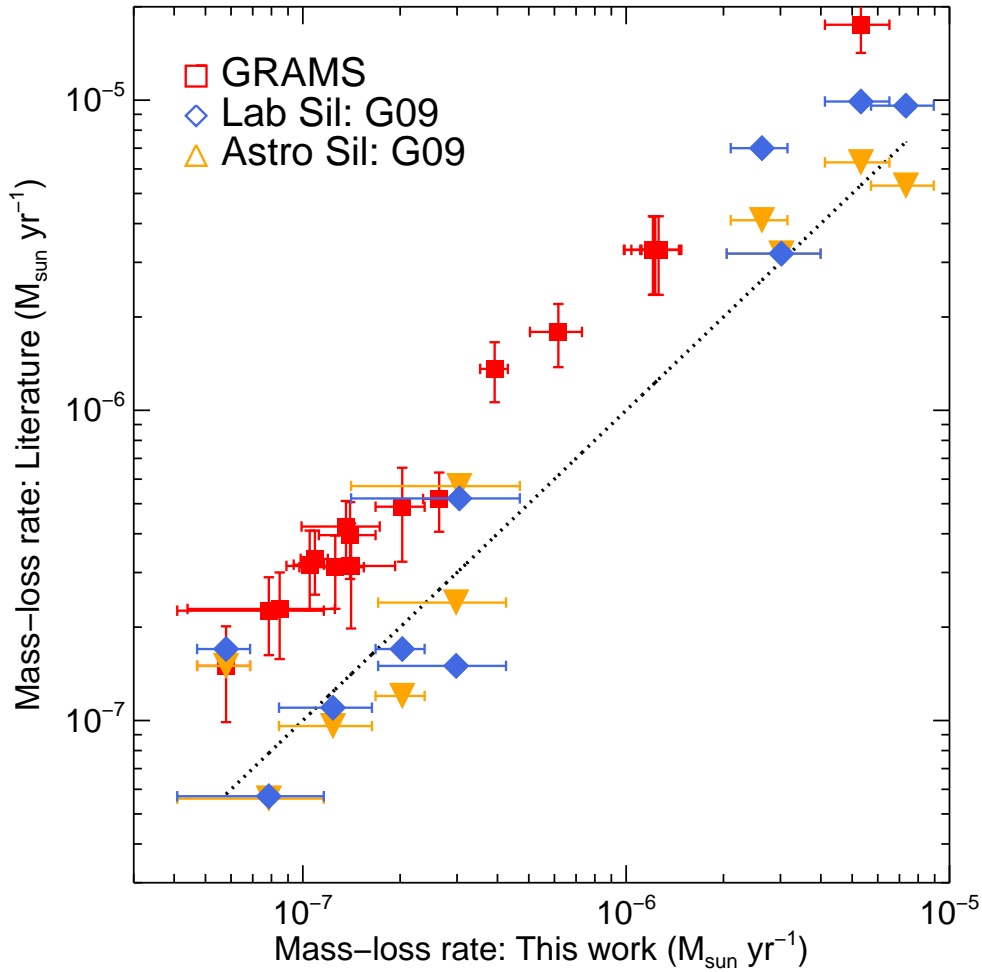
Figure 5.15: Comparison of mass-loss rated derived in this work with objects in common with our sample from Groenewegen et al. (2009) and the   model results from Riebel et al. (2012).

Figure 5.16 shows the fractional abundance of alumina plotted against the mass-loss rate. As noted by other authors (Heras & Hony 2005; Blommaert et al. 2006; Lebzelter et al. 2006), there is a correlation between the dust composition and mass-loss rate; the lower the mass-loss rate the higher the percentage of alumina in the shell.

Stars in the early stages of the AGB phase, tend to be less luminous and have lower mass-loss rates than their more evolved counterparts. This makes reliable determi-
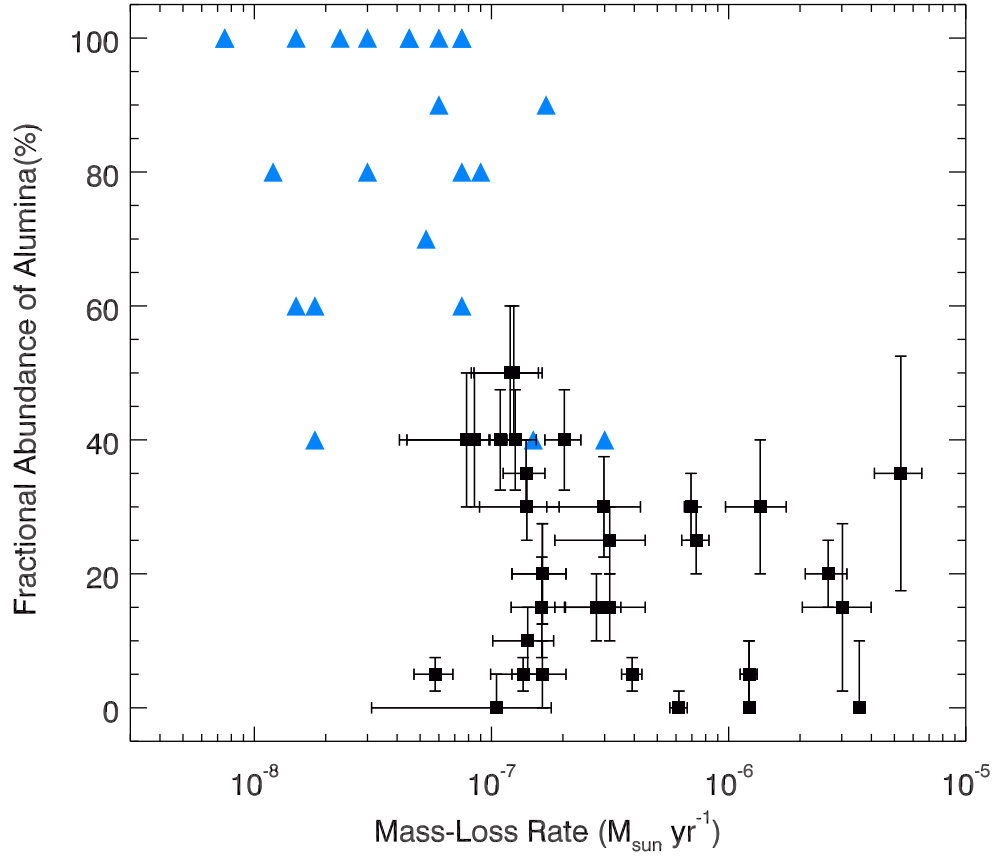
Figure 5.16: The fractional abundance of alumina in the dust shell of LMC O-AGB stars as a function of mass-loss rate (black squares). Based on Spearman's ρ statistics, the correlation coefficient is -0.41 with a significance value of 0.01. For comparison the blue triangles show the distribution of Galactic Bulge O-AGB sources from Blommaert et al. (2006).

nation of the dust composition challenging, especially for spectra with a low signal-to-noise ratio or with a low contrast dust excess. AGB stars dominated by alumina dust tend to have mass-loss rates below $10^{-7}\,M_\odot\,\mathrm{yr}^{-1}$ (Blommaert et al. 2006). Indeed, the SEDs of a large fraction of Galactic Bulge sources in this mass-loss range can be fit solely with amorphous alumina. The oxygen-rich AGB stars in our LMC sample, which show a dust emission contrast, tend to be more luminous, with M_{init}

of ~5 $M_\odot$. Our sample is dominated by stars with mass-loss rates between 10^{-7} and $5 \times 10^{-6} M_\odot$ yr^{-1}. These stars display dust components which are from the more advanced stages of the dust condensation sequence; indicated by the low percentage of alumina dust. It should therefore come as no surprise that silicates are the dominant dust type in the present sample. Metallicity effects on the dust-formation efficiency in oxygen-rich stars may also be important.

Future telescopes such as the *JWST* and *SPICA* will be able to obtain high-quality spectra of low mass-loss rate, low luminosity AGB stars in the Magellanic Clouds and other resolved stellar populations, eliminating the observational bias towards silicate-rich stars in the current sample. We expect these stars to contain a high percentage of alumina-rich dust.

5.6   Conclusions

We have presented a grid of dust radiative transfer models which explores a range of alumina and silicate dust compositions and stellar and dust shell parameters. The models have been used to simultaneously fit the spectra and broadband SED of 37 oxygen-rich AGB stars in the LMC with optically-thin circumstellar envelopes. The mass-loss rates of our sample range from $\sim 8 \times 10^{-8}$ to 5×10^{-6} $M_\odot$ yr^{-1}. We find that a combination of amorphous silicates, amorphous alumina and metallic iron is successful at reproducing the observed shape of the 10-μm feature, and the general shape of the SED. All our sources we found to be silicate-rich, though alumina and iron are often present in significant amounts. This dust composition is consistent with the thermodynamic dust condensation sequence for oxygen-rich AGB stars. Furthermore, we show from dust models that the *AKARI* [11]–[15] versus [3.2]–[7] colour, is able to determine the fractional abundance of alumina in oxygen-rich AGB stars.

6

The Stellar Population of M32

In this chapter we investigate the population of cool, evolved stars in the Local Group dwarf elliptical galaxy M32, using IRAC observations from the *Spitzer* Space Telescope. This enables us to study evolved stellar populations at the edge of the Local Group that would otherwise be obscured in optical and near-infrared surveys, and examine how dust production from stellar populations vary with metallicity.

6.1   Introduction

Discovered in 1749 by Le Gentil, M32 was the first elliptical galaxy to be observed. Our relative proximity to M32 (distance = 785 ± 25 kpc; McConnachie et al. 2005) allows us to resolve individual stars. Consequently, it presents us with an opportunity to study the stellar populations of an elliptical galaxy in great detail. M32's stellar populations have been extensively studied (e.g. Baade 1944; Rose 1985; Grillmair et al. 1996; Worthey et al. 2004; Monachesi et al. 2011; Sarajedini et al. 2012). M32 has a complicated star-formation history, with the age and chemical composition of the stellar population (in spectroscopic studies) showing a radial dependency (Rose et al. 2005). However, photometric observations with the NIRI imager on the Gemini North telescope by Davidge & Jensen (2007) indicate AGB stars and their progenitors are smoothly distributed throughout the galaxy.

Table 6.1: Properties of M32

Parameter		Ref.
Distance, d (kpc)	785 ± 25	McConnachie et al. (2005)
E(B-V) (mag)	0.08	Brown et al. (2008)
M ($M_\odot$)	$(1.1 \pm 0.3) \times 10^9$	Nolthenius & Ford (1986)
$M_{nucleus}$ ($M_\odot$)	$(3.4 \pm 0.7) \times 10^7$	van der Marel et al. (1998)
Core radius (arcsec)	$\lesssim 0.42$	Bendinelli et al. (1992)

It is thought that M32 has two main populations: an intermediate-age, metal-rich population thought to be ~2–8 Gyr old (Coelho et al. 2009), and an old (8–10 Gyr) stellar population with slightly sub-solar metallicity ([Fe/H] = –0.2; Monachesi et al. 2011). Additionally, a small number of ancient metal-poor ([Fe/H] = –1.42) RR Lyr variables in M32 have recently been identified by Fiorentino et al. (2010, 2012). The extremely high surface brightness and sharply peaked brightness profile towards the nucleus of M32 indicates a strong increase in the stellar density thus, given the extreme crowding, the stellar populations within the core (~ 1arcmin of the nucleus) of M32 are incompletely probed. This high surface brightness also prevents studies of the fainter stars in M32. Some properties of M32 are listed in Table 6.1.

6.2   Observational Data

6.2.1   Observations

Spitzer observations of M32 (Program Identification [PID] 3400, PI. M. Rich) were obtained on 18 January 2005 UT with the Infrared Array Camera (IRAC; Fazio et al. 2004) at 3.6, 4.5, 5.8 and 8 μm. Observations were centred at R.A. = $00^h42^m41^s.6$, decl. = $+40°55'53''.6$ and cover an area of approximately $6'\times7'$ in all four IRAC channels around the centre of M32, plus an off-field region of the same size to the northwest for IRAC bands 2 and 4 or south-east for IRAC bands 1 and 3 (Figure 6.1). For
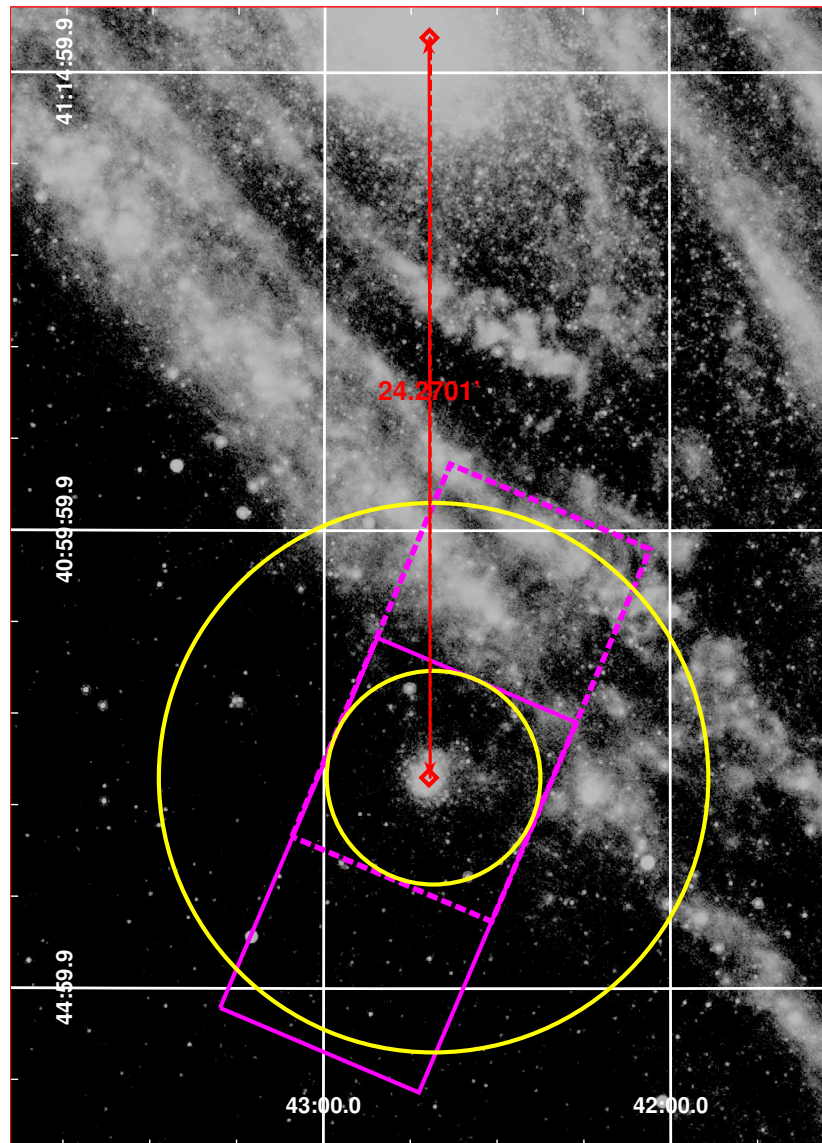
Figure 6.1: Location of our *Spitzer* IRAC pointings towards M32 superimposed on a MIPS 24 μm mosaic of Andromeda that also includes M32. The 3.6 and 8 μm coverages are represented by magenta solid and dashed lines, respectively. Elliptical annuli of 3.5′ and 9′ centred on M32 used to estimate point-source contamination from Andromeda are indicated by the solid yellow lines.

each IRAC channel, 92 frames at 23 dither positions were taken in a cycling pattern with 30-second exposures to build redundancy against outliers and artifacts, resulting in total integration time on M32 of 2760s over most of the map. No dedicated background control fields were observed to complement these observations.

6.2.2 Data Reduction

The raw data was processed by the *Spitzer* Science Centre (SSC) reduction pipeline version S18.7.0; which removes electronic bias, subtracts a dark image, applies a flat-field correction, and linearises the pixel response. I then corrected the resulting Basic Calibrated Data (BCD) images for various instrumental artifacts (e.g. muxbleeds and column pull-down effects) and combined the images using the   reduction package (Makovoz & Marleau 2005) to produce a single mosaic for each channel.

The   routine was implemented to match the backgrounds of individual frames in overlapping areas of the images producing a smooth background, and the   in addition to image interpolation and co-addition, eliminated cosmic rays and other outliers in the data. The final IRAC mosaics are not sub-sampled; thus, each image has a pixel scale of $1''.22$ pixel^{-1}.

MIPS 24 micron mosaics of M32 were provided by G. Bendo (priv. com), this data was originally published by Gordon et al. (2006) and reprocessed using the methods and software described by Bendo et al. (2012).

A three-colour image combining the 3.6, 8.0, and 24 μm images is presented in Figure 6.2, where the red stellar objects are clearly visible. Additionally, we see no emission indicative of interstellar dust within M32. This would be particularly evident in the 8.0-μm map, which is sensitive to non-stellar polycyclic aromatic hydrocarbon (PAH) emission or the MIPS 24-μm mosaic which is sensitive to cool dust.
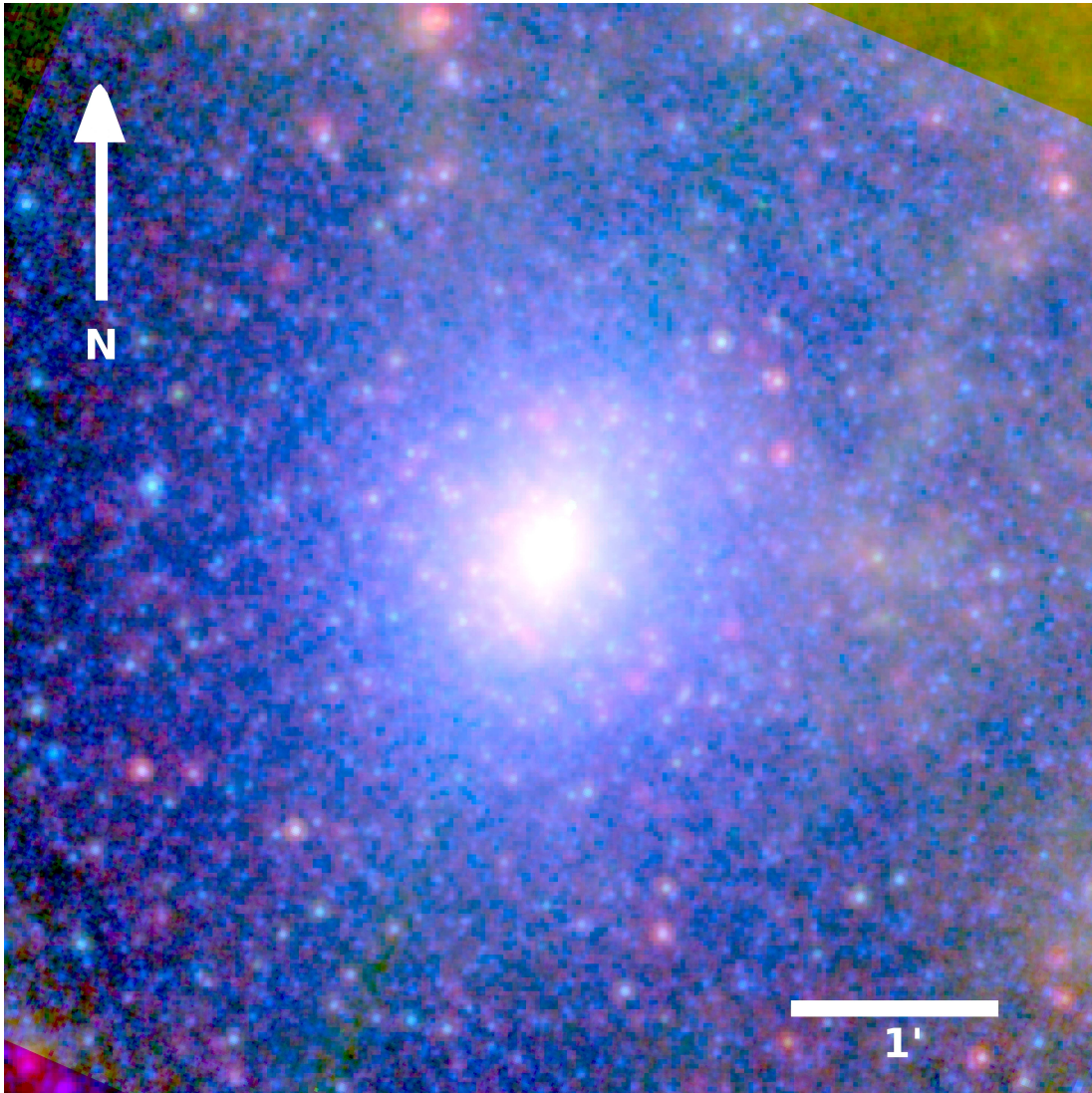
Figure 6.2: Three-colour image of M32. Blue is 3.6 μm, green is 8.0 μm and red is 24 μm. Stars with a dust excess become visible at 8.0 μm and 24 μm and appear red in the image.

6.2.3   Photometry

Point-source extraction was performed on individual IRAC frames and on the mosaicked images using Point Source Function (PSF) fitting with the DAO   and   photometry packages (Stetson 1987). To determine the shape of the PSF DAO   requires that you select isolated stars in the field; this is quite challenging in very crowded fields such as M32. PSFs were created from a minimum of 10 isolated bright stars in each IRAC channel, and sources 4σ above the local background were chosen for extraction.

A   was then used to perform PSF-fitting to all sources found on the image. This is an iterative process that simultaneously fits each source in the frame with the PSF profile and subtracts converged sources from the input image. As sources are removed, new estimates for the local background are calculated improving the flux estimates for crowded and faint sources. Sharpness and roundness cuts were employed to eliminate extended sources, cosmic rays and unrecognised blends that are broader or narrower than the PSF from the sample. Cosmic rays are also eliminated from the point-source list when detections in the same band are combined. The resulting source lists are then cross-correlated with the point-source photometry from the mosaicked data.

The flux densities and uncertainties are colour–corrected using a 5000 K blackbody, according to the method described in the IRAC Data Handbook, version 3.0[1]. Additionally, a pixel-phase-dependent correction (Reach et al. 2005) was applied to the 3.6-μm photometry. Finally, magnitudes relative to Vega were derived using the zero-magnitude flux calibrations provided in the *Spitzer* IRAC Data Handbook. The representative photometric uncertainty as a function of source magnitude is given in Figure 6.3.

Severe stellar crowding towards the nucleus of M32 means that reliable PSF photometry is challenging. Completeness limits for each wavelength were determined via

---

[1]See http://ssc.spitzer.caltech.edu/irac/dh/iracdatahandbook3.0.pdf.
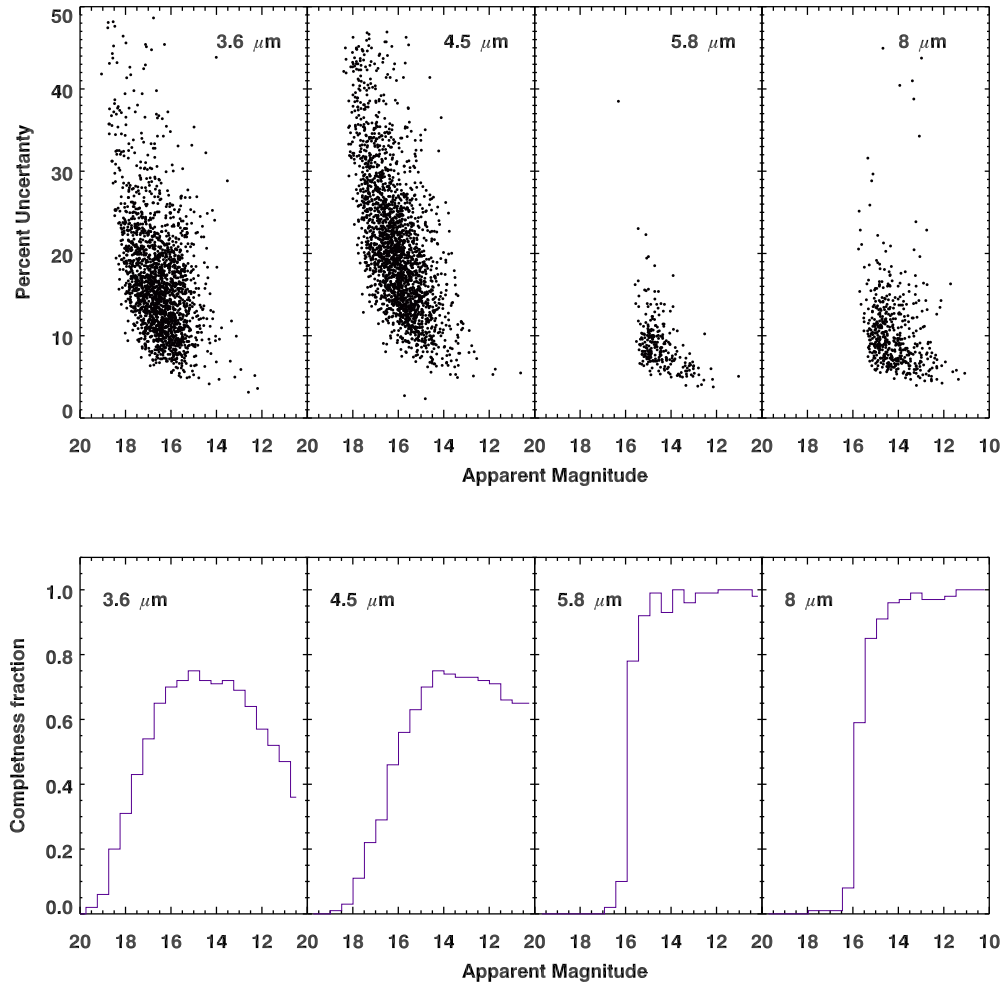
Figure 6.3: Photometric uncertainty and completeness fraction as a function of apparent magnitude for each IRAC band. The one-dimensional completeness fraction as a function of magnitude is shown in the bottom panels. Limits are averaged over the galaxy: photometry is more complete in the outskirts of the galaxy compared to the core.

the extraction of artificially-inserted stars. These false stars were placed at random pixel locations and have a limiting magnitude ~ 2 mag fainter than observed. To avoid a significant increase in the source density of the field we limit the fraction of artificial stars introduced per image to ~ 5 per cent of the real stars detected. PSF-fitting photometry was then performed on the modified image. This process is then repeated multiple times for each image to statistically analyse the photometric completeness of each band. False stars are considered to be recovered if they are within a 1 pixel radius of the input position and their magnitude differs by $|\delta m| \leq 1$ from their input magnitudes. If the magnitude difference is greater than this we consider the sources to be an unresolved blend of two or more stars and hence we do not consider them as recovered. The bottom panel in Figure 6.3 compares the fraction of injected and recovered stars for each IRAC band. For IRAC bands 1 and 2 the completeness factor of recovered stars in a given magnitude bin is much lower than bands 3 and 4. In these channels the high stellar density proves to be the major source of incompleteness.

6.3 Correcting Star Count Numbers

6.3.1 M32 Field Contamination

Contamination due to M31 stars

As M32 has a projected separation of 24′ (5.4 kpc) from M31's centre, disk and halo stars from M31 are the dominant source of contamination in the field. Furthermore, stars belonging to the nearby Andromeda galaxy will have similar IR colours to the evolved stellar population of M32. This makes it extremely difficult to isolate the individual stars belonging to M32 and the presence of some intruders is unavoidable. Combined with crowding, contamination from M31 is the most important limitation in the analysis of M32's rich stellar field.

As contamination from M31 will not be homogeneously distributed across the field of view, the best estimate of the fraction of contaminating objects would be from a suit-

able control field located at the same isophotal level in the outer disk of M31 but away from M32's nucleus. Unfortunately, archival *Spitzer* IRAC observations of M31 and its surroundings only mapped the outer regions of M31 to a depth of about 120 seconds per sky position (Barmby et al. 2006; Mould et al. 2008), as such these observations do not provide sufficient depth to serve as a control field.

The approximate level of contamination from M31 can be estimated from star counts within the off-field regions if we were able to assume that the population of M31 stars is statistically the same in both fields. However, this will result in an underestimate of the contamination in the IRAC 3.6 and 5.8 μm bands and an overestimate of the contamination in the IRAC 4.5 and 8.0 μm bands, since the off-field regions are not located at the same distance from the centre of M31, hence they are not at the same isophotal level.

Contamination due to Galactic foreground stars

As M32 is located at a Galactic latitude of b=-22 degrees, Galactic foreground stars and unresolved background galaxies will also contribute to the source contamination. Monachesi et al. (2011) estimate the degree of contamination in the V band of their M32 *Hubble Space Telescope* (HST) ACS/HRC field of ~29 arcsec^2 and find 14 foreground stars; this corresponds to ~2500 objects in the V band for our IRAC field of view. These sources will emit the majority of their light at bluer wavelengths than considered in this work, and typically will be fainter than cool evolved stars with circumstellar envelopes. Foreground stars will have a spatially uniform distribution across our field of view. An estimate of the foreground star and background galaxy contamination may be obtained via colour-magnitude diagrams (Section 6.4.2).

6.3.2 Source Density Profiles

Using the radial density profiles we attempt to measure the IR contamination from M31 and Galactic foreground stars in each field of view. To measure the stellar radial

density profile of M32 we counted the sources contained in concentric annuli from its centre (where the bulk stellar population peaks) in steps of $0.5'$. The number of sources per unit area was then obtained by dividing by this value by the corresponding area covered by the annuli after correcting for regions not covered by our observations. Source density profiles for the M32 IRAC data are shown in Figure 6.4.

In all channels the source density declines significantly toward the centre of M32, where incompleteness due to crowding effects in the core of M32 becomes significant. Both the 5.8 and 8 μm bands show a smooth decline in source density beyond a radius of $R > 1.0'$, until contamination from field stars and Andromeda begins to dominate the source density. This is particularly noticeable in the 8 μm band beyond $R > 4.5'$, where there is a steady rise in source counts towards M31. As a result the density profiles cannot be mapped reliably to large radial distances from M32's centre.

The flattening of the star counts at $R = 2.5 - 4.0'$ was used to estimate the contamination from M31 and foreground stars. This corresponds to a point-source density of ~5 sources per arcmin^2 for the 5.8 μm band and ~7 sources per arcmin^2 for the 8 μm band.

The flat stellar density profiles in the IRAC 3.6 and 4.5 μm bands beyond $R > 2.0'$ indicates a high degree of point source confusion with M31. Because of these high stellar surface densities we exclude these channels from the M32 stellar population analysis in Section 6.4.1.

To determine the radius at which our data becomes confusion limited we fitted the radial profiles of M32 with an empirical King (1962) profile of the form:

$$I(R) = I_0 \left[\frac{1}{\sqrt{1 + \left(\frac{R}{R_c}\right)^2}} - \frac{1}{\sqrt{1 + \left(\frac{R_t}{R_c}\right)^2}} \right]^2 \quad ; R \leq R_t \tag{6.1}$$

where $I(R)$ is the density profile at projected radius R, I_0 is a normalising factor, R_c the core radius, and R_t is the photometric tidal cut-off radius. The best-fit King profiles to the background corrected IRAC 5.8 and 8 μm density profiles are shown in Figure 6.5. In both channels the data deviates from a King profile and becomes confusion limited
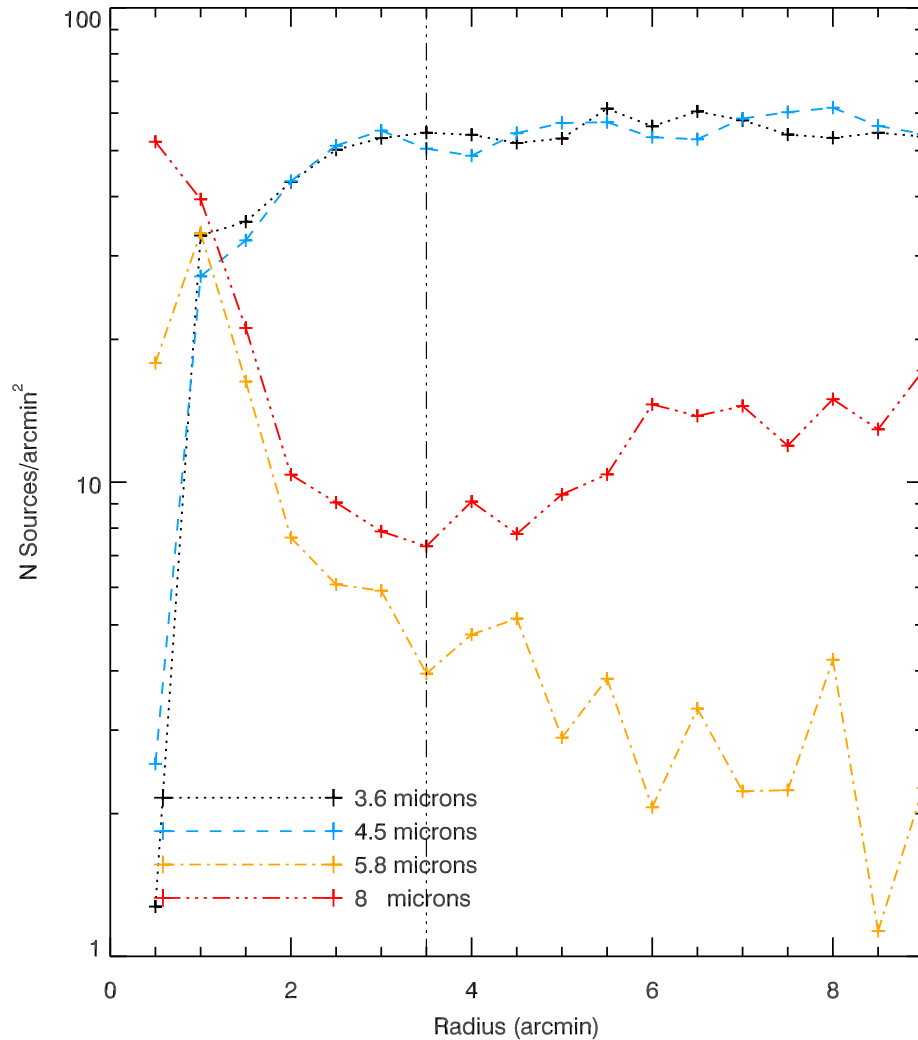
Figure 6.4: Source density profiles for M32. The bright stellar populations in the outer halo of M32 are resolved with *Spitzer*. However, the extremely high surface brightness and crowding in the bulge hinders detections in the central regions. The dashed line marks the radial limit where we have coverage in all four IRAC bands.
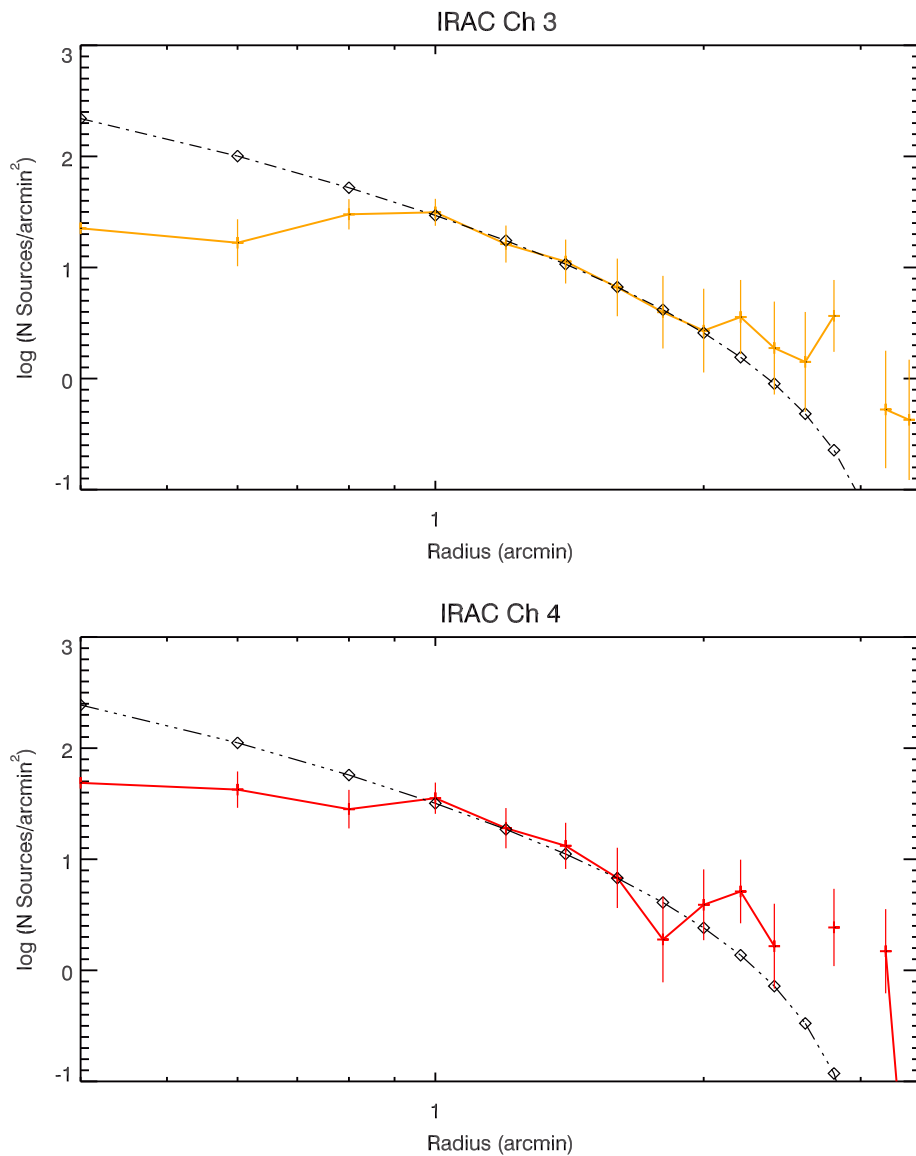
Figure 6.5: King profiles fit to the background corrected IRAC 5.8 and 8 micron density profiles for M32. The data deviates from the King profiles due to source confusion inside 1 arc-minute. This indicates that we are underestimating the stellar density in the centre of M32.

Table 6.2: King profile function best-fit parameters

Parameter	IRAC 5.8 μm	IRAC 8.0 μm
I_0	1103.68	1236.96
R_c (arcmin)	0.241	0.245
R_t (arcmin)	3.36	3.16

at $R < 1'$, which prevents us from studying the stellar populations in the innermost part of M32. At larger radial distances ($R > 2.5'$), uncertainties in the background source density causes deviations from the profile shape. This also limits how well we can constrain the tidal radii. The best-fit parameters are listed in Table 6.2. Due to the flat stellar density profiles in the IRAC 3.6 and 4.5 μm bands we were unable to determine the corresponding King profiles for these channels.

6.3.3 Stellar Spatial Distribution

The spatial distributions of the IR sources detected towards M32 are displayed in Figure 6.6. Star counts measured in concentric annuli centred on the off-field regions were also used to estimate the M32 field contamination. By using annuli, the difference in stellar density due to M31 should average out across the map producing a flat density profile. Located furthest away from M31, the IRAC 5.8-μm field suffered the least contamination, with an average background point-source density of 2.5 sources per arcmin^2, while the 8-μm field (which intersects the disk of M31) has an average density of 11 sources per arcmin^2. Based on the ratios of sources in the off-fields, we expect $\sim$ 60 per cent of the stars in the on-field region to be contaminants from M31 in the 5.8 and 8 μm bands.

Crowding is severe towards the nucleus of M32. Unresolved blended sources in our catalogue will show a magnitude enhancement compared to individual point sources. In Figure 6.7 we plot the apparent magnitude as a function of radial distance. The relatively flat profile indicates that blended sources form only a minor component of
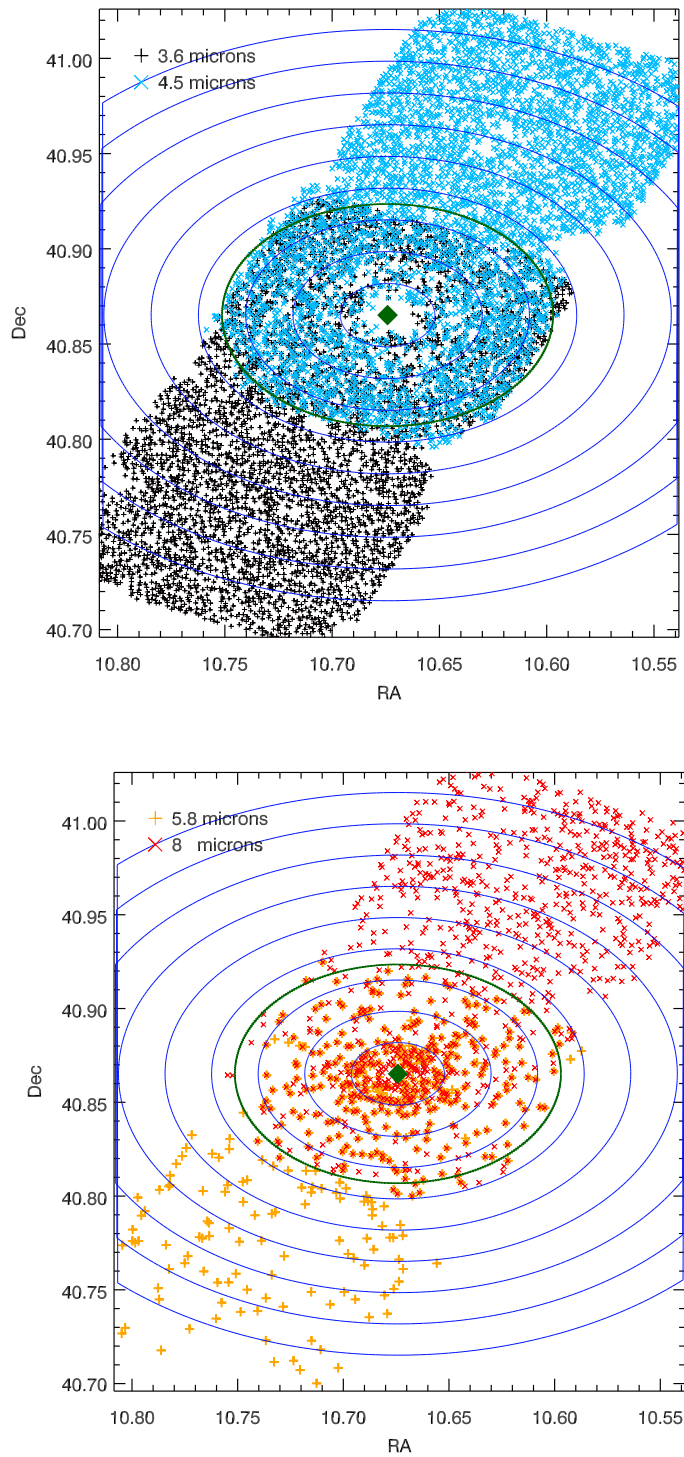
Figure 6.6: Spatial distributions of the point sources detected towards M32. The galactic centre is indicated by a green diamond. The circles represent contours of constant radii corresponding to semi-major axis bins of 1′. The green line indicates the on-field region.
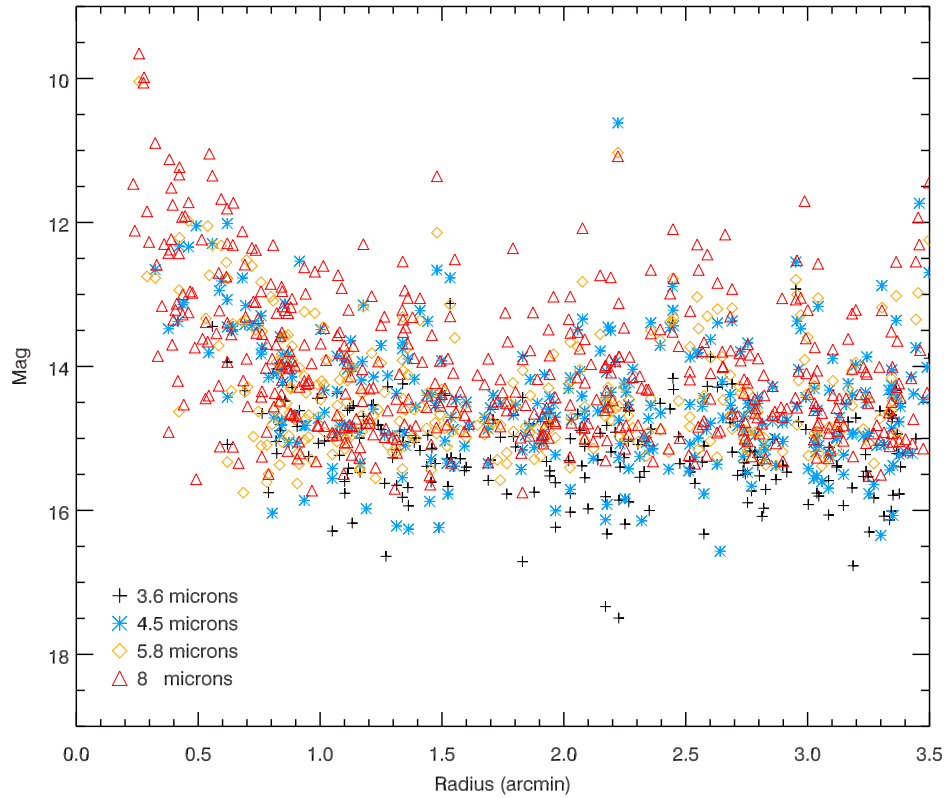
Figure 6.7: Magnitude versus Radial Distance. Towards the nucleus of M32 crowding is severe, sources with a magnitude enhancements in the core regions are probable blends.

our catalogue. Any sources in the inner regions that show a significant magnitude enhancement are removed from our catalogue.

6.4   Results & Discussion

6.4.1   M32 Luminosity Functions

In this section, we examine the mid-IR stellar luminosity function of M32. The luminosity functions for each of the IRAC bands were constructed by sorting the point-sources into bins based on their magnitude. The bin size of the luminosity functions is

0.2 magnitudes, to account for photometric errors in our catalogue.

The luminosity functions have to be corrected for both foreground/background contamination and photometric incompleteness before we can correctly analyse the luminosity function. To reduce the effects of M31 contamination as much as possible while still retaining a reasonable sample size, stars within 3.5′ of M32's centre were the only ones considered to be associated with M32 in the star count analysis; we dub this the 'on-field region'. The remaining sources are used to estimate the contamination from M31 and foreground stars in each magnitude bin. Furthermore, we consider only luminosity functions in the 5.8 and 8 μm bands, as the photometric completeness in other bands is generally much poorer and there is no quantitative estimate of the contamination rate in each magnitude bin. Any attempt to estimate these from the off-field regions is hampered by the strong dependence on the position in the galaxy and the distance from M31.

Correcting the luminosity functions for photometric completeness in each band is a simple procedure, as the completeness fraction of each bin is known from false star tests. The corrected luminosity function is thus obtained by dividing the total number of objects in a bin by its completeness fraction. However, as contamination from M31 is not expected to be homogeneously distributed across the field of view, correcting the luminosity function for point-source contamination using the off-field regions is not a trivial task and may significantly alter the profile shape. Also, because of the small numbers, the background corrected luminosity functions are highly uncertain. The uncertainties in the luminosity functions are set both by Poisson statistics of the sample and by the uncertainties in the background counts for each magnitude bin.

The *Spitzer* IRAC luminosity functions for M32 are shown as a histogram in Figure 6.8. The luminosity functions shown as black lines are based on the full star list derived from the entire IRAC field of view in each bandpass. The dotted-dashed line marks the limiting magnitudes used in this work, which corresponds to the 50 per cent completeness level. For the present survey, where the background estimates in each magnitude bin have a large uncertainty, it is instructive to compare the 'on-field'

luminosity function (blue line) to other stellar populations rather than the corrected luminosity function (dashed line), as this provides an upper limit to the luminosity distribution.

The tip of the AGB (TAGB) can be estimated from the luminosity functions by identifying the magnitude where the source count decreases significantly. Although source counts are low, an inspection of the luminosity functions suggests that tip of the AGB for M32 is located near $M_{8.0}$ ~14 ± 0.5 mag. M32 candidate stars brighter than the TAGB are either luminous RSGs in M31 or foreground sources. As shown in Figure 6.8, both the 5.8 and 8 μm luminosity functions reach depths of approximately 3 mag fainter than the AGB tip. However, the IRAC photometry of M32 is not deep enough to reach the red giant branch tip (TRGB).

Figures 6.9 and 6.10 compare the on-field mid-IR luminosity functions of M32 with both the simple stellar populations of Galactic globular cluster 47 Tuc and the diverse stellar systems of the Magellanic Clouds. For 47 Tuc the distance modulus used to determine absolute magnitudes is 13.32 mag (Percival et al. 2002), for the LMC it is 18.5 mag (Schaefer 2008) and the SMC is 18.91 mag (Hilditch et al. 2005).

The location of the TRGB is relatively insensitive to the metallicity of the host population. In contrast to the luminosity function of 47 Tuc where there is only a sparse population of AGB stars above the TRGB, the Magellanic Cloud luminosity functions are strongly dominated by the evolved stellar populations. This division at $M_{\rm abs}$ ~ −6 mag acts as a watershed between mass-losing evolved star candidates and the rest of the stellar population. Comparison of the M32 luminosity with these stellar populations acts as a crude diagnostic of the stellar populations in M32, and confirms the presence of a dusty evolved stellar population in M32. This stellar population is younger than the Population II stars in 47 Tuc, which suggests we are tracing a metal-rich population of intermediate age (2–8 Gyr).

5.8 microns

8.0 microns
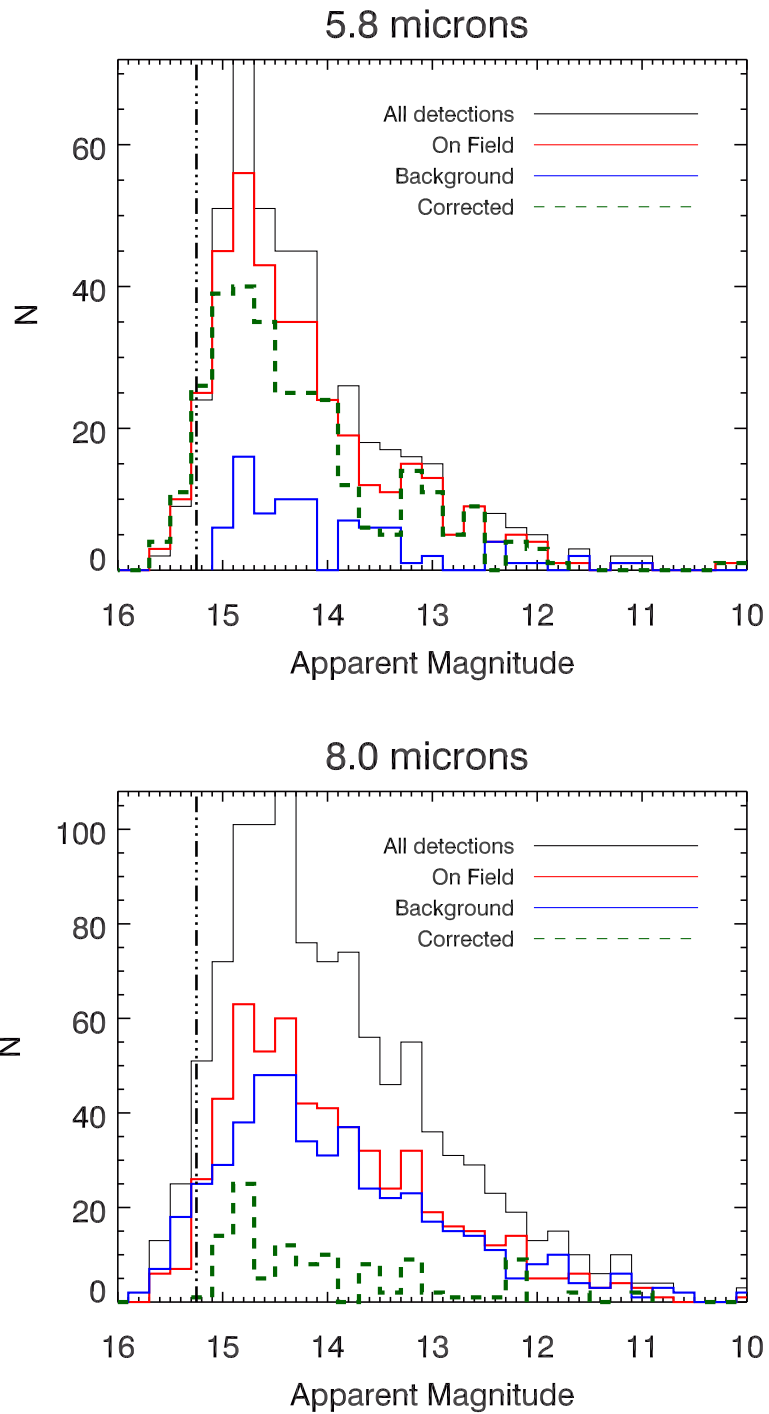
Figure 6.8: IRAC Luminosity Functions. The black line represents all sources detected in our field of view; the red line represents all sources within 3.5′ of M32's centre; the blue line is an estimate of the background and the dashed green line is the background corrected luminosity function.
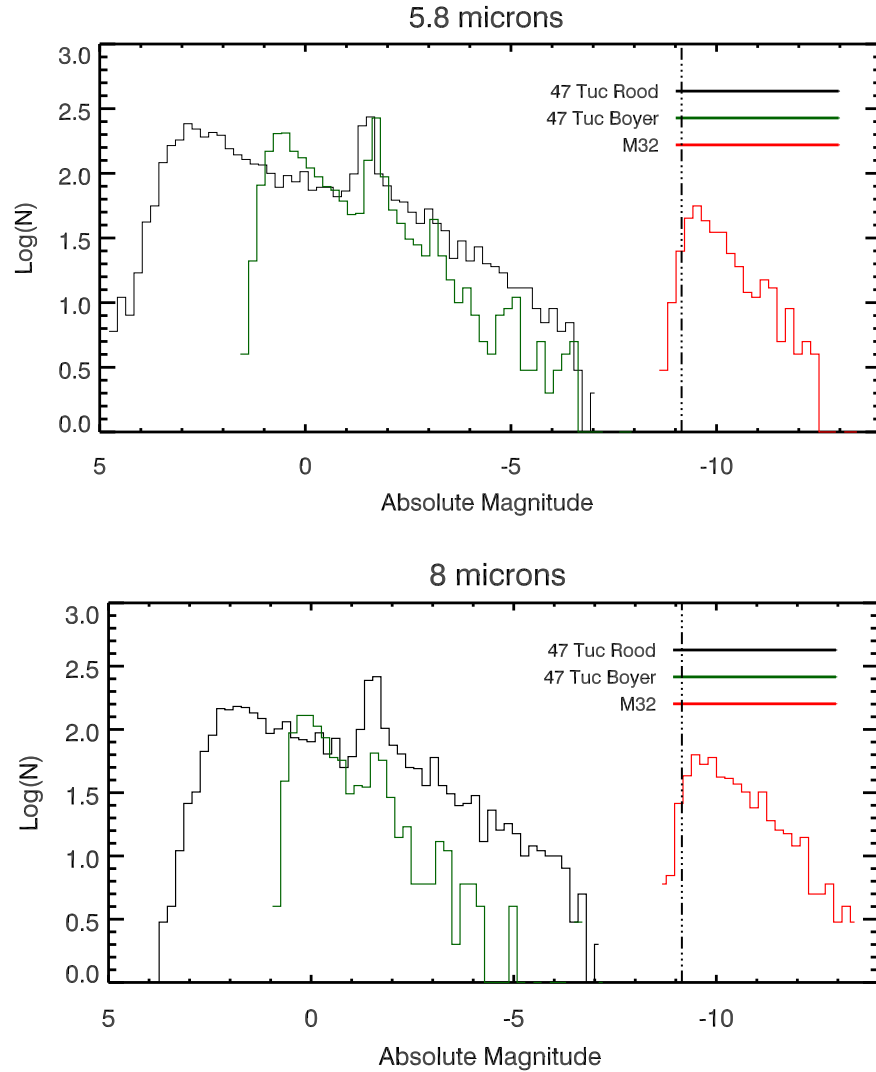
Figure 6.9: Comparison of the M32 and 47 Tuc Luminosity Functions. The red line represents all sources detected within 3.5′ of M32's centre; the black line represents the IRAC deep 'Rood' observations of 47 Tuc (Origlia et al. 2007; Boyer et al. 2010) and the green line represents the SAGE-SMC observations of 47 Tuc (Boyer et al. 2010). This indicates that the recovered stars in M32 are significantly brighter than the TRGB.
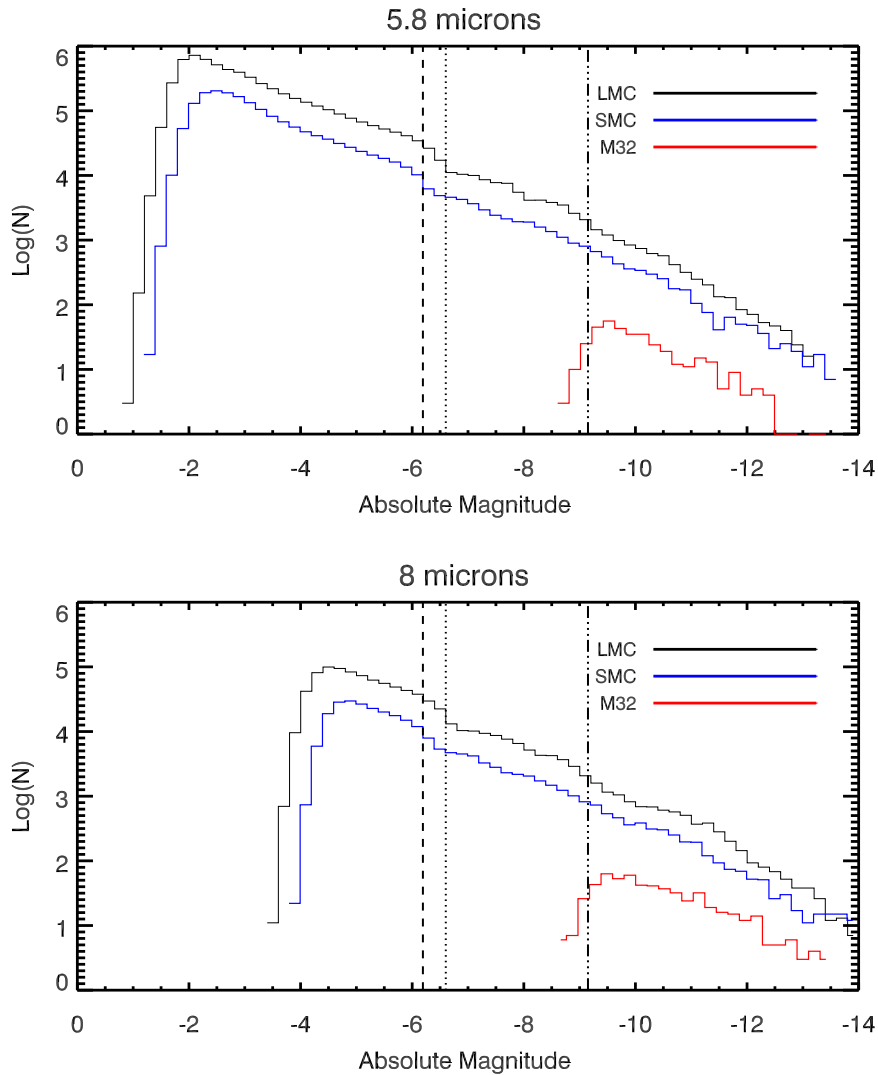
Figure 6.10: Comparison of the M32 and Magellanic Cloud luminosity functions. The red line represents all sources detected within 3.5′ of M32's centre; the black line represents the SAGE-LMC observations and the blue line represents the SAGE-SMC observations (Boyer et al. 2011). The dotted-dashed line marks the 50% completeness limit. The dotted line marks the 3.6 μm TRGB for the LMC and the dashed line shows the TRGB for the SMC.

6.4.2   IRAC Colour-Magnitude Diagrams

Mid-IR colour-magnitude diagrams (CMDs) for the inner regions of M32 ($R < 3.5'$) are presented in Figures 6.11 and 6.12. At these wavelengths stellar temperature no longer affects the CMD, and any features seen are due to the absorption and emission by circumstellar molecular and dust species. The well-defined vertical branch with zero colour in these diagrams traces foreground stars and dust free blue-supergiants in M31. The relatively low number of sources that fall on this branch indicates a nominal level of contamination from foreground sources within 3.5′ of the centre of M32.

The [8.0] vs. [5.8]–[8.0] colour-magnitude diagram provides the best representation of the 'true' stellar population of M32, as these bands are least effected by contamination from M31.

As we probe to fainter magnitudes photometric errors become more significant, this may be responsible for the large spread in colour for $[3.6] \leq 16.5$ in the [3.6] vs. [3.6]–[4.5] colour-magnitude diagram. It should be noted that sources towards the centre of M32 may be not accurately extracted at one or more wavelengths due to crowding. Although care had been taken to remove blended sources from the catalogue, blends may potentially affect the derived colours by enhancing the IRAC flux. We expect this to influence $\lesssim 4$ per cent of the sources in the CMDs, if we assume all detections with a magnitude enhancements greater than 3σ are blends.

The stellar sequences traced by the diagonal branches in the CMDs are difficult to isolate, making it difficult to accurately classify the different populations of cool evolved stars. Using the mid-IR colour-classification scheme from Boyer et al. (2011), we identify a large population of heavily dust-enshrouded extreme evolved stars (X-AGB stars) with $[3.6]-[8] > 0.8$. This correspond to 54.5 per cent of the sources with detections in both channels. In non-star-forming galaxies like M32 contamination from young stellar objects should be negligible, however unresolved background galaxies may contaminate the X-AGB sample. To eliminate these we apply an additional colour-cut in the $[3.6]-[8]$ vs. [8] CMD, which is adjusted for M32's distance
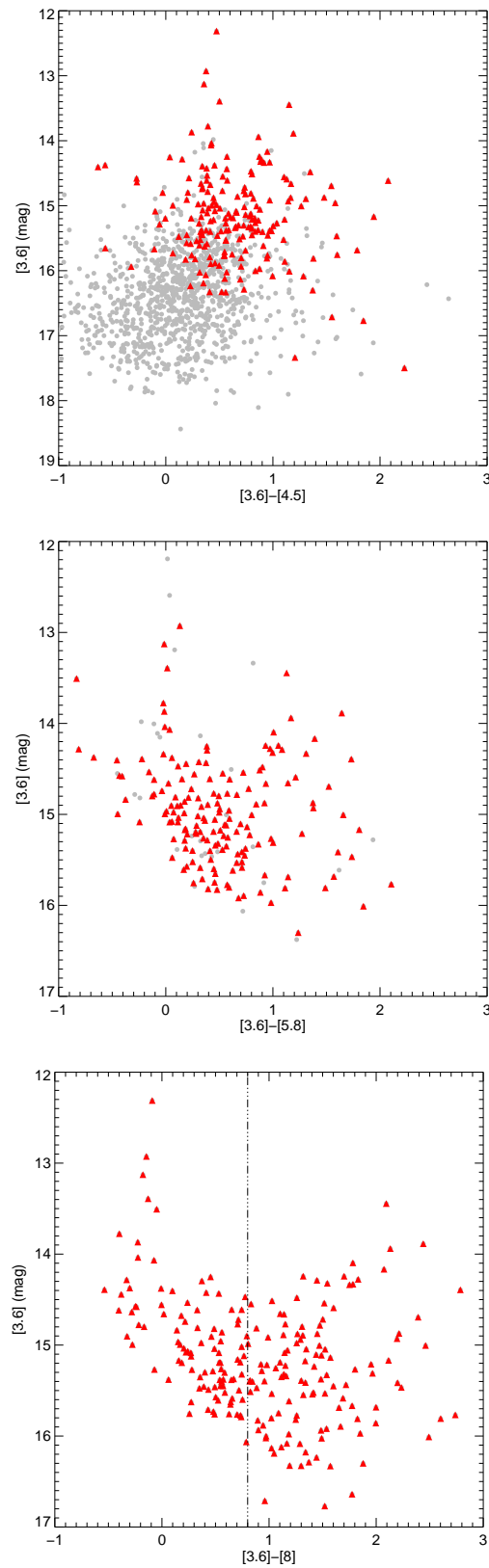
Figure 6.11: *Spitzer* IRAC CMDs of M32. For all panels the y-axis is the apparent 3.6 μm magnitude. The red triangles indicate a 8-μm counterpart. The initial colour-cut used to select X-AGB stars is indicated by the dashed line.
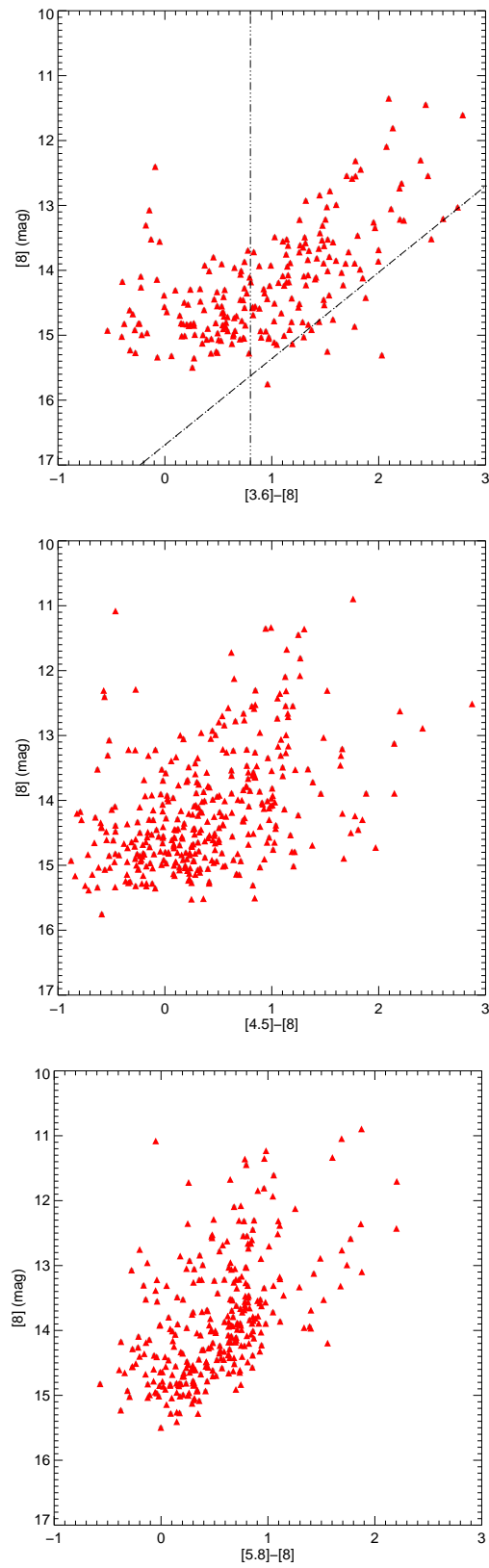
Figure 6.12: *Spitzer* IRAC CMDs of M32. For all panels the y-axis is the apparent 8.0 μm magnitude. The colour-cuts used to select X-AGB stars are indicated by the dashed lines.
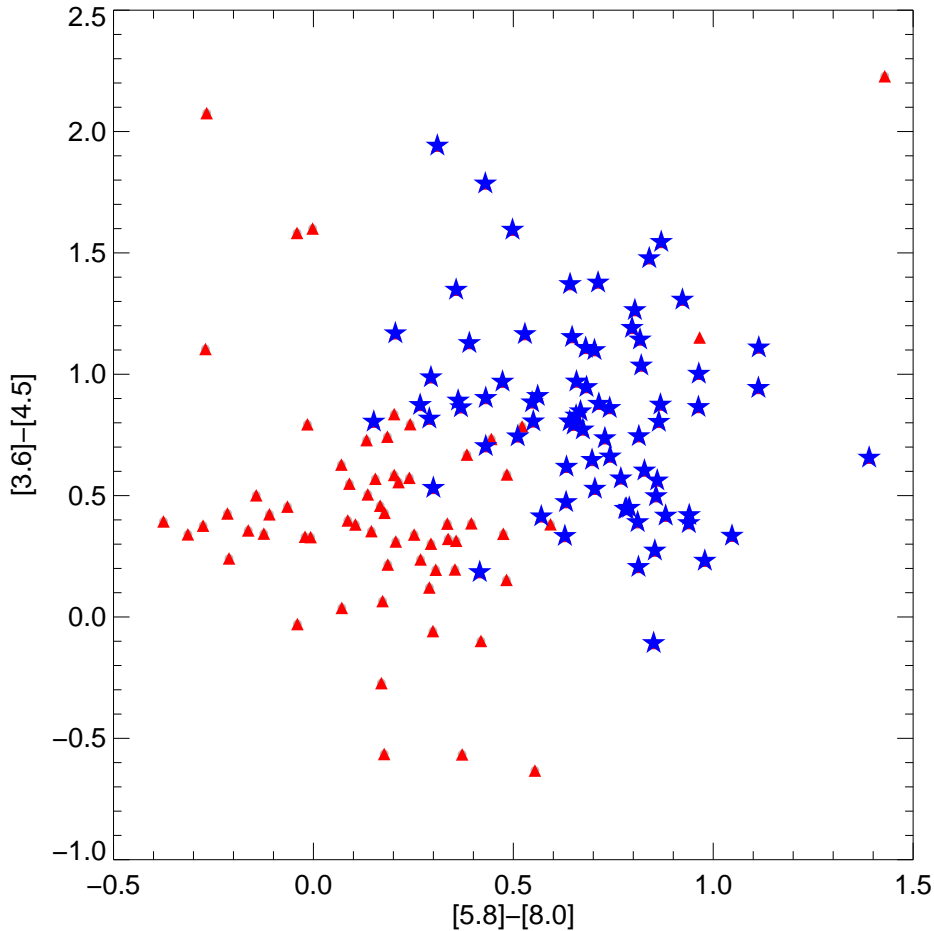
Figure 6.13: IRAC [3.6] − [4.5] vs. [5.8] − [8.0] colour-colour diagram of M32. The extreme AGB stars in our sample are indicated by blue stars.

from Boyer et al. (2011) and defined as:

$$[8] = 17.4 - (1.33 \times [3.6] - [8]); \quad [3.6] - [8] < 3.0. \tag{6.2}$$

11 X-AGB sources do not fall with in this range, reducing the final number of X-AGB stars to 110. The colour-cuts used to identify the X-AGB stars are plotted in Figures 6.11 and 6.12. Other colour-cuts used to identify O-AGB and C-AGB stars require additional near-IR photometry.

In Figure 6.13 we show the IRAC [3.6]−[4.5] vs. [5.8]−[8.0] colour-colour diagram of all the sources within 3.5′ of M32's centre. The extreme AGB stars in our sample

are indicated by blue stars. These sources are often obscured in the optical and near-IR due to circumstellar dust extinction and are bright at 8 μm due to thermal emission by the same dust. The red colours for the majority of the other sources are consistent with mass-losing AGB stars.

6.5   Future Prospects

The aim of this work was to investigate the resolved stellar populations of M32 via its mid-IR luminosity functions. Unfortunately, our analysis is hampered by contamination from M31 and our data is of limited diagnostic value. Our data suggests that we are probing an intermediate age metal-rich population of stars, but a less contaminated point-source catalogue is required for confirmation. In the following section we give an overview of some future prospects for IR population studied of M32.

Although the coolant for *Spitzer* was depleted in May 2009 rendering the long-wavelength instruments redundant; the two shortest wavelength channels of the IRAC instrument are still operational. *Spitzer* is currently undergoing a 'warm' phase of observations operating with full efficiency and approximately the same sensitivity at 3.6 and 4.5 μm .

Using Warm Spitzer in the 3.6 and 4.5 micron bands we plan to obtain a dedicated background pointing at an appropriate location near M32 and at the same isophotal level within M31. These measurements will clearly provide an ideal counterpart to our data, enabling us us measure the IR profile of M31 and subtract this from the analysis of M32's stellar populations.

We could also estimate the infrared stellar background due to M31 by constructing a stellar density profile using *Hubble* observations of M31 and M32, and combining these with stellar population estimates for M31 in the infrared. This would provide some additional constraints on the overall level of contamination, although it would not provide enough detail to constrain the magnitude distribution of the M31 stars, required to correct the luminosity functions.

The luminosity functions we have obtained for M32 are deep enough to resolve stars to a few magnitudes below the AGB Tip. If we could constrain the contamination from M31 in each magnitude bin it would be possible to compare our data to predicted luminosity functions derived from evolutionary stellar population synthesis models. By comparing the IR luminosity functions with model predictions we would be able to constrain the age and metallicity of the stellar populations and thus provide an insight into the star formation history of M32 and determine how this has evolved with time.

The population of extreme AGB stars in M32 identified in Section 6.4.2 is composed of both C-rich and O-rich stars. To discriminate between an oxygen-rich or carbon-rich chemistry we plan to fit their SEDs with the   models; this will provide an oxygen-rich or carbon-rich classification for these sources. Furthermore, by applying the   model grid to the whole population of evolved stars in M32 we will obtain some preliminary estimates of the dust-production rates for individual sources and the mass return to the ISM of the galaxy. Due to the limited wavelength coverage of the SEDs the uncertainties in the fits will be large, thus it is highly desirable to extend the SED using the MIPS observations to constrain our fitting. However, care will need to be taken as the beamsize will increase from 1.9″at 8 μm to 5.8″for MIPS 24 μm .

6.5.1   Observing M32 with the JWST

The next infrared space telescope, the *James Webb Space Telescope* (JWST), will have a superior angular resolution and greater sensitivity to *Spitzer* in the mid-IR. The expected beam-size of ~0.065″pixel^{-1} at 3.56 μm and ~0.11″pixel^{-1} at 7.7 μm will provided the spatial resolution necessary to identify stars close to the core of M32. At larger radial distances it will be able to better separate the individual evolved stars, allowing for cleaner measurements of M32's stellar population. Furthermore, its improved sensitivity will also allow a deeper examination of the stellar populations to below the red-giant branch tip.

Given the high stellar density near the centre of M32, the superior resolution of *JWST* may be offset by its increased sensitivity. Thus, the magnitudes and spatial distribution of M32 stars found by this work combined with stellar population models (to estimate what fraction of stars emit at these wavelengths) may act as a useful pathfinder for future observations with *JWST*.

6.6   Summary and Conclusions

In this chapter we have presented mid-infrared observations of the dwarf elliptical galaxy M32, obtained with the Infrared Array Camera on board the *Spitzer Space Telescope*. These images resolve individual stars in the bulge of M32, revealing a rich population of dusty evolved stars. Despite the crowded nature of the field, the presence of 8-μm sources at large radial distances from the nucleus of M32 and the lack of a brightness gradient is consistent with these being single stars.

Despite the strong levels of contamination from M31, we find that luminous stars with significant dust emission dominate the 5.8- and 8-μm luminosity functions. We estimate the tip of the AGB to be $M_{8.0} = 14$ mag and resolve stars to depths ~3 mag fainter than this limit. We do not reach the red giant branch tip. These luminous AGB stars may be the traces of an intermediate age population in M32 with lifetimes of ~ 2–8 Gyr.

Using mid-IR photometric criteria, we identify 110 extreme (X-AGB) star candidates, corresponding to approximately half of all sources detected at 3.6 and 8 μm. These are extremely red stars and are highly enshrouded by dust, thus they will often be missed in optical and near-IR surveys. In the Magellanic Clouds the majority of the dust input into the ISM comes from the extreme AGB stars; we expect a similar scenario to occur in M32.

The next generation of IR telescopes such as *JWST* and *SPICA* will offer a remarkable improvement in sensitivity and spacial resolution. With these instruments it will be possible to study the stellar content to M32 to well below the RGB tip. Future ob-

servations of M32 would benefit from a comparison field at the same isophotal level in the outer disk of M31 to provide a more complete picture of the contamination by sources nearby in the M31 disk.

7

Conclusions and Future Work

7.1 Conclusions

The aim of this thesis was to address some of the open questions surrounding the effect of metallicity on the production of dust around oxygen-rich evolved stars and the stellar populations of Local Group galaxies. By disentangling the stellar content of nearby galaxies, and by constraining how the mineralogy and chemistry of dust produced by individual evolved stars depends on metallicity, a global picture on the enrichment of the ISM by evolved stars can be obtained.

The SAGE-Spec collaboration (Kemper et al. 2010) has compiled a homogeneously reduced catalogue of mid-IR observations of point sources in the Magellanic Clouds. As part of this large collaboration I have been involved in calculating bolometric magnitudes for the point sources, and was one of the main contributors to the subsequent spectroscopic classification process (see Chapter 2). My work on bolometric magnitudes provides a means to discriminate O-AGB stars and RSGs based on their 5–38 μm spectra, which otherwise exhibit similar dust emission characteristics. These classifications improve our understanding of the stellar populations of the Magellanic Clouds and allow verification of the photometric classifications (i.e., the colour-colour and colour-magnitude cuts) used by the SAGE-LMC, SAGE-SMC and HERITAGE surveys. We find that the photometric classifications are generally in good agreement

with the spectroscopic classifications, however, the colour-cuts used to select AGB stars often omit the reddest O-rich evolved stars (Woods et al., 2011, Ruffle et al., in prep., Woods et al., in prep.).

Comparing large spectroscopic samples of O-rich evolved stars from the Galaxy, LMC and SMC is of particular interest because of the different metal content in the dust-forming region of their circumstellar envelopes. To investigate dust production around O-rich evolved stars, I have collated a sample of *Spitzer Space Telescope* and *Infrared Space Observatory* spectra of 217 oxygen-rich AGB stars and 98 RSGs in the Milky Way, the Magellanic Clouds and Galactic globular clusters. These spectra cover a range of metallicities and dust-production rates.

I have used this sample to investigate the formation mechanism of crystalline silicates (Chapter 3). I determined the strength of the crystalline silicate features in oxygen-rich evolved stars across a range of metallicities, in order to break the degeneracy between the dust and gas density in the outflow, and hence constrain the formation process of crystalline grains. I computed dust mass-loss rates using a grid of radiative transfer models calculated by Sargent et al. (2011), whilst gas mass-loss rates were calculated by scaling the dust mass-loss rates using an assumed gas-to-dust ratio based on the metallicity. My results show that the crystallinity appears to be more strongly correlated with the dust mass-loss rate than the gas mass-loss rate, which suggests that annealing of the amorphous silicate grains by radiation is probably the primary formation mechanism.

I also examined how the mineralogy of crystalline silicate dust around oxygen-rich stars depends on metallicity (Chapter 4). From variations in the position and strength of the crystalline silicate features it is possible to accurately determine the minerals present, by comparing the observed spectral features to laboratory spectra of different dust species. I found strong evidence of a change in the crystalline silicate mineralogy with metallicity: while forsterite (Mg_2SiO_4) is the dominant crystalline species at solar metallicity, enstatite ($MgSiO_3$) becomes preferentially formed at low metallicity. This variation in the olivine-to-pyroxene ratio can be explained by a number of possible

mechanisms. This also provides an insight into how oxygen-rich evolved stars enrich the ISM as galaxies evolve.

Standard dust condensation sequences for O-rich AGB stars propose the formation of alumina-rich grains before silicates. In order to evaluate the alumina abundances in the circumstellar envelopes of oxygen-rich AGB stars in the Magellanic Clouds, I computed a grid of   radiative transfer-models for a range of dust compositions, mass-loss rates, dust shell inner radii and stellar parameters. This grid is presented in Chapter 5 where I compare the resulting synthetic colours in the 2MASS, *Spitzer*, *AKARI* and *WISE* bands with the observed oxygen-rich AGB stars and RSGs from the SAGE-Spec LMC sample, finding good overall agreement for stars with a mid-infrared excess. The *AKARI* satellite contains filters that can directly measure the 10-μm emission feature, making them important for constraining the fractional abundance of alumina in oxygen-rich evolved stars. I show from dust models that the *AKARI* [11]–[15] versus [3.2]–[7] colour is a robust indicator of the alumina abundance.

A minimisation procedure was used to fit the models to the *Spitzer* IRS spectra and broadband photometry of 37 O-AGB stars in the LMC with optically thin circumstellar envelopes. From the modelling, I find mass-loss rates in the range $\sim 8 \times 10^{-8}$ to 5×10^{-6} $M_\odot$ yr^{-1}, and show that a grain mixture consisting primarily of amorphous silicates, with contributions from amorphous alumina and metallic iron, provides a good fit to the observed spectra. In agreement with previous studies, I find a correlation between the dust composition and mass-loss rate; the lower the mass-loss rate the higher the percentage of alumina in the shell.

In Chapter 6 I expand the infrared stellar population studies to the Local Group dwarf elliptical galaxy M32 (NGC 221), using deep *Spitzer* IRAC observations. M32 is of interest as it contains a substantial population of stars in the late stages of evolution that are prominent in the infrared; these stars are often obscured in optical and near-infrared surveys. Previous photometric studies of M32 have been limited to shorter wavelengths, thus by obtaining IRAC observations of M32 we sample a population of stars in M32 that have been hitherto unknown. Furthermore, it enables us to compile a

preliminary mass loss inventory for this old stellar population.

Although there is a high degree of stellar crowding and strong levels of contamination from M31, our images spatially resolve the dust-producing AGB population of M32 at 3.6–8.0 μm. We identify 110 extreme (X-AGB) star candidates in our field of view; these are extremely red stars and are highly enshrouded by dust. We estimate the tip of the AGB to be $M_{8.0}$ = 14 mag and believe our photometric data to be reasonably complete to depths ~3 mag fainter than this limit. These luminous AGB stars may be the traces of an intermediate age population in M32. Future research in this area would benefit from a more complete picture of the contamination from M31.

7.2   Future Work

Theoretical predictions of the composition and amounts of dust returned to the ISM by evolved stars have been calculated by Ferrarotti & Gail (2006) and Zhukovska et al. (2008) for a range of initial stellar masses and metallicities. The validity of these models can be tested by comparing the dust composition of evolved stars in the Local Group to the predicted compositions and theoretical dust yields. The point source classifications returned by SAGE–Spec (Woods et al., 2011, Ruffle et al., in prep., Woods et al., in prep.) provide an ideal sample with which to test these predictions for sub–solar metallicities.

Current estimates of the global dust production from AGB and RSG stars indicate that 'extreme' AGB stars (which comprise 4% of the population) are responsible for most (~ 88%) of dust input into the ISM (Riebel et al. 2012). Given the importance of these extreme sources to the total dust budget, it is interesting to note that 12 of these 'extreme' sources lie outside the defined evolved star colour cuts but are spectroscopically identified as carbon stars (Gruendl et al. 2008). The revised photometric classifications will enable better estimates of the total dust input from evolved stellar populations in the Magellanic Clouds. It also enables rare objects, which would be missed by conservative cuts, to be classified.

Extreme AGB stars are poorly constrained by the current grids of radiative transfer models. Although not very common, *Spitzer* spectroscopy is available for six extreme O-rich AGB stars in the LMC. These spectra have partially self-absorbed 10-micron silicate features and are similar in appearance to WX Psc, a well studied AGB star in the Milky Way. In order to derive the properties of the dust and the rate of dust production by these stars, I am planning to model these sources using the 2D dust radiative transfer codes M M , as VLTI observations suggest that axisymmetric structures in the shells of extreme stars are relativly common (Ohnaka et al. 2008). The results of this modelling will be compared to the extreme O-rich AGB stars in the Milky Way.

Another avenue for future investigation is the relation between pulsation-phase and mid-IR spectral profile variations of long-period variable stars in the LMC. Two sources in our sample, IRAS 04544−6849 (SSID 4076–4081) and HV 2446 (SSID 4324–4329) have been observed at different phases of their pulsation cycle. These spectra display large variations in the shape and strength of the 10-μm feature over the observed period. Detailed radiative modelling of the dust shell as a function of pulsation phase will provide an accurate breakdown of the wind characteristics at a precise phase of the pulsation cycle. These temporal variations can then be taken into account when interpreting large-scale modelling efforts, as all other stars in our sample are known pulsating stars observed at a single phase in their cycle.

To quantify the total rate of the chemical enrichment of the ISM by dusty evolved stars it is essential to correctly take into account their total mass loss. As was mentioned in Chapter 3, determining the total mass-loss rate requires detailed knowledge of the stars' expansion velocity and the dust-to-gas ratio in the stellar wind; these are not well constrained, even for Milky Way sources. Measurements of expansion velocities from OH maser emission at 1612 MHz (Marshall et al. 2004) provide some indication of the outflow velocity during the superwind phase of evolution for AGB stars in the LMC. However, OH masers are found only in oxygen-rich stars with high mass-loss rates and thus cannot provide wind speed measurements across the whole AGB population. A better constraint of both the wind speed and gas density may be

provided by submillimeter observations of carbon monoxide (CO). Large surveys of emission from CO in the envelopes around carbon stars and oxygen-rich AGB stars and RSGs in the Magellanic Clouds will become possible with the completion of the full ALMA array. The high sensitivity and spatial resolution provided by ALMA in the 3 mm to 400 μm wavelength range will enable the detection of spectral line emission from CO in extragalactic AGB stars within a few minutes for the CO J = 2–1 and J = 3–2 transitions at 230 and 345 GHz (Woods et al. 2012). This will yield reliable values for the wind expansion velocities and improve the accuracy of the derived gas mass-loss rates.

ALMA can also be used look for cold dust emission at submm wavelengths in massive evolved stars. High–resolution imaging of the dust emission structure from the condensation zone to the wind–ISM interface, combined with dynamical information from the outflow, will enable the full mass-loss history of the AGB star to be determined. Variations from an r^{-2} density distribution will probe the different mass loss processes occurring on the AGB over different timescales, for example, the thermal pulse cycle (few 10^4 years) and stellar pulsation (hundred of days). Deviations from spherical symmetry would also provide insights into the mass loss process. In collaboration with several colleagues, an ALMA proposal was submitted to image these structures for a Galactic AGB star. We intend re-submit this proposal and extend the study to a large, statistically significant survey once ALMA's full capabilities are available.

These measurements will also provide radii for input into radiative transfer models; this is required to constrain emission from cold dust. Prior assumptions may overestimate the extent of the dust shell, which results in a significant underestimate of the dust production rate. This is a consequence of the emerging properties of the spectral energy distribution depending strongly on the value of the outer radius.

Establishing reliable dust-production and total mass-loss rates for AGB stars is vital. Currently, dust mass-loss rates are estimated using a number of independent radiative transfer models with an arbitrary choice of model. Similar model inputs

between codes may return vastly different results, however no detailed study has been performed to quantify these differences.

As a first step in standardising radiative transfer computations it is important to constrain these differences for different chemical types over a wide range of mass-loss rates. There are nine commonly used codes, which I plan to compare using one simple scenario and one realistic scenario for AGB stars with different photospheric chemistries, at both high and low mass-loss rates. This will yield an unbiased view on the influence of the radiative transfer code on the model outputs and the reliability of mass-loss rate estimates can be evaluated.

To obtain an assessment of contribution from the different classes of stellar object to the dust budget of the Milky Way, a comprehensive and unbiased volume-limited imaging survey is required. With SOFIA (Stratospheric Observatory for Infrared Astronomy), large multi-band photometric surveys of dusty point sources in the Galaxy can be conducted. SOFIA is not limited to the brightest point sources, it can also study the faint (~1 Jy) stellar populations. For the first time, these photometric measurements can be combined with accurate distances of stars in the Milky Way obtained from *GAIA* (due to be launched in November 2013). *GAIA* will provide accurate distances to ~10^5 AGB stars by measuring their parallaxes. This will enable the production of colour-magnitude diagrams for our own Galaxy.

This will place significant constraints on the mass-loss rates from evolved stars which is crucial in determining the dust-budget in our Galaxy. Following up these observations with a colour selected spectroscopic sample would yield a wealth of data to trace the life-cycle of dust in the Milky Way. This step is vital for a proper understanding of the role of metallicity in the mass-loss and dust-formation processes in evolved stars. Moreover, it will establish the framework for the interpretation of the dust composition of more distant galaxies in the near and far in the Universe.

Followup observations with the SOFIA/FORCAST spectrograph for a sample of O-rich AGB stars in the Milky Way with low-contrast amorphous dust would also be of interest. While the silicates produced by O-rich AGB stars tend to be mostly

magnesium–rich (Molster et al. 2002), iron-rich crystalline silicates have been tentatively detected in some Galactic O-rich AGB stars with low density dust shells (Guha Niyogi et al., 2011). This detection calls the classic dust condensation sequence into question. These observations would allow us to: i) confirm or refute the presence of iron–rich crystalline silicates in AGB stars; ii) understand how these crystalline silicates evolve along the AGB; and finally: iii) assess the contribution from these stars to the mass budget of galaxies.

The next generation of telescopes will be able to observe the stellar populations in M31 and to quantify its total dust budget. M31 is the nearest spiral galaxy, at 780 kpc (Peacock et al., 2011). It is also the only galaxy within the Local Group that is comparable to the Milky Way in terms of morphology and mass. Future large scale mid-IR surveys with the *JWST* and *SPICA* would complement the recent Panchromatic Hubble Andromeda Treasury survey (PHAT; Dalcanton et al., 2012) of M31, and the existing SAGE *Spitzer* legacy surveys of the Magellanic Clouds and aid our understanding of how dust has affected the evolution of galaxies.

7.3   Concluding Remarks

Prior to the launch of *Spitzer*, IR observations of extragalactic AGB stars was limited to the brightest sources in near-by galaxies. The capabilities of *Spitzer* has enabled a complete census of AGB dust production in the Magellanic Clouds, Galactic globular clusters and other Local Group dwarf galaxies. From these observations we have been able to determine the composition of circumstellar dust at different metallicities and quantify the dust-production rate of entire populations of AGB stars in galaxies. Our observations of M32 have pushed the sensitivity and resolving capabilities of *Spitzer* to its limits, detecting only the brightest stellar components of this system. In the *JWST* era, it will be possible to achieve observations comparable to those of M32 in galactic systems outside the Local Group.

References

Aden, A. 1951, Journal of Applied Physics, 22, 1242

Allard, F., Homeier, D., & Freytag, B. 2011, in Astronomical Society of the Pacific Conference Series, Vol. 448, Astronomical Society of the Pacific Conference Series, ed. C. Johns-Krull, M. K. Browning, & A. A. West, 91

Ashman, K. M. & Zepf, S. E. 1998, Globular Cluster Systems

Baade, W. 1944, ApJ, 100, 137

Barmby, P., Ashby, M. L. N., Bianchi, L., et al. 2006, ApJL, 650, L45

Barnbaum, C., Kastner, J. H., Morris, M., & Likkel, L. 1991, A&A, 251, 79

Begemann, B., Dorschner, J., Henning, T., et al. 1997, ApJ, 476, 199

Beichman, C. A., Neugebauer, G., Habing, H. J., Clegg, P. E., & Chester, T. J., eds. 1988, Infrared astronomical satellite (IRAS) catalogs and atlases. Volume 1: Explanatory supplement, Vol. 1

Bekki, K. & Chiba, M. 2007, MNRAS, 381, L16

Benacquista, M. 2002, Living Reviews in Relativity, 5, 2

Bendinelli, O., Zavatti, F., Parmeggiani, G., & Djorgovski, S. 1992, AJ, 103, 110

Bendo, G. J., Galliano, F., & Madden, S. C. 2012, MNRAS, 423, 197

Biermann, P. & Harwit, M. 1980, ApJL, 241, L105

Blanco, B. M., Blanco, V. M., & McCarthy, M. F. 1978, Nature, 271, 638

Blanco, V. M., Blanco, B. M., & McCarthy, M. F. 1980, ApJ, 242, 938

Blöcker, T., Herwig, F., & Driebe, T. 2000, Mem. Soc. Astron. Italiana, 71, 711

Bloecker, T. 1995, A&A, 297, 727

Blommaert, J. A. D. L., Groenewegen, M. A. T., Okumura, K., et al. 2006, A&A, 460, 555

Blum, R. D., Mould, J. R., Olsen, K. A., et al. 2006, AJ, 132, 2034

Bohren, C. F. 1983, Tellus Series B Chemical and Physical Meteorology B, 35, 65

Bohren, C. F. & Huffman, D. R. 1983, Absorption and scattering of light by small particles, ed. Bohren, C. F. & Huffman, D. R.

Bolatto, A. D., Simon, J. D., Stanimirović, S., et al. 2007, ApJ, 655, 212

Boothroyd, A. I., Sackmann, I., & Ahern, S. C. 1993, ApJ, 416, 762

Boulanger, F., Cox, P., & Jones, A. P. 2000, in Infrared Space Astronomy, Today and Tomorrow, ed. F. Casoli, J. Lequeux, & F. David, 251

Bouwman, J., de Koter, A., van den Ancker, M. E., & Waters, L. B. F. M. 2000, A&A, 360, 213

Bouwman, J., Meeus, G., de Koter, A., et al. 2001, A&A, 375, 950

Bowen, G. H. 1988, ApJ, 329, 299

Bowen, G. H. & Willson, L. A. 1991, ApJL, 375, L53

Bowey, J. E. & Adamson, A. J. 2002, MNRAS, 334, 94

Boyer, M. L., Srinivasan, S., Riebel, D., et al. 2012, ApJ, 748, 40

Boyer, M. L., Srinivasan, S., van Loon, J. T., et al. 2011, AJ, 142, 103

Boyer, M. L., van Loon, J. T., McDonald, I., et al. 2010, ApJL, 711, L99

Bradley, J. P. 1994, Science, 265, 925

Brown, T. M., Smith, E., Ferguson, H. C., et al. 2008, ApJ, 682, 319

Brucato, J. R., Mennella, V., Colangeli, L., Rotundi, A., & Palumbo, P. 2002, Planet. Space Sci., 50, 829

Buchanan, C. L., Kastner, J. H., Forrest, W. J., et al. 2006, AJ, 132, 1890

Caciolli, A., Mazzocchi, C., Capogrosso, V., et al. 2011, A&A, 533, A66

Cami, J. 2002, PhD thesis, University of Amsterdam

Cami, J., de Jong, T., Justtannont, K., Yamamura, I., & Waters, L. B. F. M. 1998, Ap&SS, 255, 339

Cami, J., Yamamura, I., de Jong, T., et al. 2000, A&A, 360, 562

Cau, P. 2002, A&A, 392, 203

Chen, X. & Shen, Z.-Q. 2008, ApJ, 681, 1574

Chihara, H., Koike, C., Tsuchiyama, A., Tachibana, S., & Sakamoto, D. 2002, A&A, 391, 267

Cioni, M. & Habing, H. J. 2003, A&A, 402, 133

Cioni, M., van der Marel, R. P., Loup, C., & Habing, H. J. 2000, A&A, 359, 601

Cioni, M.-R. L., Girardi, L., Marigo, P., & Habing, H. J. 2006, A&A, 452, 195

Coelho, P., Mendes de Oliveira, C., & Cid Fernandes, R. 2009, MNRAS, 396, 624

Cohen, M., Wheaton, W. A., & Megeath, S. T. 2003, AJ, 126, 1090

David, P. & Papoular, R. 1990, A&A, 237, 425

Davidge, T. J. & Jensen, J. B. 2007, AJ, 133, 576

Day, K. L. & Donn, B. 1978, ApJL, 222, L45

De Beck, E., Decin, L., de Koter, A., et al. 2010, A&A, 523, A18

de Graauw, T., Haser, L. N., Beintema, D. A., et al. 1996, A&A, 315, L49

de Vries, B. L., Klotz, D., Lombaert, R., et al. 2011, in Astronomical Society of the Pacific Conference Series, Vol. 445, Why Galaxies Care about AGB Stars II: Shining Examples and Common Inhabitants, ed. F. Kerschbaum, T. Lebzelter, & R. F. Wing, 621

de Vries, B. L., Min, M., Waters, L. B. F. M., Blommaert, J. A. D. L., & Kemper, F. 2010, A&A, 516, A86

Decin, L., De Beck, E., Brünken, S., et al. 2010, A&A, 516, A69

Decin, L., Hony, S., de Koter, A., et al. 2007, A&A, 475, 233

Decressin, T., Meynet, G., Charbonnel, C., Prantzos, N., & Ekström, S. 2007, A&A, 464, 1029

Demyk, K., Dartois, E., Wiesemeyer, H., Jones, A. P., & d'Hendecourt, L. 2000, A&A, 364, 170

Dijkstra, C., Speck, A. K., Reid, R. B., & Abraham, P. 2005, ApJL, 633, L133

Dijkstra, C., Waters, L. B. F. M., Kemper, F., et al. 2003, A&A, 399, 1037

Dominik, C., Gail, H.-P., & Sedlmayr, E. 1989, A&A, 223, 227

Dorschner, J., Begemann, B., Henning, T., Jaeger, C., & Mutschke, H. 1995, A&A, 300, 503

Draine, B. T. & Lee, H. M. 1984, ApJ, 285, 89

Draine, B. T. & Salpeter, E. E. 1979, ApJ, 231, 438

Dullemond, C. P. & Dominik, C. 2005, A&A, 434, 971

Dunne, L., Eales, S., Ivison, R., Morgan, H., & Edmunds, M. 2003, Nature, 424, 285

REFERENCES

Dupree, A. K. & Reimers, D. 1987, in Astrophysics and Space Science Library, Vol. 129, Exploring the Universe with the IUE Satellite, ed. Y. Kondo, 321–353

Dwek, E. 2004, ApJ, 607, 848

Egan, M. P., Van Dyk, S. D., & Price, S. D. 2001, AJ, 122, 1844

Fabian, D., Henning, T., Jäger, C., et al. 2001, A&A, 378, 228

Fabian, D., Jäger, C., Henning, T., Dorschner, J., & Mutschke, H. 2000, A&A, 364, 282

Fazio, G. G., Hora, J. L., Allen, L. E., et al. 2004, ApJS, 154, 10

Feast, M. 1999, in IAU Symposium, Vol. 190, New Views of the Magellanic Clouds, ed. Y.-H. Chu, N. Suntzeff, J. Hesser, & D. Bohlender, 542

Feautrier, P. 1964, Comptes Rendus Academie des Sciences (serie non specifiee), 258, 3189

Ferrarotti, A. S. & Gail, H. 2001, A&A, 371, 133

Ferrarotti, A. S. & Gail, H. 2002, A&A, 382, 256

Fiorentino, G., Contreras Ramos, R., Tolstoy, E., Clementini, G., & Saha, A. 2012, A&A, 539, A138

Fiorentino, G., Monachesi, A., Trager, S. C., et al. 2010, ApJ, 708, 817

Fleischer, A. J., Gauger, A., & Sedlmayr, E. 1992, A&A, 266, 321

Fluks, M. A., Plez, B., The, P. S., et al. 1994, A&AS, 105, 311

Fraser, O. J., Hawley, S. L., & Cook, K. H. 2008, AJ, 136, 1242

Fraser, O. J., Hawley, S. L., Cook, K. H., & Keller, S. C. 2005, AJ, 129, 768

Frogel, J. A. & Blanco, V. M. 1990, ApJ, 365, 168

Frogel, J. A. & Richer, H. B. 1983, ApJ, 275, 84

Frogel, J. A. & Whitelock, P. A. 1998, AJ, 116, 754

Furlan, E., Hartmann, L., Calvet, N., et al. 2006, ApJS, 165, 568

Gail, H. 2003, in Lecture Notes in Physics, Berlin Springer Verlag, Vol. 609, Astromineralogy, ed. T. K. Henning, 55–120

Gail, H. & Sedlmayr, E. 1988, A&A, 206, 153

Gail, H. & Sedlmayr, E. 1999, A&A, 347, 594

Gail, H.-P. 2010, in Lecture Notes in Physics, Berlin Springer Verlag, Vol. 815, Lecture Notes in Physics, Berlin Springer Verlag, ed. T. Henning, 61–141

Gauger, A., Sedlmayr, E., & Gail, H.-P. 1990, A&A, 235, 345

Gautschy-Loidl, R., Höfner, S., Jørgensen, U. G., & Hron, J. 2004, A&A, 422, 289

Gehrz, R. 1989, in IAU Symposium, Vol. 135, Interstellar Dust, ed. L. J. Allamandola & A. G. G. M. Tielens, 445

Gehrz, R. D. & Woolf, N. J. 1971, ApJ, 165, 285

Gielen, C., Bouwman, J., van Winckel, H., et al. 2011, A&A, 533, A99

Gielen, C., van Winckel, H., Min, M., Waters, L. B. F. M., & Lloyd Evans, T. 2008, A&A, 490, 725

Gilman, R. C. 1972, ApJ, 178, 423

Gomez, H. L., Clark, C. J. R., Nozawa, T., et al. 2012, MNRAS, 420, 3557

Gordon, K. D., Bailin, J., Engelbracht, C. W., et al. 2006, ApJL, 638, L87

Gordon, K. D., Clayton, G. C., Misselt, K. A., Landolt, A. U., & Wolff, M. J. 2003, ApJ, 594, 279

Gordon, K. D., Meixner, M., Meade, M. R., et al. 2011, AJ, 142, 102

Goumans, T. P. M. & Bromley, S. T. 2012, MNRAS, 420, 3344

Gratton, R. G., Bonifacio, P., Bragaglia, A., et al. 2001, A&A, 369, 87

Grebel, E. K. 1999, in IAU Symposium, Vol. 192, The Stellar Content of Local Group Galaxies, ed. P. Whitelock & R. Cannon, 17

Grillmair, C. J., Lauer, T. R., Worthey, G., et al. 1996, AJ, 112, 1975

Groenewegen, M. A. T. 1993, PhD thesis, Univ. of Amsterdam

Groenewegen, M. A. T. 1999, in IAU Symposium, Vol. 191, Asymptotic Giant Branch Stars, ed. T. Le Bertre, A. Lebre, & C. Waelkens, 535

Groenewegen, M. A. T. 2000, A&A, 363, 901

Groenewegen, M. A. T. 2006, A&A, 448, 181

Groenewegen, M. A. T., Sloan, G. C., Soszyński, I., & Petersen, E. A. 2009, A&A, 506, 1277

Groenewegen, M. A. T., Wood, P. R., Sloan, G. C., et al. 2007, MNRAS, 376, 313

Grossman, L. 1972, Geochim. Cosmochim. Acta, 36, 597

Guha Niyogi, S., Speck, A. K., & Onaka, T. 2011, ApJ, 733, 93

Habing, H. J. 1996, A&A Rev., 7, 97

Habing, H. J. & Olofsson, H., eds. 2003, Asymptotic giant branch stars (Springer)

Hackwell, J. A. 1972, A&A, 21, 239

Hallenbeck, S. L., Nuth, J. A., & Daukantas, P. L. 1998, Icarus, 131, 198

Härm, R. & Schwarzschild, M. 1961, AJ, 66, 45

Harris, J. & Zaritsky, D. 2004, AJ, 127, 1531

Harris, W. E. 1996, AJ, 112, 1487

Helling, C. & Winters, J. M. 2001, A&A, 366, 229

Heras, A. M. & Hony, S. 2005, A&A, 439, 171

Herman, J., Burger, J. H., & Penninx, W. H. 1986, A&A, 167, 247

Herwig, F. 2005, ARA&A, 43, 435

Higdon, S. J. U., Devost, D., Higdon, J. L., et al. 2004, PASP, 116, 975

Hilditch, R. W., Howarth, I. D., & Harries, T. J. 2005, MNRAS, 357, 304

Hirashita, H. 2012, MNRAS, 422, 1263

Höfner, S. 2007, in Astronomical Society of the Pacific Conference Series, Vol. 378,
    Why Galaxies Care About AGB Stars: Their Importance as Actors and Probes, ed.
    F. Kerschbaum, C. Charbonnel, & R. F. Wing, 145

Höfner, S. 2008, A&A, 491, L1

Höfner, S. 2009, in Astronomical Society of the Pacific Conference Series, Vol. 414,
    Cosmic Dust - Near and Far, ed. T. Henning, E. Grün, & J. Steinacker, 3

Höfner, S. & Andersen, A. C. 2007, A&A, 465, L39

Höfner, S., Jorgensen, U. G., Loidl, R., & Aringer, B. 1998, A&A, 340, 497

Hony, S., Heras, A. M., Molster, F. J., & Smolders, K. 2009, A&A, 501, 609

Houck, J. R., Roellig, T. L., van Cleve, J., et al. 2004, ApJS, 154, 18

Howley, K., Guhathakurta, P., van der Marel, R., et al. 2012, ArXiv e-prints

Hron, J., Aringer, B., & Kerschbaum, F. 1997, A&A, 322, 280

Hron, J., Aringer, B., Kerschbaum, F., et al. 2006, in Visions for Infrared Astron-
    omy, Instrumentation, Mesure, Métrologie, ed. V. Coudé du Foresto, D. Rouan, &
    G. Rousset, 107–110

Humphreys, R. M. 1978, ApJS, 38, 309

Iben, I. 1968, Nature, 220, 143

Iben, Jr., I. 1975, ApJ, 196, 525

Iben, Jr., I. & Renzini, A. 1983, ARA&A, 21, 271

Ita, Y., Matsuura, M., Ishihara, D., et al. 2010, A&A, 514, A2

Ita, Y., Onaka, T., Kato, D., et al. 2008, PASJ, 60, 435

Ivezic, Z. & Elitzur, M. 1995, ApJ, 445, 415

Ivezic, Z. & Elitzur, M. 1997, MNRAS, 287, 799

Jäger, C., Fabian, D., Schrempel, F., et al. 2003, A&A, 401, 57

Jäger, C., Molster, F. J., Dorschner, J., et al. 1998, A&A, 339, 904

Jensen, J. B., Tonry, J. L., Barris, B. J., et al. 2003, ApJ, 583, 712

Jeong, K. S., Winters, J. M., Le Bertre, T., & Sedlmayr, E. 2003, A&A, 407, 191

Jiang, B. W., Zhang, K., Li, A., & Lisse, C. M. 2013, ApJ, 765, 72

Jones, A. P. & Nuth, J. A. 2011, A&A, 530, A44

Jones, A. P., Tielens, A. G. G. M., & Hollenbach, D. J. 1996, ApJ, 469, 740

Jones, A. P., Tielens, A. G. G. M., Hollenbach, D. J., & McKee, C. F. 1994, ApJ, 433, 797

Jones, O. C., Kemper, F., Sargent, B. A., et al. 2012, MNRAS, 427, 3209

Justtanont, K., Olofsson, G., Dijkstra, C., & Meyer, A. W. 2006, A&A, 450, 1051

Karakas, A. & Lattanzio, J. C. 2007, Publications of the Astronomical Society of Australia, 24, 103

Kastner, J. H., Buchanan, C., Sahai, R., Forrest, W. J., & Sargent, B. A. 2010, AJ, 139, 1993

Kastner, J. H., Thorndike, S. L., Romanczyk, P. A., et al. 2008, AJ, 136, 1221

Kataza, H., Wada, T., Sakon, I., et al. 2012, in Society of Photo-Optical Instrumentation Engineers (SPIE) Conference Series, Vol. 8442, Society of Photo-Optical Instrumentation Engineers (SPIE) Conference Series

Kato, D., Ita, Y., Onaka, T., et al. 2012, AJ, 144, 179

Kemper, F., de Koter, A., Waters, L. B. F. M., Bouwman, J., & Tielens, A. G. G. M. 2002, A&A, 384, 585

Kemper, F., Vriend, W. J., & Tielens, A. G. G. M. 2004, ApJ, 609, 826

Kemper, F., Waters, L. B. F. M., de Koter, A., & Tielens, A. G. G. M. 2001, A&A, 369, 132

Kemper, F., Woods, P. M., Antoniou, V., et al. 2010, PASP, 122, 683

Kholopov, P. N., Samus, N. N., Frolov, M. S., et al. 1998, in Combined General Cata-

logue of Variable Stars, 4.1 Ed (II/214A). (1998), 0

King, I. 1962, AJ, 67, 471

Knapp, G. R. & Bowers, P. F. 1988, ApJ, 331, 974

Knapp, G. R., Sandell, G., & Robson, E. I. 1993, ApJS, 88, 173

Koike, C., Chihara, H., Tsuchiyama, A., et al. 2003, A&A, 399, 1101

Koike, C., Kaito, C., Yamamoto, T., et al. 1995, Icarus, 114, 203

Koike, C., Mutschke, H., Suto, H., et al. 2006, A&A, 449, 583

Koike, C., Suto, H., Tuchiyama, A., Shibai, H., & Tanabe, T. 1998, in IAU Symposium, Vol. 191, IAU Symposium, 305

Kraemer, K. E., Sloan, G. C., Price, S. D., & Walker, H. J. 2002, ApJS, 140, 389

Kraft, R. P., Sneden, C., Smith, G. H., et al. 1997, AJ, 113, 279

Krause, O., Birkmann, S. M., Rieke, G. H., et al. 2004, Nature, 432, 596

Kumar, B., Sagar, R., & Melnick, J. 2008, MNRAS, 386, 1380

Kwok, S. 2005, Journal of Korean Astronomical Society, 38, 271

Lafon, J. & Berruyer, N. 1991, A&A Rev., 2, 249

Lagadec, E. & Zijlstra, A. A. 2008, MNRAS, 390, L59

Lagadec, E., Zijlstra, A. A., Matsuura, M., et al. 2008, MNRAS, 383, 399

Lagadec, E., Zijlstra, A. A., Sloan, G. C., et al. 2009, MNRAS, 396, 598

Lamers, H. J. G. L. M., Zickgraf, F.-J., de Winter, D., Houziaux, L., & Zorec, J. 1998, A&A, 340, 117

Lattanzio, J. 2003, in IAU Symposium, Vol. 209, Planetary Nebulae: Their Evolution and Role in the Universe, ed. S. Kwok, M. Dopita, & R. Sutherland, 73

Lattanzio, J. C. & Wood, P. R. 2004, in Asymptotic Giant Branch Stars, ed. H. J. Habing & H. Olofsson, 23

Le Bertre, T. 1997, in Lecture Notes in Physics, Berlin Springer Verlag, Vol. 497, Stellar Atmospheres: Theory and Observations, ed. J. P. de Greve, R. Blomme, & H. Hensberge, 133

Le Gentil, G. 1755, Sav. étrangers, 137

Le Sidaner, P. & Le Bertre, T. 1996, A&A, 314, 896

Lebzelter, T., Posch, T., Hinkle, K., Wood, P. R., & Bouwman, J. 2006, ApJL, 653, L145

Levesque, E. M., Massey, P., Olsen, K. A. G., et al. 2005, ApJ, 628, 973

Little-Marenin, I. R. 1986, ApJL, 307, L15

Little-Marenin, I. R. & Little, S. J. 1990, AJ, 99, 1173

Lloyd Evans, T. 1991, MNRAS, 249, 409

Lodders, K. & Fegley, Jr., B. 1999, in IAU Symposium, Vol. 191, Asymptotic Giant Branch Stars, ed. T. Le Bertre, A. Lebre, & C. Waelkens (ASP), 279

Loup, C., Forveille, T., Omont, A., & Paul, J. F. 1993, A&AS, 99, 291

Luck, R. E., Moffett, T. J., Barnes, III, T. G., & Gieren, W. P. 1998, AJ, 115, 605

Maas, T., Van Winckel, H., & Lloyd Evans, T. 2005, A&A, 429, 297

Madau, P., Ferguson, H. C., Dickinson, M. E., et al. 1996, MNRAS, 283, 1388

Makovoz, D. & Marleau, F. R. 2005, PASP, 117, 1113

Marigo, P. 2002, A&A, 387, 507

Marigo, P. & Girardi, L. 2007, A&A, 469, 239

Marshall, J. R., van Loon, J. T., Matsuura, M., et al. 2004, MNRAS, 355, 1348

Massey, P., Lang, C. C., Degioia-Eastwood, K., & Garmany, C. D. 1995, ApJ, 438, 188

Massey, P. & Thompson, A. B. 1991, AJ, 101, 1408

Mathis, J. S., Rumpl, W., & Nordsieck, K. H. 1977, ApJ, 217, 425

Matsunaga, N., Mito, H., Nakada, Y., et al. 2008, PASJ, 60, 415

Matsuura, M., Dwek, E., Meixner, M., et al. 2011, Science, 333, 1258

Matsuura, M., Yamamura, I., Cami, J., Onaka, T., & Murakami, H. 2002, A&A, 383, 972

Matsuura, M., Zijlstra, A. A., Bernard-Salas, J., et al. 2007, MNRAS, 382, 1889

Matsuura, M., Zijlstra, A. A., van Loon, J. T., et al. 2005, A&A, 434, 691

McConnachie, A. W., Irwin, M. J., Ferguson, A. M. N., et al. 2005, MNRAS, 356, 979

McDonald, I., Boyer, M. L., van Loon, J. T., et al. 2011a, ApJS, 193, 23

McDonald, I., Sloan, G. C., Zijlstra, A. A., et al. 2010, ApJL, 717, L92

McDonald, I., van Loon, J. T., Decin, L., et al. 2009, MNRAS, 394, 831

McDonald, I., van Loon, J. T., Sloan, G. C., et al. 2011b, MNRAS, 417, 20

McDonald, I., White, J. R., Zijlstra, A. A., et al. 2012, MNRAS, 427, 2647

McQuinn, K. B. W., Woodward, C. E., Willner, S. P., et al. 2007, ApJ, 664, 850

Meixner, M., Galliano, F., Hony, S., et al. 2010, A&A, 518, L71

Meixner, M., Gordon, K. D., Indebetouw, R., et al. 2006, AJ, 132, 2268

Mie, G. 1908, Ann. Phys. Leipzig, 25, 377

Min, M., Dominik, C., & Waters, L. B. F. M. 2004, A&A, 413, L35

Min, M., Hovenier, J. W., & de Koter, A. 2003, A&A, 404, 35

Min, M., Waters, L. B. F. M., de Koter, A., et al. 2007, A&A, 462, 667

Molster, F. & Kemper, C. 2005, Space Science Reviews, 119, 3

Molster, F. J., Waters, L. B. F. M., Tielens, A. G. G. M., & Barlow, M. J. 2002a, A&A, 382, 184

Molster, F. J., Waters, L. B. F. M., Tielens, A. G. G. M., Koike, C., & Chihara, H. 2002b, A&A, 382, 241

Molster, F. J., Waters, L. B. F. M., Trams, N. R., et al. 1999a, A&A, 350, 163

Molster, F. J., Yamamura, I., Waters, L. B. F., et al. 2001, A&A, 366, 923

Molster, F. J., Yamamura, I., Waters, L. B. F. M., et al. 1999b, Nature, 401, 563

Monachesi, A., Trager, S. C., Lauer, T. R., et al. 2011, ApJ, 727, 55

Monnier, J. D., Geballe, T. R., & Danchi, W. C. 1998, ApJ, 502, 833

Moshir, M., ed. 1989, IRAS Faint Source Survey, Explanatory supplement version 1 and tape (California Institute of Technology, Pasadena)

Mould, J., Barmby, P., Gordon, K., et al. 2008, ApJ, 687, 230

Mutschke, H., Begemann, B., Dorschner, J., et al. 1998, A&A, 333, 188

Nelson, R., Thiemens, M., Nuth, J., & Donn, B. 1989, in Lunar and Planetary Science Conference Proceedings, Vol. 19, Lunar and Planetary Science Conference Proceedings, ed. G. Ryder & V. L. Sharpton, 559–563

Neugebauer, G., Habing, H. J., van Duinen, R., et al. 1984, ApJL, 278, L1

Nolthenius, R. & Ford, H. 1986, ApJ, 305, 600

Norris, B. R. M., Tuthill, P. G., Ireland, M. J., et al. 2012, Nature, 484, 220

Nowotny, W., Lebzelter, T., Hron, J., & Höfner, S. 2005, A&A, 437, 285

Nuth, III, J. A., Rietmeijer, F. J. M., & Hill, H. G. M. 2002, Meteoritics and Planetary Science, 37, 1579

Ohnaka, K., Bergeat, J., Driebe, T., et al. 2005, A&A, 429, 1057

Ohnaka, K., Driebe, T., Hofmann, K.-H., Weigelt, G., & Wittkowski, M. 2008, A&A, 484, 371

Olivier, E. A., Whitelock, P., & Marang, F. 2001, MNRAS, 326, 490

Olofsson, H. 2004, in Asymptotic Giant Branch Stars, ed. H. J. Habing & H. Olofsson, 325

Olofsson, H., González Delgado, D., Kerschbaum, F., & Schöier, F. L. 2002, A&A, 391, 1053

Onaka, T., de Jong, T., & Willems, F. J. 1989, A&A, 218, 169

Ordal, M. A., Bell, R. J., Alexander, Jr., R. W., Newquist, L. A., & Querry, M. R. 1988, Appl. Opt., 27, 1203

Origlia, L., Rood, R. T., Fabbri, S., et al. 2007, ApJL, 667, L85

Ossenkopf, V., Henning, T., & Mathis, J. S. 1992, A&A, 261, 567

Paczyński, B. 1971, Acta Astronomica, 21, 417

Pei, Y. C., Fall, S. M., & Hauser, M. G. 1999, ApJ, 522, 604

Percival, S. M., Salaris, M., van Wyk, F., & Kilkenny, D. 2002, ApJ, 573, 174

Pietrzyński, G., Graczyk, D., Gieren, W., et al. 2013, Nature, 495, 76

Pitman, K. M., Dijkstra, C., Hofmeister, A. M., & Speck, A. K. 2010, MNRAS, 406, 460

Pojmanski, G. 2002, Acta Astron., 52, 397

Posch, T., Kerschbaum, F., Mutschke, H., Dorschner, J., & Jäger, C. 2002, A&A, 393, L7

Posch, T., Kerschbaum, F., Mutschke, H., et al. 1999, A&A, 352, 609

Pritzl, B. J., Venn, K. A., & Irwin, M. 2005, AJ, 130, 2140

Reach, W. T., Megeath, S. T., Cohen, M., et al. 2005, PASP, 117, 978

Rebeirot, E., Martin, N., Prevot, L., et al. 1983, A&AS, 51, 277

Reimers, D. 1975, in Problems in stellar atmospheres and envelopes., ed. Baschek, B., Kegel, W. H., and Traving, G., 229–256

Richards, A. M. S., Yates, J. A., & Cohen, R. J. 1999, MNRAS, 306, 954

Riebel, D., Srinivasan, S., Sargent, B., & Meixner, M. 2012, ApJ, 753, 71

Rieke, G. H., Blaylock, M., Decin, L., et al. 2008, AJ, 135, 2245

Rietmeijer, F. J. M., Nuth, III, J. A., & Karner, J. M. 1999, ApJ, 527, 395

REFERENCES

Rietmeijer, F. J. M., Pun, A., & Nuth, III, J. A. 2009, MNRAS, 396, 402

Robitaille, T. P., Whitney, B. A., Indebetouw, R., & Wood, K. 2007, ApJS, 169, 328

Rose, J. A. 1985, AJ, 90, 1927

Rose, J. A., Arimoto, N., Caldwell, N., et al. 2005, AJ, 129, 712

Sackmann, I. 1980, ApJ, 235, 554

Sage, L. J., Welch, G. A., & Mitchell, G. F. 1998, ApJ, 507, 726

Samus, N. N., Durlevich, O. V., & et al. 2004, VizieR Online Data Catalog, 2250, 0

Sarajedini, A., Yang, S.-C., Monachesi, A., Lauer, T. R., & Trager, S. C. 2012, MN-RAS, 425, 1459

Sargent, B. A., Forrest, W. J., Tayrien, C., et al. 2009, ApJS, 182, 477

Sargent, B. A., Srinivasan, S., & Meixner, M. 2011, ApJ, 728, 93

Sargent, B. A., Srinivasan, S., Meixner, M., et al. 2010, ApJ, 716, 878

Schaefer, B. E. 2008, AJ, 135, 112

Schwarzschild, M. & Härm, R. 1965, ApJ, 142, 855

Seab, C. G. & Shull, J. M. 1983, ApJ, 275, 652

Sedlmayr, E. & Dominik, C. 1995, Space Science Reviews, 73, 211

Simis, Y. J. W., Icke, V., & Dominik, C. 2001, A&A, 371, 205

Skrutskie, M. F., Cutri, R. M., Stiening, R., et al. 2006, AJ, 131, 1163

Sloan, G. C., Kraemer, K. E., Goebel, J. H., & Price, S. D. 2003a, ApJ, 594, 483

Sloan, G. C., Kraemer, K. E., Matsuura, M., et al. 2006, ApJ, 645, 1118

Sloan, G. C., Kraemer, K. E., Price, S. D., & Shipman, R. F. 2003b, ApJS, 147, 379

Sloan, G. C., Kraemer, K. E., Wood, P. R., et al. 2008, ApJ, 686, 1056

Sloan, G. C., Matsunaga, N., Matsuura, M., et al. 2010, ApJ, 719, 1274

Sloan, G. C., Matsuura, M., Zijlstra, A. A., et al. 2009, Science, 323, 353

Sloan, G. C. & Price, S. D. 1995, ApJ, 451, 758

Sloan, G. C. & Price, S. D. 1998, ApJS, 119, 141

Sofia, U. J., Cardelli, J. A., & Savage, B. D. 1994, ApJ, 430, 650

Sogawa, H. & Kozasa, T. 1999, ApJL, 516, L33

Soszyński, I., Poleski, R., Udalski, A., et al. 2008, Acta Astron., 58, 163

Soszyński, I., Udalski, A., Szymański, M. K., et al. 2009, Acta Astron., 59, 1

Soszyński, I., Udalski, A., Szymański, M. K., et al. 2011, Acta Astron., 61, 217

Speck, A. K., Barlow, M. J., Sylvester, R. J., & Hofmeister, A. M. 2000, A&AS, 146, 437

Speck, A. K., Whittington, A. G., & Hofmeister, A. M. 2011, ApJ, 740, 93

Speck, A. K., Whittington, A. G., & Tartar, J. B. 2008, ApJL, 687, L91

Srinivasan, S., Meixner, M., Leitherer, C., et al. 2009, AJ, 137, 4810

Srinivasan, S., Sargent, B. A., & Meixner, M. 2011, A&A, 532, A54

Stencel, R. E., Nuth, III, J. A., Little-Marenin, I. R., & Little, S. J. 1990, ApJL, 350, L45

Stetson, P. B. 1987, PASP, 99, 191

Straniero, O., Chieffi, A., Limongi, M., et al. 1997, ApJ, 478, 332

Sugerman, B. E. K., Ercolano, B., Barlow, M. J., et al. 2006, Science, 313, 196

Sugimoto, D. & Nomoto, K. 1975, PASJ, 27, 197

Suh, K.-W. 1999, MNRAS, 304, 389

Suttner, G., Yorke, H. W., & Lin, D. N. C. 1999, ApJ, 524, 857

Sylvester, R. J., Kemper, F., Barlow, M. J., et al. 1999, A&A, 352, 587

Szewczyk, O., Pietrzyński, G., Gieren, W., et al. 2009, AJ, 138, 1661

Tielens, A. G. G. M. 1990, in From Miras to Planetary Nebulae: Which Path for Stellar Evolution?, ed. M. O. Mennessier & A. Omont (Editions Frontieres), 186–200

Tielens, A. G. G. M. 1998, ApJ, 499, 267

Timmes, F. X., Woosley, S. E., & Weaver, T. A. 1995, ApJS, 98, 617

Toon, O. B. & Ackerman, T. P. 1981, Appl. Opt., 20, 3657

Travaglio, C., Galli, D., Gallino, R., et al. 1999, ApJ, 521, 691

Treffers, R. & Cohen, M. 1974, ApJ, 188, 545

Tsuji, T., Ohnaka, K., Aoki, W., & Yamamura, I. 1997, A&A, 320, L1

Ueta, T. & Meixner, M. 2003, ApJ, 586, 1338

van Boekel, R., Min, M., Waters, L. B. F. M., et al. 2005, A&A, 437, 189

van den Bergh, S. 2000, The Galaxies of the Local Group (Cambridge)

van der Marel, R. P. & Cioni, M.-R. L. 2001, AJ, 122, 1807

van der Marel, R. P., Cretton, N., de Zeeuw, P. T., & Rix, H.-W. 1998, ApJ, 493, 613

van Langevelde, H. J., van der Heiden, R., & van Schooneveld, C. 1990, A&A, 239, 193

van Leeuwen, F., ed. 2007, Astrophysics and Space Science Library, Vol. 350, Hipparcos, the New Reduction of the Raw Data

van Loon, J. T. 2000, A&A, 354, 125

van Loon, J. T. 2006, in Astronomical Society of the Pacific Conference Series, Vol. 353, Stellar Evolution at Low Metallicity: Mass Loss, Explosions, Cosmology, ed. H. J. G. L. M. Lamers, N. Langer, T. Nugis, & K. Annuk, 211

van Loon, J. T., Cioni, M., Zijlstra, A. A., & Loup, C. 2005, A&A, 438, 273

van Loon, J. T., Cohen, M., Oliveira, J. M., et al. 2008, A&A, 487, 1055

van Loon, J. T., Groenewegen, M. A. T., de Koter, A., et al. 1999, A&A, 351, 559

van Loon, J. T., McDonald, I., Oliveira, J. M., et al. 2006, A&A, 450, 339

van Loon, J. T., Zijlstra, A. A., Bujarrabal, V., & Nyman, L.-Å. 2001, A&A, 368, 950

van Winckel, H. 2003, ARA&A, 41, 391

Vassiliadis, E. & Wood, P. R. 1993, ApJ, 413, 641

Ventura, P., D'Antona, F., & Mazzitelli, I. 2002, A&A, 393, 215

Ventura, P., D'Antona, F., Mazzitelli, I., & Gratton, R. 2001, ApJL, 550, L65

Verhoelst, T., van der Zypen, N., Hony, S., et al. 2009, A&A, 498, 127

Vijh, U. P., Meixner, M., Babler, B., et al. 2009, AJ, 137, 3139

Voshchinnikov, N. V., Il'in, V. B., Henning, T., & Dubkova, D. N. 2006, A&A, 445, 167

Wallerstein, G. & Knapp, G. R. 1998, ARA&A, 36, 369

Waters, L. B. F. M. & Leinert, C. 2008, in The Power of Optical/IR Interferometry: Recent Scientific Results and 2nd Generation, ed. A. Richichi, F. Delplancke, F. Paresce, & A. Chelli, 163

Waters, L. B. F. M., Molster, F. J., de Jong, T., et al. 1996, A&A, 315, L361

Werner, M. W., Roellig, T. L., Low, F. J., et al. 2004, ApJS, 154, 1

Westerlund, B. E. 1997, Cambridge Astrophysics Series, 29

Westerlund, B. E., Olander, N., Richer, H. B., & Crabtree, D. R. 1978, A&AS, 31, 61

Wheeler, J. C., Sneden, C., & Truran, Jr., J. W. 1989, ARA&A, 27, 279

Whitelock, P., Menzies, J., Feast, M., et al. 1994, MNRAS, 267, 711

Whitelock, P. A., Feast, M. W., & van Leeuwen, F. 2008, MNRAS, 386, 313

Whitelock, P. A., Feast, M. W., van Loon, J. T., & Zijlstra, A. A. 2003, MNRAS, 342, 86

Whittet, D. C. B., ed. 1992, Dust in the galactic environment (IoP)

Whittet, D. C. B. 2004, in IAU Symposium, Vol. 213, Bioastronomy 2002: Life Among the Stars, ed. R. Norris & F. Stootman, 163

Wickramasinghe, N. C., Donn, B. D., & Stecher, T. P. 1966, ApJ, 146, 590

Willson, L. A. 2000, ARA&A, 38, 573

Woitke, P. 2006, A&A, 460, L9

Woitke, P., Helling, C., Winters, J. M., & Jeong, K. S. 1999, A&A, 348, L17

Wood, P. R. 1990, in From Miras to Planetary Nebulae: Which Path for Stellar Evolution?, ed. M. O. Mennessier & A. Omont (Editions Frontieres), 67–84

Wood, P. R., Bessell, M. S., & Fox, M. W. 1983, ApJ, 272, 99

Wood, P. R., Habing, H. J., & McGregor, P. J. 1998, A&A, 336, 925

Wood, P. R. & Sebo, K. M. 1996, MNRAS, 282, 958

Wood, P. R., Whiteoak, J. B., Hughes, S. M. G., et al. 1992, ApJ, 397, 552

Woods, P. M., Oliveira, J. M., Kemper, F., et al. 2011, MNRAS, 411, 1597

Woods, P. M., Walsh, C., Cordiner, M. A., & Kemper, F. 2012, MNRAS, 426, 2689

Woolf, N. J. & Ney, E. P. 1969, ApJL, 155, L181

Worthey, G., Mateo, M., Alonso-García, J., & España, A. L. 2004, PASP, 116, 295

Wright, E. L., Eisenhardt, P. R. M., Mainzer, A. K., et al. 2010, AJ, 140, 1868

Xiong, G. Z., Chen, P. S., & Gao, H. 1994, A&AS, 108, 661

Yamamura, I., de Jong, T., & Cami, J. 1999, A&A, 348, L55

Young, K. 1995, ApJ, 445, 872

Zaritsky, D., Harris, J., Thompson, I. B., & Grebel, E. K. 2004, AJ, 128, 1606

Zhukovska, S., Gail, H.-P., & Trieloff, M. 2008, A&A, 479, 453

Zijlstra, A. A. 2004, MNRAS, 348, L23

Zijlstra, A. A., Matsuura, M., Wood, P. R., et al. 2006, MNRAS, 370, 1961

EVOLVED STARS IN THE LOCAL GROUP

We are now cruising at a level of two to the power of twenty-five thousand to one against and falling, and we will be restoring normality just as soon as we are sure what is normal anyway.

Douglas Adams